REPORT DOCUMENTATION PAGE

Form Approved
OMB No. 0704-0188

1. REPORT DATE (DD-MM-YYYY) 21-10-2008	2. REPORT TYPE Final Report	3. DATES COVERED (From - To) Dec.2002 – Sept. 2007

4. TITLE AND SUBTITLE	5a. CONTRACT NUMBER
Blast and Fragment Protective Sandwich Panel Concepts for Stainless Steel Monohull Designs	
	5b. GRANT NUMBER N00014-03-1-0281
	5c. PROGRAM ELEMENT NUMBER

6. AUTHOR(S)	5d. PROJECT NUMBER
H.N.G. Wadley	118031-101-GG10497-31340
	5e. TASK NUMBER
	5f. WORK UNIT NUMBER

7. PERFORMING ORGANIZATION NAME(S) AND ADDRESS(ES)	8. PERFORMING ORGANIZATION REPORT NUMBER
University of Virginia Office of Sponsored Programs P. O. Box 400195 Charlottesville, Virginia 22904-4195	

9. SPONSORING / MONITORING AGENCY NAME(S) AND ADDRESS(ES)	10. SPONSOR/MONITOR'S ACRONYM(S)
Office of Naval Research Materials Science Division 800 N. Quincy Street Arlington, VA 22217	N/A
	11. SPONSOR/MONITOR'S REPORT NUMBER(S) N/A

12. DISTRIBUTION / AVAILABILITY STATEMENT

Approved for public release, distribution unlimited.

13. SUPPLEMENTARY NOTES
N/A

14. ABSTRACT

The prevention or mitigation of ship hull damage from underwater explosions (UNDEX) is of vital need for surface combatant Naval ships. This research program sought to devise blast and ballistic protection concepts applicable to the design and fabrication of ship hull structures using AL6XN stainless steel sandwich panel constructions, which met threat and protection levels defined by the Navy. Efforts were undertaken in two phases to design, fabricate, experimentally investigate and analyze the quasi-static and dynamic behavior of sandwich beams and plates for several sandwich core topologies, at different size scales to evaluate their performance in underwater explosion (UNDEX), in air (AIREX), surface (SURFEX) and ballistic test environments. Several periodic cellular sandwich cores were assessed by performing dynamic uni-axial compression tests, stretch-bend type sub-scale ($1/12^{th}$ and $1/5^{th}$ full-scale) panel tests, and full-scale ballistic tests. Constitutive models were developed for the down selected core topologies to enable the implementation of more convenient large (ship) scale analyses. Soft response cores such as the prismatic cores and multilayer pyramidal cores were found better suited for water blast loading applications and ship hull blister attachments.

15. SUBJECT TERMS

16. SECURITY CLASSIFICATION OF:			17. LIMITATION OF ABSTRACT	18. NUMBER OF PAGES	19a. NAME OF RESPONSIBLE PERSON H.N.G. Wadley
a. REPORT Unclassified	b. ABSTRACT Unclassified	c. THIS PAGE Unclassified	UL		19b. TELEPHONE NUMBER (include area code) (434)982-5671

Standard Form 298 (Rev. 8-98)
Prescribed by ANSI Std. Z39.18

Final Report

Blast and Fragment Protective Sandwich Panel Concepts for Stainless Steel Monohull Designs

Grant Number N00014-03-1-0281

SUBMITTED TO

Office of Naval Research

SUBMITTED BY

Principal Investigator
Haydn N.G. Wadley
University Professor
Department of Materials Science and Engineering
School of Engineering and Applied Science
University of Virginia
Charlottesville, Virginia 22903

Co-Investigators
Anthony G. Evans, Robert M. McMeeking and Frank Zok
Departments of Mechanical Engineering and Materials
University of California
Santa Barbara, California 93106

20081031020

EXECUTIVE SUMMARY

This research program sought to devise blast and ballistic protection concepts applicable to the design and fabrication of ship hull structures using AL6XN stainless steel sandwich panel constructions, which met threat and protection levels defined by the Navy. Efforts were undertaken in two phases to design, fabricate, experimentally investigate and analyze the quasi-static and dynamic behavior of sandwich beams and plates for several sandwich core topologies, at different size scales to evaluate their performance in underwater explosion (UNDEX), in air (AIREX), surface (SURFEX) and ballistic test environments. Several periodic cellular sandwich cores were assessed by performing dynamic uni-axial compression tests, stretch-bend type sub-scale (1/12th and 1/5th scale) panel tests, and full-scale ballistic tests. Constitutive models were developed for the down selected core topologies to enable the implementation of more convenient large (ship) scale analyses. Soft response cores such as the prismatic cores and multilayer pyramidal cores were found better suited for water blast loading applications and ship hull blister attachments.

Technical Approach

The approach used in this research program exploited progress made in metallic sandwich panel design and optimization concepts and advances made in fabrication techniques. Guidance from collaborating groups performing modeling work (ATR, Burtonsville, MD, Naval Surface Warfare Center, Indian Head, MD and University of California, Santa Barbara) was used to select sandwich panel design parameters for face sheet, core thicknesses, the relative density of the core, and panel sizes for quasi-static and dynamic load testing. Panels were fabricated using a transient liquid phase bonding approach while an alternate joining technique such as laser welding was explored for scaled-up panel fabrication. The ballistic protection capability of selected sandwich panels were investigated either by integrating a hard ceramic within the sandwich core or as a backing placed against the sandwich panel. Underwater explosion (UNDEX) tests were performed on several candidate sandwich panel designs at the Naval Surface Warfare Center in Carderock, MD. A breakdown of key research performed during the two phases is given below and a list of more detailed papers resulting from the overall research effort is given at the end of the report (Appendices A-G).

Achievements (Phase I)

Periodic cellular material cores can be broadly categorized in to three classes, (a) prismatic, (b) honeycomb, and (c) microtruss cores. The core deformation, strength, and energy absorption of each of these classes is a function of the sandwich panel design geometry, the material properties, and specific loading condition. (e.g. compression, shear, bending). The core deformation, strength, and energy absorption of each of these topology classes is a function of the sandwich panel design geometry, the material properties, and specific loading condition. (e.g. compression, shear, bending). During Phase I, sandwich panels with periodic cellular cores covering all three topology classes were fabricated for dynamic compression tests ("Dynocrusher" test) in a modified paddlewheel test device used by the Naval Surface Warfare Center, Carderock, MD for underwater explosion (UNDEX) tests. For the dynocrusher tests, 8-inch diameter, 4-inch thick cylindrical shaped, 304 and AL6XN grade stainless steel alloy samples were designed, fabricated by the University of Virginia and tested at NSWC Carderock in the regular corrugation, diamond corrugation, square honeycomb, triangular honeycomb, and pyramidal core topologies. Four out of the five topologies are shown in Figure 1.
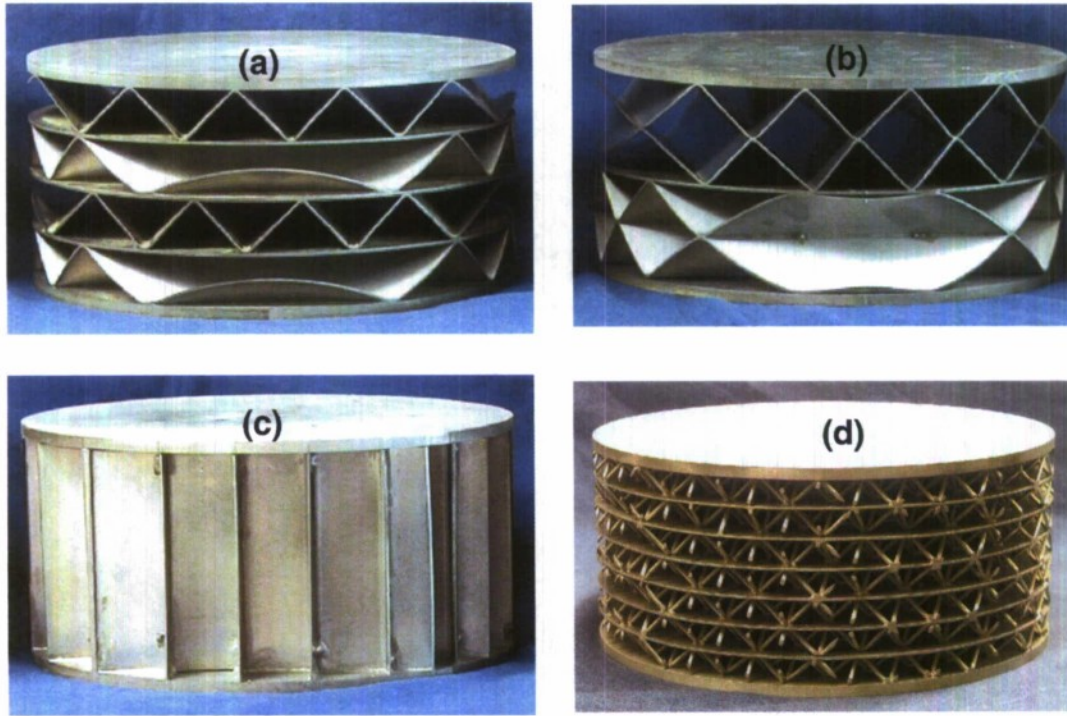
Figure 1. 8-inch diameter, 4-inch thick "dynocrusher" test specimens with periodic cellular sandwich cores. (a) regular corrugation (b) diamond corrugation (c) square honeycomb (d) pyramidal core.

Prototype 29" x 29" x 2" thick AL6XN sandwich panels with a 'Navtruss' corrugated core topology (based on a design provided by Advanced Technology and Research (ATR) Inc.) were then fabricated and brazed in a picture frame assembly (Figure 2). The 2" core thickness selection represented a 1/12th scaled size of a full-scale (24" thick core) panel design. The fabrication technology and the optimized brazing cycle information were transferred to Cellular Materials International, Inc. for the fabrication of additional sets of 29-inch square mini-paddlewheel test samples, with the other candidate core topologies (square honeycomb, triangular honeycomb, multilayer pyramidal, X-truss, Y-truss).
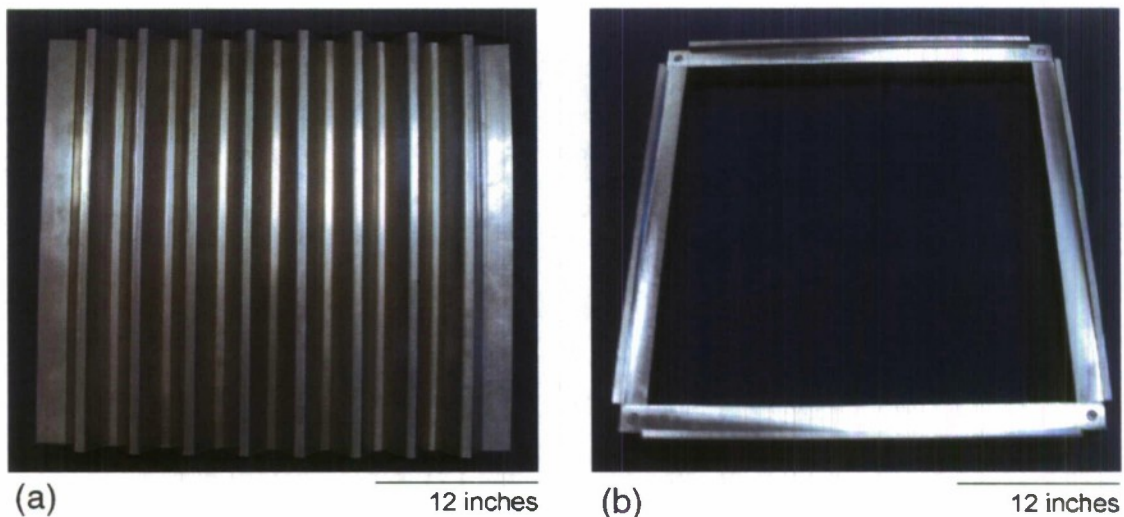

Figure 2. Photographs of, (a) "Navtruss" corrugated core (b) A "picture frame" type panel edge support.

Although a focal emphasis in this program was the design, fabrication, testing, and analysis of sandwich panels for blast mitigation, parallel efforts were initiated in investigating the use of these sandwich panels in ballistic protection, primarily by means of incorporating suitable ceramics within or outside of the sandwich structure design. The response to 20 mm diameter fragment simulating projectiles (FSP) and two other projectiles threats designated by the Navy were tested. The use of both porous ceramics and hard ceramics of different materials were evaluated by NSWC Carderock, MD and ATR as candidates for ballistic protection.

In support of a research effort in this program at NSWC Carderock of incorporating porous ceramic as a cast structure with the open core architecture, a set of brazed AL6XN panels with a pyramidal core topology was delivered to the Navy (Figure 3).
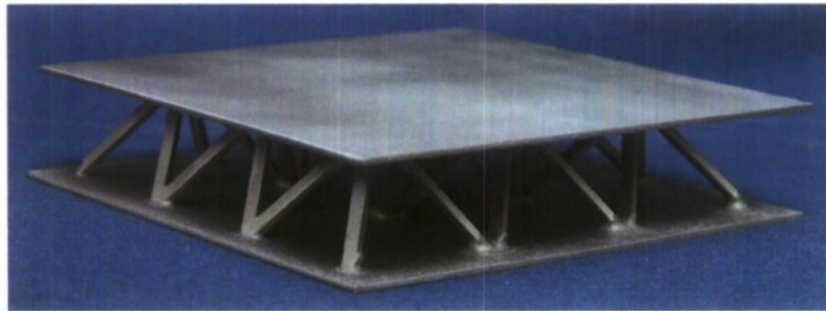

Figure 3. A brazed AL6XN sandwich panel (5.25" x 5" x 1") with a pyramidal core for the integration of porous ceramic within the open cellular structure for ballistic protection.

A study of using dense ceramic powders to fill the free space of the low density cellular metal cores for fragment protection was initiated at the University of California, Santa Barbara. Under ballistic loadings (e.g., projectile impact), ceramic powders undergo compaction and shear deformations, which were expected to consume a significant amount of the kinetic energy of the projectile. It was also postulated that the existence of ceramic powders may spread the impact load over a larger area on the bottom face sheet of the sandwich panel, thus delaying failure of the face sheet. Numerical simulations were performed on axisymmetric models of monolithic plates and square honeycomb core sandwich panels impacted by 20 mm diameter fragment simulating projectiles (Figure 4).
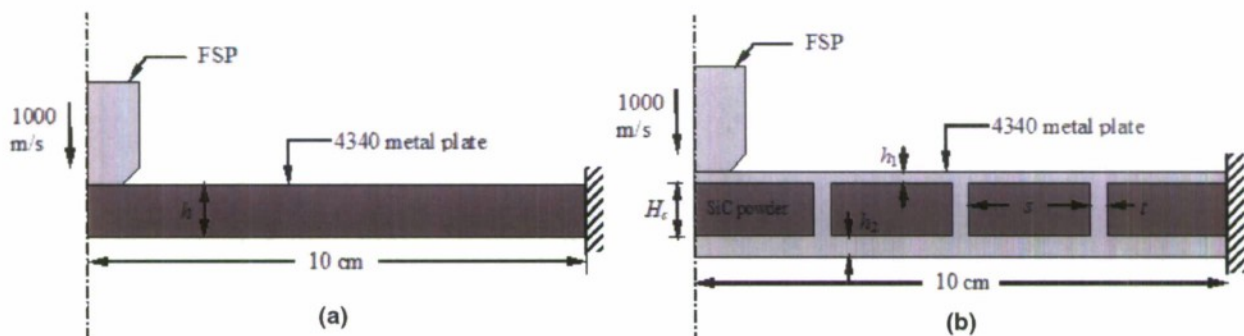

Figure 4. Schematic drawing of the numerical model of a fragment simulating projectile penetrating, (a) a monolithic metal plate, (b) a square honeycomb core sandwich panel filled with SiC ceramic powders.

A series of finite element simulations were initially carried for a 4340 alloy plate of different thicknesses to compute the residual velocity of a fragment simulating projectile (FSP) after complete penetration. The thickness of the plate (h) was increased incrementally until the residual velocity of the FSP became zero. This critical thickness and the associated areal density of the metal plate were identified as the ballistic limit of the metal plate for the chosen FSP. Similar simulations were then performed for a square honeycomb core sandwich panel filled with dense SiC powders. The core thickness of the sandwich panel (H_c) was varied until such time the residual velocity of the projectile reached zero. Figure 5 show the comparison of the results of the monolithic plate with the square honeycomb core sandwich panel.
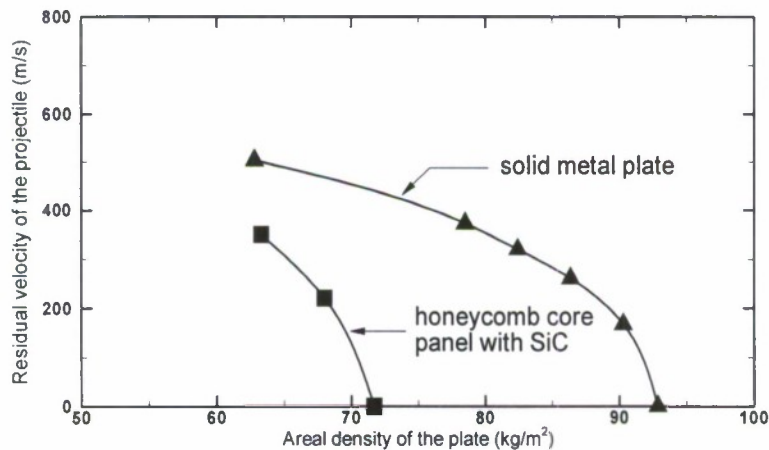

Figure 5. Residual velocity of the fragment simulating projectile (FSP) versus the areal densities of the targets. For the honeycomb panel with SiC powders, h_1 = 2 mm, h_2 = 3 mm, t = 2 mm, s = 23.5 mm

It is observed from Figure 5, that the projectile was arrested at a much lower areal density with the SiC filled sandwich panel than with the solid plate, i.e. the sandwich panel outperformed the monolithic plate in ballistic loading.

The ballistic tests in this program were conducted on full-scale (i.e. 24-inch thick) sandwich panels. The proposed design configuration for these tests was a modular assembly of sandwich panel, an armor pack, and hull plate as shown in Figure 6. In this arrangement, hard ceramic tiles were placed against the back face of the 24-inch thick sandwich panel. In the chosen design, a 5 x 5 array of 4.13" x 4.13" x 0.64" alumina tiles was encased within an AL6XN honeycomb grid for containment and restriction of damage to a localized area during fragmentation (Figure 7).
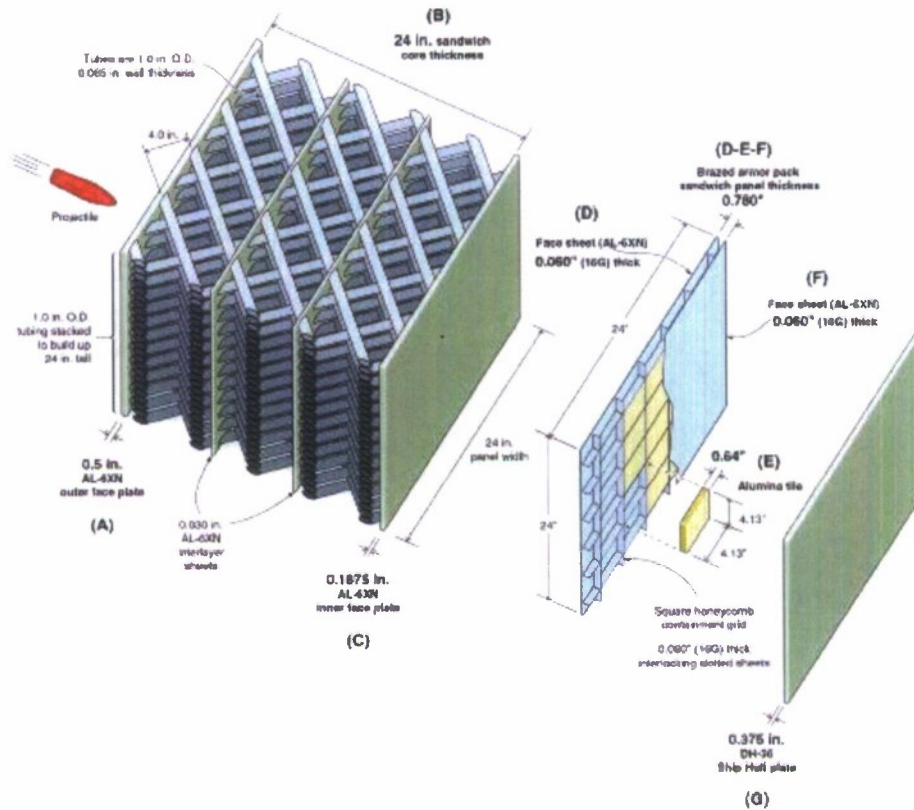
Figure 6. Ballistic test sandwich panel integration concept (hollow truss core panel shown).
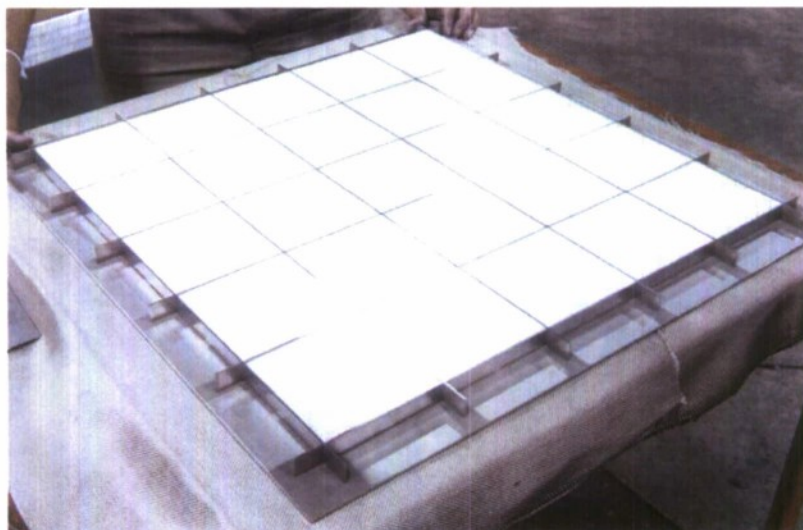
Figure 7. Ceramic tile containment arrangement for the ballistic test armor packs. Twenty five alumina tiles are contained in a 21" x 21" region of the 24" x 24" panel.

Ten armor packs were fabricated in support of the ballistic tests conducted at the Aberdeen Proving Ground in Maryland. Microtruss core sandwich panels with a core relative density of 5%, one based on a multilayered arrangement of hollow tubes (shown in Figure 6), and the other based on a multilayered arrangement of pyramidal lattice truss cores (Figure 8) were designed and fabricated for full-scale ballistic tests.

6

Figure 8. Multi-layered pyramidal core sandwich panel for full-scale ballistic tests.

Achievements (Phase II)

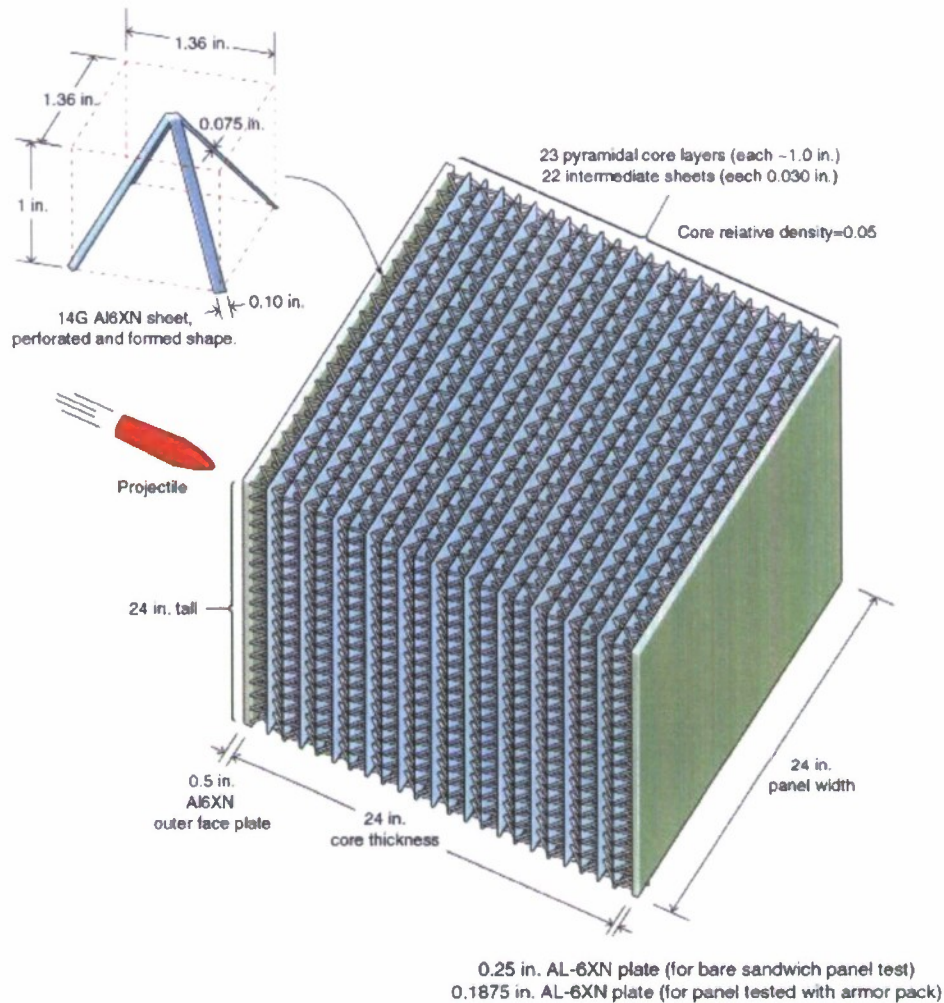During Phase I, the dynocrusher test, 8-inch diameter samples were designed with a 5% core relative density. From the quasi-static and dynocrusher test results, the honeycomb core topologies (square and triangular) were observed to have a higher crushing strength compared to the prismatic and microtruss core topology samples. A square honeycomb core sample was shown in Figure 1c. In the case of the honeycomb samples, in a compression test, the core elements (honeycomb webs) are aligned with the loading direction. For appropriate comparisons with the strength limits of the other core topologies, one way of reducing the core strength is by tailoring its relative density. In this instance, additional sets of square honeycomb dynocrusher samples with a 3% core relative density were fabricated (Figure 9b) for comparisons with the results obtained with the original 5% core relative density samples (Figure 9a).
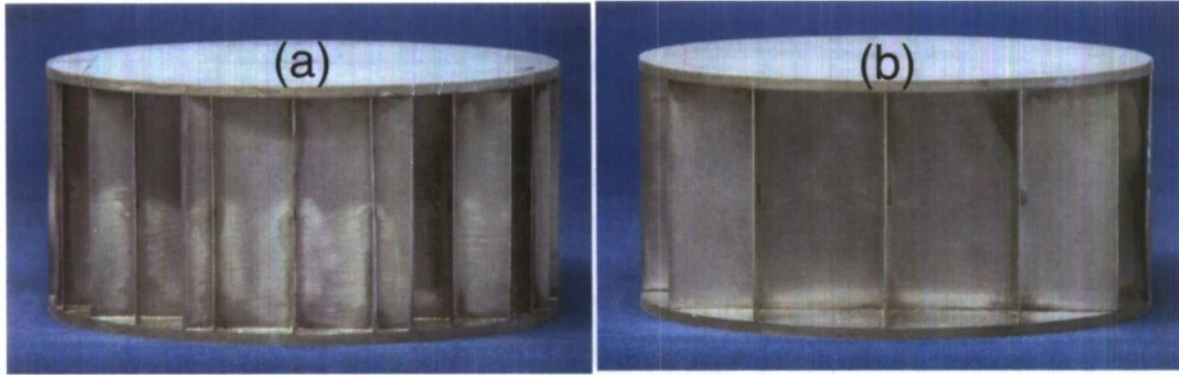
7

Figure 9(a) 5% relative density square honeycomb core dynocrusher sample with a web spacing of 1.2 inches. 9(b). 3% relative density square honeycomb core dynocrusher sample with a web spacing of 2 inches.

Additional dynocrusher samples in the double corrugation (X-truss) design (Figure 10) were fabricated and provided to the Navy for quasi-static and UNDEX tests. Due to the short aspect ratio of the sample (8-inch diameter : 4-inch height), and the necessity to have an appropriate number of unit cells within the sample, a bi-layer, X-truss core arrangement was found to be more suitable, than a "larger" unit cell, X-truss core single-layer between the top and bottom face sheets satisfying the ~3.5-4 inch sample height requirement specified for the test samples by NSWC Carderock.

Figure 10. The double layer X-truss core dynocrusher sample with a core relative density of ~5.5%.

Dynocrusher samples were also designed and fabricated in a microtruss topology using commercial woven wire mesh. Figure 11 shows a bi-layer design of the wire mesh core sandwich panel consisting of two slabs (Figure 11). Due to the laminated assembly of each slab, the properties of each slab are highly anisotropic. It was postulated that with a 0°/ 90° bi-directional lay-up, the anisotropic characteristic of the core will be reduced when subjected to sandwich panel bending.
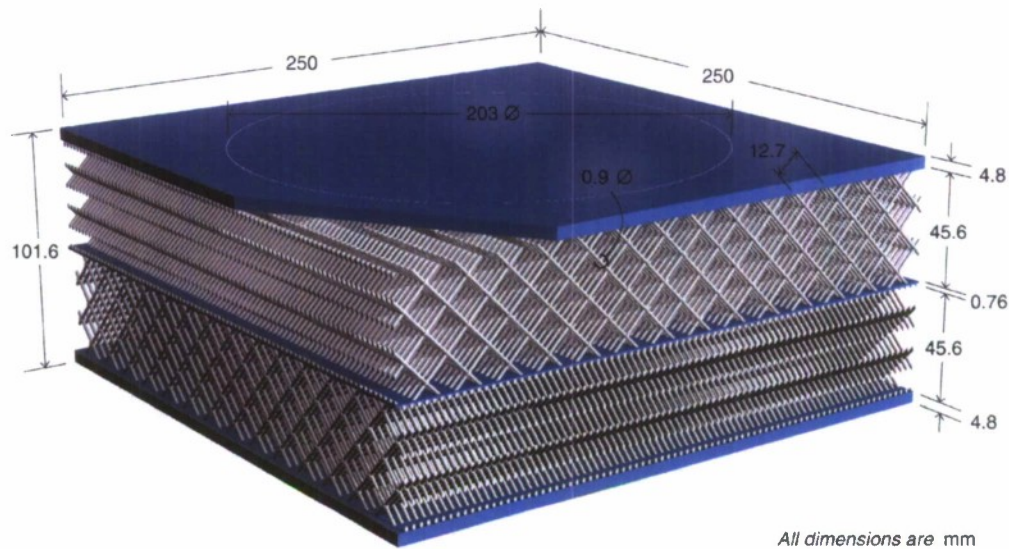
Figure 11. A bi-layer wire mesh core, "dynocrusher" sample design.

The dynocrusher test samples fabricated using a 2-Mesh (i.e. 0.5" or 12.7 mm wire-to-wire spacing), 0.035" (0.9 mm) wire diameter, commercial wire mesh is shown in Figure 12. Four samples were provided to NSWC/Carderock for testing.

Figure 12 Woven wire mesh core, 8-inch diameter, "Dynocrusher" test samples. The wire diameter is 0.035", and the wires are spaced 0.5" apart. The core relative density is 0.055

Each of the Phase I sandwich core topologies were tested for ballistic protection performance at a test range at the Aberdeen Proving Ground, MD. Due to the inability to meaningfully scale down the appropriate projectile threat levels, AL6XN sandwich panels had to be fabricated at the full-scale (24-inch) core sizes for ballistics tests that were performed with two unspecified full-scale threat levels. The University of Virginia fabricated 6, 24" x 24" x 24" block size sandwich panels with two microtruss core designs. Figure 13 shows a multilayer hollow truss (tubular) core sandwich panel which is a brazed assembly of 0.5" thick front and either 0.188" or 0.25" thick back face plates, 3 diamond oriented tube core slabs and two intermediate solid layers. The tubular core assembly consisted of 1" O.D, 0.065" wall thickness AL6XN tubes spaced ~4.25 inches apart with the three slabs separated by two 16GA (0.060") thick sheets giving an effective core relative density of ~5%. Figure 14 shows a multilayer pyramidal core sandwich panel, with 23, 1" core height pyramidal layers separated by 22, 22GA (0.030")

intermediate solid layers. Ballistics tests were performed by Navy personnel with 20mm diameter fragment simulating projectiles and two other projectile threat levels, on the bare panels with the 0.25" thick back face sheet, and also on the panels with the 0.188" thick back face sheet, by placing a ceramic tile contained 'armor' pack against the back face. The effect with and without the ceramic supported back face was tested for each of the core topologies, to determine whether ceramic reinforcement would be needed or not for the down selected sandwich core designs.
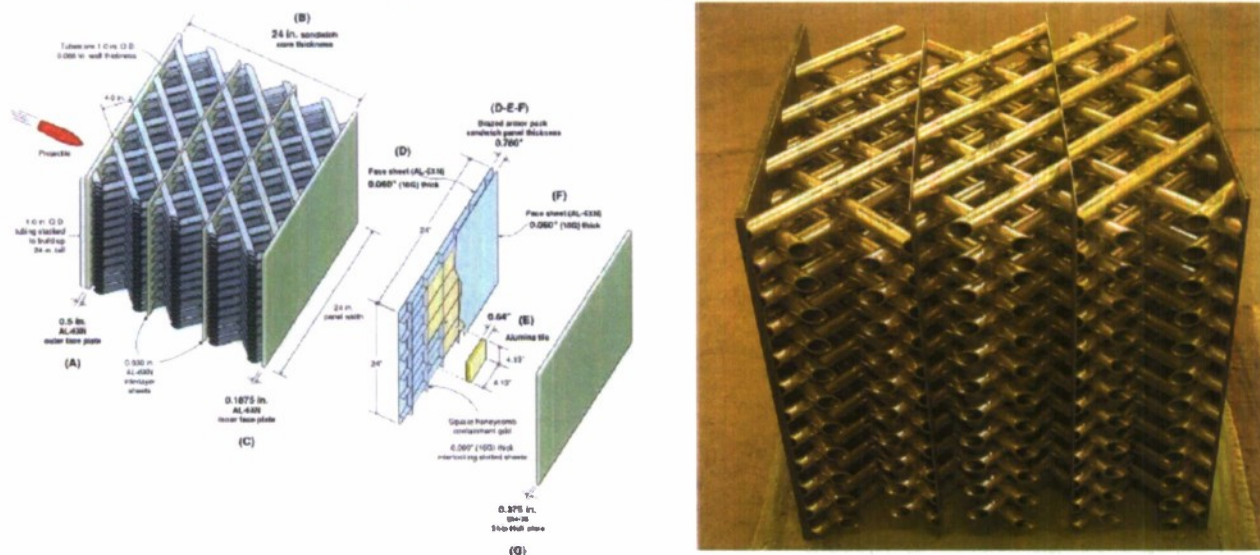
Figure 13. Brazed full-scale (24 in. thick) tube core sandwich panel for ballistic tests.
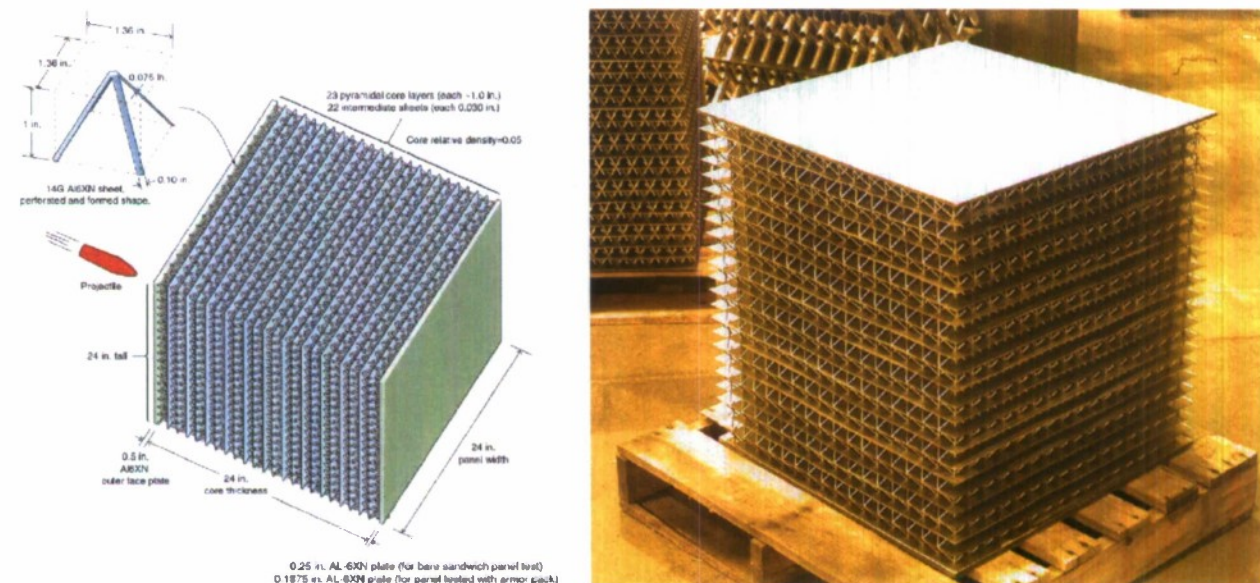
Figure 14. Brazed full-scale (24 in. thick) pyramidal core sandwich panel for ballistic tests.

The University of Virginia led a "tiger team" entrusted with the task of developing concepts for the full-scale fabrication of blast protection blister compatible with shipyard construction practices along with members from ATR, Bath Iron Works, CMI, NSWC/Carderock Division, NSWC/Indian Head division, UCSB. The following issues were addressed.

1. Methods of blister attachment to the hull
2. Methods for assembling/joining (core and face sheet) components to create panels and blisters
3. Integration of the blister with the bilge keel consistent with ship yard practices
4. Methods for welding and inspecting full scale panels which are also applicable to second generation 1/5th scale panels

A report laying out details of fabrication methods for the three down selected sandwich panel topologies (square honeycomb, X-truss and pyramidal core) and presenting approaches of attaching full-scale blisters to ship hulls was issued to ONR (Appendix H). The recommended approach uses a tiling approach to create a blister from a tile → sub-panel → panel → blister arrangement illustrated in Figure 15.
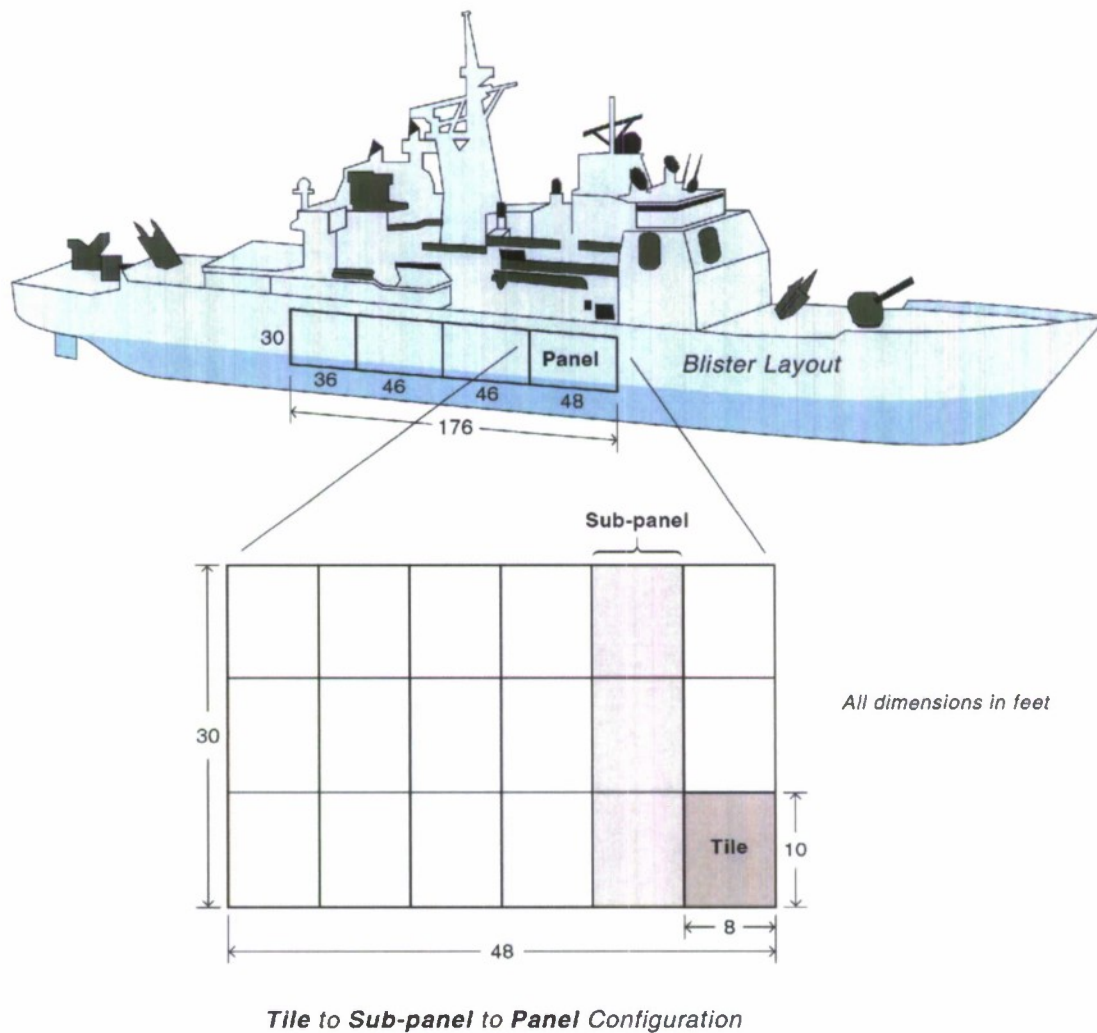

Figure 15. Blister assembly concept

CONSTITUTIVE MODEL DEVELOPMENT

Constitutive models are required as input for large ship-scale analysis, where 3-D finite element analysis methods are impractical due to the model geometry size and computational time. The downselected three topologies of interest to the Navy were the square honeycomb core, X-truss and multilayer pyramidal core topologies.

The modeling and analysis capabilities of the DYSMAS finite element hydrocode were demonstrated by ATR and NSWC on the X-truss, Y-truss and square honeycomb topologies for the $1/12^{th}$ scale (2-inch core) panel geometries. Good agreement was indicated with the UNDEX tests performed using the modified mini paddlewheel test fixture. By comparison, the topology of the multilayer pyramidal core posed a more complex modeling challenge for DYSMAS users.

A dynamic constitutive model for the square honeycomb core was developed by collaborators at Harvard University on a parallel ONR funded MURI program. Their simulations show a 2-3 fold increase in dynamic to static strength due to strain rate sensitive effects on hardening of the stainless steels of interest and inertial effects of the core consistent with experimental observations of UNDEX tests performed on "dynocrusher" test samples at NSWC Carderock. The University of California, Santa Barbara (UCSB) team developed constitutive models for the multilayer pyramidal core and multilayer prismatic cores. Continuum constitutive laws applicable to truss and prismatic cores were implemented and assessed comparing their predictions with the "dynocrusher" experiments. The laws were based on Hill's yield criterion for orthotropic materials, modified to account for the effects of mean stress and the associated compressibility upon plastic straining.

Parameters characterizing initial yield were obtained from both approximate stress analyses and finite element calculations of unit cells. Finite element calculations were also been used to calibrate the hardening. Once calibrated, the law was used to simulate the bending response of various sandwich panels under either simply-supported or clamped end conditions. An assessment of the constitutive law was made through comparisons with corresponding finite element calculations in which the core and face elements were fully meshed. Additional assessments were made through experimental measurements on a family of sandwich panels fabricated from a ductile stainless steel. Comparisons were made on the basis of the global load-displacement response as well as the distribution of shear strain within the core. Issues associated with end effects, boundary conditions and deformation localization were addressed. Overall, the comparisons revealed that the proposed constitutive law was capable of predicting most of the pertinent features of sandwich panels with high fidelity.

Specifically, the onset of yield, the hardening rate, the peak loads, and the deformations within the core were adequately predicted. The largest apparent discrepancy pertains to the prediction of the onset of strain localization, especially when failure is core-dominated. When compared with both experiments and fully-meshed FE calculations, the continuum model overestimated the critical displacement. This discrepancy was largely attributable to the isotropic nature of the hardening law. That is, because strain hardening of the core was assumed to occur uniformly (without change in shape of the yield surface), some modes of deformation localization may be artificially delayed. This is the case, for example, when the law is calibrated by the shear stress-strain curve and localization occurs by core crushing at one of the loading points. This shortcoming was remedied by extending the constitutive law to account for non-uniform hardening.

A dynamic version of the constitutive law was developed (Appendix I). It was calibrated by using dynamic unit cell simulations. The input embodies the material strain rate sensitivity as well as the inertial effect associated with buckling suppression. Comparisons with dynamic experimental measurements were performed involving impact by a metal foam projectile onto a square honeycomb panel at high impulse at strain rates of order 1,000/s and the "dynocrusher" test simulation on the multilayer pyramidal core panel and multilayer prismatic (triangular core and diamond core) panels.

The experimental and analysis efforts of this program indicated that a soft core response was preferred for water blast loading, since the soft cores such as the X-truss core and multi-layer pyramidal core enabled the dissipation of the impulse over a longer time period at lower transmitted peak pressures than stronger cores such as the square and triangular honeycomb cores. Further consideration was also given to the ease of fabrication of larger (12" and 24" thick cores, i.e. half-scale and full-scale) with these topologies in the form of blisters conforming to the curved profiles of the proposed ship hulls, and a final recommendation was made to select a X-truss core topology.

APPENDICES

[A]. Paper on the "Compressive Response of Multilayered Pyramidal Lattices During Underwater Shock Loading", H.N.G. Wadley, K. Dharmasena, Yungchia Chen, Philip Dudt, David Knight, Robert Charette, and Kenneth Kiddy, International Journal of Impact Engineering, Vol. 35, pp. 1102-1114, 2008.

[B]. Paper on the "Analysis and Interpretation of a Test for Characterizing the Response of Sandwich Panels to Water Blast", Z. Wei, A.G. Evans, K.P. Dharmasena and H.N.G. Wadley, International Journal of Impact Engineering, 34, pp.1602-1618, 2007.

[C]. Paper on the "Dynamic Compression of Square Honeycomb Structures During Underwater Impulsive Loading", H.N.G. Wadley, K.P. Dharmasena, D.T. Queheillalt, Y. Chen, P. Dudt, D. Knight, K. Kiddy, Z. Xue and A. Vaziri, J.Mechanics of Materials and Structures,Vol.2(10), pp.2025-2048, 2007.

[D]. Paper on the "Deformation and Fracture Modes of Sandwich Structures Subjected to Underwater Impulsive Loads", L. F. Mori, S. Lee, Z. Y. Xue, A. Vaziri, D. T. Queheillalt, K. P. Dharmasena, H. N. G. Wadley, J. W. Hutchinson, H. D. Espinosa, Journal of Mechanics of Materials and Structures, Vol. 2, No. 10, pp. 1981-2006, 2007.

[E]. Paper on "The Resistance of Metallic Plates to Localized Impulse", Z. Wei, V.S. Deshpande, A.G. Evans, K.P. Dharmasena, D.T. Queheillalt, H.N.G. Wadley, Y. Murty, R.K. Elzey, P. Dudt, Y. Chen, D. Knight, and K. Kiddy, Journal of Mechanics & Physics in Solids, Vol 56, pp. 2074-2091, 2008.

[F]. Paper on the "Dynamic Response of a Multilayer Prismatic Structure to Impulsive Loads Incident from Water," K.P. Dharmasena, D.T. Queheillalt, H.N.G. Wadley, Y.Chen, P.Dudt, D.Knight, Z. Wei and A.G Evans, Int. J. Impact Engineering, In Press (2008),doi: 10.1016/j.ijimpeng.2008.06.002.

[G]. Paper on the "Dynamic Compression of Metallic Sandwich Structures During Planar Impulsive Loading in Water," K.P. Dharmasena, D.T. Queheillalt, H.N.G. Wadley, P. Dudt, Y. Chen, D. Knight, A.G. Evans and V.S. Deshpande, European Journal of Mechanics – A/Solids, accepted (2008).

[H]. SSM Shipyard Fabrication Tiger Team Report (2005). J.Goeller,J. McNelia, P.Dudt, R. Michaelson, K.Kiddy, Y.Murty, K.Elzey, H. Burns, M.Riley, T. Evans, K.Dharmasena, P.Parrish, and H. Wadley.

[I]. Constitutive Laws for Metallic Sandwich Panels, A.G. Evans, R.M. McMeeking and F.W. Zok.

Appendix A

Compressive response of multilayered pyramidal lattices during underwater shock loading

Haydn Wadley[a], Kumar Dharmasena[a,*], Yungchia Chen[b], Philip Dudt[b], David Knight[b], Robert Charette[b], Kenneth Kiddy[c]

[a]Department of Materials Science & Engineering, University of Virginia, Charlottesville, VA 22904, USA
[b]Naval Surface Warfare Center, Carderock, MD 20817, USA
[c]Indian Head Division, Naval Surface Warfare Center, Indian Head, MD 20640, USA

Abstract

The quasi-static and dynamic compressive mechanical response of a multilayered pyramidal lattice structure constructed from stainless-steel was investigated. The lattices were fabricated by folding perforated 304 stainless steel sheets and bonding them to thin intervening sheets using a transient liquid-phase bonding technique. The resulting structure was attached to thick face sheets and the through thickness mechanical response was investigated quasi-statically and dynamically, in the latter case using a planar explosive loading technique. The lattice is found to crush in a progressive manner by the sequential (cooperative) buckling of truss layers. This results in a quasi-static stress strain response that exhibits a significant "metal foam" like stress plateau to strains of about 60% before rapid hardening due to truss impingement with the intermediate face sheets. During dynamic loading, sequential buckling of the truss layers was manifested as a series of transmitted pressure pulses measured at the back face of the test samples. The sequential buckling extended the duration of the back face pressure–time waveform and significantly reduced the transmitted pressure measured at the back face. The impulse transmitted to the structure is found to be about 28% less than that predicted by analytic treatments of the fluid-structure interaction for fully supported structures. This transmitted impulse reduction appears to be a consequence of the wet side face sheet movement away from the blast wave and is facilitated by the low crush resistance of the lattice structure.
© 2007 Elsevier Ltd. All rights reserved.

Keywords: Compressive response; Sandwich panels; Pyramidal lattice; Impulse loading

1. Introduction

There is a growing interest in extending shock protection concepts developed for low-velocity impacts (such as component packaging, head impact protection and vehicle occupant injury prevention during automobile accidents) [1] to the high-intensity, dynamic loading situations encountered when explosively created shock waves impinge upon structures [2–4]. Numerous blast mitigation approaches can be envisioned including increasing the strength or mass of protective structures, using impact energy absorbing schemes [5], adding polymer coatings/films to retard fracture [6] and perhaps the use of active

approaches that cancel in whole or in part, the momentum imparted to a structure by a shock wave [7]. In the blast-loading situation, the deformation rates of structures correspond to velocities of motion in the 100 m/s or greater range [8]. This is more than an order of magnitude greater than those typically encountered in automobile collisions and most other impact events [1]. Dynamic effects might therefore be more significant and need to be addressed during design of blast mitigation structures.

One approach to blast mitigation exploits crushable cellular materials [1]. Consider the processes that follow an underwater explosion near a sandwich panel structure with a cellular topology core (Fig. 1). Within the explosive, detonation converts solids to gases across a detonation front that propagates at speeds of ∼5000–10,000 m/s [9]. The solid to vapor transition results in a highly pressurized

*Corresponding author.
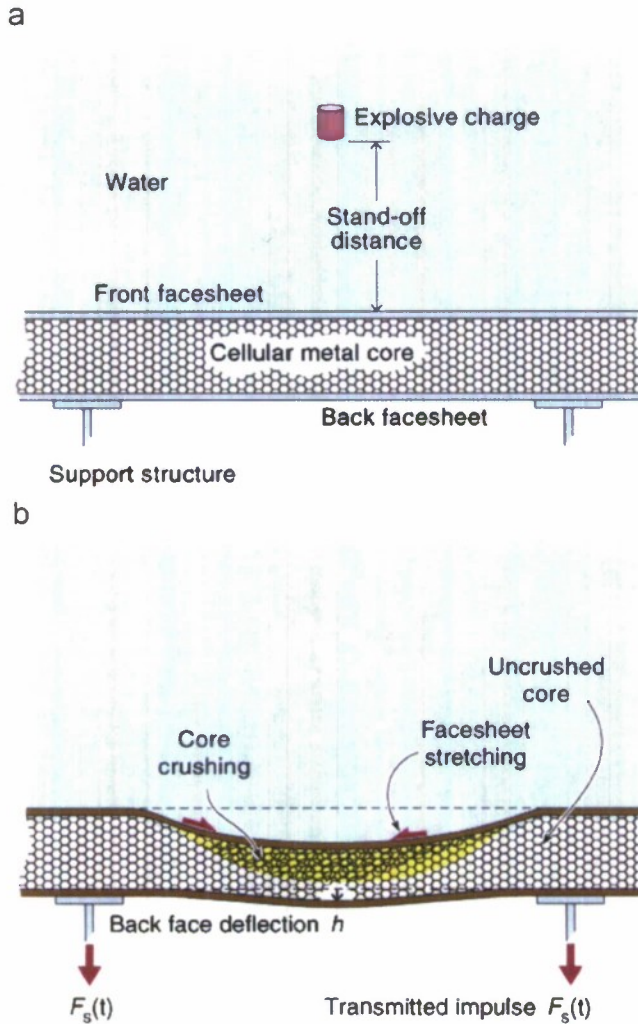E-mail address: kpd2t@virginia.edu (K. Dharmasena).

a

b

Fig. 1. Schematic illustration of the protection of a structure using a cellular metal core sandwich panel. For an explosion (here in water), blast wave mitigation is achieved by control of the fluid-structure interaction at the face sheet–water interface and by core collapse and face sheet stretching of the structure. (a) Before explosion; (b) after explosion.

gas bubble (with internal pressures of 1–10 GPa). The bubble rapidly expands, initially at the detonation velocity of the explosive. This is greatly in excess of the acoustic sound speed in water (~1400 m/s). This supersonically forces water outwards, creating an intense high-speed shock wave traveling towards the sandwich structure. Nonlinear effects in water are less significant than those in air and the blast front speed quickly approaches the acoustic velocity limit.

The pressure pulse in water rises sharply (with a rise time of tens of microseconds established by the detonation time of the explosive) and then decays with a characteristic time constant, t_0. The decay in pressure, $p(t)$, can be approximated as

$$p(t) = p_0 e^{-t/t_0}, \tag{1}$$

where p_0 is the peak pressure, t the time measured from the peak in pressure and t_0 is a characteristic time constant.

The impulse per unit area, I_0, transported by the pressure pulse is given by

$$I_0 = \int_0^\infty p(t)dt = p_0 t_0. \tag{2}$$

When the pressure pulse impinges upon a rigid, fully supported solid plate (one that is restricted from moving away from the blast wave), the incident pulse is reflected from the surface back into the water [10]. At the surface of the plate, the pressures of the two disturbances are in phase, and Taylor [10] and others have shown that the plate is subjected to a peak pressure $2p_0$, and the transferred momentum is $2I_0$. Taylor also calculated the momentum imparted to unsupported solid plates that were able to freely accelerate in response to the applied pressure and showed that the transferred impulse was governed by the mass/unit area of the plate. Thick solid plates were shown to receive the same impulse as rigid, fully supported structures but thin face sheets pick up much less impulse because they are able to move away from the blast [10].

When a plate moves with velocity V_f, the fluid elements (with density ρ_w and sound speed c_w) close to the plate move with the same velocity and a rarefaction wave of magnitude $\rho_w c_w V_f$ is radiated back into the fluid. The net water pressure due to the incident, reflected and rarefaction waves results in a total plate loading:

$$p(t) = 2p_0 e^{-t/t_0} - \rho_w c_w V_f. \tag{3}$$

For a sandwich panel, it has been assumed that the fluid–structure interaction is controlled by the front (wet side) face sheet and the relevant mass per unit area can be taken as that of the front face sheet [11]. In this case, the impulse transmitted into the sandwich structure depends only upon the thickness of the front face sheet and the density of the material it is made of. The impulse, I, transferred to the front face of an unsupported sandwich structure is then given by [10,11]

$$I = 2I_0 q^{q/(1-q)}, \tag{4}$$

where

$$q = \frac{\rho_w c_w}{\rho h_f} t_0, \tag{5}$$

in which ρ is the density of the face sheet material and h_f is the thickness of the face sheet. The ρh_f product is also the mass per unit area, m_f, of the face sheet. If $\rho_w = 1000$ kg/m^3, $c_w = 1400$ ms^{-1}, $t_0 = 0.1$ ms and $m_f = 40$ kg/m^2 (equivalent to a 5 mm thick 304 stainless-steel plate), $q = 3.5$. For sandwich panel structures with steel face sheet thicknesses in the 5 mm range, Eq. (4) indicates that the impulse transmitted from water to the sandwich structure is around 0.35 times that incident on a thick rigid plate, or one that is fully back supported. This impulse reduction arises because the front face is able to move away from the pressure pulse.

However, neither Taylor's analysis nor several recent applications of it [11–13], fully address the fluid-structure

interaction for the sandwich panel problem. The initial front face velocity of the sandwich structure is reduced by the deformation resistance of the core and the water attached to the front face is then able to reload the structure. This results in an increase of the momentum transfer by a factor that depends on the core strength [11–14] and inertial effects at high velocities. In the solid plate situation analyzed by Taylor, the tensile reflected wave in water results in cavitation at the water–plate interface. However, in a sandwich panel structure, cavitation can be delayed (by rapid acceleration of the light front face) and the plane of tensile failure in the water then occurs some distance above the front face. The additional loading depends upon the velocity of the front face sheet, which is established by the momentum originally imparted to it and the front face retarding force resulting from the crushing resistance of the cellular material. Hutchinson and Xue [13] and Liang et al. [15] have recently shown that the core's dynamic crush strength, σ_{yD}^c scaled by p_0 governs the additional impulse transferred to the core.

In this modified Taylor scenario [13,15], the momentum per unit area transferred to the front face sheet and the added water layer is given by

$$I_T = I_0\left\{2q^{q/(1-q)} + 1.27\frac{\sigma_{yD}^c}{p_0}[1 - q^{q/(1-q)}]\right\}. \quad (6)$$

For a core with a dynamic strength of $0.15p_0$ [13], the ratio of the total momentum of the front face sheet and added water layer to the incident impulse, I_T/I_0 is ~0.5 compared to 0.35 for a freely moving target surface. Various groups have sought to develop a fuller understanding of these extended Taylor effects [13–16].

There are many ways to create a sandwich panel structure of the type schematically illustrated in Fig. 1 [17]. The mass of the system can be distributed in different ways between the two faces and the core. Recent analysis has indicated that the mass distribution significantly affects the sandwich panel's performance during water blast loading [15]. Analytical and numerical studies also indicate that the strength and topology of the cellular core have a significant effect upon the dynamic response of the system [12,13,15]. Many core topologies for metallic systems have begun to be theoretically assessed [18]. Broadly, they can be classified as honeycombs, lattice trusses, prismatic structures and foams. Several groups have used small-scale impact testing and numerical analysis to probe the dynamic response of these different structures and to experimentally ascertain those best suited for blast mitigation applications [19–23].

Several guiding design rules are emerging from these studies. The dynamic core crushing resistance, σ_{yD}^c, is important since it contributes to the forces that damp the front face motion and governs the loads applied to the support structure. High core strengths also ensure that the face sheets of the panel remain well separated so that the structure retains a high bending resistance. The core also needs to possess significant in-plane stretching

resistance to impede bending deflections (Fig. 1). The ideal core will depend upon the protection strategy. Cores optimized for reducing the peak transmitted pressure to the sandwich panel supports might be different from those seeking to minimize back face deflection, or the avoidance of front face sheet tearing or shear off at hard points.

The notional behavior of an idealized lattice truss core panel for peak shock pressure mitigation is schematically illustrated in Fig. 2. The system (Fig. 2(a)) consists of a cellular structure with a nominal stress–plastic strain response during through thickness compression shown in Fig. 2(b). Under quasi-static loading, this response is characterized by lattice collapse at a fixed, plateau stress, σ_y^c, until a plastic densification strain, ε_D, is reached where upon cell wall/truss interference and friction cause a rapid increase in strength. The plateau stress is a function of the loading rate if the core is made from strain rate hardening materials and if the deformation velocity is sufficiently high that inertial stabilization of the (buckling) failure modes occurs [24].
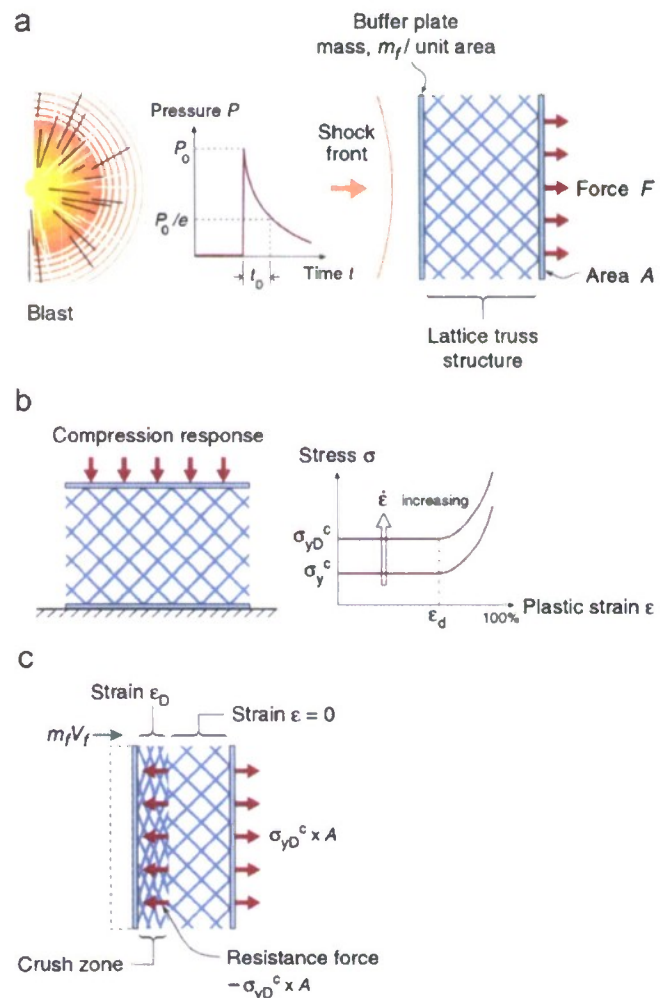

Fig. 2. Dynamic core crushing of a cellular core sandwich panel used to reduce the peak pressure applied to the back face support structure.

Suppose a faceplate with a mass, m_f, per unit area is attached to the front and back of a lattice core. When a blast wave arrives at the front face of the system, a fluid-structure interaction occurs and momentum is transferred to the buffer plate. The plate then acquires a momentum $m_f V_f$ per unit area where V_f, the initial plate velocity, varies inversely with m_f. The plate's kinetic energy is $\frac{1}{2}m_f V_f^2$. The motion of the buffer plate is retarded by the reaction force arising from the dynamic crush strength, σ_{yD}^c of the lattice structure (Fig. 2(c)) and inertial effects, which become more important as the front face velocity increases beyond $\sim$30 m/s [24]. A plastic shock wave (across which crushing occurs) is propagated at the plastic wave speed from the front of the cellular structure towards the back face sheet. For low front face velocities and a core with the ideal mechanical response shown in Fig. 2(b), the force transferred to the protected structure behind the system never rises above $\sigma_{yD}^c A$ (where A is the back face area) provided the crush zone deformation never exceeds the densification strain and the crush zone front is arrested within the cellular structure.

Higher velocity ($>$20 m/s) motion of the front face can result in significant increases in the reaction force applied to the front face. These increases result from the inertial resistance of the core (from the forces required for acceleration of the material mass in and behind the crush zone), inertial stabilization against buckling of core members (webs and trusses) and material hardening at high strains and strain rates. These effects all scale with a dimensionless velocity, $V_f/c\varepsilon_y$, where c is the acoustic wave speed and ε_y is the yield strain of the material used to create the cellular structure [25]. Radford et al. [20,21] and Lee et al. [22] propose that for a foam core the dynamic strength is given by

$$\sigma_{yD}^c = \sigma_y^c + \rho_c V_f^2/\varepsilon_d, \tag{7}$$

where σ_{yD}^c is the core strength when strain rate hardening and inertially stabilized truss buckling are accounted for, ρ_c the cellular sandwich core relative density, ε_d the core densification strain and V_f is the front face velocity. For a bi-linear material with linear hardening rate, Xue and Hutchinson have proposed a dynamic strength law of the form [25]:

$$\frac{\sigma_{yD}^c}{\rho_c \sigma_y} \approx 1 + \sqrt{\frac{E_t}{E}}\left(\frac{V_f}{c_{el}\varepsilon_y} - 1\right), \tag{8}$$

where, E_t is the tangent modulus and $c_{el} = \sqrt{E/\rho}$ is the elastic wave speed in the constituent material. During a blast mitigation event, the front face velocity varies between $\sim$200 m/s and zero, and so the overall response of the core and the pressure applied to a supporting structure is likely to be a complicated sampling of the effects described above.

This study investigates the dynamic response of a passive mitigation approach combining crushable cellular lattice structure metals [8] with structurally efficient sandwich panel concepts. The proposed approach has attracted interest for underwater shock loading situations where the structure located behind the sandwich panel experiences reduced pressure as a result of four interrelated effects: (i) modification of the fluid structure interaction at the front (wet) face sheet, (ii) time dispersal of the blast wave's pressure–time waveform by controlled core crushing and face sheet stretching, (iii) the increased bending resistance of sandwich panel structures and (iv) kinetic energy dissipation by plastic deformation of all components of the panel. These blast mitigation effects are expected to be sensitive to the dynamic response of the core structure.

We investigate the reduction in transmitted pressures by a back-supported lattice truss structure subjected to water-borne shock loading resulting from the underwater detonation of an explosive. Numerous lattice structure topologies have been proposed and examples of three types are shown in Fig. 3. Any of these structures can be assembled to create lattices with a repeating space-filling unit cell. An example of a pyramidal lattice assembled in a 3D structure to create a lattice block material is shown in Fig. 4(a). In this case, the structure is composed entirely of trusses. Fig. 4(b) shows a different configuration where the lattice consists of layers of pyramidal trusses juxtaposed with thin solid intermediate face sheets. These face sheets provide increased in-plane stretch resistance and is the structure explored in this study. We have developed methods for its fabrication from stainless steels and report its response to quasi-static compression and underwater blast testing. We use hydrocode simulations to calculate the dynamic loads applied to the explosively tested structure and experimentally investigate its core collapse. We find that a multilayered pyramidal lattice structure is effective at dispersing high-intensity impulses, and this significantly reduces the peak pressure transmitted to the underlying structure. A 28% reduction in transmitted

Fig. 3. Examples of three-lattice truss structures used as cores of sandwich panels. (a) Tetrahedral topology, (b) pyramidal lattice and (c) 3D Kagome structure.
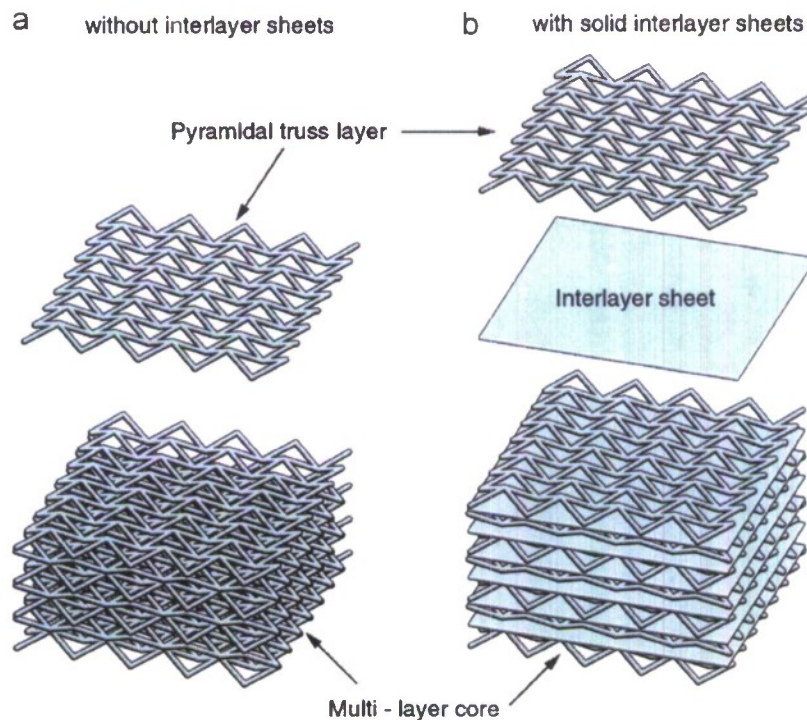
Fig. 4. Examples of pyramidal lattice multilayers using (a) truss connections and (b) thin solid plates to create multilayered structures.

impulse is also observed for the sandwich panel. This suggests a beneficial fluid structure interaction effect, which is realized even though the sample was tested with full back support.

2. Lattice test structure fabrication

A sheet perforation and node folding method was used to fabricate the test samples. The process is schematically illustrated in Fig. 5. Sheets of 304L stainless steel were die punched to create an array of elongated diamond perforations. These were then folded at rows of nodes to create a single layer of the pyramidal lattice. The sheet thickness was 1.52 mm and the included angle formed during the folding operation was 70°.

Intermediate face sheets, 0.76 mm in thickness, were coated with a Ni–Cr–P braze alloy powder (Wall Colmonoy Nicrobraz 51). Single layers of the pyramidal lattice were then sandwiched between the intermediate face sheets and stacked node to node to create a multilayer core assembly approximately 82 mm high. This entire structure was then placed between Nicrobraz 51 coated, 4.8 mm thick, 304 stainless-steel face plates and the assembly was brazed at 1050 °C for 60 min in a vacuum furnace at a pressure of 0.13 Pa. After brazing, the panels were cut using wire electro discharge machining to create 203 mm diameter cylindrical samples that were approximately 92 mm in thickness. A photograph of a typical sample is shown in Fig. 6.

The relative density of the multilayer lattice structure (including the intermediate face sheets) can be calculated (as the volume of material to total cell volume) from the unit cell shown in Fig. 7. If the trusses have a width, w, length, l, and thickness, t, and the lattice is defined by a truss-intermediate face-sheet angle, $\omega = 45°$ (corresponding to a 70° bend angle of the perforated sheet, Fig. 5), then given an intermediate face sheet of thickness, t_i, the predicted relative density of the core is given by

$$\bar{\rho} = \frac{\rho}{\rho_s} = \frac{\sqrt{2}(4wt + t_i l)}{l(l + \sqrt{2}t_i)}. \tag{9}$$

The measured core relative density for the samples fabricated here (including the intermediate face sheets and a small amount of the braze alloy) was 9%, of which 4.5% (50%) consisted of truss layers.

The 304L stainless-steel alloy in the as-brazed heat-treated condition had a Young's modulus $E = 200$ GPa, a yield strength $\sigma_y = 189$ MPa, a tensile strength $\sigma_{UTS} = 600$ MPa, a plastic strain to fracture $\varepsilon_f = 50\%$ and a tangent modulus $E_t = 2$ GPa. The dynamic properties are anticipated to be similar to those of other austenitic stainless steels [26].

3. Quasi-static compressive response

One of the cylindrical specimens was loaded in compression across the front face at a strain rate of 5×10^{-4} s^{-1} and
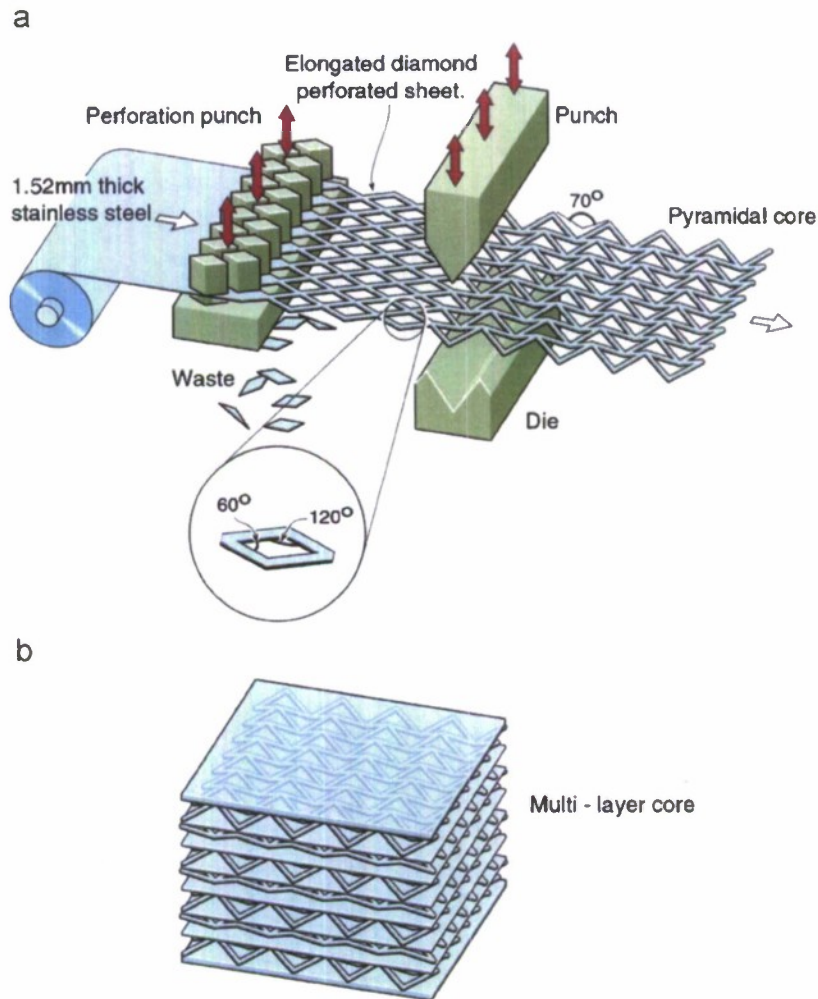
a

b

Multi - layer core

Fig. 5. Fabrication sequence for a pyramidal multilayer lattice structure. (a) Lattice fabrication; (b) multilayer assembly.
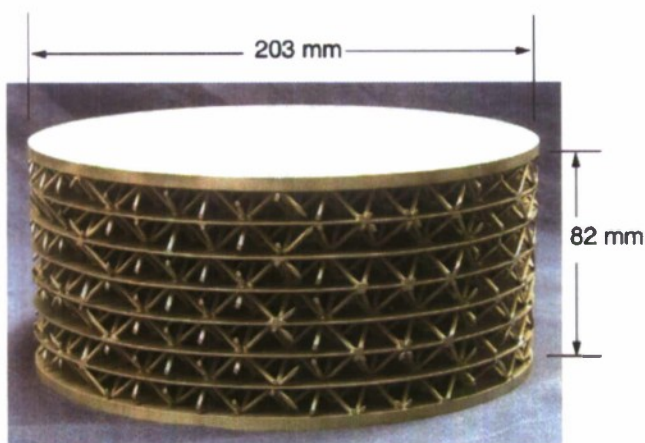

Fig. 6. Photograph of one of the 304 stainless-steel pyramidal lattice truss structures. The core mass was approximately evenly divided between the lattices and intermediate face sheets.

Fig. 7. A representative, 3D space-filling unit cell for the multilayered pyramidal lattice structure.

the stress–plastic strain response is shown in Fig. 8. The normalized stress, $\sigma/\bar{\rho}\sigma_y$ [where σ_y is the parent 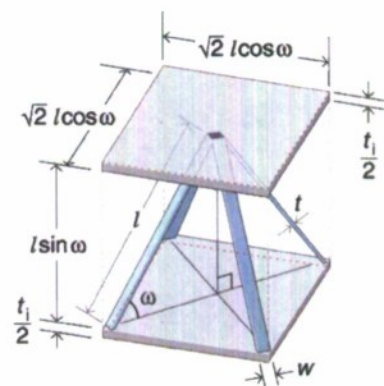alloy's quasi-static yield strength] is also shown. The response is similar to some metal foams. Upon yielding at a stress of 4 MPa, the lattice exhibited a nearly flat plateau behavior and then began to modestly harden to a flow stress of about 7 MPa at a strain of ~60% before the onset of rapid hardening due to lattice densification.

Visual observations indicated that in the plateau region, the plastic strain was accommodated by truss plastic deformation followed by inelastic truss buckling and intermediate face sheet wrinkling. Six markers on the stress–plastic strain response shown in Fig. 8 corresponded to the strains at which cooperative buckling of the pyramidal truss layers occurred. Each buckling event resulted in a small load instability.

The normalized plateau strength of the core, $\sigma/\bar{\rho}\sigma_y$, was approximately 0.2 using a core relative density ($\bar{\rho}$) of 9%, which includes the mass of the interlayer sheets. However, the truss members of the pyramidal lattice (considered in isolation) had an aspect ratio equivalent to that of a lattice with a relative density of 4.5% increasing the normalized strength metric to 0.4. This value of strength metric is consistent with recent measurements of single-layer pyramidal lattices, which indicated a strength coefficient of ~0.4–0.5 for annealed 304 stainless-steel lattices in this relative density (truss aspect ratio) range [27].

The micro-truss pyramidal core model was analyzed using ABAQUS/Explicit Version 6.4 (ABAQUS, Inc., 2003). The model was based on the geometry of the test specimen. One-quarter of the structure was modeled, so symmetry conditions were applied to the nodes on the x–z plane at $y = 0$ and to the nodes on the y–z plane at $x = 0$. A velocity of ~2.25 mm/s was applied in the downward z-direction to the nodes located on the top surface of the top exterior plate. This is well below the rate at which dynamic effects become important. Built-in constraint conditions were applied to the nodes located on the bottom surface of the bottom exterior plate. Eight-node brick elements were used to construct the model. The total number of elements in the model was 146,528. The general contact algorithm in ABAQUS/Explicit was used to model contact between surfaces as the core of the structure crushed.

The deformation history for the model is shown in Fig. 9. Lines for the different finite elements were removed to improve clarity and different colors were used to make it easier to see the various parts of the model. The pattern of crushing in the analysis was similar to the behavior observed with the test. The initial peak stress of the model was within 3% of that measured. Crushing of core layers was progressive, one layer after another. This process continued until all of the micro-truss layers compacted into a densified core.

A comparison of the engineering stress–strain behavior between the micro-truss pyramidal core finite element model and the corresponding test specimen is shown in
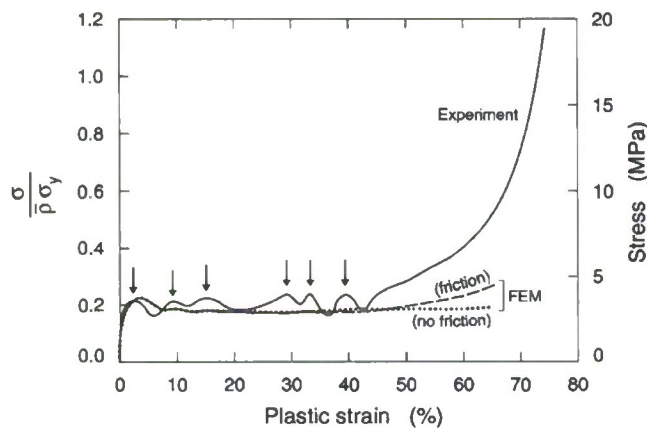

Fig. 8. The quasi-static compression test response of the multilayered pyramidal lattice structure and comparisons with ABAQUS/Explicit finite element analysis results.
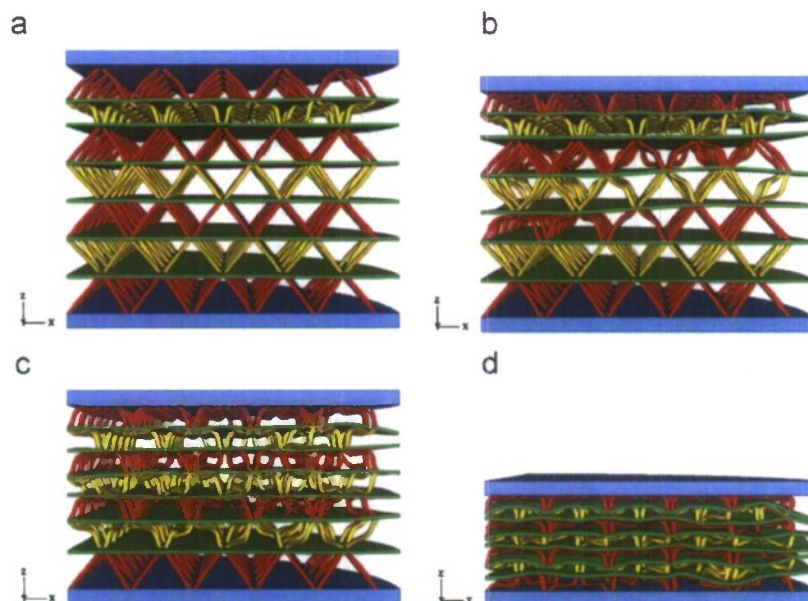

Fig. 9. Core crushing sequence from finite element analysis of multilayer pyramidal core quasi-static compression test at core strains of (a) 8.1%; (b) 16.2%; (c) 32.5% and (d) 65.0%.

Fig. 8. The stress increased to the initial peak and then decreased as the first core layer began to buckle and crush. The applied strain rate was accommodated by this layer's collapse until it reached its densification strain. At this point, it was redistributed among the other core layers and the stress increased to a second peak coincident with the initiation of buckling in a second layer. This pattern continued as each of the layers was crushed and core densification occurred.

This lattice core design maintains a consistent level of strength because it has multiple layers. In the analyses, even after a layer fails, the remaining intact layers are able to support a large part of the initial peak load. The FEM analysis stress–strain curves reflect a nearly constant load-carrying capacity after the initial peak is passed with some modest peaks and troughs. The test stress–strain curve exhibits more pronounced peaks and troughs and has subsequent peaks that are even higher than the initial peak. At about 42% core strain, the stress starts to increase continuously because all of the core layers have compacted into a denser form. The core then begins to behave increasingly like a solid cylinder and supports larger load levels as it densifies and work hardens.

The influence of friction between truss surfaces can be seen when comparing the analysis with friction, to the analysis without friction (Fig. 8). With friction present in the analysis, the core behavior follows a pattern more similar to the behavior seen with the test. When friction is ignored, it takes much longer for the stress to start a continuous upward trend.

4. Dynamic behavior

4.1. Test methodology

An underwater explosive test method schematically illustrated in Fig. 10 was used to investigate the dynamic crushing behavior of the pyramidal lattice structure. The test specimens were slip fitted into a thick, high-strength steel cover plate with a central opening and positioned on four HY-100 steel columns each ~3.8 cm in diameter and ~12 cm long. Four strain gauges were attached to each of the specimen support columns and calibrated in a compression test machine so that their averaged output voltage could be converted to pressure applied by the back face of the (203 mm diameter) test sample. An approximately 0.9 m diameter cardboard hollow cylinder was then placed above the specimen and filled with water. In order to produce a symmetric, plane wave type loading of the sample, a 203 mm × 203 mm × 1 mm thick explosive sheet was positioned centrally above the specimen at a distance of 100 mm from the top surface of the test sample and a detonator placed at the center of the explosive sheet. The sandwich panel back face pressure was recorded as a function of time after detonation of the charge.

The test system's response following detonation of the charge was also obtained for a solid aluminum cylinder calibration block. The back face pressure–time waveform is shown in Fig. 11. In Fig. 11(a) the pressure at the back face of the calibration test block is seen to rapidly rise to a peak of 52 MPa and then decay to zero in about 0.3 ms. This explosive event resulted in a transmitted impulse (measured
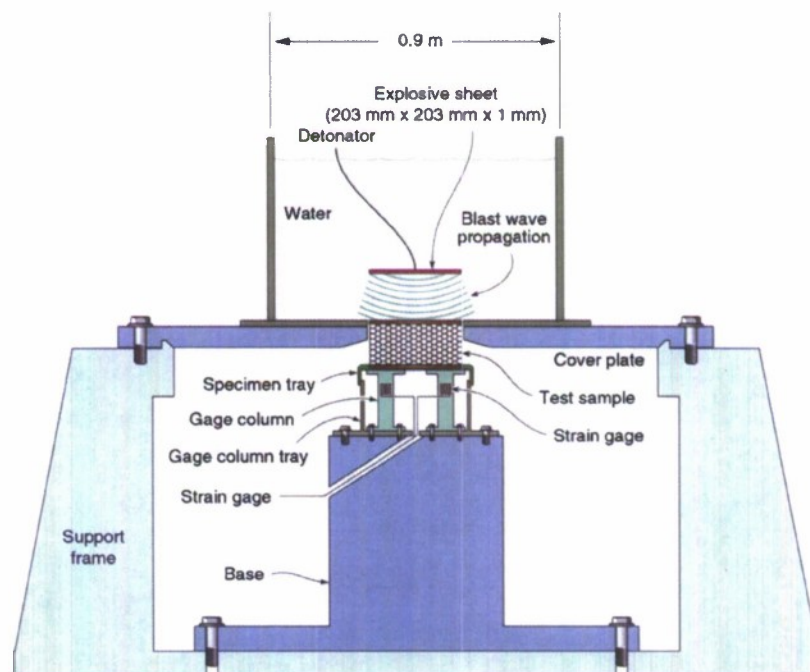

Fig. 10. Schematic illustration of the test method used to investigate the dynamic crush response of the pyramidal lattice structure. Calibration of the system was also conducted using a solid aluminum sample test piece of identical dimensions to those of the sandwich panels.
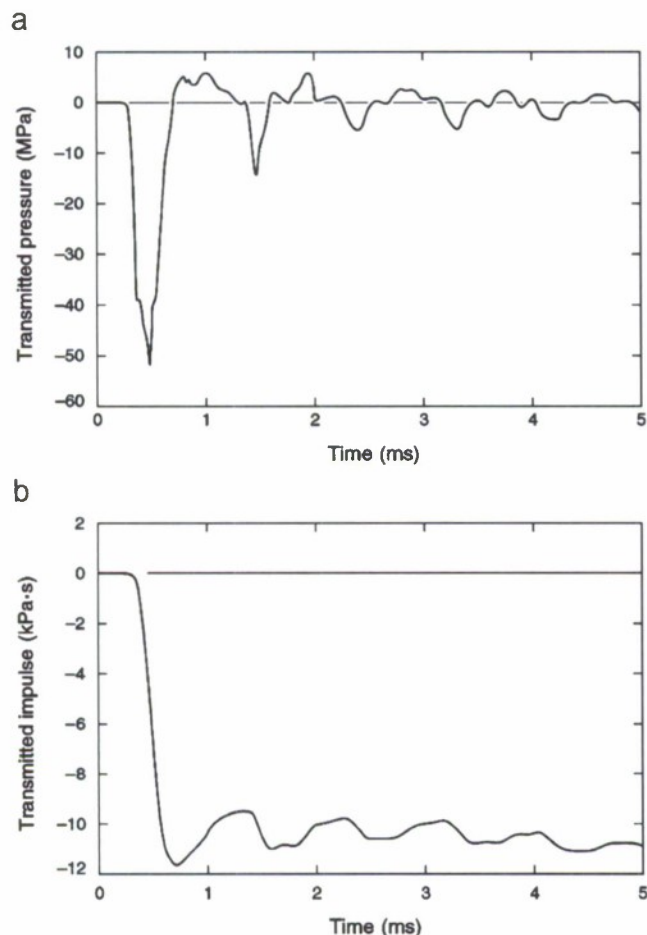
a

b

Fig. 11. (a) Transmitted pressure response and (b) transmitted impulse response on the back face of the solid cylinder.

a

b

Fig. 12. (a) Transmitted pressure response and (b) transmitted impulse response on the back face of the multilayer pyramidal core sandwich panel.

at the solid sample's back face) of 11.8 kPa s (Fig. 11(b)). The oscillatory behavior exhibited by both wave forms is believed to result from reverberation within the test system.

4.2. Pyramidal lattice response

The back face pressure wave form following detonation of an explosive sheet (at time $t = 0$) is shown in Fig. 12(a). The wave form is very different to that of the aluminum reference block response (Fig. 11(a)). The peak pressure is approximately 1/5th of the solid cylinder (11 MPa compared with 52 MPa), and the narrow initial pressure pulse had been spread in time from ∼0.3 ms for the solid reference sample to 1.8 ms for the sandwich panel. At least four separate load spikes (peaks) can be seen in the first 2 ms of the signal shown in Fig. 12(a). These spikes are thought to correspond to load peaks associated with cooperative buckling of truss layers convolved with the measurement system's impulse response. The two strongest pressure peaks transmitted to the back face were 9.8 and 10.5 MPa. The average pressure was about 4.6 MPa, which is about 15% above the quasi-statically measured plateau strength.
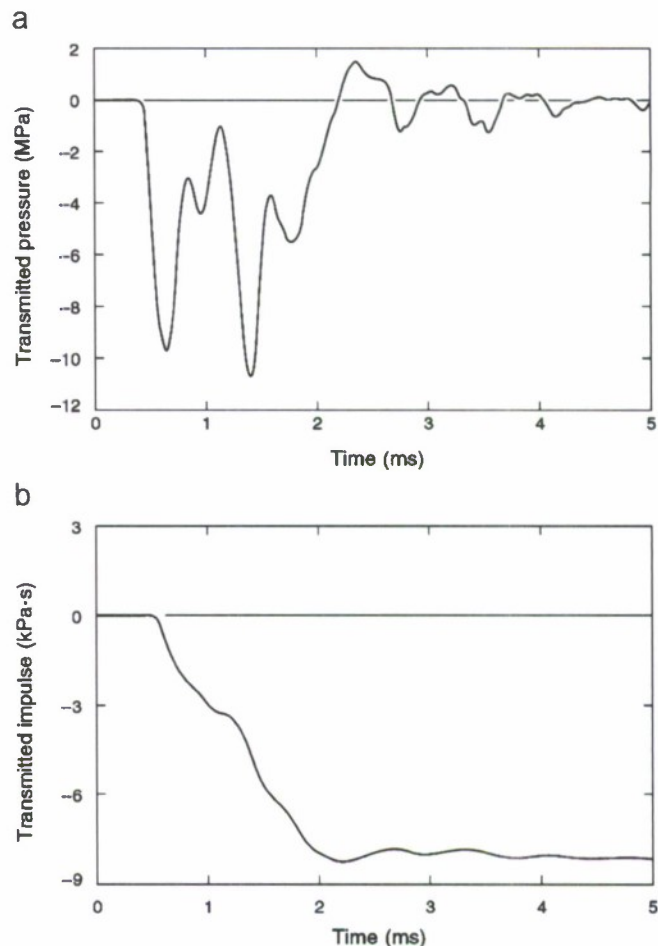
The sandwich panel back face impulse is shown in Fig. 12(b). The saturation impulse was 28% less than that recorded for the aluminum reference block (8.5 kPa s compared with 11.8 kPa s) and its rise time was increased by a factor of ∼3 compared to that of the solid cylinder. Comparison of the solid and pyramidal lattice pressure waveform results suggests that the sandwich panel core crushing occurred over a period of about 1.8 ms.

A sectioned side view of the sandwich panel specimen is shown in Fig. 13. All seven layers of the structure had collapsed by truss buckling. The thickness of the specimen core had decreased from 82 to 40 mm corresponding to a compressive plastic engineering strain of 51%, which correlates to the strain at the end of the stress plateau observed in the quasi-static test (Fig. 8). If the 42 mm of core crushing occurred over 1.8 ms, the average crush velocity would be approximately 23 m/s. During the dynamic test, one layer of lattice nodes fractured and the sample had separated into two parts about a quarter of the way from the top of the sample. Examination of Fig. 13 shows that asymmetric buckling of the four trusses
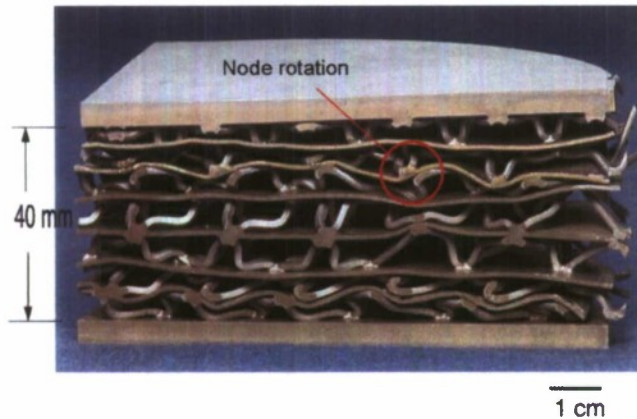
Fig. 13. Photograph of a quarter section of the pyramidal lattice structure after dynamic testing. Note the significant intermediate face sheet bending and truss buckling. Node rotation at the intermediate face sheets can be seen.

Fig. 14. High magnification view of the truss buckling and node rotation after dynamic testing.

emanating from the contact node with the interlayer sheets had occurred. This then resulted in node fractures that were not in the plane of the specimen but had all tilted about 30° out plane in the same direction. These two observations are consistent with node rotation during truss buckling. This rotation can be clearly seen in the circled region of Fig. 13. Fig. 14 shows a close up view of the truss-buckling pattern. Some trusses were bent upwards while others were depressed and were similar to the pattern predicted by the finite element analysis. The buckled trusses made contact with the intermediate face sheet and the forces the trusses applied to the face sheet appear to have been responsible for its bending.

5. Hydrocode simulations

The dynamic loading experiments described above involved measurements of the transmitted forces on the back faces through strain gage recordings on four support columns. Measurements of the dynamic force (and resulting impulse load) on the front face are difficult close to an explosion. Unfortunately, there are also no analytical solutions for the underwater pressure loading resulting from the detonation of an explosive sheet. Therefore, fully coupled Euler–Lagrange finite element hydro code simulations [28,29] were used to compute the pressure fields in the fluid and at the solid cylinder–water interface. The code captures the shock propagation following an explosion within a fluid medium using an Eulerian solver, and couples it to the structural response of the target medium (the solid cylinder), whose response is found using a Lagrange solver [30].

Due to the thinness of the explosive sheet (1 mm) and high spatial and time gradients of pressure in the fluid medium, a fine mesh is desired in the Eulerian mesh in the direction towards the target. The Euler run was started with 0.2 mm cells in the explosive sheet thickness direction, and 0.4 mm divisions in the other two directions (plane
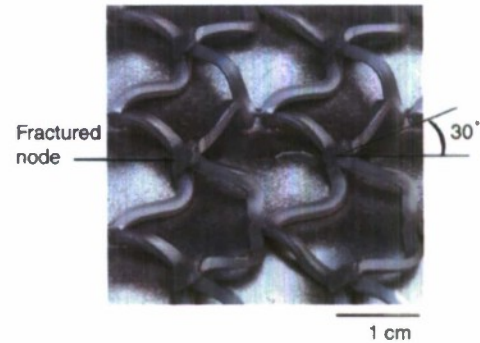
parallel to the explosive sheet). To make the computational problem more tractable, the symmetry of the solid cylinder was exploited by selecting 1/4th of the model geometry for computations (Fig. 15). The explosive sheet was specified in terms of its geometry, explosive material properties, the detonation velocity and JWL equations of state for shock calculations. Fig. 15 shows a time sequence as the propagating blast wave reached the front face of the solid cylinder and underwent reflection. The incident wave front is nearly planar at a standoff distance of 0.1 m.

At each time step, the pressure within each element of the water column was calculated and the pressure data at the water–sample interface were conveyed to the DYNA Lagrange solver using a standard coupling interface. With this pressure–time loading information, the dynamic structural response of the cylinder (or sandwich panel) was computed in terms of the stresses and strains of the sample. The calculated nodal velocities and locations at each time step were conveyed back to the Euler solver to recalculate the pressures at the next time step and the process was repeated.

Fig. 16(a) shows the calculated pressure loading on the front face of the solid aluminum cylinder. It shows a peak pressure of around ~350 MPa and a time decay constant of approximately 0.035 ms. The integration of the pressure–time plot gives the impulse loading (per unit area) on the cylinder. The test measurements with the solid cylinder back face (Fig. 11(a)) indicated a peak pressure of ~52 MPa and a ~0.4 ms time constant for impulse saturation to occur. It appears that significant dispersion occurs in the solid cylinder test resulting in a seven-fold reduction in peak pressure and an increase in pulse width from 0.035 to ~0.4 ms. Nevertheless, the calculated applied impulse (11.5 kPa s) (Fig. 16(b)), is almost identical with the experimental measurement (11.8 kPa s) (Fig. 11(b)).

6. Discussion

The quasi-static behavior of a multilayer pyramidal lattice is close to the ideal response of an impact mitigating material. Under quasi-static loading, the structure crushes by sequential buckling of individual lattice layers with each
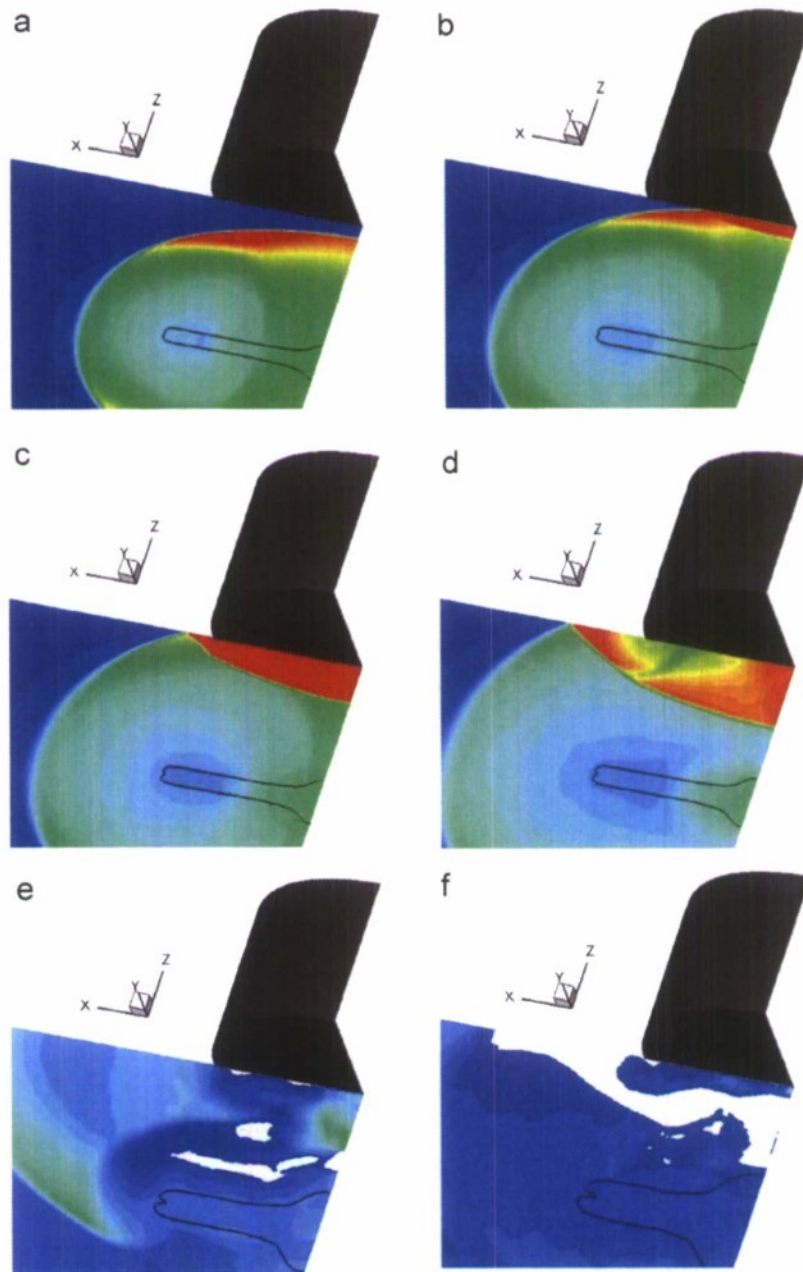
Fig. 15. A time sequence of the blast wave propagation and interaction with a solid cylinder: (a) $t = 0.047$ ms; (b) $t = 0.055$ ms; (c) $t = 0.065$ ms; (d) $t = 0.075$ ms; (e) $t = 0.14$ ms and (f) $t = 0.2$ ms.

layer-buckling event resulting in a small rise and drop in flow stress. This behavior is analogous to that of metal foams [8] and pre-buckled honeycombs [31]. The small reduction in flow stress accompanying the cooperative buckling of a layer of the lattice appears to be a consequence of (i) the high work hardening rate of the 304 stainless-steel alloy, (ii) a small variation in the buckling resistance of the individual trusses and (iii) post-buckling stretching (bending) of the intermediate face sheets.

During dynamic loading of the pyramidal lattice sandwich panel, the average back face pressure was

~4.6 Mpa, which is slightly higher than the 4 MPa measured quasi-statically. Two pressure pulses (at 0.3 and 0.9 ms after the start of the pressure rise) applied much larger pressures (9.5 and 10.5 MPa, respectively) to the back face. The average and secondary pulse pressures were all significantly reduced from that calculated to be imparted to (~350 MPa) or measured (~52 MPa) at the back face of the solid reference cylinder sample.

This reduction in transmitted pressure can only occur if the applied impulse (the time integral of the pressure waveform) is either reduced or stretched out over time during plastic propagation through the structure. Both
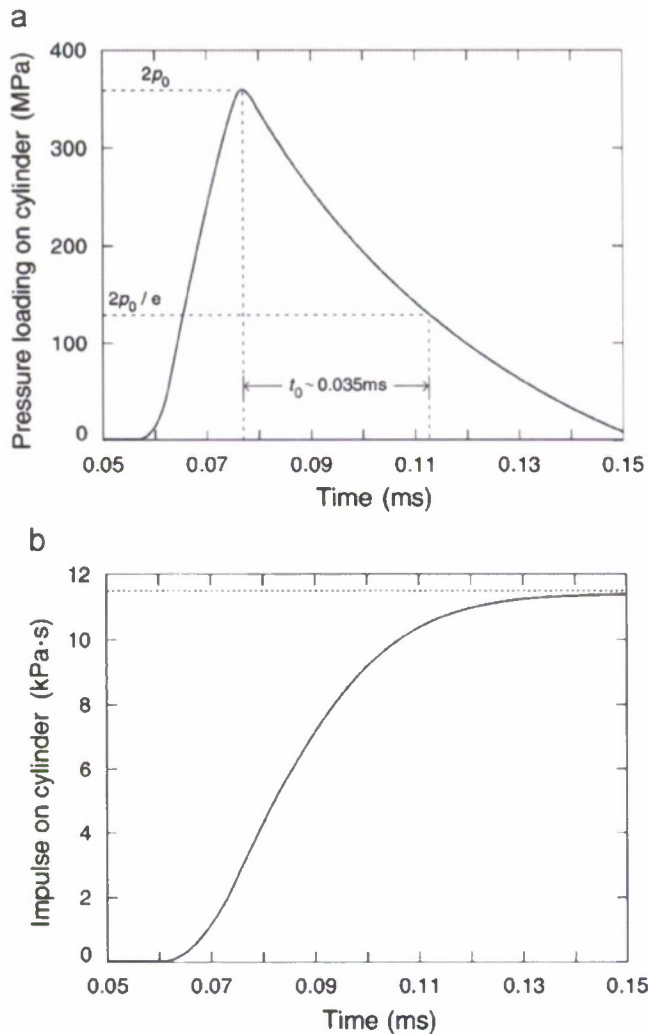
a

b

Fig. 16. (a) Calculated pressure loading on solid cylinder front face. (b) Calculated impulse loading on solid cylinder front face.

appear to have occurred in the dynamic test. The transmitted impulse was less than that transmitted to a solid cylindrical sample (8.5 versus 11.8 kPa s) but this reduction alone was insufficient to fully account for the reduced back face pressure of the sandwich panel structure. The seven-layer lattice structure tested here also dispersed the pressure pulse extending its width from about 0.4 to 1.8 ms thereby reducing the transmitted pressure for a fixed impulse.

The reduced impulse transferred to the sandwich panel is presumed to be a consequence of front face sheet motion away from the blast wave during fluid loading of the structure. This motion is not possible for a fully supported rigid plate and an impulse, $2I_0$, is transferred to the structure as measured in the experiments with the solid reference block. The extended Taylor calculation above for a 5 mm thick steel plate (the thickness of the face sheet used for the sandwich panel) indicates that the impulse transferred to an unsupported plate would be $0.35I_0$. For

core strains less than the densification limit, the momentum impulse transferred to a sandwich panel therefore lies between that of the unsupported plate and one that was fully supported. The precise value will be controlled by the force exerted by the dynamically deforming core during the time over which the impulse is being transferred to the core [32]. This will depend upon the instantaneous velocity of the front face sheet, inertial effects associated with acceleration of the core at the shock front boundary and the dynamic strength of the core [13–16,20–24].

The location of the cylindrical test samples within the test fixture was not conducive to the measurement of the (changing) velocity of the front face of the deforming sandwich panel. The average velocity of the crushing was estimated to be about 23 m/s. The average back face pressure of the sandwich sample is slightly higher than that of the quasi-statically measured and FEA predicted strength, which is consistent with modest dynamic core strength enhancements. Since the multilayer pyramidal structure has metal foam-like response, a 1-D shock model developed for the analysis of metal foams can be used to estimate the initially peak front face velocity [33]. It gives a velocity of around 70 m/s, which decreased to zero in about 1.8 ms. Larger dynamic strengthening effects from strain rate hardening of the metal, inertial stabilization of truss buckling and the inertial resistance of the system would be expected during the high-velocity period of crushing.

Since the front face of the sandwich panel is moving, a rarefaction wave of magnitude $\rho_w c_w V_f \sim 106$ MPa pressure is radiated back into the fluid from the front face [14]. This results in a peak pressure loading reduction from ~ 350 MPa for the rigid solid cylinder to ~ 244 MPa ($\sim 70\%$ of solid cylinder loading), consistent with the reduced impulse loading measured experimentally. The series of 4 strong sub-peaks present in the pressure wave form may have been associated with high-velocity deformation events associated with the sequential buckling of the individual layers. Dynamic finite element analysis is needed to investigate this behavior.

7. Conclusions

The compressive response of a multilayered pyramidal lattice constructed from a 304 stainless steel has been investigated quasi-statically and by explosive testing. We find:

– The structure collapses by truss inelastic buckling with intermediate face sheet stretching.
– The structure has near-ideal impact mitigation characteristics exhibiting a nearly flat stress plateau to a plastic strain of approximately 60% during quasi-static compression testing. A series of small stress peaks are identified with individual truss layer cooperative buckling.
– The dynamic response of the lattice results in a reduction in the peak pressure transmitted at the back

face (11 versus 52 MPa for a solid structure) and disperses the pressure waveform resulting in a waveform width increase from 0.35 to ~1.8 ms.

- The dynamic compressive response indicates a series of hardening/softening phases with pressures transmitted to the back face varying from a low of 1 MPa to a maximum of 11 MPa with an average slightly above the quasi-statically measured core strength. These softening phases are thought to be a consequence of the cooperative collapse of one or more truss layers during progressive propagation of a densification front through the structure. Further studies are needed to evaluate this phenomenon.
- The impulse transferred to the fully supported sandwich structure is about 28% less than that transferred to a solid plate. This arises from front face motion away from the blast during the period of fluid structure interaction with the sandwich panel.
- The results suggest that a two-layered core that provides a soft response during the fluid structure interaction and a stiff response during later panel bending might outperform a single core layer sandwich panel. The fabrication approach developed in this study provides a potentially useful method for creating such structures.

Acknowledgments

References

[1] Jones N. Structural impact. Cambridge University Press; 1997.

[2] Bulson PS. Explosive loading of engineering structures. E&FN Spon; 1997.

[3] Smith PD, Hetherington JG. Blast and ballistic loading of structures. London: Butterworth Heinemann; 1994.

[4] Krauthammer T, Altenberg AE. Assessing negative phase blast effects on glass panels. Int J Impact Eng 2000;24:1–17.

[5] Johnson W, Reid SR. Metallic energy dissipating systems. Appl Mech Rev 1978;31:277–88 [updated 1986;39:315–9].

[6] Dudt P. private communication, 2005.

[7] Wadley HNG, Dharmasena KP, He M, McMeeking RM, Evans AG, Kambouchev N, Radovitzky R. Cellular materials concepts for air blast mitigation. 2007; in preparation.

[8] Ashby MF, Evans AG, Fleck NA, Gibson LJ, Hutchinson JW, Wadley HNG. Metal foams: a design guide. London: Butterworth-Heinemann; 2000.

[9] Meyer R, Kohler J, Homberg A. Explosives. Wiley-VCH; 2001.

[10] Taylor GI. The scientific papers of G.I. Taylor, vol. III. In: Batchelor GK, editor. Aerodynamics and the mechanics of projectiles and explosions. Cambridge: Cambridge University Press; 1963. p. 287–303.

[11] Fleck NA, Deshpande VS. The resistance of clamped sandwich beams to shock loading. J Appl Mech 2004:386–401.

[12] Xue Z, Hutchinson JW. A comparative study of impulse-resistant metal sandwich plates. Int J Impact Eng 2004;30:1283–305.

[13] Hutchinson JW, Xue Z. Metal sandwich plates optimized for pressure impulses. Int J Mech Sci 2005;47:545–69.

[14] Deshpande VS, Fleck NA. One-dimensional shock response of sandwich plates. J Mech Phys Solids 2005;53:2347–83.

[15] Liang Y, Spuskanyuk AV, Flores SE, Hayhurst DR, Hutchinson JW, McMeeking RM, et al. The response of metallic sandwich panels to water blast. J Appl Mech 2007;74:81–99.

[16] Rabczuk T, Kim JY, Samaniego E, Belytschko T. Homogenization of sandwich structures. Int J Numer Methods Eng 2004;61: 1283–305.

[17] Wadley HNG, Evans AG, Fleck NA. Fabrication and structural performance of periodic cellular metal sandwich structures. Compos Sci Technol 2003;63(16):2331–43.

[18] Deshpande VS, Fleck NA. Collapse of truss core beams in 3-point bending. Int J Solids Struct 2001;38:6275–305.

[19] Rathbun HJ, Radford DD, Xue Z, He MY, Yang J, Deshpande V, et al. Performance of metallic honeycomb-core sandwich beams under shock loading. Int J Solids Struct 2006;43:1746–63.

[20] Radford DD, Deshpande VS, Fleck NA. The use of metal foam projectiles to simulate shock loading on a structure. Int J Impact Eng 2005;31(9):1152–71.

[21] Radford DD, McShane GJ, Deshpande VS, Fleck NA. The response of clamped sandwich plates with metallic foam cores to simulated blast loading. Int J Solids Struct 2006;43:2243–59.

[22] Lee S, Barthelat F, Moldovan N, Espinosa HD, Wadley HNG. Deformation rate effects on failure modes of open-cell Al foams and textile cellular materials. Int J Solids Struct 2006;43:53–73.

[23] Lee S, Barthelat F, Hutchinson JW, Espinosa HD. Dynamic failure of metallic pyramidal truss core materials—experiments and modeling. Int J Plast 2006;22:2118–45.

[24] McShane GJ, Radford DD, Deshpande VS, Fleck NA. The response of clamped sandwich plates with lattice cores subjected to shock loading. Eur J Mech A Solids 2006;25:215–29.

[25] Xue Z, Hutchinson JW. Crush dynamics of square honeycomb sandwich cores. Int J Numer Methods Eng 2006;65:2221–45.

[26] Stout MG, Follansbee PS. Strain rate sensitivity, strain hardening, and yield behavior of 304L stainless steel. Trans ASME J Eng Mater Tech 1986;108:344–53.

[27] Queheillalt DT, Wadley HNG. Pyramidal lattice structures with hollow trusses. Mater Sci Eng A 2005;397:132–7.

[28] Wardlaw Jr A, Luton J, Renzi J, Kiddy K. Fluid–structure coupling methodology for undersea weapons. Fluid structure interaction II. WIT Press; 2003. p. 251–63.

[29] Wardlaw Jr A, Luton JA. Fluid–structure interaction mechanisms for close-in explosions. Shock Vibrat J 2000;7:265–75.

[30] Whirley R, Engelman B, Hallquist JO, Dyna-3D: a nonlinear, explicit three-dimensional finite element code for solid mechanics, user manual. LLNL Report UCRL-MA 107254, November 1993.

[31] Bitzer T. Honeycomb technology. London: Chapman & Hall; 1997.

[32] Deshpande VS, Heaver A, Fleck NA. An underwater shock simulator. Proc R Soc A 2006;462:1021–41.

[33] Deshpande V. private communication, 2005.

Appendix B.

Analysis and interpretation of a test for characterizing the response of sandwich panels to water blast

Z. Wei[a,*], K.P. Dharmasena[b], H.N.G. Wadley[b], A.G. Evans[a]

[a]*Materials Department, University of California, Santa Barbara, CA 93106, USA*
[b]*Department of Materials Science and Engineering, University of Virginia, Charlottesville, VA 22903, USA*

Abstract

Metallic sandwich panels are more effective at resisting underwater blast than monolithic plates at equivalent mass/area. The present assessment of this benefit is based on a recent experimental study of the water blast loading of a sandwich panel with a multilayered core, using a Dyno-crusher test. The tests affirm that the transmitted pressure and impulse are significantly reduced when a solid cylinder is replaced by the sandwich panel. In order to fully understand the observations and measurements, a dynamic finite element analysis of the experiment has been conducted. The simulations reveal that the apparatus has strong influence on the measurements. Analytic representations of the test have been developed, based on a modified-Taylor fluid/structure interaction model. Good agreement with the finite element results and the measurements indicates that the analytic model has acceptable fidelity, enabling it to be used to understand trends in the response of multilayer cores to water blast.
© 2006 Elsevier Ltd. All rights reserved.

Keywords: Sandwich panels; Multilayered pyramidal lattice; Underwater blast; Fluid/structure interaction

1. Introduction

Metallic sandwich panel structures offer significant advantages over equivalent mass per unit area monolithic plates when exposed to underwater blast loading [1–9]. These benefits arise from a reduced momentum transfer from the water to the structure, combined with shock mitigation by core crushing, as well as enhanced resistance to bending [1–9]. These effects are influenced by the geometry of the sandwich panel; namely, the apportionment of mass between each face and the core, the core thickness (or relative density for a fixed face separation) and the core topology [1–8]. They are also sensitive to the material used to fabricate the structure since its mechanical properties (modulus, yield strength, strain hardening), in conjunction with the geometry and rate, determine the loads, the mechanisms of core collapse and the face deformation and failure [1–8].

*Corresponding author. Tel.: +1 805 893 5871; fax: +1 805 893 8486.
E-mail address: zhensong@engineering.ucsb.edu (Z. Wei).

Nomenclature

c_{el}	elastic wave speed in base material
c_w	sound speed in water
E, E_T	Young's modulus and plastic tangent modulus of base material
h_c	height of a single layer
H_c	total height of the core
H_w	height of the water column
I_0	free field momentum, $I_0 = p_0 t_0$
I_b	impulse reaching the back face of the panel
I_T	transmitted impulse
k	spring stiffness
KE	kinetic energy (due to front face plus attached water)
M_T	transmitted momentum (front face and attached water)
m_f	mass/area of front face
m_w	mass/area of attached water at $t = t_c$
p_0	peak pressure of free field impulse
t_0	characteristic time of incident pressure pulse
t_c	time corresponding to maximum velocity of front face
t_c^+	time incrementally longer than t_c
t_{crush}	core crushing duration
t_f	characteristic time scale of front face velocity
v_f	velocity of front face
v_{face}	maximum velocity of front face
v_r	residual velocity of cavitated water
W_c	energy/volume absorbed by the core
x	distance from front face of the panel (with water residing in $x < 0$)
x_c	location where cavitation first occurs in water
β	fluid-structure interaction parameter, $\beta = \rho_w c_w t_0 / m_f$
ε_{crush}	core crushing strain
$\dot{\varepsilon}_{eff}$	effective crushing strain-rate
ε_Y	yield strain of base material at imposed strain-rate
η	dashpot viscosity
$\bar{\rho}$	relative density of the core
ρ_w	density of water
$\bar{\sigma}_{33}^c$	average crushing stress of the core at a constant crushing strain-rate
σ_{crush}	stress transmitted through the core during crushing
σ_{UTS}	tensile strength of base material
σ_y	quasi-static yield strength of base material
σ_Y	yield strength of base material at imposed strain-rate
σ_{YD}^c	dynamic yield strength of the core

The present assessment addresses a recent experimental study of the water blast loading of a sandwich with a multilayered pyramidal lattice structure (Fig. 1) [9]. In this study, a Dyno-crusher test methodology (Fig. 2a) was utilized to create a planar pressure pulse by using an explosive sheet in water (Fig. 3), with incident impulse $I_0 = 5.2$ kPa s. This pressure front interacted with the wet side of the sandwich panel, resulting in momentum transfer and acceleration of the face. Subsequent core crushing (with accompanying reaction forces) decelerated the face, arresting it after a crushing strain of about 50% (Fig. 4a). The test revealed that the stress transmitted through the core (Fig. 5a) was reduced by more than a factor of 25, while the pulse broadened from its incident value of ~0.1 ms in the water to ~1.7 ms. To fully interpret this information,
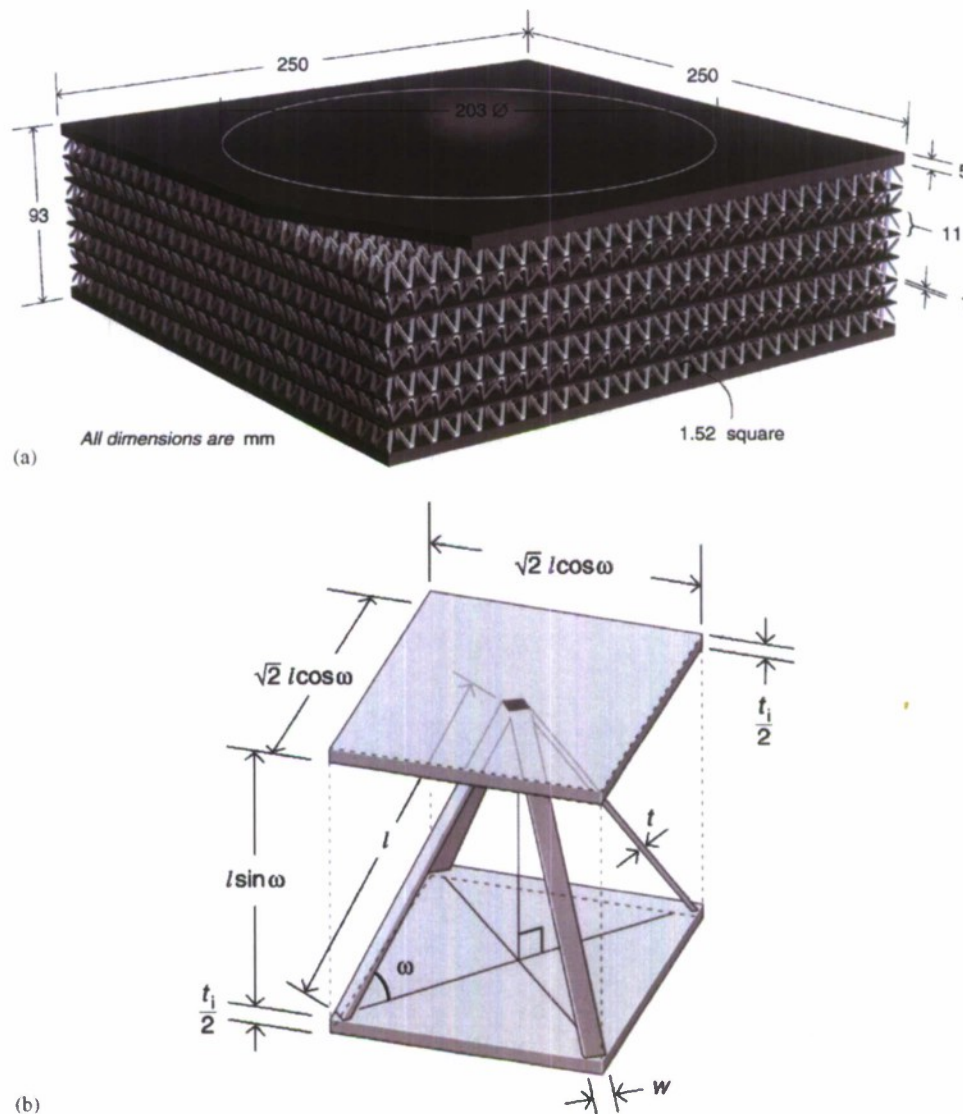
Fig. 1. (a) The geometry of the multilayered pyramidal lattice core sandwich panel and (b) its unit cell dimensions.

analysis is needed, because the stress/time waveform is influenced by the test apparatus. Developing such analysis is the primary objective of this article.

The specific objective is to fully understand the significance of these observations and measurements by using a dynamic finite element analysis of the experiment, followed by the development of analytic representations that relate the test results to the performance of panels subject to water blast. We describe the sample geometry and essential details of the test, which become inputs to the dynamic analysis. One outcome will be a quantification of the dispersion of the incident pressure pulse enabled by sequential crushing of the multilayered structure.

2. The Dyno-crusher test

The Dyno-crusher experiments were conducted with cylindrical sandwich panels made from 304 stainless steel (Fig. 2b). The core had a relative density of 9% with the mass distributed equally between the seven layers of truss elements and the six intermediate face sheets. The structures were fabricated by a brazing method (see
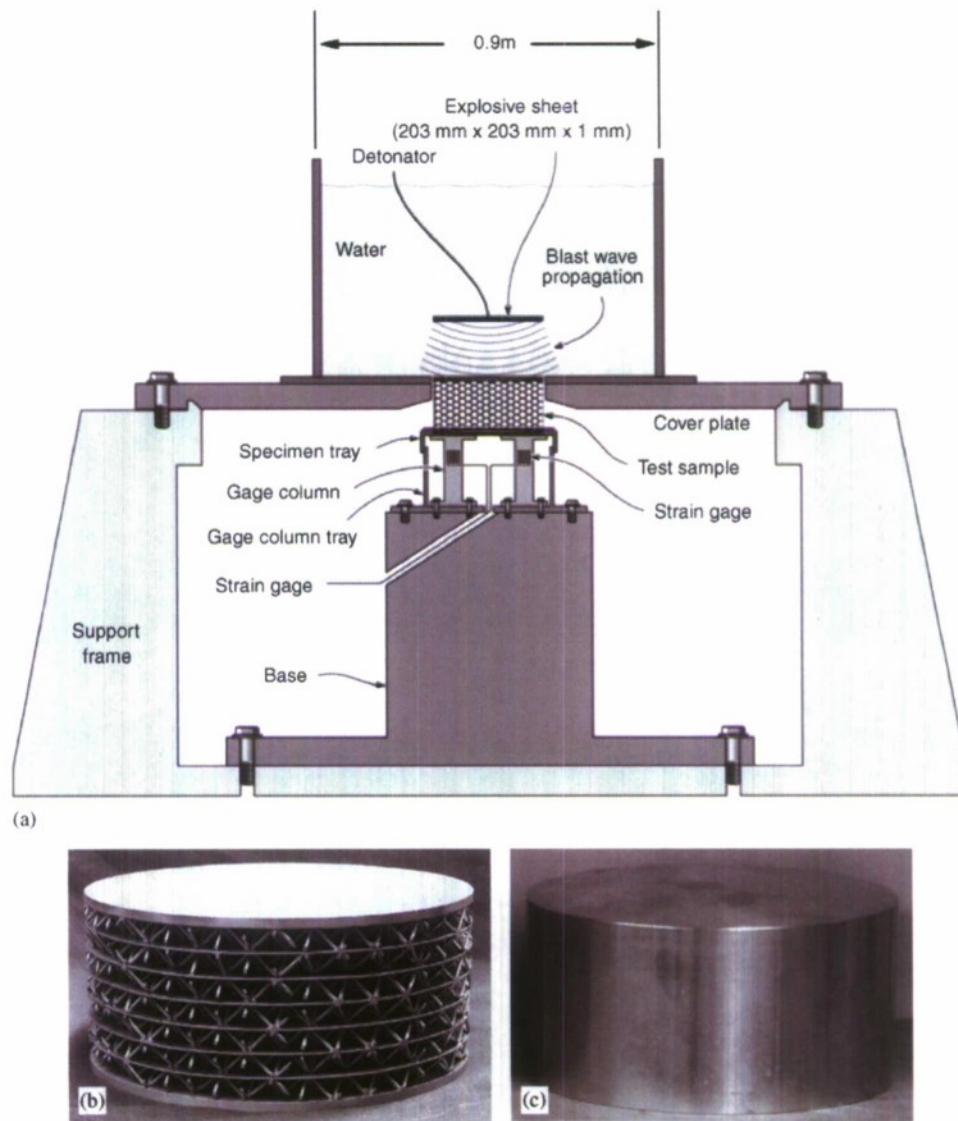
Fig. 2. (a) A schematic of the Dyno-crusher test. (b) The multilayered pyramidal core sandwich panel tested in (a). (c) The solid aluminum alloy cylinder with the same dimensions as the sandwich panel shown on (b).

Ref. [9] for details). The 304 stainless steel alloy in the as-brazed condition had a Young's modulus, $E = 200\,\text{GPa}$, a quasi-static yield strength $\sigma_y = 189\,\text{MPa}$, a tensile strength $\sigma_{UTS} = 600\,\text{MPa}$, a ductility of 50% and a tangent modulus $E_T = 2\,\text{GPa}$. The dynamic properties are similar to those of other austenitic stainless steels [10]. In quasi-static compression, the material crushes at plateau stress, $\sigma_{crush} \approx 4\,\text{MPa}$ and begins to densify at 60% strain [9].

The sample was placed flush with the top surface of a thick metal plate with a 203 mm diameter central hole (Fig. 2a). A 0.9 m diameter cardboard cylinder was placed above the sample and filled with water to a depth of 1 m. A 1 mm thick, 203 × 203 mm diameter explosive sheet was centrally positioned 100 mm above the center of the test sample. The explosive was detonated from the center of the top surface, imposing the pressures on the wet face indicated on Fig. 3. When the pressure reflected, the cardboard cylinder disintegrates eliminating some of the momentum imparted by the cavitated water [5]. The pressure on the bottom surface of the test sample was measured using pre-calibrated strain gauges attached to four pedestals that supported the sample. A dynamic calibration was conducted by replacing the sandwich panel with a solid 6061-T6 aluminum alloy
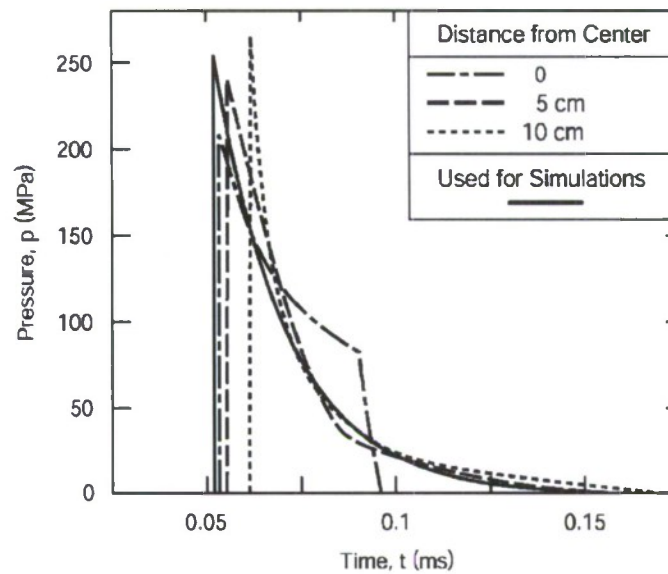
Fig. 3. The characteristics of the impulse generated in the Dyno-crusher tests obtained by independent calculation [12]. Also shown is the pulse used in the present simulations (solid line).

block (Fig. 2c) having identical exterior dimensions and exposing it to the same explosive loading. The stress-time pulse transmitted in these tests is presented in Fig. 6.

3. The numerical model

Simulation of the 3D (fully meshed) truss system is computationally impractical. Instead, a continuum representation of each layer is required (Fig. 7a). A dynamic constitutive law, and an assessment of its fidelity, has been provided elsewhere [11–13]. The input stress/strain curves have been obtained using dynamic unit cell calculations conducted for the truss members [13]. For all simulations, the commercial finite element code ABAQUS Explicit has been used [14].

The pressure/time/radial location (p, t, r) characteristics for the incident impulse imposed at the top of the column are chosen to duplicate values calculated when the impulse reaches the panel (Fig. 3) [15]. The impulse is regarded as planar and represented by a pulse (Fig. 3, solid line), having equivalent peak pressure and impulse. That is, the small time delay between the arrival of the impulse at the center of the panel and the perimeter is ignored. Because an axi-symmetric model is required for computational tractability, the four separate gage columns cannot be reproduced. Instead, a single central column is used having the same total cross-sectional area as the four columns. A spring and a dashpot have been introduced beneath the column to address the elasticity and energy absorption of the base. The coefficients of the spring and dashpot are calibrated by using the simulation model in Fig. 7b for the reference test, as described below. To duplicate the measurements it has been found that the spring and dashpot must be connected in parallel (not in series).

In order to delve into possible discrepancies with experiments caused by the homogenization, the 3D unit cell model depicted on Fig. 7c has been constructed, with symmetry boundary conditions imposed on the four sides. Following prior assessments [11,13], small imperfections have been introduced into every truss member with the shape of the first buckling mode (Fig. 7d). The response of the 3D model when exposed to dynamic compression at high strain rate (corresponding to a face velocity, 100 m/s) is depicted in Fig. 8. Note that the system collapses at a nominal stress, $\sigma_{crush} \approx 5\,\text{MPa}$, somewhat larger than that for quasi-static crushing [9,16]. As this proceeds, stress drops occur, attributed to sequential member buckling, exemplified by that occurring at time c. The final peak, at time f, occurs because of contact between the back face and the core members located within the bottom layer.
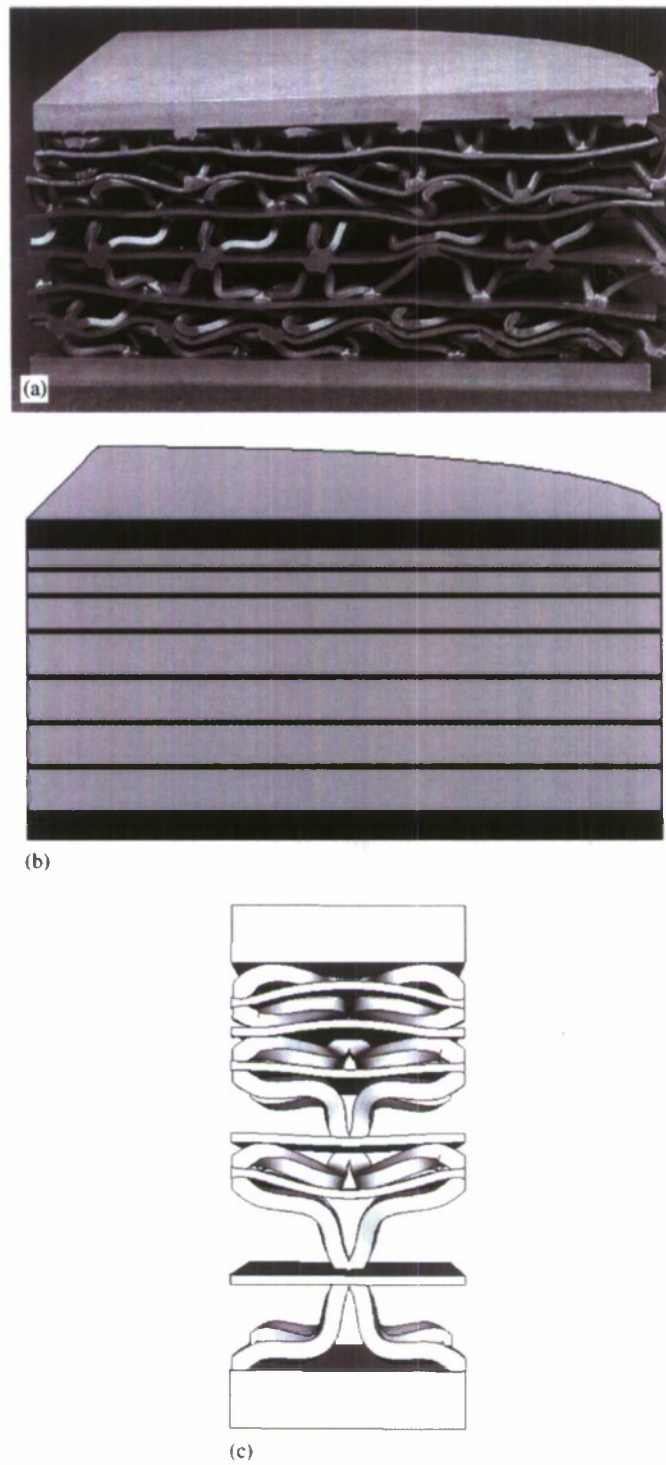
Fig. 4. The seven-layer truss panel after testing. (a) Experimental sample. (b) The numerical model with homogenized cores. (c) 3D unit cell model.
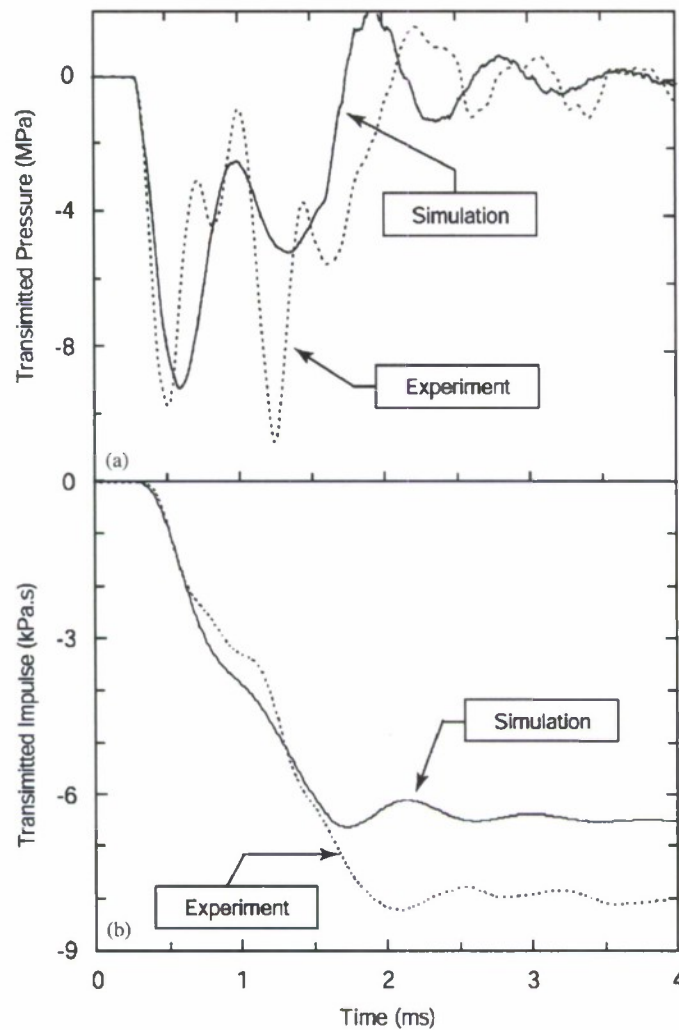
Fig. 5. (a) The pressures transmitted through the multilayered pyramidal panel measured at the gage columns. (b) The corresponding transmitted impulses. Comparisons between the measurements and the calculations conducted using the continuum model are shown.

4. Calibration of the system compliance

The coefficients of the dashpot and spring have been calibrated by the reference test conducted using the solid Al alloy cylinder. Initial calculations performed by assuming that the base is rigid (Fig. 6a) gave stresses much higher than measured levels, accompanied by violent oscillations. The discrepancy has been attributed to the viscoelastic response of the base. Accordingly, the calculations were repeated by incorporating a spring to represent the elasticity of the base. The spring influences the spacing between the stress oscillations. By adjusting the spring stiffness, k, the separation between peaks has been matched, as shown in Fig. 6b. When matched, the first peak coincides closely with the measured value. The dashpot determines the height of the ensuing peaks. A best match has been obtained by selecting the appropriate viscosity, η, as shown in Fig. 6c. The values of k and η determined in this manner are regarded as the calibration levels applicable to the system.

Additional insights about the test emerge from comparisons of the measured and calculated variations in impulse with time (Fig. 9). The transmitted impulse, I_T, calculated using a rigid base is essentially the same as the measured value. Moreover, both are twice the free field impulse, $I_T = 2I_0$, consistent with the magnitude of the pulse reflected back into the water (Fig. 10) [17]. However, the impulse calculated in the presence of the supports exceeds $2I_0$. The reason is evident from plots of the velocity field in the water at various times after
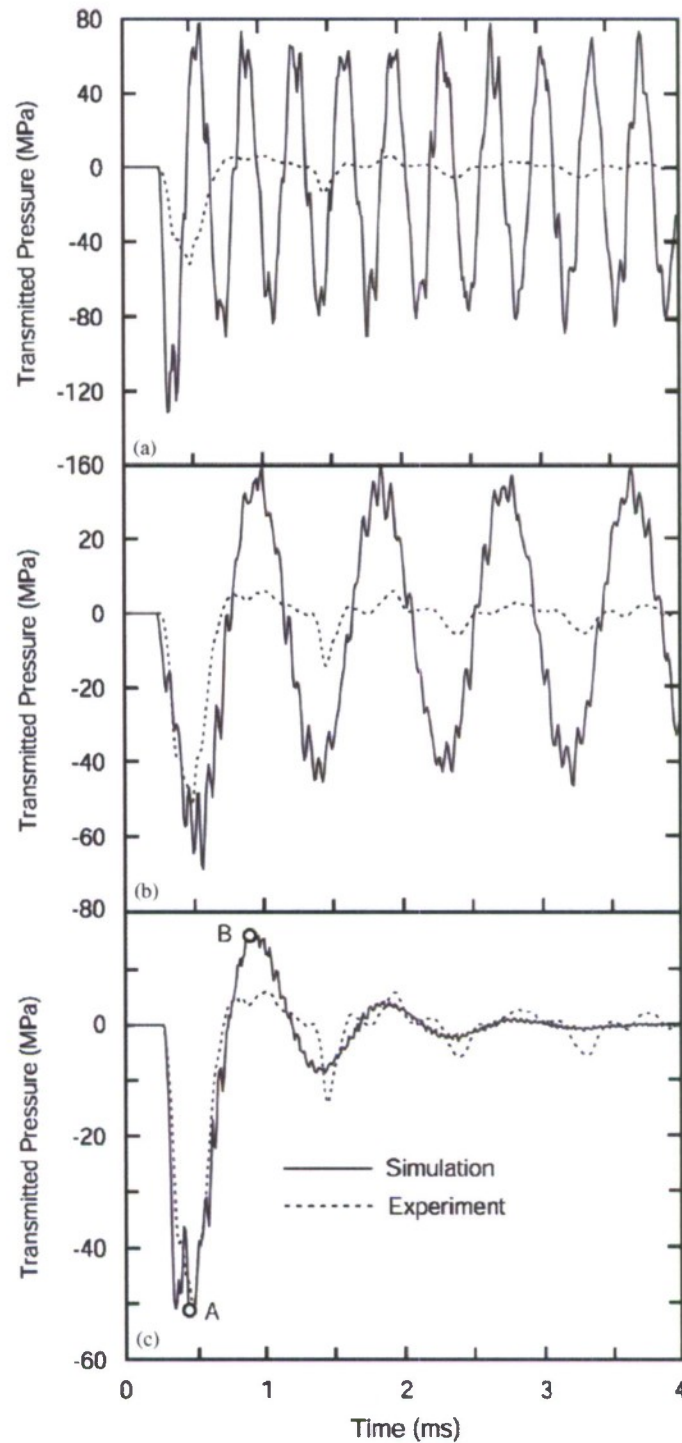
Fig. 6. Transmitted pressures obtained from the simulations of the reference test. (a) Assuming that the base is rigid. (b) After incorporating a spring to represent the elasticity of the base. (c) Upon further adding a dashpot to address the energy absorption of the base. Also shown on each figure is the transmitted pressure obtained from the experiments. Note the differences in scale on the ordinate of each figure.
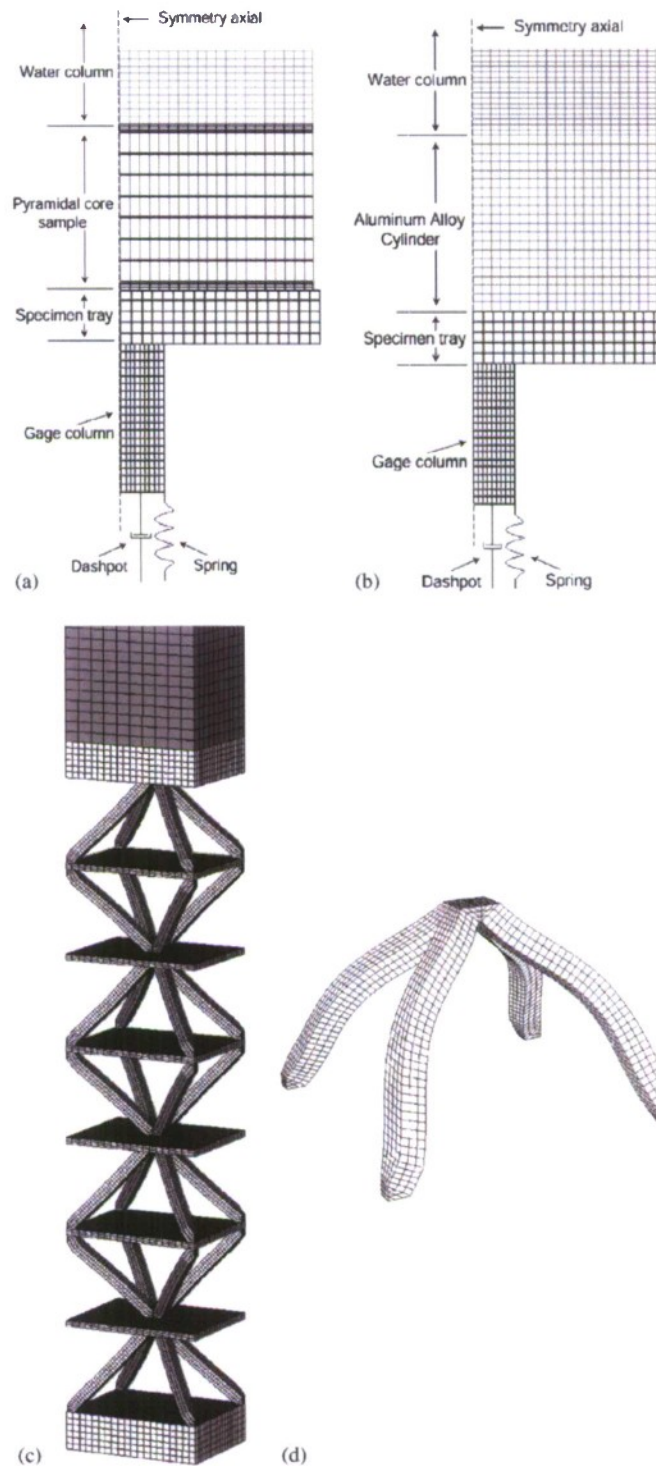
Fig. 7. Illustration of the finite element models. (a) The axi-symmetric continuum model for the Dyno-crusher test. (b) The reference test used to calibrate the model. (c) The 3D unit cell model constructed to delve into possible discrepancies between experiments and continuum simulations. (d) The first buckling mode of a single pyramidal core unit, used to incorporate imperfections.
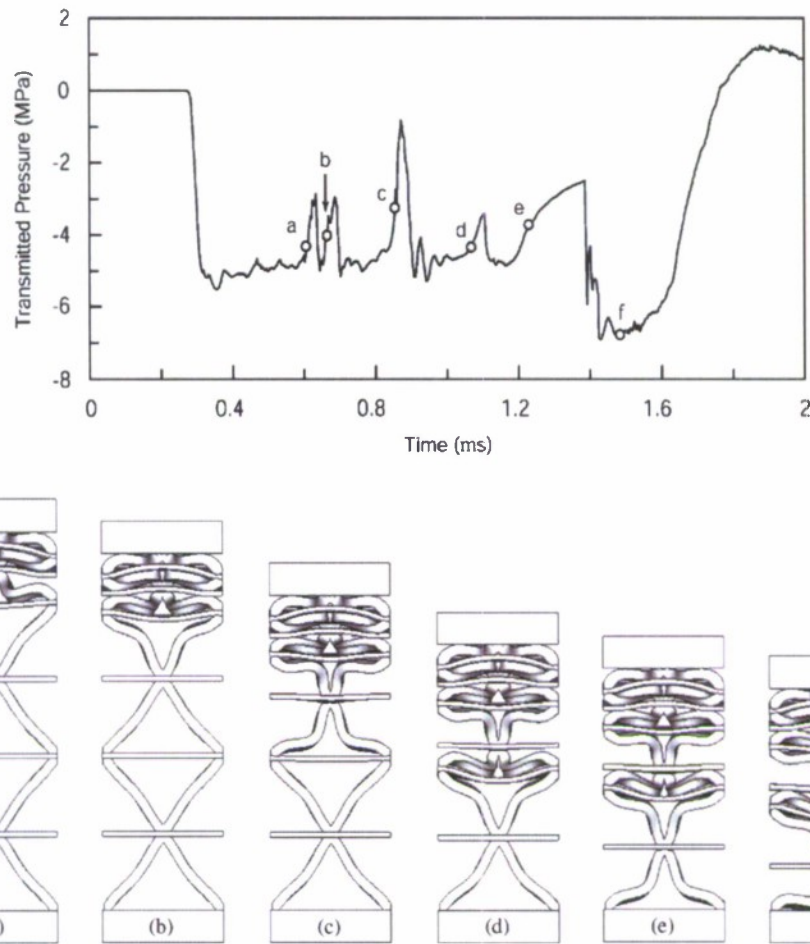
Fig. 8. Deformed shapes of 3D one-unit column of seven-layer core at six different times during crushing at high strain-rate (face velocity 100 m/s). Also shown is the corresponding temporal dependence of the transmitted pressure. Comparisons reveal that member buckling in sequential layers cause a series of stress drops.

detonation (Fig. 10). Soon after the initial impulse ($t \approx 0.4$ ms) the water near the cylinder has positive velocity (downward is assigned to be positive, consistent with the analytic estimates described below): that is, adjacent to the cylinder, it is moving downward as the system compresses. At a later time, the stress on the supports decreases, resulting in a spring back effect that causes the water near the cylinder to develop negative (upward) velocity. Consequently, the water delivers another (smaller) impulse. The consequence is a second reflected wave, evident at $t \approx 0.8$ ms. This additional impulse causes I_T to exceed $2I_0$. This impulse is not delivered in the experiments because the cardboard containment cylinder bursts before the spring back event takes place.

5. Transmitted pressures and crushing strains

The response of the multilayer pyramidal structure has been ascertained by using the same calibration values for the spring stiffness and viscosity. Initial simulations have been performed by placing the panel on a rigid base (no gage column) and computing the back-face stress and impulse as a function of time. For this boundary condition both the continuum and 3D models can be used. The transmitted stresses are plotted on Fig. 11. Note that the stresses determined using both models are consistent. Namely, dynamic crushing again occurs at a nominal stress, $\sigma_{crush} \approx 5$ MPa. However, the oscillations in stress caused by sequential layer buckling are missed when the continuum model is used. This deficiency is believed to be the source of the discrepancy between measurement and calculation discussed next.
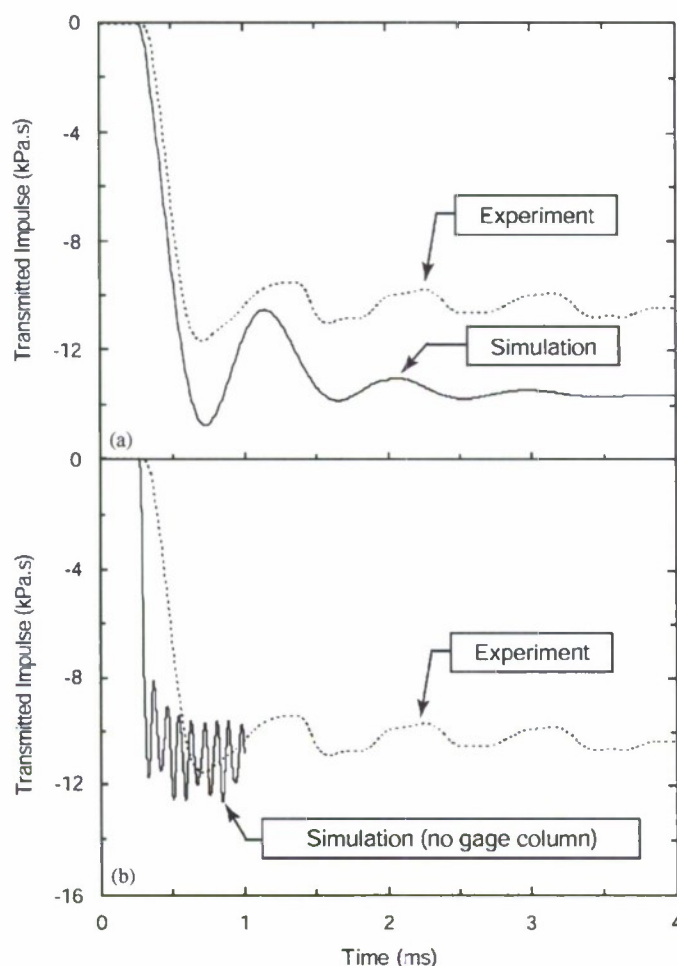
Fig. 9. Transmitted impulses in the reference test. (a) With gage column included. (b) Gage column replaced by a rigid base. The experimental measurements and simulations are compared.

When the support column is inserted, the stresses calculated at the strain gages (Fig. 5a) differ from those determined using a rigid base (Fig. 11). The difference is attributed to stress wave effects occurring in the columns and supports. In particular, the stress at the first peak is *higher* (10 MPa instead of 5 MPa) because the column acts as a wave guide. Thus, the stresses measured at the gages are not the same as the stresses transmitted through the core. This is the manifestation of the influence of the apparatus on the measurements.

The continuum simulations reproduce the initial pressure pulse with excellent fidelity (Fig. 5), but miss some of the ensuing details. The three basic discrepancies are as follows: (i) The crushing duration required to fully compact the core, $t_{crush} = 1.3$ ms, is less than the measured crushing duration, $t_{crush} = 1.7$ ms. (ii) There is a corresponding difference in the total transmitted impulse (Fig. 5b): $I_T \approx 6.5$ kPa s instead of $I_T \approx 8$ kPa s. Note that both are larger than the free field impulse but smaller than the impulse imparted to the solid Al alloy cylinder. (iii) The third pressure peak found in the experiments, occurring at time, $t = 1.2$ ms, is not duplicated. These discrepancies are attributed to the absence of discrete load drops in the continuum simulations (noted above). Attempts to introduce additional features into the continuum model to capture these events have not been insightful.

The variation in the velocity of the wet face with time, plotted in Fig. 12, provides insights about the response to be pursued in the following section. The result when the face arrests predicts the crushing strain (Fig. 4), $\varepsilon_{crush} = 0.5$. This strain closely reproduces the measurements, contrasting with the discrepancies in the stresses and in the impulse.
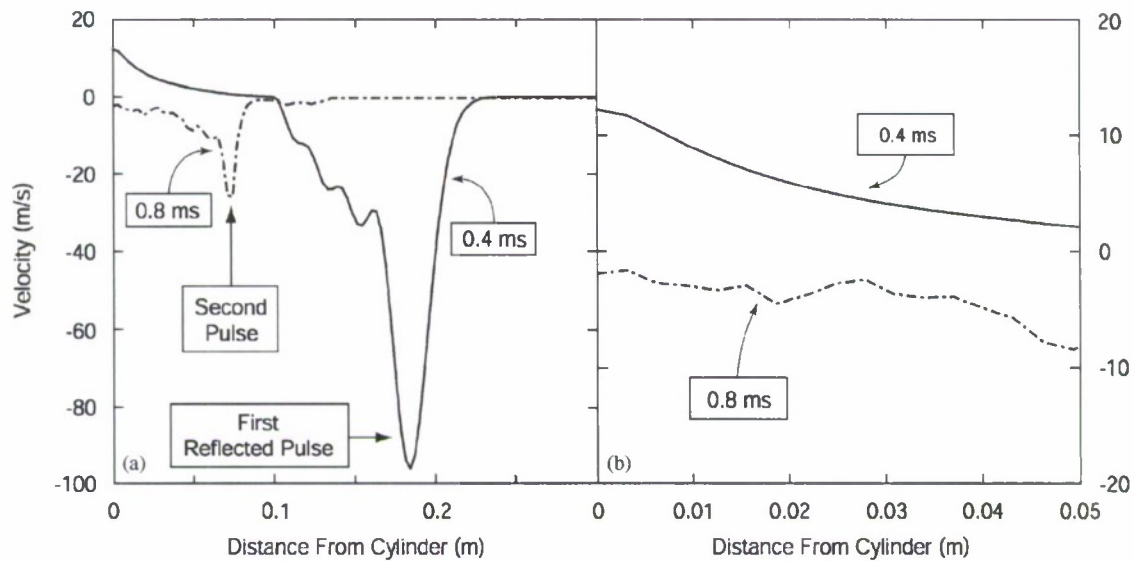
Fig. 10. Velocity fields in the water adjacent to the solid cylinder at two different times (0.4 and 0.8 ms; corresponding to two of the circles marked as A and B in Fig. 6b). Note the large reflected pressure pulse at 0.4 ms caused by the primary impulse from the explosion. The smaller, secondary pulse at 0.8 ms is caused by spring back of the support structure and gage column. It is responsible for the larger impulse obtained in the simulation than in the measurements.
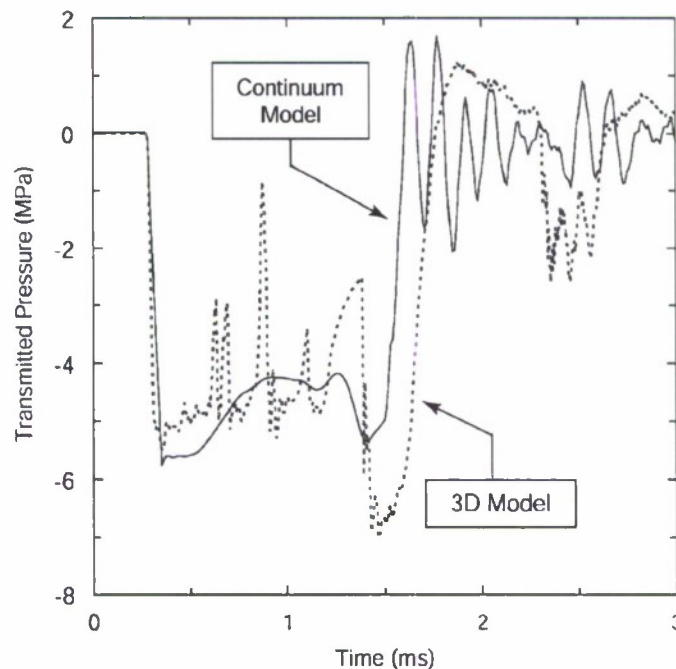

Fig. 11. The transmitted pressures at a rigidly held bottom face (absent support columns) comparing the continuum and 3D simulations.

It is concluded that a combination of Dyno-crusher tests with simulations conducted using a dynamic constitutive law and a 3D unit cell enable a comprehensive assessment of the response of multilayer sandwich structures to water blast. The method provides insight into the fluid/structure interaction, especially the relation between the core characteristics and the momentum imparted to the structure. This feature is extended in the following section into analytic estimates.
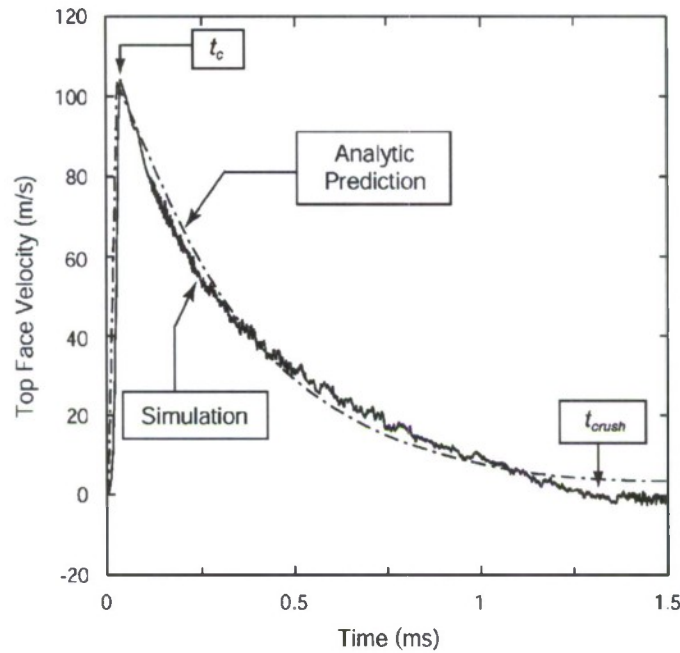
Fig. 12. Velocity of the top face as a function of time determined by simulation. Also shown is the prediction from Eq. (A.1) with t_f determined by Eq. (A.3).

6. Analytic estimates

Front face velocity: A modified Taylor solution relates the peak velocity acquired by the top face, v_{face}, to the incident impulse [3–5]:

$$v_{face} = \frac{p_0}{\rho_w c_w}\left[e^{-t_c/t_0} + \left(\frac{2\beta}{1-\beta} + \frac{\sigma_{YD}^c}{p_0}\right)e^{-\beta t_c/t_0} - \frac{1+\beta}{1-\beta}e^{-t_c/t_0} - \frac{\sigma_{YD}^c}{p_0}\right] \tag{1}$$

with,

$$\beta = \rho_w c_w t_0 / m_f,$$

$$t_c \approx t_0(\ln \beta)/(\beta - 1),$$

where ρ_w and c_w are the density of the water and its sound speed, respectively, m_f is the mass per unit area of the front face and t_c is the time when the front face reaches the maximum velocity (with time commencing when the blast first arrives at the structure); β is the fluid–structure interaction parameter; p_0 and t_0 are the peak pressure and decay time for the impinging wave, respectively, with the blast impulse, $I_0 = p_0 t_0$ [3–5]. Here σ_{YD}^c is the "dynamic yield strength" of the core. It is the stress imposed by the core on the top face when the face velocity is at its maximum value. It can be estimated using [18]

$$\sigma_{YD}^c \approx 0.5\sigma_Y \bar{\rho}\left[1 + \sqrt{\frac{E_T}{E}}\left(\frac{v_{face}}{c_{el}\varepsilon_Y} - 1\right)\right], \tag{2}$$

where σ_Y and ε_Y are the yield strength and yield strain of the constituent material at the imposed strain rate (that is, at strain rate, v_{face}/H_c, with H_c the total core height); $\bar{\rho}$ is the relative volume density of the core; c_{el} is the speed of elastic wave. (This formula differs from that for a square honeycomb core by a factor of 0.5, reflecting the 45° inclination between the truss members and faces [16]). Combining (1) and (2) provides an implicit expression for v_{face} and σ_{YD}^c. The accuracy of the analytic predictions is demonstrated by comparing the temporal dependence of the front face velocity with the simulated result (Fig. 12). Moreover, we note that

v_{face} is relatively insensitive to σ_{YD}^c, such that equally good correlations can be obtained by simplifying (2) as: $\sigma_{YD}^c \approx 0.5\sigma_Y\bar{\rho}$.

Velocity of cavitated water: When $t = t_c$, the water begins to cavitate at location, $x = x_c$ (with $x = 0$ defining the position of the front face) [3–5]:

$$x_c = -0.71c_w t_0 \frac{\sigma_{YD}^c}{p_0}.$$ (3)

The cavitation front moves through the water, away from the panel. It reaches the surface in a time frame much shorter than the core crushing duration, t_{crush}. Subsequently, the cavitated water moves *toward the panel* with velocity, $v_r(x)$, [5]:

$$v_r = \frac{Ap_0}{\rho_w c_w} e^{x/c_w t_0 T},$$ (4)

with

$$A \approx (0.08 + 2.2\beta)f\left[1 - 0.28\frac{\sigma_{YD}^c}{p_0} - 0.18\left(\frac{\sigma_{YD}^c}{p_0}\right)^2\right],$$

$$T \approx (0.63 - 0.028\beta + 0.003\beta^2)\left(1 - 0.047\frac{\sigma_{YD}^c}{p_0}\right).$$

where $f = \beta^{\beta/(1-\beta)}$. Again, to affirm fidelity, the analytic predictions of the velocity of the cavitated water have been compared with the simulations (Fig. 13). Consequently, the cavitated water imparts additional momentum [5]. In order to predict the core crushing strain and its duration, as well as the total transmitted momentum, it is essential that this momentum be determined.
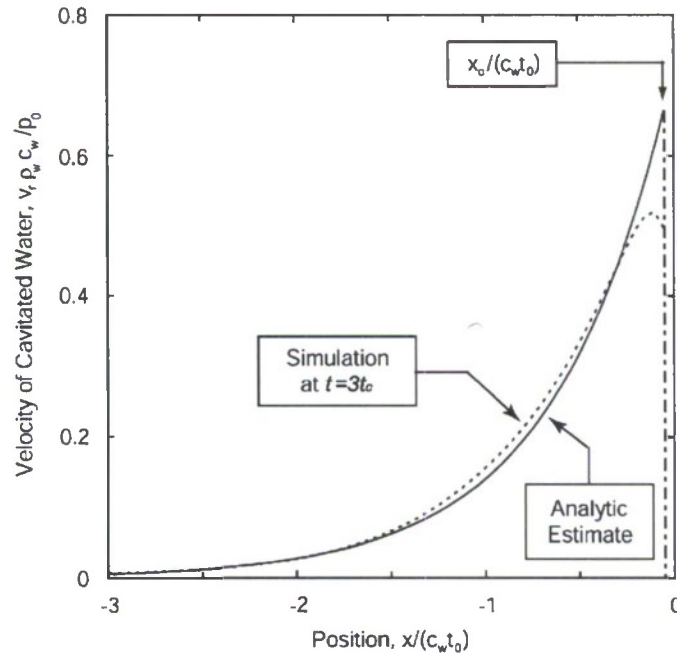

Fig. 13. The analytic approximation for the velocity of the cavitated water. Also shown is the velocity profile at $t = 3t_c$ determined by simulation. The only discrepancy arises close to the cavitation boundary, at $x_c/(c_w t_0)$.

The transmitted momentum: M_T, is that in the top face and attached water plus the additional momentum from the cavitated water [5]:

$$M_T \approx (m_f + m_w)v_{face} + \rho_w \int_{-H_w}^{x_c} v_r(x)\,dx, \tag{5a}$$

with $m_w = \rho_w x_c$ the mass of attached water and H_w the height of the water column. The corresponding kinetic energy acquired by the system is

$$KE \approx \frac{1}{2}(m_f + m_w)v_{face}^2 + \frac{1}{2}\rho_w \int_{-H_w}^{x_c} v_r^2(x)\,dx. \tag{5b}$$

The impulse reaching the back face of the panel (Fig. 11) is [5]

$$I_b \approx \sigma_{crush} t_{crush}. \tag{6}$$

The crushing duration can be determined by combining Eqs. (5a) and (6) and invoking conservation of momentum ($M_T = I_b$) to give:

$$t_{crush} = \frac{M_T}{\sigma_{crush}}. \tag{7}$$

Core crushing strain. The energy absorbed per unit volume, up to a strain ε, is

$$W_c = \int_0^{\varepsilon} \sigma(\varepsilon)\,d\varepsilon \approx \bar{\sigma}_{33}^c \varepsilon \tag{8}$$

with the average core crushing stress characterized by Wei et al. [13]:

$$\frac{\bar{\sigma}_{33}^c}{\sigma_y \bar{\rho}} \approx 0.035 \sqrt{\frac{\dot{\varepsilon}_{eff} h_c}{\dot{\varepsilon}_0 h_0}}, \tag{9}$$

where h_c is the height of a single layer, $\dot{\varepsilon}_0$ is a unit normalization factor ($\dot{\varepsilon}_0 = 1/s$) and $h_0 = 0.1$ m, with the effective crushing strain rate

$$\dot{\varepsilon}_{eff} \approx v_{face}/H_c \varepsilon_{crush}, \tag{10}$$

with ε_{crush} the core crushing strain. The plastic dissipation during crushing, $H_c \bar{\sigma}_{33}^c \varepsilon_{crush}$, absorbs the kinetic energy (5b) [19], such that:

$$\varepsilon_{crush} = \left(\frac{KE}{0.035\sigma_y \bar{\rho}}\right)^2 \frac{\dot{\varepsilon}_0 h_0}{v_{face} h_c H_c}. \tag{11}$$

A simpler procedure having reasonable fidelity for soft multilayer cores is discussed in the Appendix. It gives (A.4):

$$\varepsilon_{crush} \approx \frac{v_{face} t_c}{2H_c} + \frac{m_f v_{face}^2}{\sigma_{YD}^c H_c},$$

Application of the analysis: The utility of the preceding analysis is ascertained by comparisons with experiment and simulation. The assessment is facilitated by simplifications, applicable to multilayer cores especially (2) and (A.4). The analysis has the following steps.

(a) The maximum top face velocity and dynamic strength of the core are implicitly obtained from Eqs. (1) and (2).
(b) With (a), the face velocity is ascertained from Eqs. (A.1) and (A.3).
(c) Based on (a), the velocity of the cavitated water is determined from Eq. (4).
(d) Given (a) and (c), the transmitted momentum is calculated from Eq. (5a) and the kinetic energy from Eq. (5b).
(e) Based on the transmitted momentum, the crush duration is obtained from (7).
(f) Using the kinetic energy, the crushing strain is determined from (11). The approximate formula (A.4) can also be used.

Table 1
Comparisons between experiment, simulation and analytic approximation

	Experiment	Simulation		Analytic approximation
		Continuum model	3D model	
Transmitted Momentum, M_T (kPa s)	8.0	6.5	6.6	6.2
Core Crushing Duration, t_{crush} (ms)	1.7	1.3	1.4	1.2
Core Crushing Strain, ε_{crush}	0.51	0.50	0.55	0.56 (11)
				0.48 (A.4)

The results are summarized in Table 1, where they are compared with simulations conducted using the continuum and 3D models, as well as the experiments. It is apparent that the analytic model has acceptable fidelity, enabling it to be used to understand trends in the response of multilayer cores. It remains to demonstrate similar fidelity for other cores.

7. Conclusions

The response of a sandwich panel with a multilayered pyramidal lattice core subject to underwater blast was investigated by a combination of experimental tests, finite element simulations and theoretical analysis. Such an approach enables a comprehensive assessment of the response of multilayer sandwich structures to water blast, providing insights into the fluid/structure interaction, especially the relation between the core characteristics and the momentum imparted to the structure. The main findings can be summarized as follows:

(1) The stress and impulse transmitted through a multilayered pyramidal panel subject to underwater blast are significantly lower than for a solid cylinder tested under the same conditions.
(2) Finite element simulations conducted using a dynamic constitutive law are capable of predicting most of the features determined experimentally with reasonable fidelity. Some detailed aspects of the core member response are missed.
(3) Strain gage measurements used in the Dyno-crusher test do not provide a direct measure of the transmitted pressure because of the influence of the apparatus. A dc-convolution conducted using a simulation protocol is needed if precise pressure levels are required.
(4) Analytic procedures for predicting the transmitted pressures and impulse and crushing strains have been provided. The estimates are in good agreement with numerical simulations and experiments, indicating that the model has acceptable fidelity. Consequently, it may be used to understand trends in the response of any multilayer core.

Acknowledgments

Appendix. Approximation for the face velocity

The velocity of the top face varies exponentially with time (Fig. 12), enabling the approximation:

$$v_f(t) \approx \begin{cases} v_{face} t/t_c, & 0 \leqslant t \leqslant t_c, \\ v_{face} \exp[-(t - t_c)/t_f], & t > t_c. \end{cases} \tag{A.1}$$

Here t_f is an unknown time scale, which can be ascertained using:

$$\left.\frac{\mathrm{d}v_f(t)}{\mathrm{d}t}\right|_{t\to t_c^+} \approx -\frac{\sigma_{YD}^c}{m_f}. \tag{A.2}$$

where t_c^+ indicates a time incrementally longer than t_c. Equating (A.1) and (A.2) gives

$$t_f = \frac{m_f v_{face}}{\sigma_{YD}^c}. \tag{A.3}$$

By combining Eqs.(A.1) and (A.3) with $\sigma_{YD}^c \approx 0.5\sigma_Y\bar{\rho}$, the top face velocity predicted for the present tests is plotted in Fig. 12. The good fidelity enables the crushing strain to be estimated as

$$\varepsilon_{crush} \equiv \frac{\int_0^{l_{crush}} v_f\,\mathrm{d}t}{H_c} = \frac{v_{face}t_c}{2H_c} + \frac{m_f v_{face}^2}{\sigma_{YD}^c H_c}. \tag{A.4}$$

References

[1] Fleck NA, Deshpande VS. The resistance of clamped sandwich beams to shock loading. J Appl Mech 2004;71:386–401.

[2] Xue Z, Hutchinson JW. A comparative study of impulse-resistant metallic sandwich plates. Int J Impact Eng 2004;30:1283–305.

[3] Hutchinson JW, Xue Z. Metal sandwich plates optimized for pressure impulses. Int J Mech Sci 2005;47:545–69.

[4] Deshpande VS, Fleck NA. A One-dimensional response of sandwich plates to underwater shock loading. J Mech Phys Solids 2005;53:2347–83.

[5] Liang Y, Spuskanyuk AV, Flores SE, Hayhurst DR, Hutchinson JW, McMeeking RM, et al. The response of metallic sandwich panels to water blast. J Appl Mech 2005; in press.

[6] Qiu X, Deshpande VS, Fleck NA. Finite element analysis of the dynamic response of clamped sandwich beams subject to shock loading. Euro J Mech A-Solid 2003;22:801–14.

[7] Qiu X, Deshpande VS, Fleck NA. Dynamic response of a clamped circular sandwich plate subject to shock loading. J Appl Mech 2004;71:637–45.

[8] Xue Z, Hutchinson JW. Preliminary assessment of sandwich plates subject to blast loads. Int J Mech Sci 2003;45:687–705.

[9] Wadley HNG, Dharmasena KP, Chen Y, Dudt P, Knight D, Charette R. et al. Compressive response of multilayered pyramidal lattices during underwater shock loading. Int J Impact Eng 2006; in press.

[10] Nemat-Nasser S, Guo WG, Kihl DP. Thermomechanical response of AL-6XN stainless steel over a wide range of strain rates and temperatures. J Mech Phys Solids 2001;49:1823–46.

[11] Xue Z, Hutchinson JW. Crush dynamics of square honeycomb sandwich cores. Int J Numer Method Eng 2006;65:2221–45.

[12] Xue Z, Vaziri A, Hutchinson JW. Non-uniform hardening constitutive model for compressible orthotropic materials with application to sandwich plate cores. Comp Model Eng Sci 2005;10:79–95.

[13] Wei Z, He MY, Evans AG. Application of a dynamic constitutive law to multilayer metallic sandwich panels subject to impulsive loads. J Appl Mech 2005; in press.

[14] ABAQUS Analysis user's manual, version 6.5. ABAQUS, Inc., 2005.

[15] Kiddy K. Private communication.

[16] Zok FW, Waltner SA, Wei Z, Rathbun HJ, McMeeking RM, Evans AG. A protocol for characterizing the structural performance of metallic sandwich panels: application to pyramidal truss cores. Int J Solids Struct 2004;41:6249–71.

[17] Taylor GI. The pressure and impulse of submarine explosion waves on plates. The scientific papers of G. 1. Taylor, vol. III. Cambridge: Cambridge University Press; 1963. p. 287–303.

[18] Vaughn DG, Canning JM, Hutchinson JW. Coupled plastic wave propagation and column buckling. J Appl Mech 2005;72:139–46.

[19] Ashby MF, Evans AG, Fleck NA, Gibson LJ, Hutchinson JW, Wadley HNG. Metal foams: a design guide. London: Butterworth-Heinemann; 2000.

Appendix C

DYNAMIC COMPRESSION OF SQUARE HONEYCOMB STRUCTURES DURING UNDERWATER IMPULSIVE LOADING

HAYDN N. G. WADLEY, KUMAR P. DHARMASENA, DOUG T. QUEHEILLALT, YUNGCHIA CHEN,
PHILIP DUDT, DAVID KNIGHT, KEN KIDDY, ZHENYU XUE AND ASHKAN VAZIRI

Significant reductions in the fluid structure interaction regulated transfer of impulse occur when sandwich panels with thin (light) front faces are impulsively loaded in water. A combined experimental and computational simulation approach has been used to investigate this phenomenon during the compression of honeycomb core sandwich panels. Square cell honeycomb panels with a core relative density of 5% have been fabricated from 304 stainless steel. Back supported panels have been dynamically loaded in through thickness compression using an explosive sheet to create a plane wave impulse in water. As the impulse was increased, the ratio of transmitted to incident momentum decreased from the Taylor limit of 2, for impulses that only elastically deformed the core, to a value of 1.5, when the peak incident pressure caused inelastic core crushing. This reduction in transmitted impulse was slightly less than that previously observed in similar experiments with a lower strength pyramidal lattice core and, in both cases, was well above the ratio of 0.35 predicted for an unsupported front face. Core collapse was found to occur by plastic buckling under both quasistatic and dynamic conditions. The buckling occurred first at the stationary side of the core, and, in the dynamic case, was initiated by reflection of a plastic wave at the (rigid) back face sheet-web interface. The transmitted stress through the back face sheet during impulse loading depended upon the velocity of the front face, which was determined by the face sheet thickness, the magnitude of the impulse, and the core strength. When the impulse was sufficient to cause web buckling, the dynamic core strength increased with front face velocity. It rose from about 2 times the quasistatic value at a front face initial velocity of 35 m/s to almost 3 times the quasistatic value for an initial front face velocity of 104 m/s. The simulations indicate that this core hardening arises from inertial stabilization of the webs, which delays the onset of their buckling. The simulations also indicate that the peak pressure transmitted to a support structure from the water can be controlled by varying the core relative density. Pressure mitigation factors of more than an order of magnitude appear feasible using low relative density cores. The study reveals that for light front face sandwich panels the core strength has a large effect upon impulse transfer and the loading history applied to support structures.

1. Introduction

Metallic sandwich panels with cellular cores have attracted significant attention for dynamic energy absorption and impact mitigation [Baker et al. 1998; Fleck and Deshpande 2004; 2005; Hutchinson and Xue 2005; Deshpande et al. 2006; Rathbun et al. 2006; Dharmasena et al. 2007b; Liang et al. 2007]. During impact with rigid objects, they reduce damage to the structures they protect by core crushing and face sheet stretching at pressures significantly less than those created when an equivalent solid is

impacted. When sandwich panel structures are impulsively loaded in water, additional mitigation is possible because of beneficial fluid structure interactions (FSI) with thin face sheets [Fleck and Deshpande 2004; Hutchinson and Xue 2005].

The origin of the FSI enhancement arises from a reduction in the reflection coefficient of a normally incident shock front with a solid structure. The pressure pulse from a detonation in water exhibits a sharp rise to a peak pressure and is followed by a slower decay [Cole 1948]. The pressure, $p(t)$, can be written

$$p(t) = p_0 e^{-t/t_0},$$

where p_0 is the peak pressure, t is time measured from the peak in pressure and t_0 is a characteristic time constant. The impulse per unit area, I_0, transported by the pressure pulse through the fluid is given by

$$I_0 = \int_0^\infty p(t)dt = p_0 t_0.$$

Taylor [1963] showed that in the linear (acoustic) fluid propagation limit, the pressure pulse is totally reflected at the surface of a rigid structure, or one with very heavy face sheets. The impulse I transmitted to the structure is then twice that of the incident pulse. An extension of Taylor's theory for FSI in air blasts, which accounts for nonlinear compressibility and finite shock behavior, was recently proposed [Kambouchev et al. 2006] and employed to assess the performance of all-metal sandwich plates under high intensity air shocks [Vaziri and Hutchinson 2007]. In this the reflection coefficient depends upon the peak pressure, and can reach a value of 8 for ideal gases, and higher values when dissociation occurs.

When an unsupported thin (light) panel or a sandwich panel with thin faces and a very weak core is impulsively loaded in water, the front face sheet can move away from the impulse, and the transmitted pressure and impulse are then less than the Taylor prediction [Taylor 1963; Fleck and Deshpande 2004; Hutchinson and Xue 2005]. The effect is strongest for water borne impulses. In the acoustic limit, the transmitted impulse I when a core has no strength depends only upon the thickness of the front face sheet, the density of the material it is made of, and the decay time (t_0) of the pulse, as

$$I = 2I_0 q^{q/(1-q)}, \tag{1}$$

where

$$q = \frac{\rho_w c_w}{\rho h_f} t_0,$$

in which ρ_w is the density of and c_w the speed of sound in the acoustic medium, and ρ is the density and h_f the thickness of the face sheet. The mass per unit area of the face sheet, m_f, is the ρh_f product. The ratio $\rho_w c_w / m_f$ is an important dimensionless quantity which controls the impulse transferred to a plate structure. For very heavy plates, Equation (1) gives Taylor's result, but for thinner plates, large reductions in impulse can occur. For example, a 5 mm thick, 304 stainless steel plate loaded in water has $m_f = 40 \, \text{kg/m}^2$, $\rho_w = 1000 \, \text{kg/m}^3$, and $c_w = 1400 \, \text{m/s}$. If $t_0 = 0.1 \, \text{ms}$, $q = 3.5$, and the impulse transmitted from water to such a face sheet is only 0.35 times that of the incident pulse.

In sandwich panels with strong cores, front face sheet motion is resisted by the core [Xue and Hutchinson 2006; Liang et al. 2007]. Recent measurements of the impulse transmitted into fully back supported sandwich panels with pyramidal lattice cores and 4.8 mm thick stainless steel face sheets indicate the

transmitted to incident impulse ratio is increased (from 0.35 for a free 5 mm thick plate) to $\sim$ 1.4 during underwater impulsive loading [Wadley et al. 2007a]. This is significantly less than the Taylor result for the rigid plate of the same mass per unit area as the sandwich panel. This result indicates that even when the face sheet thickness is held constant, considerable changes in the impulse transferred to a back supported structure can result from variations to the core crush resistance.

Recent analytical and numerical studies of edge supported panels subjected to dynamic loading have confirmed that core crushing during distributed impulsive loading does affect impulse transfer [Baker et al. 1998; Fleck and Deshpande 2004; 2005; Hutchinson and Xue 2005; 2006; Rathbun et al. 2006; Tilbrook et al. 2006; Dharmasena et al. 2007b; Liang et al. 2007; McShane et al. 2007]. This crushing behavior depends upon the cell topology, the material used to construct the cells, and the volume fraction of cell material (the core relative density, $\bar{\rho}$) [Tilbrook et al. 2006; McShane et al. 2007]. Numerous sandwich panel core topologies have been investigated, including simple I cores [Liang et al. 2007], various honeycombs [Xue and Hutchinson 2004; 2006; Dharmasena et al. 2007b], (prismatic) corrugations [Xue and Hutchinson 2004; Dharmasena et al. 2007a; McShane et al. 2007], and lattice truss structures [Wadley et al. 2007a; Wei et al. 2007a]. Examples of these are schematically illustrated in Figure 1. These theoretical assessments are being complimented with a variety of experiments designed to probe the dynamic crush response of cellular structures. This required development of experimental methods for the fabrication of sandwich panels from high ductility alloys [Tilbrook et al. 2006; McShane et al. 2007]. Honeycombs with cell dimensions in the 10 mm range can be made using a slotted sheet method followed by transient liquid phase bonding [Wadley et al. 2003; Wadley 2006]. The corrugations and lattices shown in Figure 1 can be made using sheet folding methods (in the latter case using a perforated metal sheet) [Wadley et al. 2003; Wadley 2006].
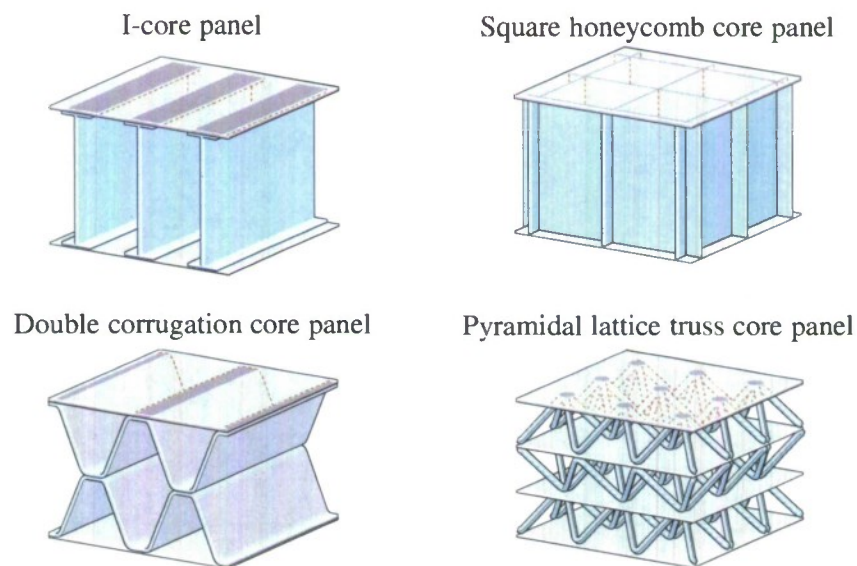
I-core panel   Square honeycomb core panel

Double corrugation core panel   Pyramidal lattice truss core panel

Figure 1. Cellular core topologies.

Several experimental techniques can be utilized to investigate the dynamic mechanical response of sandwich panel structures [Radford et al. 2005; Lee et al. 2006a; 2006b; Rathbun et al. 2006; Dharmasena et al. 2007b; Mori et al. 2007; Wadley et al. 2007a]. These include Kolsky bar methods [Lee et al. 2006a; 2006b] and gas gun experiments using metal foam projectiles [Radford et al. 2005; Rathbun et al. 2006] and other impactors [Lee et al. 2006a; 2006b; Mori et al. 2007]. These have been coupled with high speed photography to observe core crush mechanisms over a wide range of strain rates and incident pressures [Radford et al. 2005; Lee et al. 2006a; 2006b; Rathbun et al. 2006; Mori et al. 2007]. Recent water shock tube experiments have also been conducted on small scale metallic test structures with either stochastic foam [Radford et al. 2005; Deshpande et al. 2006], pyramidal lattice [Lee et al. 2006a; Mori et al. 2007], or square honeycomb [Rathbun et al. 2006; Mori et al. 2007] core topologies. These have enabled the dynamic response of sandwich panel structures to be examined as a function of the front face velocity (core crushing rate). All of these experiments indicate significant elevations of the quasistatic core strength once the front face velocity is increased above about 20 m/s [Deshpande et al. 2006].

Experimental assessments of the core dynamic compressive strength of sandwich panels can also be made using a novel explosive test technique, in which an explosive sheet is detonated inside a water column positioned on top of a well supported sandwich panel [Wadley et al. 2007a]. The response of the sandwich panel to the water borne impulse is then controlled by the charge mass, the charge to sample (standoff) distance, and the FSI which defines the momentum transferred to the structure [Fleck and Deshpande 2004; Hutchinson and Xue 2005; Liang et al. 2007]. The momentum transferred to the front face of the sandwich panels in these tests depends in part upon the face sheet mass per unit area [Hutchinson and Xue 2005; Liang et al. 2007]. As the momentum is acquired, the face sheet is quickly accelerated to a peak velocity. The characteristic time for this is governed by the decay constant of the exponentially decreasing pressure pulse [Cole 1948]. Movement of the front face compresses the core; the front face is decelerated by the dynamic resistance force of the core and eventually brought to rest. This resisting pressure can be measured at the back face, providing a good estimate of the core's dynamic compressive strength.

Finite element models (FEM) have been used to investigate the mechanisms of core crushing during dynamic loading [Qiu et al. 2003; Rabczuk et al. 2004; Xue and Hutchinson 2004; Xue et al. 2005; Tilbrook et al. 2006; Liang et al. 2007; McShane et al. 2007; Vaziri and Xue 2007]. The inelastic deformation of the axially loaded webs in a honeycomb panel begins by propagation of a plastic wave down the plate. If the back of the structure can support stress, reflection of the wave at the bottom face sheet can cause a buckle to form near the bottom face sheet [Vaughn and Hutchinson 2006]. Dynamic core hardening then results from three mechanisms: inertial resistance (to acceleration) of the core mass, inertial stabilization against web buckling, and material strain rate hardening of the webs [Xue and Hutchinson 2006]. The FEM analyses indicate that the three effects combine to dissipate the kinetic energy acquired by an impulsively loaded sandwich panel structure.

The energy absorbed during the crushing of a square honeycomb lattice increases with the critical buckling strain and is therefore sensitive to the mode of web collapse [Xue and Hutchinson 2006]. This depends upon the web thickness, width and height (which also establish the cell size and relative density), and the tangent modulus of the web material. Moreover, combining with an eigenvalue analysis, Xue and Hutchinson [2006] have also conducted a set of computations to systematically explore the effects of initial imperfection on the dynamic response of square honeycomb cores. They concluded that the

velocity imparted to the front face also plays a significant role in governing the buckling mode of web collapse such that the higher the velocity the shorter the buckling wavelength.

These studies reveal that the effective crush strength of a honeycomb core structure is a strong function of the velocity of the front face during dynamic loading. For small crush strains, motion of the front face is resisted by the reaction forces created when a plastic wave is propagated along the straight webs. If strain hardening effects are weak, and therefore ignored, the dynamic strength of the core in the nonbuckling regime is governed by the core's dynamic yield stress, σ_{YD}^c. In the plastic yield region of core crushing, this can be estimated by

$$\sigma_{YD}^c \cong \sigma_{YD}\bar{\rho},$$

where σ_{YD} is the dynamic yield strength of the alloy and $\bar{\rho}$ is the relative density of the core defined as the volume fraction of the core occupied by the material. The dynamic strength of 304 stainless steel at the loading rates of interest is not more than 20% higher than that measured quasistatically [Stout and Follansbee 1986].

At higher impulses, web buckling is the dominant deformation mode. The analysis of honeycomb web buckling from [Xue and Hutchinson 2006] led to the approximate relation between the dynamic yield strength and core density

$$\sigma_{YD}^c \cong \left[1 + \left(\frac{E_t}{E}\right)^{1/2}\left(\frac{\upsilon_f}{c_{el}\varepsilon_Y} - 1\right)\right]\sigma_Y\bar{\rho}, \tag{2}$$

where E_t is the linear hardening tangent modulus (measured quasistatically), E is the Young's modulus, c_{el} is the elastic wave speed, υ_f is the front face (crush) velocity, and σ_Y and ε_Y are the yield strength and strain of the alloy, respectively. Equation (2) indicates that for fixed E and $\bar{\rho}$, it is beneficial to use alloys with high E_t. Austenitic stainless steels exhibit this characteristic.

Here we use a simple corrugation method to fabricate square honeycomb sandwich panel structures from a high ductility, high tangent modulus 304 stainless steel [Stout and Follansbee 1986], explained in Section 2. In Section 3, the quasistatic compression response of the core has been measured and found to be approximately three times stronger than the recently tested pyramidal lattice structures made from the same alloy [Wadley et al. 2007a]. It therefore provides an opportunity to experimentally assess the role of core strength (via a change in topology) upon impulse transmission during explosive loading. Test panels with identical thickness face sheets to those of the pyramidal lattice were subjected to a range of impulsive loads by varying the stand off distance between the test structure and a planar explosive source (see Section 3). The backside pressure-time waveforms of the fully back supported test structures were then monitored as they dynamically collapsed. Similar experiments were conducted with solid cylinders to determine the incident impulse. A complementary numerical modeling study investigated various aspects of the mechanical response of square honeycomb cores under this high intensity loading. A 3-dimensional finite element model of the experimental setup was constructed, and is described in detail in Section 4.1. The material models used in the computational schemes to represent the behavior of the water column and sandwich panel material are discussed in Section 4.2. In Section 4.3, a finite element hydrocode analysis was carried out to predict the pressure applied to the panel due to the underwater explosion. Finally, in Section 4.4, a simplified finite element unit cell model was used to investigate the effect of core relative density upon the dynamics of the square honeycomb core. These

finite element calculations were carried out using the commercially available software ABAQUS/Explicit. Experimental and numerical results are presented in Section 5 followed by a discussion of the results. The study confirms significant, front face velocity dependent core strengthening in square honeycomb structures. However, even though the dynamic honeycomb core strength is more than three times that of pyramidal lattices, the impulse transferred to heavily loaded panels is only increased slightly. The transmitted pressure appears controllable over wide ranges by varying the core density.

2. Sandwich panel fabrication

A sheet bending and brazing method was used to fabricate square honeycomb core sandwich panels from 304 stainless steel (see Figure 2). The core was fabricated by periodically bending 0.76 mm thick, 99 mm wide steel sheet to create a corrugated structure with a 90° bend angle. The peak to peak corrugation height was approximately 22 mm. Twelve of these corrugated panels were spot welded to create a square honeycomb block. A brazing paste (Wall Colmonoy, Nicrobraz 51 alloy) was applied along the contact edges. This assembly was placed between a pair of 4.8 mm thick, 304 stainless steel face plates which had been spray coated with the same brazing alloy powder carried in a polymer binder. Four structures were placed in a vacuum furnace and subjected to a high-temperature brazing treatment. The thermal cycle consisted of heating at 10° C/min to 550° C, holding for 20 minutes (to volatilize and remove the polymer binder), then further heating to 1050° C for 60 minutes at a base pressure of $\sim 10^{-4}$ torr before furnace cooling to ambient temperature at ~ 25° C/min. After brazing, 203 mm diameter cylindrical samples were cut using a wire electro discharge machine to obtain the circular test samples for quasistatic and dynamic testing. A photograph of one of the test structures is shown in Figure 3.
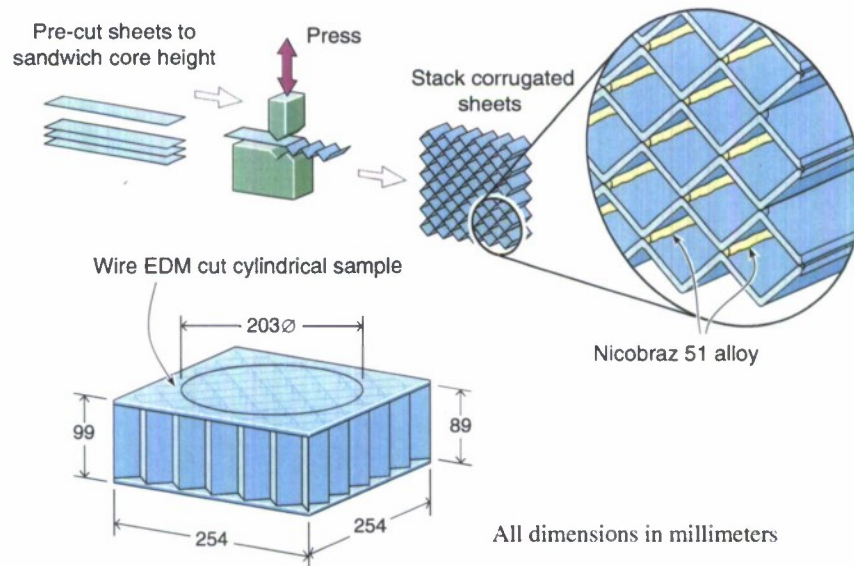

Figure 2. Square honeycomb core and sandwich panel fabrication process.
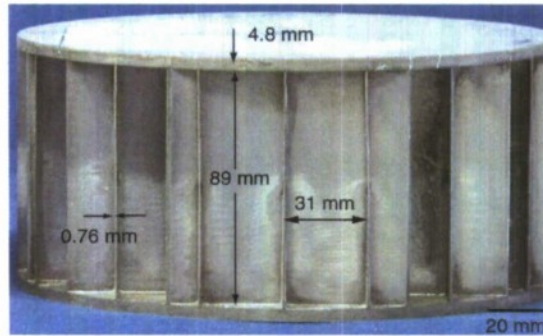
Figure 3. 304SS square honeycomb "dynocrusher" test sample.

The relative density, $\bar{\rho}$, of a square honeycomb structure can be calculated from the ratio of the metal to unit cell volumes (see Figure 4),

$$\bar{\rho} = \frac{t(2l - t)}{l^2} \cong 2\frac{t}{l}.$$

For the samples fabricated here, $h = 89$ mm, $l = 31$ mm, and $t = 0.76$ mm. This gives a core relative density of $\sim 5\%$.

3. Quasistatic compression and impulse loading tests

3.1. *Alloy mechanical properties.* The fabrication process resulted in a core made of annealed 304 stainless steel. The yield strength and strain hardening characteristics of this alloy are sensitive to its thermal history so the uniaxial stress strain response of similarly heat treated alloy specimens was measured according to ASTM E8-01 specifications at a strain rate of 10^{-4} s^{-1}. The elastic modulus and 0.2% offset yield strength were 203 GPa and 176 MPa, respectively. The strain hardening was well approximated by a bilinear fit to the true stress strain data up to a strain of 20%. The tangent modulus in this strain region was ~ 2.1 GPa.

3.2. *Quasistatic compression.* One sandwich panel sample was loaded in uniaxial compression at a strain rate of 5×10^{-4} s^{-1}; its normalized stress strain response is shown in Figure 5a. The specimen
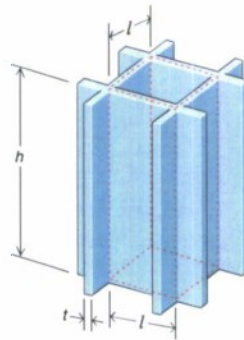

Figure 4. Square honeycomb core unit cell.

exhibited a peak strength of 12 MPa coincident with the onset of web buckling (marked by the first arrow). Two additional buckles were formed at strains of $\sim 25\%$ and $\sim 50\%$ before the core began to harden rapidly at a strain of $\sim 70\%$. The first buckling event occurred near the bottom (stationary) end of the sample. Figure 5b shows a cross section of the fully compressed sample. The onset of hardening at a strain of 70% resulted from the impingement of the three buckles in each honeycomb web.

3.3. *Dynamic loading tests.* The dynamic response of the square honeycomb structures was determined using the explosive test technique schematically illustrated in Figure 6. The test procedures were identical to those previously reported [Wadley et al. 2007a]. Each test sample was placed on a specimen tray resting on four high strength steel columns to which strain gauges were attached as shown. Prior calibrations in a mechanical testing frame were used to convert the strain gauge signals to average pressure measured at the back face of the specimen. Suitable band pass filtering techniques were used to increase the signal to noise ratio. A steel cover plate was positioned over the specimen such that the top sample face was flush with the top surface of the cover plate. A 0.9 m diameter cardboard cylinder (and plastic liner) was then placed over the cover plate and filled with water. A 20.3 cm × 20.3 cm × 0.1 cm explosive sheet was then positioned in the water at standoff distances $H = 25.4$ cm, 15.2 cm, or 10.2 cm above the top sample surface. An analysis of the test and effects of the reverberations in the support columns upon the results is presented elsewhere [Dharmasena et al. 2007a; Wei et al. 2007a].

3.4. *Dynamic test calibration.* The dynamic pulse loading system was calibrated using a solid 6061-T6 aluminum alloy cylinder whose outer dimensions were identical to the sandwich panel specimens. The
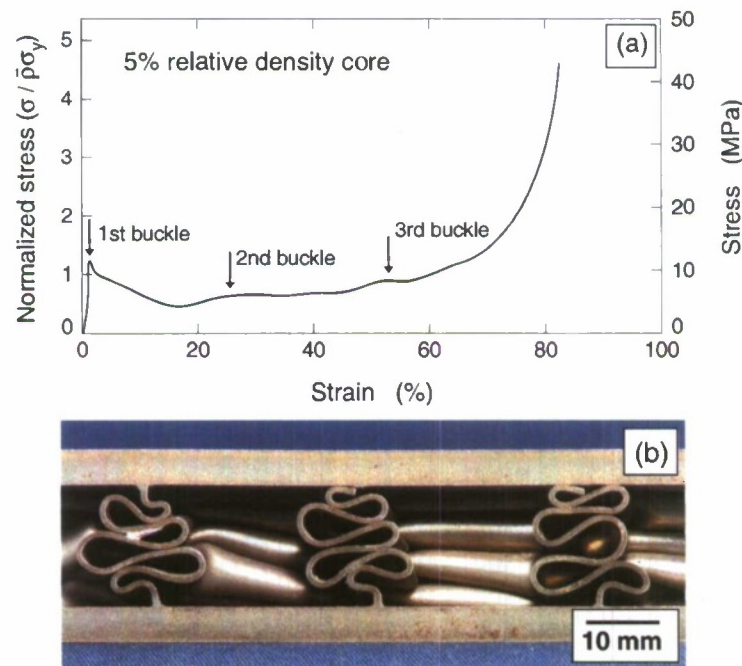

Figure 5. (a) Quasistatic response of 5% relative (core) density square honeycomb sample. (b) Compressed sample after quasistatic test.
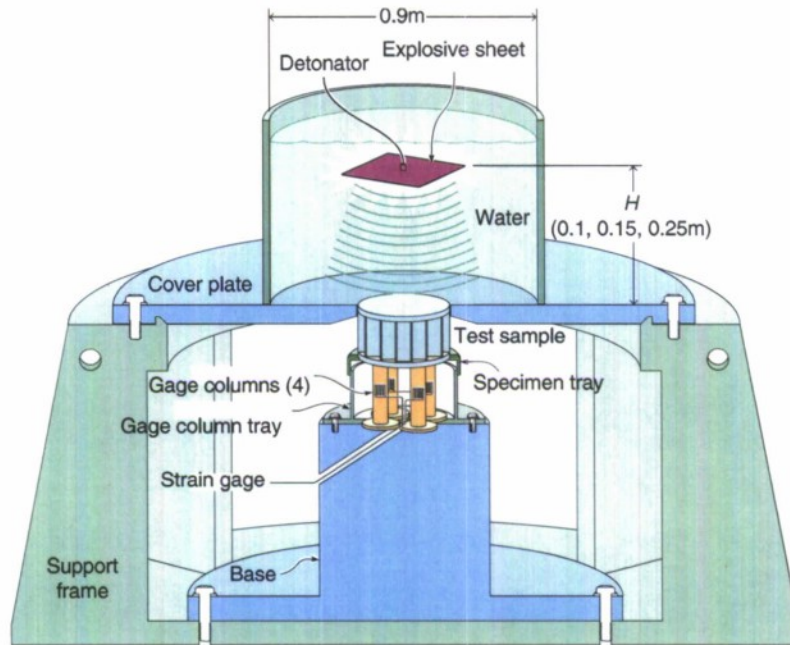
Figure 6. "Dynocrusher" test configuration.

"dry" side pressure for each test was obtained from the average of the four pressures converted from the strain gage signals. Each of the pressure-time traces for the four load column signals was very similar in amplitude and time response. The transmitted impulses were calculated by time integration of the pressure-time waveforms. The "dry" side pressure versus time response and the transmitted impulse per unit area waveforms for the different standoff distances have been reported elsewhere [Dharmasena et al. 2007a; Wadley et al. 2007a]. The peak pressure and transmitted impulses for the three standoffs are summarized in Table 1.

4. Finite element simulations

4.1. *Finite element model of the experimental setup.* A computational model of the experimental setup was developed to mimic the experiments performed on the dynamically loaded square honeycomb panels, and to study various aspects of the mechanical response of the sandwich panel core. A schematic illustration of the model is shown in Figure 7. In the model, the water, face sheets, specimen tray, and four gage columns were fully meshed using eight-node linear brick elements with reduced integration. Each

Standoff distance (cm)	Peak pressure (MPa)	Transmitted impulse (kPa·s)
25.4	27	6
15.2	40	9.9
10.2	52	11.8

Table 1. Effect of standoff on the transmitted pressure and impulse for solid cylinders.

face sheet was discretized with two elements through the thickness. The honeycomb core walls were meshed using four-node shell elements with finite membrane strains. Five section integration points with Simpson's integration rule were used in each shell element. Fifty elements were uniformly distributed through the core thickness. The core webs were perfectly welded to the face sheet at the corresponding connections. The contact between the bottom surface of the sandwich panel and the top surface of the specimen tray was taken to be frictionless. As suggested by [Wei et al. 2007a; 2007b], the support base beneath the gage columns was modeled as a parallel spring and dashpot pair capable of capturing its elasticity and energy dissipation in terms of its overall response. The top surface of each gage column was perfectly bonded to the specimen tray, while the bottom surface of each gage column was tied to a rigid surface connected to the spring-dashpot pair. The bottom ends of the spring and dashpot were fixed. The base, the spring, and the dashpot were allowed to move only vertically, with no transverse displacements and rotations allowed.

4.2. *Material properties.* The water was modeled as an acoustic medium, with a bulk modulus set to 2.05 GPa and a density of 998.23 kg/m^3 [Abaqus 2005]. To model fluid cavitation during reflection of a waterborne impulse with the structure a cavitation pressure was simply set as zero, such that the fluid undergoes free volume expansion when the pressure reaches zero. The sandwich panel was made of a stainless steel alloy having a density of 7900 kg/m^3 and a Poisson ratio of 0.3. In the simulations, the Mises criterion was adopted to model yielding of the material. The true stress (σ) versus true strain (ε)
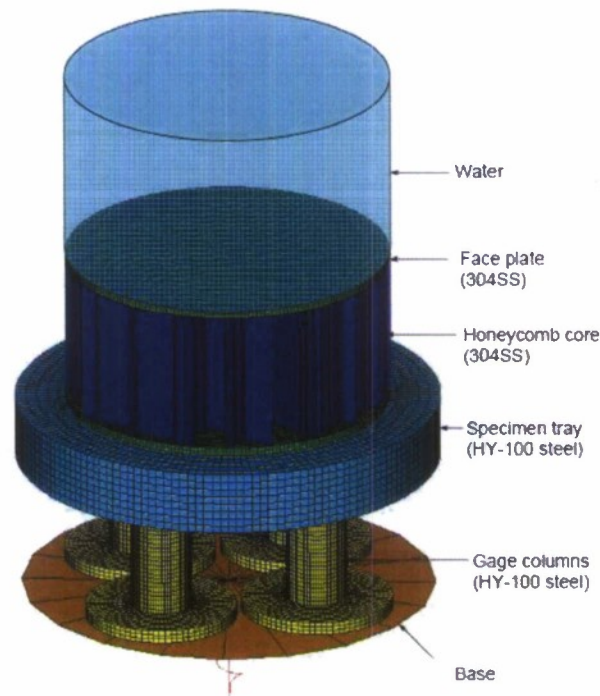

Figure 7. Finite element model representation of the "dynocrusher" test.

relation for the steel was taken to be bilinear for each value of plastic strain-rate, $\dot{\varepsilon}_p$, as

$$\sigma = \begin{cases} E\varepsilon, & \varepsilon \leq \dfrac{\sigma_Y}{E}\left(1+\left(\dfrac{\dot{\varepsilon}_p}{\dot{\varepsilon}_0}\right)^m\right), \\[2em] \sigma_Y\left(1+\left(\dfrac{\dot{\varepsilon}_p}{\dot{\varepsilon}_0}\right)^m\right) + E_t\left(\varepsilon - \dfrac{\sigma_Y}{E}\left(1+\left(\dfrac{\dot{\varepsilon}_p}{\dot{\varepsilon}_0}\right)^m\right)\right), & \varepsilon > \dfrac{\sigma_Y}{E}\left(1+\left(\dfrac{\dot{\varepsilon}_p}{\dot{\varepsilon}_0}\right)^m\right). \end{cases}$$

Here, $E = 203\,\text{GPa}$, $\sigma_Y = 176\,\text{MPa}$, and $E_t = 2100\,\text{MPa}$. Dynamic measurements on stainless steels are well represented using the values $\dot{\varepsilon}_0 = 4.916\,\text{s}^{-1}$ and $m = 0.154$. The specimen tray and the gage columns were made of HY100 steel. Since the specimen tray and all the gage columns undergo elastic deformation only, their mechanical behavior was specified by linear elasticity with elastic modulus of 205 GPa, a Poisson ratio of 0.3, and a density of 8000 kg/m^3. All the materials were assumed to be sufficiently ductile that no fracture needed to be taken into account.

In order to calibrate the coefficients of the spring and dashpot, additional finite element simulations were performed for the reference tests, where solid 6061-T6 aluminum alloy cylinders were used as the specimens, as described in Section 4.2. The solid cylinders were fully meshed using eight-node linear brick elements with reduced integration. A density of 2713 kg/m^3 and a Poisson ratio of 0.33 were used for the aluminum alloy cylinder simulations. In addition, its rate dependent stress strain relation was specified by

$$\sigma = \begin{cases} E^{Al}\varepsilon, & \varepsilon \leq \dfrac{\sigma_Y^{Al}}{E^{Al}}, \\[2em] \left(\dfrac{E^{Al}-E_t^{Al}}{E^{Al}}\sigma_Y^{Al} + E_t^{Al}\varepsilon\right)\left(1+\left(\dfrac{\dot{\varepsilon}_p^{Al}}{\dot{\varepsilon}_0^{Al}}\right)^m\right), & \varepsilon > \dfrac{\sigma_Y^{Al}}{E^{Al}}, \end{cases}$$

where the elastic modulus $E^{Al} = 70\,\text{GPa}$, the initial yield strength $\sigma_Y^{Al} = 241\,\text{MPa}$, the tangent modulus $E_t^{Al} = 188\,\text{MPa}$, $\dot{\varepsilon}_0 = 163000\,\text{s}^{-1}$, and $m = 1.75$. Other components of the test system were modeled in the same way as discussed before. The calibration procedure for identifying the system compliance is similar to that detailed in [Wei et al. 2007b]. As described in Section 4.2, three calibration tests were performed with the solid cylinders. For a given spring stiffness and dashpot viscosity, the finite element prediction of the transmitted pressure history was compared with the corresponding experimental data. By adjusting the spring stiffness and the dashpot viscosity, the amplitudes of the transmitted signal and echoes and the time intervals of the echoes were reasonably matched. A spring stiffness of 10 GN/m and dashpot viscosity of 1 MN·s/m were found to approximately represent the system compliance.

4.3. *Hydrocode analysis of the pressure history in water.* The pressure fields in the fluid and at the specimen-water interface following detonation of an explosive sheet were calculated using a fully coupled Euler–Lagrange finite element hydrocode [Wardlaw and Luton 2000; Wardlaw et al. 2003]. The code allowed the analysis of shock propagation through a fluid medium using an Eulerian solver and then coupled it to the structural response of the solid target using a Lagrange code. Since the explosive sheet was relatively thin (1 mm), and high spatial and temporal gradients of pressure existed in the fluid medium, a fine Eulerian mesh in the direction of the target was used. The Euler run was started with 0.2 mm cells in the explosive sheet thickness direction and 0.4 mm divisions in the other two directions (in the plane parallel to the explosive sheet). The explosive sheet was specified by its geometry, the

explosive's material properties, and by the detonation velocity using the Jones–Wilkins–Lee equations of state for shock calculations [Wardlaw and Luton 2000; Wardlaw et al. 2003]. The pressure loading on a rigid wall, representing the front surface of the solid cylinder, was calculated at four locations along the radial direction measured from the shortest distance of impact of the blast wave.

The time sequences of pressures at various radial distances for standoff distances 25 cm, 15 cm, and 10 cm are shown in Figure 8. They show the pressure at the rigid sample surface as the wave front underwent reflection. These pressure-time histories were then used to apply the necessary loading conditions at the top surface of the water column for the FEM sandwich panel calculations described in Section 4.2.

4.4. *Numerical investigation on the fundamental dynamics of the unit cell response.* Due to the periodicity of the square honeycomb core configuration, a simplified finite element model using only one unit cell of the structure can be analyzed, and captures many aspects of dynamic responses of the core [Rabczuk et al. 2004; Xue et al. 2005; Vaziri et al. 2006]. Full three-dimensional models of the square honeycomb unit cell subjected to high intensity loading transmitted through water were developed by detailed meshing of the core. The geometry of the unit cell model was consistent with the samples used in the experimental investigations, and is shown in Figure 9. In this set of calculations, the high intensity loading was simulated as an exponential decay pressure history applied to the top face of the water column, which was modeled using acoustic elements. The material constants required for representing the water characteristics and the sample alloy properties were same as those in Section 4.2. The unit cell model was attached to a fixed rigid plate at its bottom face. In the computational model, the faces and the core webs, as well as the water column, were fully meshed. The boundary conditions applied to the unit cell on the edges of the face sheets and the core webs were consistent with sample symmetry and periodicity. The developed unit cell model is essentially one periodic unit of a plate that is infinite in both directions and which is subject to deformation due a pressure history that is transmitted through water. A second series of simulations were conducted using cells of varying width to assess the effect of the core density, and therefore strength, upon the transmitted pressure. The details of the calculations were similar to previous studies [Rabczuk et al. 2004; Xue et al. 2005; Vaziri et al. 2006].
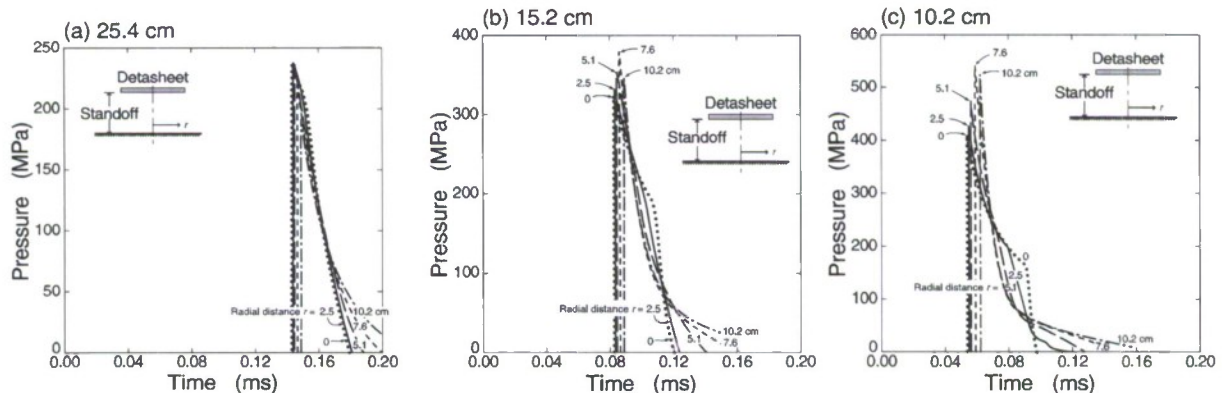

Figure 8. Pressure time loading on a rigid surface calculated from a DYSMAS hydrocode analysis for standoff distances of (a) 25.4 cm, (b) 15.2 cm, and (c) 10.2 cm.
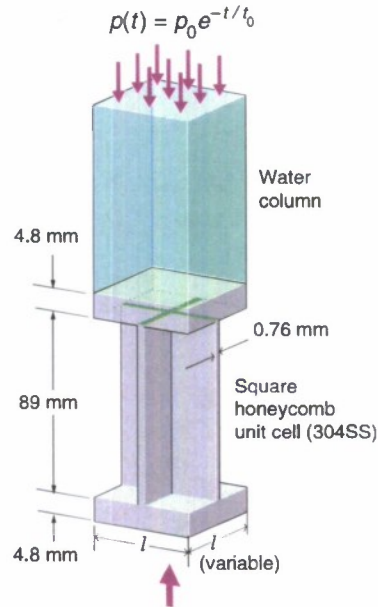
$$p(t) = p_0 e^{-t/t_0}$$

Figure 9. Square honeycomb unit cell finite element model.

5. Results

5.1. *Sandwich panel responses.* Figures 10 and 11 show the (dry side) pressure and impulse waveforms for sandwich panel structures following detonations at standoffs of 25.4, 15.2, and 10.2 cm. Both experimental measurements and simulation results (using the approach described in Sections 4.2 and 4.3) from the full 3-dimensional geometry model are shown. The peak pressure measured on the back side of the specimens initially increased and then remained roughly constant as the standoff distance was decreased. At the furthermost standoff of 25.4 cm, the transmitted pressure waveform, Figure 10a, was very similar to that measured on the calibration solid cylinder [Dharmasena et al. 2007a; Wadley et al. 2007a], and consisted of a single dominant peak with weak ringing. The peak pressure was ~ 25 MPa and the maximum transmitted impulse was 5.6 kPa·s. The experimental and full geometry finite element simulation results were generally in good agreement. This sandwich sample exhibited no evidence of permanent buckling or axial compression (verified with measurements of the sample after testing) and was therefore retested at a standoff of 10.2 cm (see Table 2).

Standoff distance (cm)	Peak pressure (MPa)	Transmitted impulse (kPa·s)	Compression (%)
25.4	25	5.6	—
15.2	35	8.2	6.2
10.2	26	9	29

Table 2. Effect of standoff on the experimentally measured transmitted pressure and impulse for a stainless steel, square honeycomb structure with a core relative density of 5%.
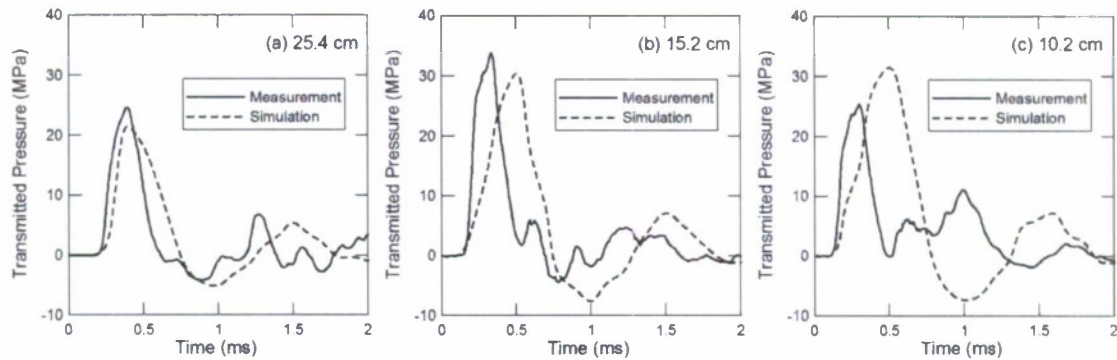
Figure 10. Measured and calculated transmitted pressure-time responses of 304SS square honeycomb core sandwich panels at standoff distances of (a) 25.4 cm, (b) 15.2 cm, and (c) 10.2 cm.
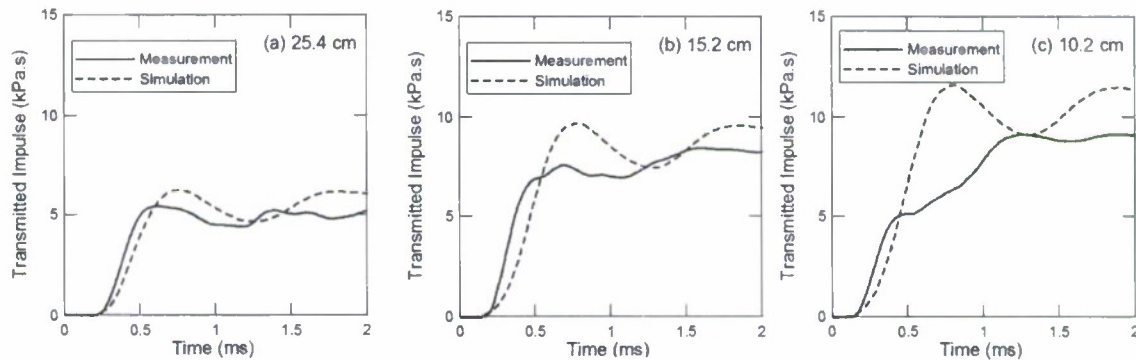

Figure 11. Measured and calculated transmitted impulse time responses of 304SS square honeycomb core sandwich panels at standoff distances of (a) 25.4 cm, (b) 15.2 cm, and (c) 10.2 cm.

Figures 10b and 11b show the dry side pressure and impulse waveforms at a standoff of 15.2 cm. The pressure response consisted of a main pressure peak with a small secondary peak followed by ring down. In this case, the measured peak pressure increased to 35 MPa and the transmitted impulse rose to ~ 8.2 kPa·s (after ~ 2 ms). The secondary peak amplitude was ~ 5 MPa and was delayed by about 0.3 ms from the main pressure peak. The simulated peak pressure and impulse were in good agreement with the experiments. The simulated peak pressure and impulse were ~ 31 MPa and ~ 8.5 kPa·s, respectively. The initial rate of impulse transfer in the simulated response was slightly less than experimentally observed.

A cross sectional view of the sample is shown in Figure 12. The sample suffered an experimentally measured, nonrecoverable axial compressive strain of 6.2%. Cooperative buckling across the full width of the sample occurred close to the bottom (stationary) face. The beginning of a second set of buckles was also evident near the top (wet side) of the specimen.

The pressure and impulse waveforms for a standoff distance of 10.2 cm are shown in Figures 10c and 11c. In this case, three pressure peaks are evident, each separated by about 0.3 ms. The main (first
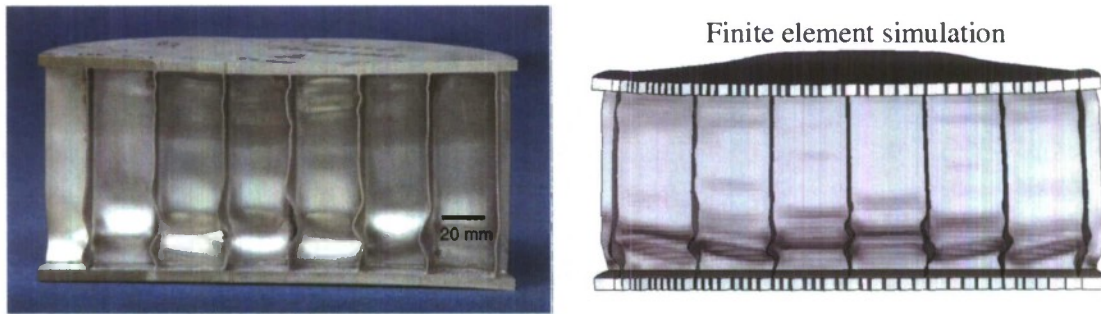
Figure 12. Experimental (left) and predicted (right) cross sections of the final deformed shapes at standoff distance of 15.2 cm.
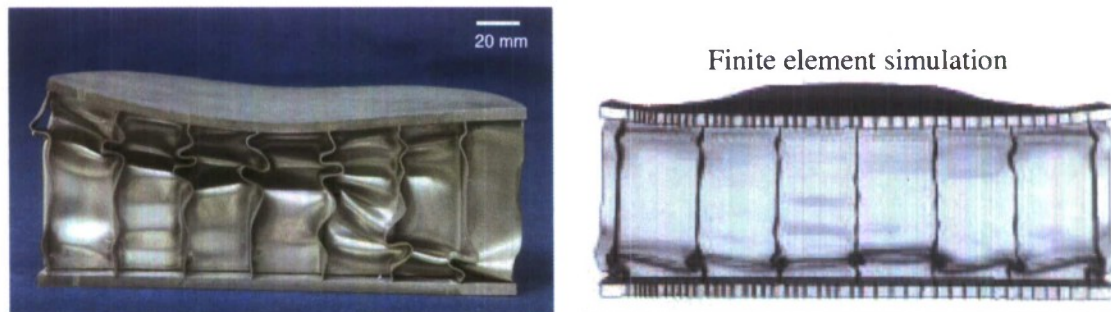

Figure 13. Experimental (left) and predicted (right) cross sections of the final deformed shapes at standoff distance of 10.2 cm.

arriving) peak had a peak pressure of ~ 26 MPa. This was slightly lower than that observed for the 15.2 cm standoff. This first peak was associated with the transfer of about a half the total impulse acquired by the sample. When the two delayed pressure pulses were included, the transmitted impulse after 3 ms reached ~ 9 kPa·s, (see Figure 11c). The predicted pressure response had a first peak of ~ 32 MPa, but failed to capture the two smaller pressure peaks in pressure-time history observed in the experiment (see Figure 10c). The total impulse was, however, similar to that measured experimentally (see Figure 11c). The experiments indicate that core crushing and impulse transfer occurred in two distinct phases, whereas only a single deformation phase was apparent in the simulations.

Cross sectional images of the experimental samples and simulation results help resolve the mechanisms of core response, and the source of the discrepancies between simulations and experiments in the most heavily loaded scenario. Figure 13 shows the cross section of the specimen after testing at the shortest standoff distance. The specimen underwent an axial plastic compressive strain of 29% (measured at the center line). Extensive web buckling is evident with between 2 and 4 folds per web. The intense loading of this sample tripped buckling near both the dry and wet side face sheets. It also resulted in the wet side face sheet debonding from the core consistent with a tensile phase of loading (see Figure 10c between 1.2 and 1.7 ms). Examination of the core interior with the dry side face sheet removed indicated that the peak to peak deflection (amplitude) of the buckles was about 40% of the honeycomb wall spacing.

A cross sectional view of the simulated final deformed configurations of the sandwich panels is also shown in Figures 12 and 13 for standoff distances of 15.2 cm and 10.2 cm. The numerical simulations capture the buckling of the core webs, as well as the face sheet deformation, reasonably well for the 15.2 cm standoff distance. For this case, both the finite element simulation and the experimental results show that the core webs buckle near the bottom face sheet as plastic wave reflection occurs at the bottom face sheet interface. For the 10.2 cm standoff case, the simulation again predicts extensive honeycomb buckling near the bottom face sheet. A much smaller region of buckling near the top face sheet is also evident. However, for the closest standoff (10.2 cm) case, the experiment exhibited buckling at the bottom and top face sheets of roughly similar lateral core web displacement amplitude. At this close standoff, the test sample also exhibited a "dishing" of the front face sheet resulting in more predominant buckles forming at the center of the front face. This observation suggests that with the use of the centrally detonated 20.3 cm × 20.3 cm explosive sheet (placed above the 20.3 cm diameter test samples), there is a noticeable standoff distance effect on the planarity of the blast wave impacting the test samples. At this highest intensity loading level, it is possible that the second set of buckles near the top face sheet of the tested sample (see Figure 13) contributed to a second distinct phase of impulse transfer in the experimental response, not observed in the simulation result (see Figure 11c). These differences in buckling patterns may be a consequence of imperfections present in the experimental samples but improperly captured in the simulation geometry. The finite element simulations do show a region of significant tensile loading similar to that observed in the experiments. This was presumed to be responsible for top face sheet debonding. Figure 14 shows a time sequence of deformed sandwich panel cross sections for the 10.2 cm standoff, and illustrates the tripping of buckles with progressive folding during the first 0.4 ms of crushing.

The predicted axial crushing strain of the core, defined as the relative displacement between the center of the top and bottom face sheets divided by the original height of core, is plotted in Figure 15a as a function of time. The simulations indicate that it takes around 0.4 ms for the honeycomb core to attain its maximum strain. This corresponds to the period of impulse transfer seen in the experiments (see Figure 11). The values of final crushing strains increased as the standoff distance was decreased, and were reasonably similar to those measured (see Table 3). Figure 15b shows the core crush strain rate as a function of time and the front face velocity (obtained by multiplying the strain rate by the core's original height). It can be seen that the predicted peak front face velocity increased with impulse from ~ 35 m/s to 104 m/s. There is some uncertainty in this estimate for the most intensely loaded experimental test, since the impulse was transferred in two stages while the velocity was deduced from a simulation that assumed more rapid impulse transfer.

Standoff distance (cm)	Experimental core strain (%)	Predicted Core strain (%)
25.4	—	7
15.2	6.2	18
10.2	29	30

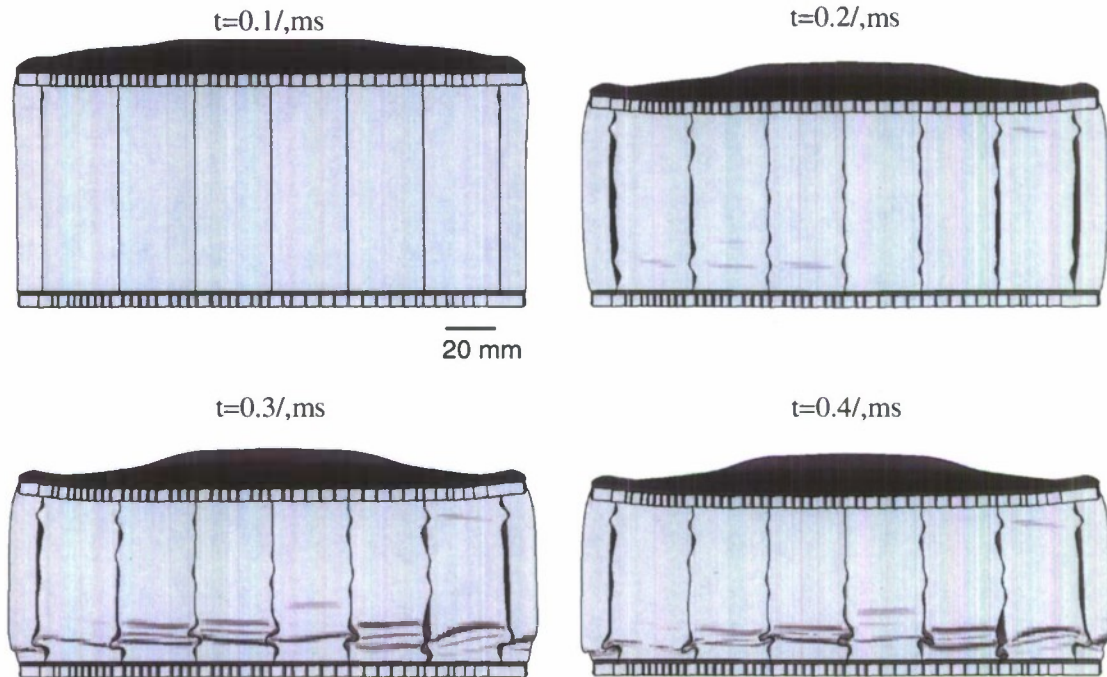**Table 3.** Comparison of the measured and predicted core strain.

Figure 14. Time sequence of deformed shapes for a sandwich panel tested at the 10.2 cm standoff.
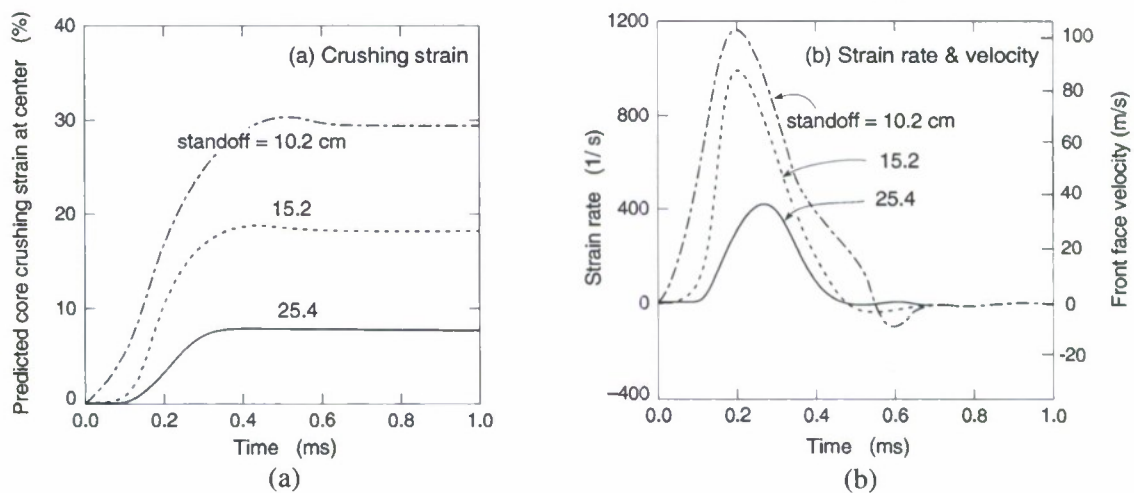

Figure 15. (a) Time dependence of the calculated effective core crushing strain of the square honeycomb panels at standoff distances of 25.4, 15.2, and 10.2 cm. (b) Calculated strain rates and front face velocities for the three standoff distances.

5.2. *Unit cell simulation results.* The unit cell computational models were used to investigate the effect of core relative density upon the pressure transmitted by a rigidly supported structure. The face sheet thickness (at 4.8 mm) was held constant to enable the role of the core's crush resistance to be

independently assessed. The core relative density was adjusted by varying the unit cell size (varying the honeycomb cell wall spacing). For each core configuration, the peak load (p_0) was increased from 5 to 200 MPa. In all cases, a characteristic time decay (t_0) of 0.035 ms was chosen to be consistent with that predicted by the hydrocode simulations.

Figure 16 shows the simulation responses for peak overpressures $p_0 = 50$, 100, 150, and 200 MPa, for relative densities between 2 and 7%. For the 7% relative density core (the strongest core analyzed), the peak transmitted pressure increased monotonically from ~ 30 MPa to ~ 52 MPa as the impulse loading was increased from 50 MPa to 200 MPa. For the 5% core, the peak pressure varied from ~ 21 MPa to ~ 38 MPa over the same overpressure range. Similar monotonic trends were observed from the simulations of the lower core density unit cell samples. These results indicate that very significant reductions in pressure can be achieved when low relative density core structures are used. For example, a 2% relative density core transmits only 16 MPa when impacted by a 200 MPa peak pressure pulse. It can be also seen that the width of the transmitted pressure pulse was inversely related to core density, indicating that the reduction in impulse was not as great as the mitigation of pressure.

Figure 17 summarizes the peak transmitted pressure variation with p_0 for each of the core relative densities. The 7% density strongest core shows a linear relationship with p_0 in the 25–200 MPa range. The 5% core shows an increasing trend with p_0 but at a lower rate of increase than the 7% core. As the core density was further decreased, a weaker dependence of the peak transmitted pressure on p_0 was observed.

6. Discussion

When back supported sandwich panel structures with square honeycomb cores are impulsively loaded in water to a level that is insufficient to cause inelastic core crushing, the transferred impulse and peak pressure are identical to those transmitted through a (back supported) solid plate. It is close to the Taylor predicted limit of $2I_0$ [Taylor 1963]. This has been corroborated by hydrocode simulations of a planar explosive sheet detonated in water at variables distances from a rigid wall [Kiddy 2006]. The experiments reported here indicated that when the incident impulse is able to cause buckling of the honeycomb webs, the transmitted impulse drops significantly from this upper limit even though the back face of the sandwich panel is fully supported and unable to move away from the water borne shock wave.

The effect of the incident overpressure, p_0, and resulting incident impulse strength, I_0, (varied here by changing the standoff) upon the transmitted pressure and impulse are summarized in Figure 18 for the experiments and simulations corresponding to the 3 standoff distances. As the incident impulse was increased to 5 kPa·s (see Figure 18b), core crushing and web buckling were initiated and the transmitted impulse was reduced by 20% compared to that of a solid sample at the same incident impulse. This reduction increased to 25% when the square honeycomb panel was more heavily loaded. In this case, a nearly 30% axial strain occurred in the sample and was accommodated by multiple cell wall buckling events (see Figure 13). This reduction in impulse transfer to the honeycomb sandwich panels arises from the motion of the wet side face sheet away from the incident impulse.

The impulse reductions achieved with honeycomb cores were only a little less than those obtained using pyramidal lattice cores, even though the honeycomb was approximately three times more resistant to quasistatic compression. This higher core strength resulted in a peak pressure transferred by the
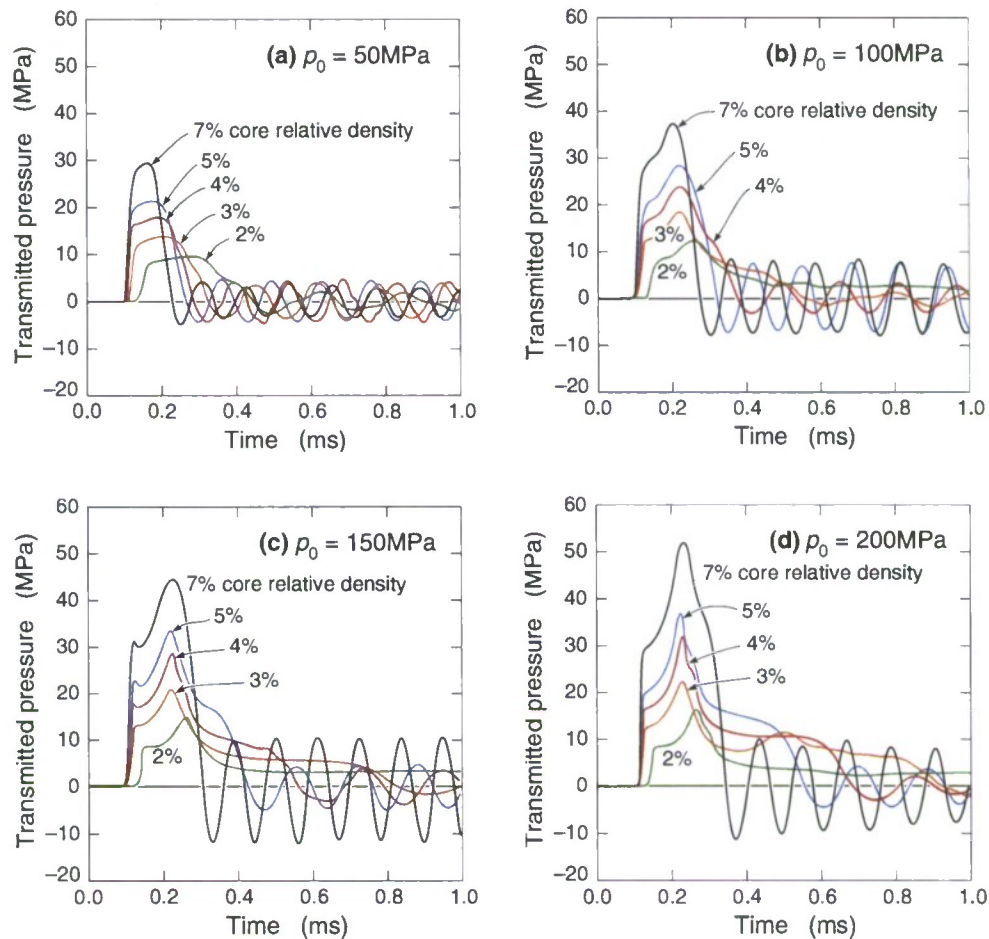
Figure 16. Calculated transmitted pressure response from the unit cell analysis, for different core densities and peak overpressures of (a) 50 MPa, (b) 100 MPa, (c) 150 MPa, and (d) 200 MPa.

honeycomb core (at the 10.2 cm standoff) of ∼ 26 MPa, whereas an identically loaded pyramidal lattice structure transmitted only 12 MPa. In the softer core system, the impulse rise time was larger, enabling the total transferred impulse to reach a similar level to that of the honeycomb. Finite element analyses of the honeycomb and pyramidal cores indicate that the maximum transmitted pressure was controlled by the core dynamic strength, which depends upon the core topology and front face velocity during core compression [Deshpande 2006; Radford et al. 2007]. Here, three different impulse loadings (corresponding to three standoff distances) were used and the front face acquired an initial velocity that depended upon the impulse. Figure 15b shows the time derivative of the calculated strain versus time response (see Figure 15a) and the calculated front face velocity of the back supported honeycomb sample of initial core thickness 0.089 m. These velocities were then used with Equation (2) to estimate the dynamic strength elevation of the square honeycomb core. In Table 4 this is compared with the peak pressure deduced strengths (scaled by that measured quasistatically) for the three standoff distances. Reasonable
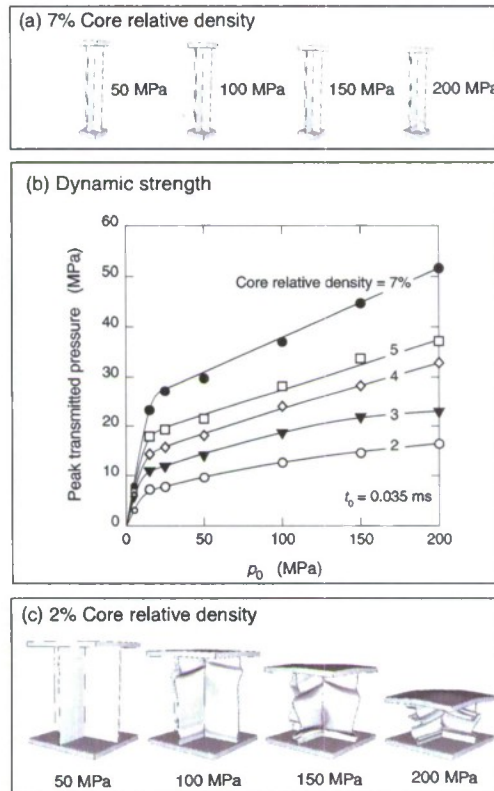
Figure 17. Deformed configurations for the 7% (a) and 2% (c) density square honey-comb unit cells. The peak transmitted back face pressure variation with overpressures (p_0), for a core density range of 2–7% (b).

agreement is observed for the two larger standoff cases, whereas the shorter standoff experiment is again consistent with a slower impulse transfer process.

Significant pressure reductions can be achieved by lowering the core relative density as illustrated in Figure 17. However, for a given impulse load, increasing crush displacements are reached as the core relative density (strength) is reduced. If core densification occurs, the impulse carried by the front face is transferred to the supports, which then experience much higher pressure levels. This can be avoided by designing sandwich panels to have a core thickness above an impulse dependent minimum value. In

Standoff distance (cm)	Calculated front face velocity (m/s)	Dynamic/quasistatic strength ratio	
		Predicted	Measured
25.4	35.6	1.73	2.08
15.2	88.9	2.98	2.92
10.2	103.7	3.32	2.12

Table 4. Effect of standoff on the front face velocity and the dynamic to static strength ratio of the square honeycomb core.
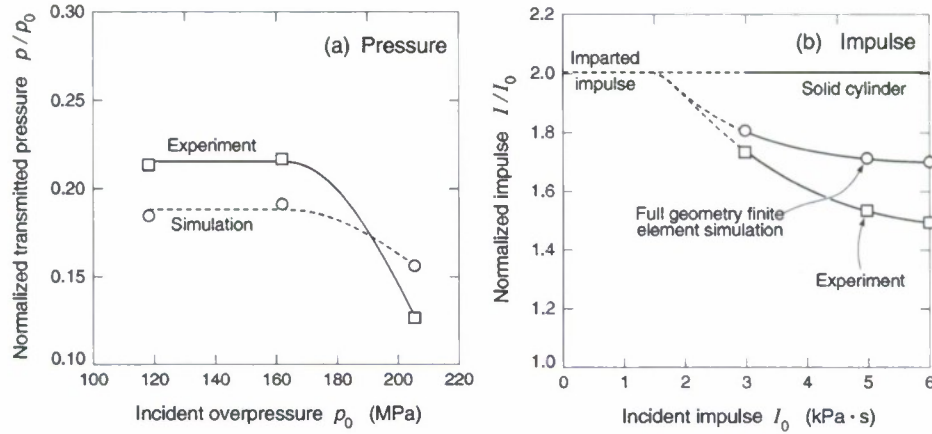
Figure 18. (a) The dependence of the transmitted pressure upon incident pressure. (b) The variation of the transmitted impulse with incident impulse.

this case, the transmitted pressure is controlled by the dynamic crush strength of the core, σ_{cD}. The required minimum thickness for the cellular core, $h_{\min}$, can be estimated from [Ashby et al. 2000] and [Wadley et al. 2007b] as

$$h_{\min} = \frac{I^2}{2m_f \sigma_{cD}(1 - \bar{\rho})},$$

where I is the impulse (momentum) per unit area imparted to the sandwich panel, m_f the mass per unit area of the front face sheet, $\bar{\rho}$ the core relative density, and σ_{cD} the dynamic crush strength of the core before densification is reached.

7. Summary

A combined experimental and computational simulation approach has been used to investigate impulse transfer during underwater shock loading of back supported sandwich structures with square honeycomb core topologies. The study indicates that significant impulse reductions occur, provided core crushing is activated. The majority of the core crushing in square honeycomb core panels occurs by web buckling. This appears to initiate at the dry side face sheet-web interface upon plastic wave reflection. The impulse transferred to these sandwich panels lies below the Taylor predicted limit ($2p_0 t_0$) for a rigidly supported plate and above that of a free plate with mass per unit area corresponding to the wet side face sheet. The impulse transferred to the square honeycomb panels was slightly higher than that transferred to pyramidal core structures whose crush strength is lower than the honeycomb. The experimental study indicates that the transmitted impulse rise time was increased in the sandwich panel systems. This appears to result from the sequential tripping of regions of buckling within the most intensely loaded test structures. For a fixed impulse, increasing the rise time of the transmitted impulse reduces the transmitted pressure and provides beneficial dynamic pulse mitigation effects. "Weaker" core designs (for example a multilayer lattice structure) enhance this beneficial feature, and reduce both the transmitted peak pressure and the impulse under similar loading conditions. The fluid structure interaction for a sandwich panel is influenced by the properties of the fluid medium, the thickness and the density of the face sheet, and

the topology and strength of the sandwich core. Using a unit cell analysis, the face sheet has been kept constant, and the core strength adjusted systematically by varying the core relative density. This has enabled the investigation of the effects of the core strength on the transmitted pressure to a back supported structure. It shows that the core relative density (for a selected sandwich core topology) can be effectively used as a parameter to control the transmitted pressure, provided an adequate core thickness can be used.

Acknowledgements

References

[Abaqus 2005] Hibbit, Karlsson and Sorensen Inc., *ABAQUS/Explicit User's Manual*, Hibbit, Karlsson and Sorensen Inc., 2005. Version 6.0.

[Ashby et al. 2000] M. F. Ashby, A. G. Evans, N. A. Fleck, L. J. Gibson, J. W. Hutchinson, and H. N. G. Wadley, *Metal foams: a design guide*, Butterworth-Heinemann, 2000.

[Baker et al. 1998] W. E. Baker, T. C. Togami, and J. C. Weyder, "Static and dynamic properties of high-density metal honeycombs", *Int. J. Impact Eng.* **21**:3 (1998), 149–163.

[Cole 1948] R. H. Cole, *Underwater explosions*, Princeton University Press, 1948.

[Deshpande 2006] V. S. Deshpande, Private communication, 2006.

[Deshpande and Fleck 2005] V. S. Deshpande and N. A. Fleck, "One-dimensional shock response of sandwich plates", *J. Mech. Phys. Solids* **53** (2005), 2347–2383.

[Deshpande et al. 2006] V. S. Deshpande, A. Heaver, and N. A. Fleck, "An underwater shock simulator", *Proc. Royal Soc. A* **462** (2006), 1021–1041.

[Dharmasena et al. 2007a] K. P. Dharmasena, D. T. Queheillalt, H. N. G. Wadley, Y. Chen, P. Dudt, D. Knight, Z. Wei, and A. G. Evans, "Dynamic response of a multilayer prismatic structure to impulsive loads incident from water", *Int. J. Impact Eng.* (2007). accepted.

[Dharmasena et al. 2007b] K. P. Dharmasena, H. N. G. Wadley, Z. Xue, and J. W. Hutchinson, "Mechanical response of metallic honeycomb sandwich panel structures to high-intensity dynamic loading", *Int. J. Impact Eng.* (2007).

[Fleck and Deshpande 2004] N. A. Fleck and V. S. Deshpande, "The resistance of clamped sandwich beams to shock loading", *J. Appl. Mech.* **71** (2004), 386–401.

[Hutchinson and Xue 2005] J. W. Hutchinson and Z. Xue, "Metal sandwich plates optimized for pressure impulses", *Int. J. Mech. Sci.* **47** (2005), 545–569.

[Kambouchev et al. 2006] N. Kambouchev, L. Noels, and R. Radovitzky, "Compressibility effects on fluid-structure interactions and their implications on the blast loading of structures", *J. Appl. Phys.* **100**:6 (2006), 063519.

[Kiddy 2006] K. Kiddy, Private communication, 2006.

[Lee et al. 2006a] S. Lee, F. Barthelat, J. W. Hutchinson, and H. D. Espinosa, "Dynamic failure of pyramidal truss core materials—experiments and modeling", *Int. J. Plast.* **22** (2006), 2118–2145.

[Lee et al. 2006b] S. Lee, F. Barthelat, N. Moldovan, H. D. Espinosa, and H. N. G. Wadley, "Deformation rate effects on failure modes of open-cell Al foams and textile cellular materials", *Int. J. Solids Struct.* **43** (2006), 53–73.

[Liang et al. 2007] Y. Liang, A. V. Spuskanyuk, S. E. Flores, D. R. Hayhurst, J. W. Hutchinson, R. M. McMceking, and A. G. Evans, "The response of metallic sandwich panels to water blast", *J. Appl. Mech. (Trans. ASME)* **74**:1 (2007), 81–99.

[McShane et al. 2007] G. McShane, V. S. Deshpande, and N. A. Fleck, "The underwater blast resistance of metallic sandwich beams with prismatic lattice cores", *J. Appl. Mech. (Trans. ASME)* **74** (2007), 352–364.

[Mori et al. 2007] L. Mori, S. Lee, Z. Xue, A. Vaziri, D. T. Queheillalt, K. P. Dharmasena, H. N. G. Wadley, J. W. Hutchinson, and H. D. Espinosa, "Deformation and fracture modes of sandwich structures subjected to underwater impulsive loads", *J. Mech. Mater. Struct.* (2007). In press.

[Qiu et al. 2003] X. Qiu, V. S. Deshpande, and N. A. Fleck, "Finite element analysis of the dynamic response of clamped sandwich beams", *Eur. J. Mech. A/Solids* **22**:6 (2003), 801–814.

[Rabczuk et al. 2004] T. Rabczuk, J. Y. Kim, E. Samaniego, and T. Belytschko, "Homogenization of sandwich structures", *Int. J. Numer. Methods Eng.* **61** (2004), 1009–1027.

[Radford et al. 2005] D. D. Radford, V. S. Deshpande, and N. A. Fleck, "The use of metal foam projectiles to simulate shock loading on a structure", *Int. J. Impact Eng.* **31**:9 (2005), 1152–1171.

[Radford et al. 2007] D. D. Radford, G. J. McShane, V. S. Deshpande, and N. A. Fleck, "Dynamic compressive response of stainless-steel square honeycombs", *J. Appl. Mech.* **74** (2007), 658–667.

[Rathbun et al. 2006] H. J. Rathbun, D. D. Radford, Z. Xue, M. Y. He, J. Yang, V. S. Deshpande, N. A. Fleck, J. W. Hutchinson, F. W. Zok, and A. G. Evans, "Performance of metallic honeycomb-core sandwich beams under shock loading", *Int. J. Solids Struct.* **43** (2006), 1746–1763.

[Stout and Follansbee 1986] M. G. Stout and P. S. Follansbee, "Strain rate sensitivity, strain hardening, and yield behavior of 304L stainless steel", *J. Eng. Mater. Technol. (Trans. ASME)* **108** (1986), 344–353.

[Taylor 1963] G. I. Taylor, "The scientific papers of G. I. Taylor", pp. 287–303 in *The pressure and impulse of submarine explosion waves on plates*, vol. volume III, Cambridge University Press, Cambridge, 1963.

[Tilbrook et al. 2006] M. T. Tilbrook, V. S. Deshpande, and N. A. Fleck, "The impulsive response of sandwich beams: Analytical and numerical investigation of regimes of behaviour", *J. Mech. Phys. Solids* **54** (2006), 2242–2280.

[Vaughn and Hutchinson 2006] D. G. Vaughn and J. W. Hutchinson, "Bucklewaves", *Eur. J. Mech. A: Solids* **25** (2006), 1–12.

[Vaziri and Hutchinson 2007] A. Vaziri and J. W. Hutchinson, "Metallic sandwich plates subject to intense air shocks", *Int. J. Solids Struct.* **44** (2007), 2021–2035.

[Vaziri and Xue 2007] A. Vaziri and Z. Xue, "Mechanical behavior and constitutive modeling of metal cores", *J. Mech. Mater. Struct.* (2007). in press.

[Vaziri et al. 2006] A. Vaziri, Z. Xue, and J. W. Hutchinson, "Metal sandwich plates with polymer foam-filled cores", *J. Mech. Mater. Struct.* **1** (2006), 95–125.

[Wadley 2006] H. N. G. Wadley, "Multifunctional periodic cellular materials", *Phil. Trans. R. Soc. A* **364** (2006), 31–68.

[Wadley et al. 2003] H. N. G. Wadley, A. G. Evans, and N. A. Fleck, "Fabrication and structural performance of periodic cellular metal sandwich structures", *Compos. Sci. Tech.* **63**:16 (2003), 2331–2343.

[Wadley et al. 2007a] H. N. G. Wadley, K. P. Dharmasena, Y. Chen, P. Dudt, D. Knight, R. Charette, and K. Kiddy, "Compressive response of multilayered pyramidal lattices during underwater shock loading", *Int. J. Impact Eng.* (2007).

[Wadley et al. 2007b] H. N. G. Wadley, K. P. Dharmasena, M. He, R. McMeeking, A. G. Evans, N. Kambouchev, and R. Radovitzky, *Cellular materials concepts for air blast mitigation*, 2007. In preparation.

[Wardlaw and Luton 2000] A. J. Wardlaw and J. A. Luton, "Fluid-structure interaction mechanisms for close-in explosions", *Shock Vib. J.* **7** (2000), 265–275.

[Wardlaw et al. 2003] A. J. Wardlaw, J. Luton, J. J. Renzi, and K. Kiddy, "Fluid-structure coupling methodology for undersea weapons", pp. 251–263 in *Fluid Structure Interaction II*, WIT Press, 2003.

[Wei et al. 2007a] Z. Wei, A. G. Evans, K. P. Dharmasena, and H. N. G. Wadley, "Analysis and interpretation of a test for characterizing the response of sandwich panels to water blast", *Int. J. Impact Eng.* **34** (2007), 1602–1618.

[Wei et al. 2007b] Z. Wei, M. Y. He, and A. G. Evans, "Application of a dynamic constitutive law to multilayer metallic sandwich panels subject to impulsive loads", *J. Appl. Mech.* **74** (2007), 636–644.

[Xue and Hutchinson 2004] Z. Xue and J. W. Hutchinson, "A comparative study of impulse-resistant metal sandwich plates", *Int. J. Impact Eng.* **30** (2004), 1283–1305.

[Xue and Hutchinson 2006] Z. Xue and J. W. Hutchinson, "Crush dynamics of square honeycomb sandwich cores", *Int. J. Numer. Methods Eng.* **65** (2006), 2221–2245.

[Xue et al. 2005] Z. Xue, A. Vaziri, and J. W. Hutchinson, "Non-uniform constitutive model for compressible orthotropic materials with application to sandwich plate cores", *Cmes-Comp. Model. Eng.* **10** (2005), 79–95.

Please accept

HAYDN N. G. WADLEY: haydn@virginia.edu
Department of Materials Science and Engineering, University of Virginia, 395 McCormick Road, Charlottesville VA 22904, United States

KUMAR P. DHARMASENA: kumar@virginia.edu
Department of Materials Science and Engineering, University of Virginia, 395 McCormick Road, Charlottesville VA 22904, United States

DOUG T. QUEHEILLALT: dtq2j@virginia.edu
Department of Materials Science and Engineering, University of Virginia, 395 McCormick Road, Charlottesville VA 22904, United States

YUNGCHIA CHEN: yungchia.chen@navy.mil
Naval Surface Warfare Center, Carderock Division, West Bethesda MD 20817, United States

PHILIP DUDT: philip.dudt@navy.mil
Naval Surface Warfare Center, Carderock Division, West Bethesda MD 20817, United States

DAVID KNIGHT: david.e.knight@navy.mil
Naval Surface Warfare Center, Carderock Division, West Bethesda MD 20817, United States

KEN KIDDY: kenneth.kiddy@navy.mil
Naval Surface Warfare Center, Indian Head Division, Indian Head MD 20640, United States

ZHENYU XUE: xue@deas.harvard.edu
School of Engineering and Applied Sciences, Harvard University, Cambridge MA 02138, United States

ASHKAN VAZIRI: avaziri@deas.harvard.edu
School of Engineering and Applied Sciences, Harvard University, Cambridge MA 02138, United States

Appendix D

DEFORMATION AND FRACTURE MODES OF SANDWICH STRUCTURES SUBJECTED TO UNDERWATER IMPULSIVE LOADS

L. F. Mori, S. Lee, Z. Y. Xue, A. Vaziri, D. T. Queheillalt,
K. P. Dharmasena, H. N. G. Wadley, J. W. Hutchinson and H. D. Espinosa

Sandwich panel structures with thin front faces and low relative density cores offer significant impulse mitigation possibilities provided panel fracture is avoided. Here steel square honeycomb and pyramidal truss core sandwich panels with core relative densities of 4% were made from a ductile stainless steel and tested under impulsive loads simulating underwater blasts. Fluid-structure interaction experiments were performed to (i) demonstrate the benefits of sandwich structures with respect to solid plates of equal weight per unit area, (ii) identify failure modes of such structures, and (iii) assess the accuracy of finite element models for simulating the dynamic structural response. Both sandwich structures showed a 30% reduction in the maximum panel deflection compared with a monolithic plate of identical mass per unit area. The failure modes consisted of core crushing, core node imprinting/punch through/tearing and stretching of the front face sheet for the pyramidal truss core panels. Finite element analyses, based on an orthotropic homogenized constitutive model, predict the overall structural response and in particular the maximum panel displacement.

1. Introduction

Structures that combine high stiffness, strength, and mechanical energy absorption with low weight, are widely used in a variety of aerospace, automotive, and Naval applications. Metallic sandwich panels with various light weight core topologies have attracted significant interest for shock mitigation in general and the mitigation of underwater propagated shocks in particular.

As a first step toward understanding the mechanical behavior of these types of sandwich structures, Chiras et al. [2002] and Rathbun et al. [2004] conducted quasistatic experiments and numerical simulations of the compressive and shear response of truss core panels with a tetragonal lattice topology. These studies identified an asymmetric structural response between compression loaded trusses collapsing by buckling and those placed in tension failing by fracture (usually near nodes). Rathbun et al. [2004] measured the behavior of tetrahedral truss sandwich panels in shear and bending. Deshpande and Fleck [2001] measured the collapse responses of truss core sandwich beams in 3-point bending and obtained upper bound expressions for the collapse loads. Wallach and Gibson [2001b] analyzed the elastic moduli and the uniaxial and shear strengths of a three-dimensional truss geometry. Other studies have addressed the role of structural core defects [Wallach and Gibson 2001a]. These studies were then used to motivate optimal design [Wicks and Hutchinson 2001; Rathbun et al. 2005] and to develop continuum constitutive models [Xue and Hutchinson 2004b]. Their compressive behavior has been measured by many groups and summarized and compared with honeycombs in [Wadley 2006].

The dynamic behavior of cores used in sandwich structures has also been extensively investigated. Vaughn et al. [2005] and Vaughn and Hutchinson [2006] performed numerical simulations of truss cores and quantified the effect of microinertia on load carrying capacity. Lee et al. [2006] analyzed the dynamic compressive behavior of pyramidal truss cores and showed that the material strain rate hardening and microinertia effects make significant contributions to the total energy absorbed by a core. A transition in failure mode with deformation rate was experimentally identified and numerically analyzed. The role of deformation rate on the crushing response of square honeycomb cores has been addressed theoretically by Xue and Hutchinson [2005] and for both folded plate and pyramidal truss cores by Vaziri and Xue [2007].

Extensive investigations of the fluid structure interaction (FSI) associated with shock impingement on a plate in both air and water were also pursued. The eventual application of these concepts will require full scale computational simulations. However, much computational power is required to conduct a complete fully core-gridded finite element analysis. Homogenized constitutive models are therefore being developed and implemented in finite element frameworks. Xue and Hutchinson [2003; 2004a] modeled circular truss cores sandwich plates subjected to uniformly distributed impulses with finite elements. The study extended the classical work of Taylor [1963] relating the far-field momentum to the momentum imparted to plates. The simulation results were then compared to those of solid plates made of the same material and having the same weight per unit area. They concluded a well-designed sandwich plate can sustain significantly larger impulses for a given maximum deflection. Moreover the analysis showed that, if the blast is under water, the fluid-structure interaction reduces the momentum transmitted to the sandwich plate by as much as a factor of two. Indeed, the fluid-structure interaction is predicted to enhance the performance of sandwich plates relative to solid plates under intense shocks even in air, in which the effects are thought not to be as significant as for water borne shocks [Vaziri and Hutchinson 2007].

Xue et al. [2005] proposed a homogenized constitutive model that incorporates rate-dependence arising from material rate-dependence and microinertial effects. The model was used with finite elements to represent the behavior of square honeycomb sandwich plates [Xue et al. 2005], folded plate and pyramidal truss cores [Vaziri and Xue 2007], and hexagonal honeycomb cores [Mohr et al. 2006] subjected to quasistatic and dynamic loads. Rabczuk et al. [2004] developed a homogenization method for sandwich structures using a quasicontinuum approach that takes into account buckling of the core; this model shows good agreement with fully discretized models for shell interlaced cores. Qiu et al. [2004; 2005a] developed an analytical model for the deformation response of clamped circular sandwich plates subjected to shock loading in air and in water. This model was verified using finite elements in [Qiu et al. 2003] and then used to define a systematic design procedure [Fleck and Deshpande 2004a].

Liang et al. [2007] used an analytic model based on the relative time scales for core crushing and water cavitation to evaluate the mechanical performance of different core topologies. The work highlighted the importance of core crushing strength for exploiting the benefits of fluid-structure interaction. Xue and Hutchinson [2005] developed a continuum model for high-rate deformation of square honeycomb cores and demonstrated that this is an effective core for sandwich plates because it combines excellent crushing strength and energy absorption with good out-of-plane stiffness and strength and in-plane stretching resistance. They also [Xue and Hutchinson 2004a; Hutchinson and Xue 2005] extended the work by Fleck and Deshpande [Fleck and Deshpande 2004b; Deshpande and Fleck 2005] and addressed the

problem of the minimum weight design of square honeycomb plates of given span that must sustain a uniformly distributed impulse. They argued that optimally designed sandwich plates could sustain water shocks that were two to three times larger than monolithic plates of the same mass and material. Further studies [Vaziri et al. 2007] investigated fracture modes of square honeycomb sandwich plates showing that the primary fracture modes are necking and subsequent tearing of the face sheets and webs, and shear delamination of the core webs from the faces. Vaziri et al. [2006] showed that there is no considerable advantage or disadvantage in filling the core interstices by low-density polymeric foams for structural purposes. Therefore, it is possible to exploit the multifunctional advantages offered by polymeric foam-filled cores, such as acoustic and thermal insulation, with only a minor weight penalty.

While all these analytical and computational models have been developed, experimental analysis of the structural behavior under blast loading is still limited. Radford et al. [2005] used Al foam projectiles fired from a gas gun at high velocities against stainless steel square honeycomb core sandwich panels. Although this technique produces pressure pulses representative of shock interactions caused by explosions [Radford et al. 2005; Qiu et al. 2005b; Rathbun et al. 2006], it cannot simulate the fluid-structure interaction (FSI), which is especially relevant for underwater explosions [Vaziri and Hutchinson 2007]. Hutchinson and Xue [2005], Liang et al. [2007] and Tilbrook et al. [2006] showed that much of the advantage of sandwich plates over solid plates subjected to underwater blast comes from the FSI and that optimal designs are highly dependant on the details of this interaction. Wave propagation in water and associated cavitation phenomena, which play an important role in FSI, make analytical and numerical modeling quite complex. Thus it is necessary to perform realistic FSI experiments to validate, calibrate, and develop models that take them into account. Wadley and his collaborators have investigated the structural response of lattice cores to shock loading in water and air [Dharmasena et al. 2007a; 2007b; Wadley et al. 2007a; 2007b]. The experiments confirm very significant reductions in the transmitted shock pressure and reduced panel deflections.

In this paper, a recently developed water shock tube technique similar to the one developed by Deshpande et al. [2006] is used to measure the dynamic structural response under a realistic, although scaled, fluid-structure interaction with a water borne shock [Espinosa et al. 2006]. Using this experimental setup, the dynamic performance of sandwich panels with honeycomb and pyramidal core topologies is compared with that of solid plates made of the same material under the same boundary conditions. Liang et al. [2007] introduced several performance metrics: the back-face deflection, the tearing susceptibility of the faces, and the loads transmitted to the supports. In this article, the performance of the different structures is compared in terms of the dynamic back-face deflection and the panel fracture modes. After describing the experimental technique and the design of the specimens, the experimental results for each kind of structure are presented; failure mechanisms in the sandwich panels are identified by exploring not only the maximum deflection but also the deformation history and the presence of fracture on the face sheets after the test. The experimental investigation is complemented by numerical simulations using a detailed computation model of the experimental setup. The model includes separate components representing the water column, tube, piston and sandwich plates, as will be described later. The core materials were modelled using a constitutive model, developed by Xue et al. [2005], for plastically orthotropic materials which allows for modelling nonuniform hardening and softening behavior in stressing in different directions. The validity of this constitutive model for simulating and predicting the structural response of sandwich plates underwater blast loading has been investigated by comparing the

experimental measurements and simulation predictions. The developed model was used to gain insight into the mechanism of deformation and the mechanics of sandwich plates subjected to underwater shock loading.

2. Methods

2.1. *Experimental approach.* A novel experimental methodology incorporating fluid-structure interaction (FSI) effects was recently developed [Lee 2005; Espinosa et al. 2006]. The set-up is a highly instrumented scaled model designed to characterize the underwater blast impulsive loading of structures and to identify their failure by means of real time measurements of deflection profiles, deformation histories, and fracture. In the FSI setup, a water chamber made of a steel tube is incorporated into a gas gun apparatus (Figure 1). A scaled structure is fixed at one end of the steel tube and a water piston seals the other end. A flyer plate impacts the water piston and produces an exponentially-decaying pressure history in lieu of blast loading caused by explosive detonation. The pressure induced by the flyer plate propagates and imposes an impulse to the structure (panel specimen), whose response elicits water cavitation. The performance of the set-up was assessed by conducting calibration experiments and by subjecting solid stainless steel panels to impulsive water loading. Pressure sensors were employed to record pressure histories. The experimental measurements confirmed that the FSI setup can generate an exponentially decaying pressure history. Shadow moiré and high speed photography were also used to record in real time the full field out-of-plane deformation profile of the solid panel [Lee 2005; Espinosa et al. 2006].

In this investigation the same setup has been employed. Stainless steel panel structures with square honeycomb and pyramidal truss cores were subjected to water borne shocks and assessed against monolithic plates using a maximum panel deflection metric. The mass per unit area of the sandwich structures is determined by the face sheet thickness and the core density. The tested sandwich panels had a relative density of 4% (see Table 1).
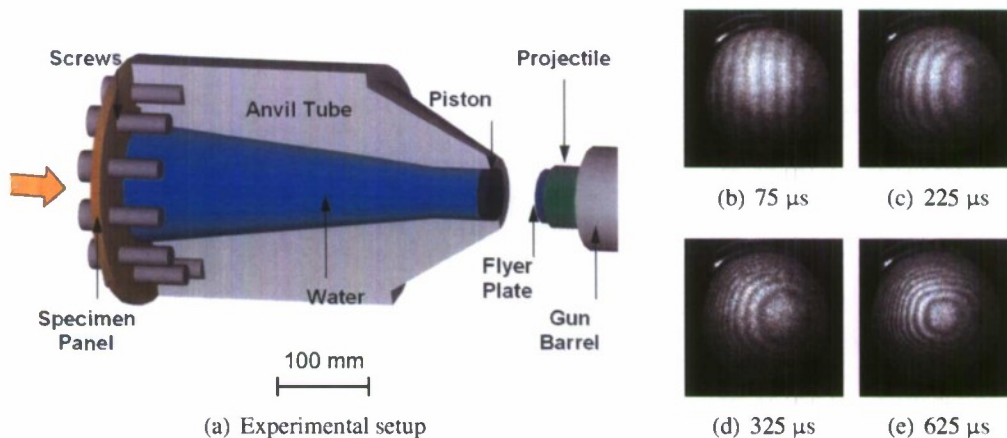

Figure 1. (a) Configuration of fluid-structure interaction (FSI) experimental setup. (b)–(e) Sequence of high-speed images obtained by shadow moiré.

Structure type	Core relative density	Mass per unit area, kg/m^2	Thickness, mm
Monolithic plate	100%	14.55	1.85
Square honeycomb sandwich	4.0%	14.00	13.97
Pyramidal truss sandwich	4.5%	13.78	12.75

Table 1. Properties of the edge clamped test specimens.

For each experiment, three loading parameters are of interest: the water pressure just ahead of the specimen panel, p_0, the characteristic decay time, t_0, and the far-field applied impulse, I_0. The incident transient load can be idealized as an exponentially decaying pressure given by:

$$p = p_0 \cdot e^{-t/t_0},$$

where p_0 is the peak water pressure measured in water just in front of the specimen panel and t_0 is a characteristic decay time [Smith and Hetherington 1994]. In the FSI setup, the peak pressure is governed by the projectile impact velocity, the acoustic impedance of the piston and the fluid, and by the experimental geometry (see Figure 1):

$$p_0 = V_0 \cdot \left(\frac{D_i}{D}\right)^2 \cdot \frac{s \cdot f}{s+f}, \tag{1}$$

where V_0 is the impact velocity, f and s are the acoustic impedances of the fluid and of the solid respectively, and D and D_i are the diameters of the water tube at the specimen and impact locations, respectively. Equation (1) has been derived using wave propagation theory with the assumption of linearity for the water equation of state [Espinosa et al. 2006]. Likewise, the time constant t_0 is obtained from evolving the nondimensional pressure profile in time:

$$\frac{p}{p_0} = e^{-t_n/t_0} = \left[\frac{s-f}{s+f}\right]^n, \qquad n = 0, 1, 2, \ldots.$$

In this equation, n is the number of wave reverberations in the flyer plate and t_n is the corresponding elapsed time. The far-field impulse I_0 per unit area is given by

$$I_0 = \sum_{n=0}^{\infty} p_0 \left[\frac{s-f}{s+f}\right]^n \Delta t \approx p_0 \cdot t_0,$$

where Δt is the time required for the elastic longitudinal wave to twice traverse the flyer plate [Espinosa et al. 2006].

To compare structures with different core geometries and materials, it is useful to employ the nondimensional impulse defined by Xue and Hutchinson [2004a] as

$$\hat{I} = \frac{I_0}{\overline{M} \cdot \sqrt{\sigma_y/\rho}},$$

where I_0 is the impulse per unit area previously defined, $\overline{M}$ the panel mass per unit area, σ_y the uniaxial tensile yield stress, and ρ the density of the specimen material.

Quantity	Symbol	Unit	Value
Young's modulus	E	GPa	200
Poisson's ratio	ν	–	0.3
Density	ρ_0	kg/m^3	7900
Melting temperature	T_{melt}	K	1673
Room temperature	T_{room}	K	293
Specific heat capacity	c	J/(kg·K)	440
Coefficient of thermal expansion	α	μm/(m·K)	17.3
Fitting parameter A	A	MPa	310
Fitting parameter B	B	MPa	1000
Fitting parameter n	n	–	0.65
Fitting parameter c	c	–	0.07
Fitting parameter $\dot{\varepsilon}_0$	$\dot{\varepsilon}_0$	s^{-1}	1.00
Fitting parameter m	m	–	1.00

Table 2. Material properties and Johnson–Cook parameters for AISI 304 stainless steel used in the numerical analyses.

3. Experimental results

3.1. *Honeycomb panels.*

3.1.1. *Specimen geometry.* The square honeycomb sandwich panels were fabricated from 304 stainless steel alloy, with an approximate composition of 67Fe-10Ni-20Cr-2Mn-1Si (wt%). The material properties for AISI 304 stainless steel are reported in Table 2. A slotted metal sheet assembly approach was used for fabrication [Wadley et al. 2003; Cote et al. 2004; Zok et al. 2004a; Wadley 2006]. Figure 2 schematically illustrates the fabrication sequence. First, a two dimensional profile was generated with a laser on a sheet metal strip incorporating the slots needed for the interlocking strip assembly and with allowances for bending the top and bottom flanges. The flanges were then bent at 90° to the core web. Finally, the core was assembled by slip fitting the laser cut and bent strips to form a square grid pattern. The core consisted of an assembly of 0.254 mm thick strips spaced 12.7 mm apart to form a 23 cell × 23 cell square grid (300 mm × 300 mm). A vacuum brazing method was used to bond 0.635 mm thick 304 stainless steel face sheets to the core to form the sandwich structure. The assemblies were vacuum brazed at an initial base pressure of ∼ 13 mPa. They were heated at 10 °C/min to 550 °C, held for 1 h (to volatilize the binder), then heated to the brazing temperature of 1050 °C, where they were held for 60 min at this temperature before furnace cooling at ∼ 25 °C/min to ambient. A braze alloy with a nominal composition of Ni-22.0Cr-6.0Si, wt.% (Nicrobraz® 31) was applied by spraying one side of the face sheet with a mixture of the braze powder and a polymer binder (Nicrobraz® 520 cement) which were both supplied by Wall Colmonoy (Madison Heights, WI).
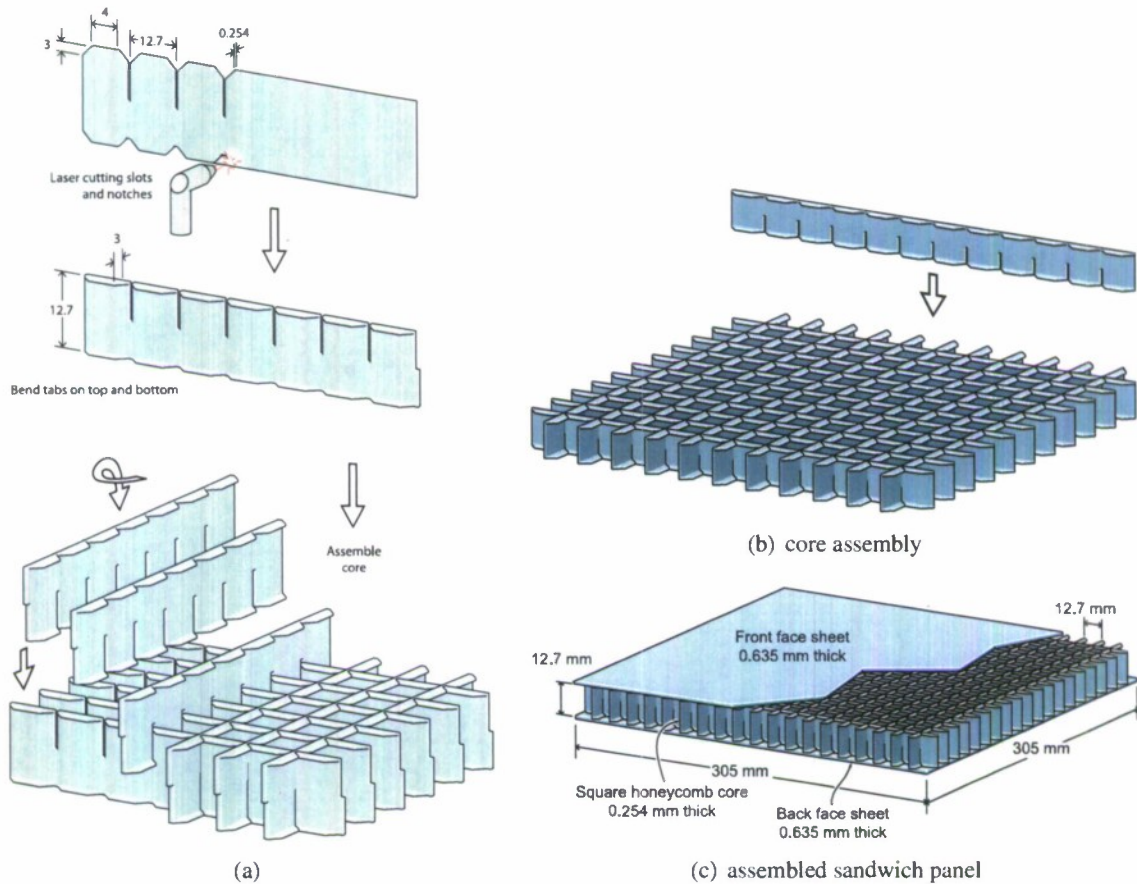
Figure 2. Fabrication of the square honeycomb sandwich panel by a transient liquid phase bonding process. All dimensions are in millimeters.

The panels were then machined to round specimens 305 mm in diameter (see Figure 3). The total thickness of the sandwich panels was 13.97 mm and the relative density of the core ρ_{cr} was 4%; the mass per unit area of the sandwich panels was $14.0 \, \text{kg/m}^2$. To clamp the panels in the periphery, 12 through holes were machined and ring spacers were inserted to prevent core crushing during the clamping process. The specimens were clamped using a steel ring and 12 high strength screws.

Three experiments were conducted on the panels with projectile impact velocities between 175 m/s and 314 m/s. The results are summarized in Table 3. Details for the case with impact velocity of 272 m/s are given next.

3.1.2. *Test results: case with impact velocity of* 272 m/s. The peak pressure p_0 was 70.6 MPa; the characteristic decay time t_0 was 25.8 μs; the corresponding applied impulse I_0 was 30.16 N · s and the nondimensional applied impulse $\hat{I}$ was 1.234. The maximum deflection measured by shadow moiré, $\delta_{\max}$, was 29.62 mm and, thus, the nondimensional maximum deflection $\delta_{\max}/L$ was 0.389. The final strain of the core in the middle of the sample was $\varepsilon_f = 26.8\%$.

(a)   (b)
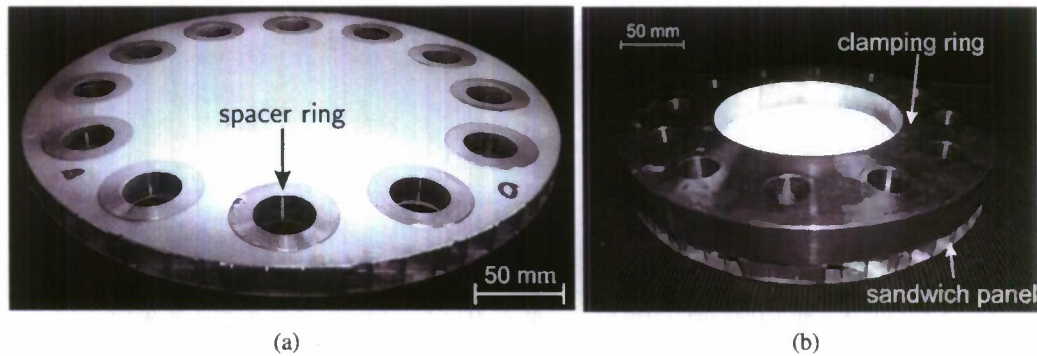
Figure 3. AISI 304 stainless steel panel with square honeycomb core. (a) Solid-ring spacers were employed to prevent core crushing while fastening the clamping ring. (b) A steel ring was employed to clamp the sandwich panel to the anvil tube with 12 screws. The test panel shown above is 305 mm in diameter and 13.97 mm thick.

Figure 4 shows the shadow moiré images between 25 µs and 625 µs after the wave front reached the specimen. The deflection along the diameter of the specimen obtained by processing the shadow moiré fringe patterns at different time instances is given in Figure 4i. Although no direct measurement of the back face velocity was performed, it is possible to compute an average velocity from the recorded history of the panel center position.

Figure 5 shows images of the honeycomb sandwich panel after the test. Square-grid imprints on both face sheets (see Figure 5a, b) are observed. The imprints on the face sheets are the result of the high crushing strength of the square honeycomb core. As discussed later, this phenomenon is characteristic of all the sandwich structures with a strong core. As observed in previous studies [Espinosa et al. 2006], the FSI configuration employing bolts to achieve a clamped boundary condition allows some in-plane

Structure type	Monolithic plate	Sandwich square honeycomb core			Sandwich pyramidal truss core
Impact velocity, V_0, m/s	315	175	272	314	307
Flyer plate thickness, t_f, mm	4.75	4.76	4.83	4.83	4.83
Water pressure, p_0, MPa	81.7	45.3	70.6	81.5	79.7
Characteristic decay time, t_0, µs	25.3	25.4	25.8	25.8	25.8
Final core strain, ε_f	—	1.7%	26.8%	7.1%	11.3%
Dimensionless applied impulse, $\hat{I}$	0.882	0.939*	1.234*	0.931	0.925
Dimensionless maximum deflection, δ_{max}/L	0.391	0.297	0.389	0.299	0.299
Normalized maximum deflection, $(\delta_{max}/L)_N$	0.391	0.279	0.278	0.283	0.285
Improvement	—	29%	29%	28%	27%
Damage on the face sheets	no damage	imprints			punctures/cracks

Table 3. Performances of blast-resistant structures with fixed boundary condition.

(a) 25 μs   (b) 75 μs   (c) 125 μs   (d) 175 μs

(e) 225 μs   (f) 325 μs   (g) 475 μs   (h) 625 μs

(i) deflection history
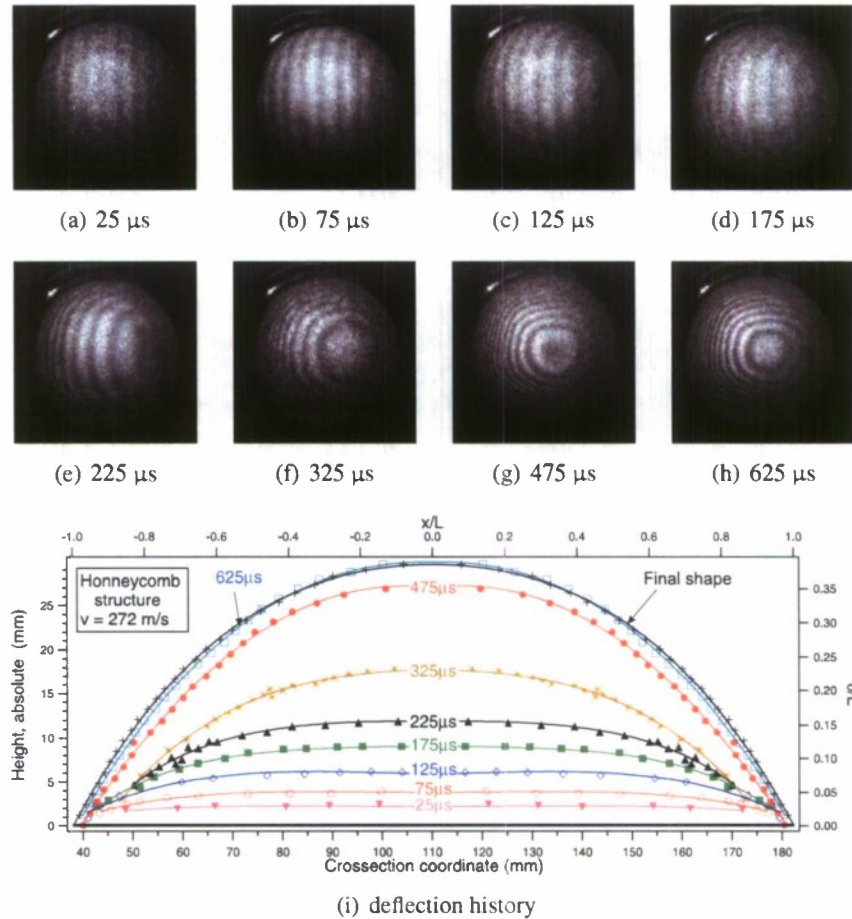
Figure 4. (a)–(h) High-speed camera images showing shadow moiré fringes for the AISI 304 stainless steel panel with square honeycomb core at different time intervals, and (i) deflection along the diameter of the specimen plate measured by shadow moiré. $t = 0$ μs corresponds to the arrival of the shock at the specimen location.

deformation of the sample at the boundary. Evidence of slippage and hole ovalization is reported in Figure 5d.

3.1.3. *Test results: comparison of the three experiments.* The three experiments that were conducted on the square honeycomb sandwich plates differ both in the speed of the projectile and on the geometry of the projectile. The external wall of the PMMA flyer holder was 8.5 mm-thick for the tests at 175 m/s and 272 m/s while it was 1.5 mm-thick for the test at 314 m/s. The additional impulse, for the cases of thicker holder tubes, was computed multiplying the compressive strength of PMMA, the cross-sectional area of the holder wall, and the time duration of the compressive stress wave propagation through the holder wall in the axial direction (for additional details see [Lee 2005]). With this correction, the tests at 175 m/s and at 314 m/s have almost the same nondimensional impulse (0.939 and 0.931) and in fact the final deflection is very similar (22.6 mm and 22.8 mm).

(a) front (wet side)   (b) back (dry side)

(d) detail of boundary

(c) back side
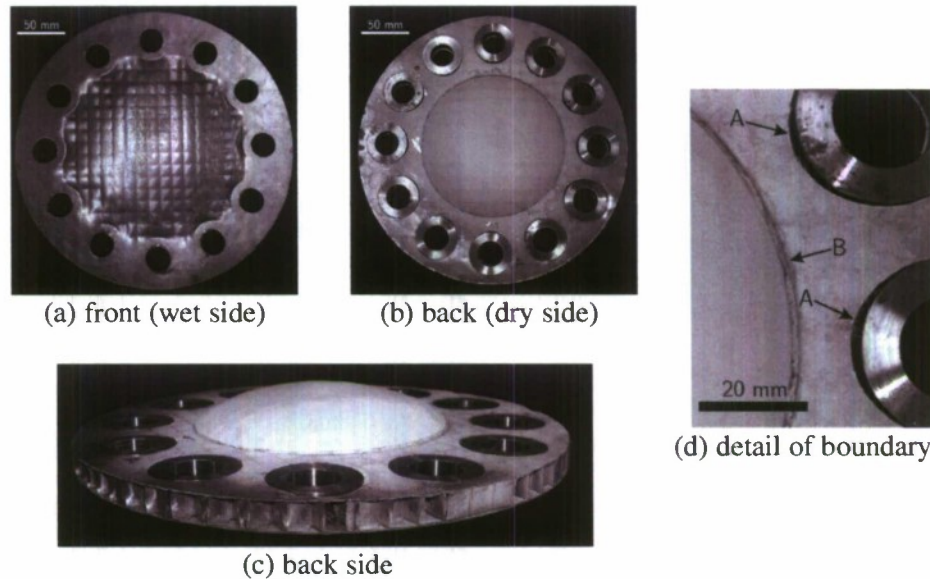
Figure 5. AISI 304 stainless steel honeycomb sandwich panel after the blast loading. (a), (b), and (c) show the front and the back of the plate while (d) shows details of hole ovalization (A) and slippage (B).

After the tests, the samples subjected to nondimensional impulses of $\hat{I} = 1.234$ and $\hat{I} = 0.939$ were cut in half by water-jet machining and are shown in Figure 6. On both cases significant core crushing close to the boundary is observed. However, the amount of core crushing in the center of the panel is very different. Only the largest impulse resulted in significant plastic buckling of the core webs in the center of the section panel (Figure 6b); the core buckled from the front (wet) side as shown in Figure 6e. The postmortem front and back face sheets profiles along the diameter of the panel subjected to a nondimensional impulse of $\hat{I} = 1.234$ are shown in Figure 7.

3.2. *Pyramidal lattice panels.*

3.2.1. *Specimen geometry.* Solid truss pyramidal lattice structures were fabricated via a folding operation that bends a diamond perforated sheet to create a single layer of trusses arranged with a pyramidal topology [Zok et al. 2004b; Queheillalt and Wadley 2005; McShane et al. 2006; Radford et al. 2006; Biagi and Bart-Smith 2007; Cote et al. 2007]. Briefly, the process consisted of punching a metal sheet to form a periodic diamond perforation pattern, folding node row by node row using a paired punch and die tool set, and then brazing this core to solid face sheets to form the sandwich structure. Figure 8 schematically illustrates this process. A solid truss structure with a core relative density of 4.5% was made from 304 stainless steel by the process described above. The sheet thickness $t = 1.52$ mm, truss width $w = 1.52$ mm, and the truss length $l = 17$ mm. The inclination angle $\omega = 45°$ and the face sheet thickness was 0.635 mm, resulting in a pyramidal lattice with square cross section trusses and a desired relative density.

(a) $\hat{I} = 0.939$, whole section

(b) $\hat{I} = 1.234$, whole section

(c) $\hat{I} = 0.939$, detail from the center

(d) $\hat{I} = 0.939$, detail from the boundary

(e) $\hat{I} = 1.234$, detail from the center

(f) $\hat{I} = 1.234$, detail from the boundary
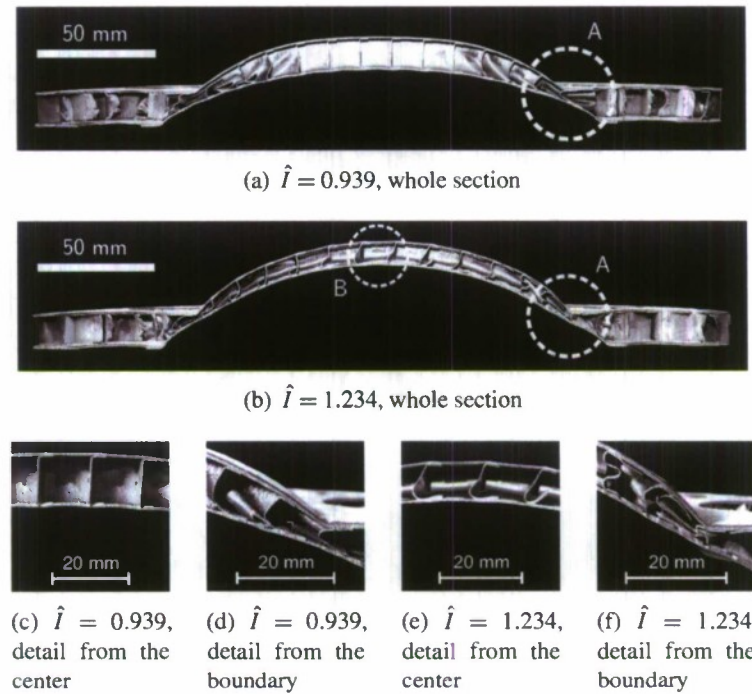
Figure 6. Cross-section of AISI 304 stainless steel honeycomb sandwich panels after blast loading. For the case of $\hat{I} = 0.939$, (a) core crushing occurs at the periphery, while for the case of $\hat{I} = 1.234$ (b) core crushing at both periphery (A) and center (B) occurs. (c)–(d) report core details for the lower impulse case and (e)–(f) for the higher impulse case.
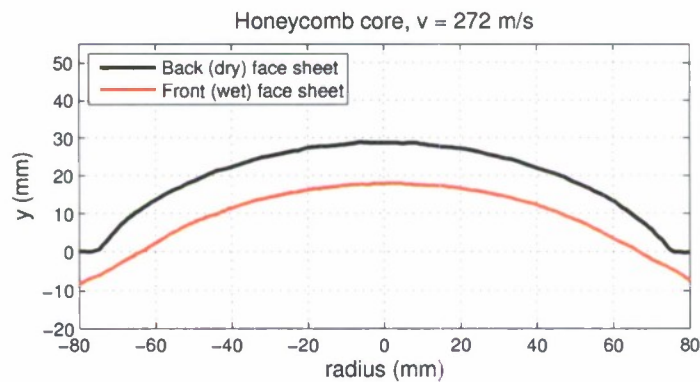
Figure 7. Postmortem profile of front and back face sheets along the diameter of the AISI 304 stainless steel panel with square honeycomb core subjected to a nondimensional impulse of $\hat{I} = 1.234$.
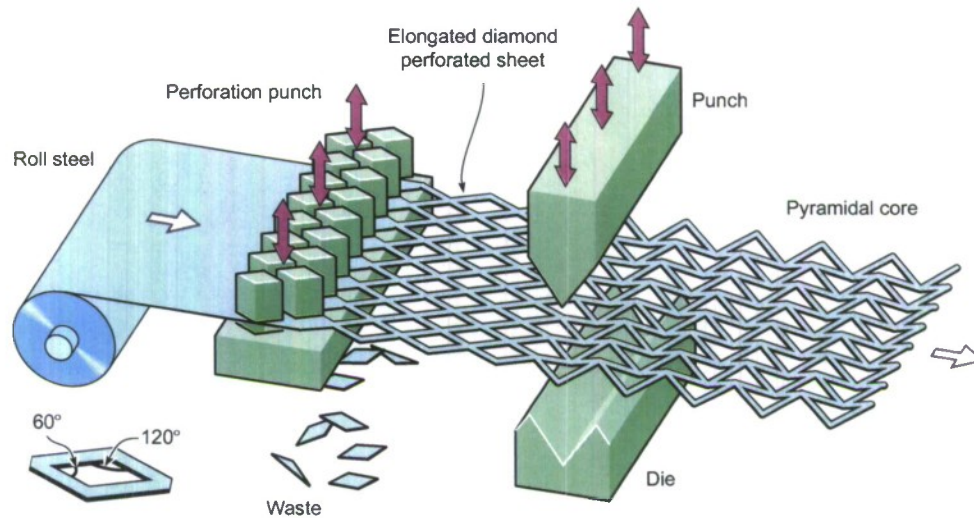
Figure 8. Fabrication of the pyramidal lattice core.

AISI 304 stainless steel panels with pyramidal truss cores were made by brazing the core to the face sheets. The brazing cycle for the truss core was the same as that previously described for the square honeycomb panels. The plates were then machined like the honeycomb panels to achieve the same boundary conditions. The overall thickness of the panels was 12.75 mm, the core relative density was 4.5% and the mass per area was 13.78 kg/m². The material properties for AISI 304 stainless steel are reported in Table 2.

3.2.2. *Test results.* The sandwich panel was tested at an impact velocity of 307 m/s using a flyer thickness of 4.83 mm and a PMMA flyer holder tube with wall thickness of 1.5 mm. This resulted in a peak pressure p_0 of 79.7 MPa and a characteristic decay time t_0 of 25.8 μs. The corresponding applied impulse I_0 was 37.47 N · s and the nondimensional applied impulse $\hat{I}$ was 0.925. The maximum deflection δ_{max} was 22.79 mm, and thus the nondimensional maximum deflection δ_{max}/L was 0.299. The final strain of the core in the middle of the sample was $\varepsilon_f = 11.3\%$.

Figures 9a–9h show fringe patterns, obtained by shadow moiré and high speed photography, at eight time instances between 93 μs and 793 μs after the wave front reached the specimen. The corresponding panel deflections along the diameter of the specimen are shown in Figure 9i.

Several distinct failure modes were observed in this experiment, as seen in Figures 10 and 11. Shear-off occurred at truss apexes on the front face sheet (wet side), (Figure 10a, c, and e). This failure mode is of main concern in sandwich panels with thin front face sheets and strong cores. On the other hand, the back face sheet partially sheared off at the supporting edge of the clamped boundary in Figure 10d and f. Ovalization of the holes and even fracture of the face sheet in the back was also observed in Figure 10b and d. The observed phenomena can be related to the influence of the boundary conditions and core properties.

After the experiment, the panel was sectioned and imaged as shown in Figure 11. Clearly, significant collapse of the pyramidal truss core is observed in the boundary region. The observed plastic buckling of the trusses is consistent with buckling modes at intermediate strain rates (see [Lee et al. 2006]). By

(a) 93 μs   (b) 193 μs   (c) 243 μs   (d) 293 μs

(e) 343 μs   (f) 443 μs   (g) 593 μs   (h) 793 μs

(i) deflection history
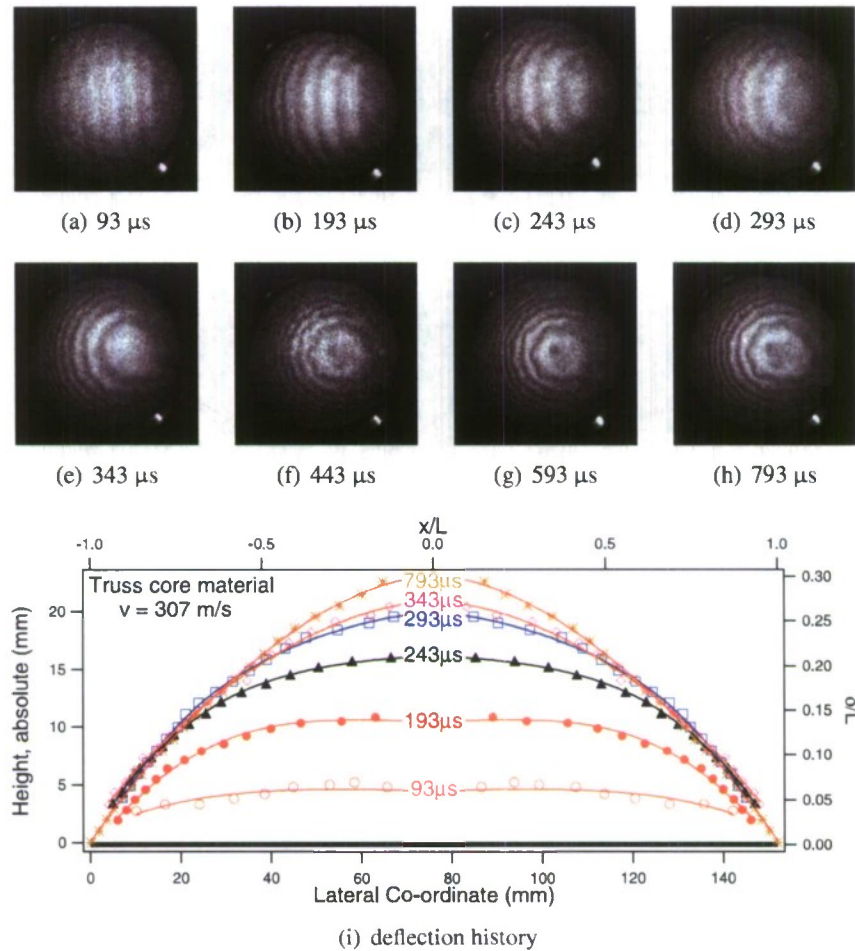
Figure 9. High-speed camera images of shadow moiré fringes for the AISI 304 stainless steel panel with pyramidal truss core at different time intervals (a)–(h), and deflection along the diameter of the specimen plate measured by shadow moiré (i). $t = 0$ μs corresponds to the arrival of the shock at the specimen location.

contrast, the core in the center of the specimen is almost undeformed, as shown in Figure 11a. The postmortem front and back face sheets profiles along the diameter of the panel are reported in Figure 12.

4. Comparison of Performances

As previously stated, comparison of performances is based on the nondimensional impulse $\hat{I}$ and the measured nondimensional maximum deflection δ_{max}/L. Since the experiments were performed at slightly different nondimensional impulses, all the results were referenced to one experiment. We chose the monolithic panel as our reference case such that any improvement by the sandwich topology automatically emerges. To scale the maximum deflection with impulse, we used the fact that nondimensional deflection

(a) front

(b) back

(c) detail of the front

(d) cracking of the back sheet be-
tween holes and on the edge

(e) front sheet punctured by the truss
core

(f) cracking of the back sheet exposes
buckled truss members
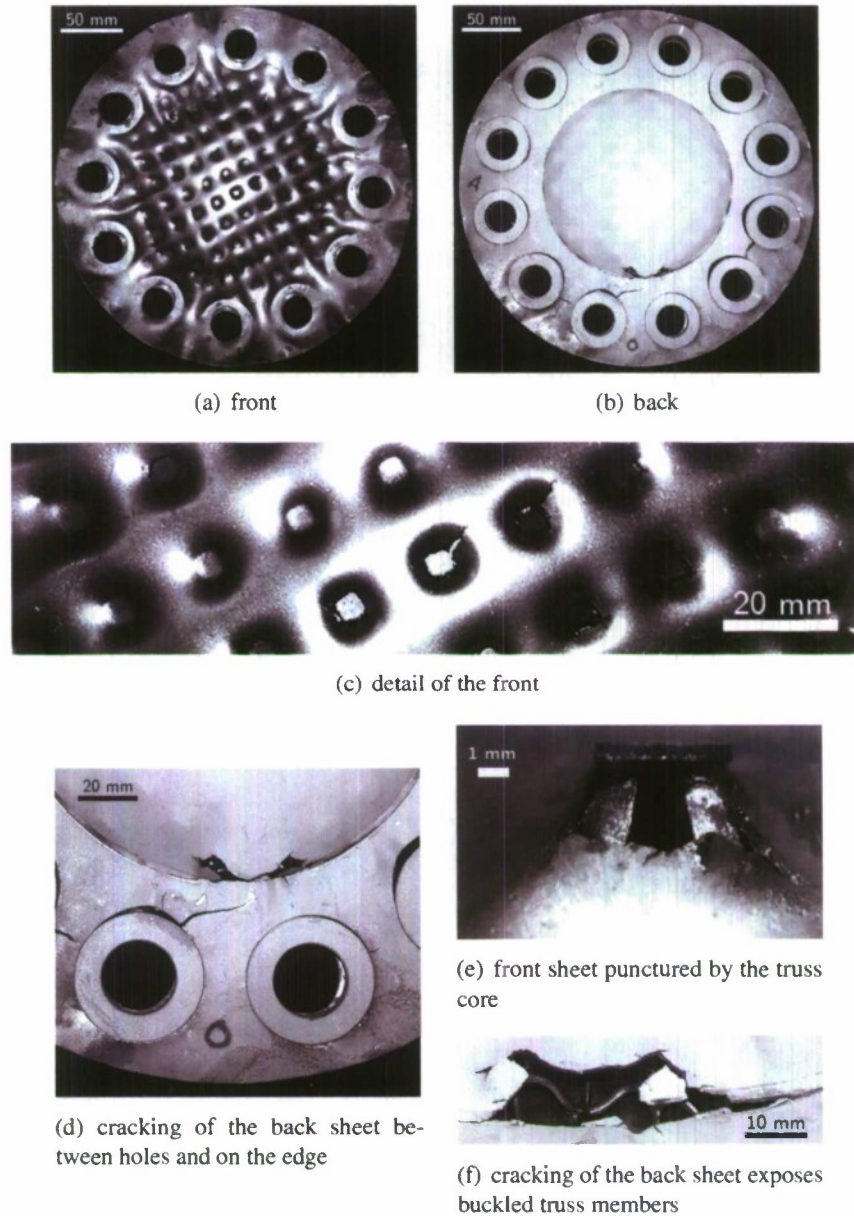
Figure 10. AISI 304 stainless steel sandwich panel with pyramidal truss core after blast
loading. (a) and (b) and show the front and the back of the plate; (c) and (e) show details
observed in (a). (d) and (f) show fracture features.

and impulse follow a linear relationship Xue and Hutchinson [2004a]. Then, the normalized maximum
deflection is given by

$$(\delta_{\max}/L)_N = I_{nf} \cdot (\delta_{\max}/L)$$

(a) cross-section

(b) detail of buckled truss members
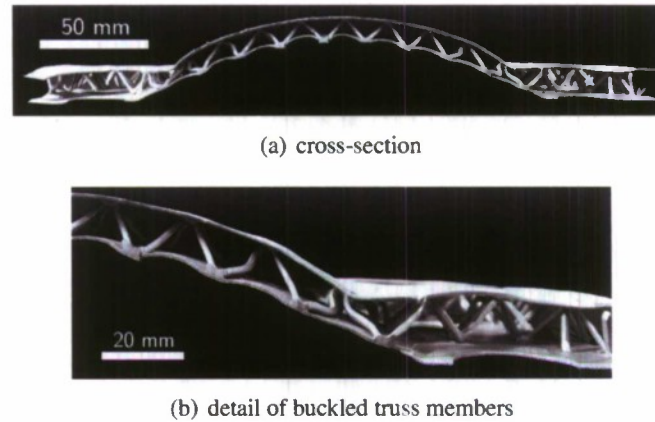
Figure 11. Cross-section of AISI 304 stainless steel sandwich panel with pyramidal truss core after blast loading.

where I_{nf} is the impulse normalization factor defined as $I_{nf} \overset{\text{def}}{=} \frac{\hat{I}_{\text{monolithic}}}{\hat{I}}$.

The calculations and improvements are reported in Table 3. Both honeycomb and pyramidal truss cores exhibit an improvement of about 30%, with the pyramidal truss core presenting significant localized damage and lost of impermeability.

5. Numerical simulations

Finite element calculations using ABAQUS/Explicit 6.4–1 [2003] were carried out to mimic the response of the sandwich plates. As shown in Figure 13, an axisymmteric model of the experimental set up was developed.

The material of the anvil tube is wrought AISI 4340 steel, that of the specimen plate is AISI 304 stainless steel, and that of the piston and flyer plate is heat-treated AISI 4140 steel. For the anvil tube the strain hardening law $\sigma = K \cdot \varepsilon^n$ is used. For AISI 4340 steel an elastic-perfectly plastic model is used. The material properties and the strain hardening law parameters for the wrought AISI 4340 steel and for heat-treated AISI 4140 steel are given in Table 4. The anvil tube and the piston were modeled with 4-node axisymmetric elements with reduced integration. The von Mises criterion was adopted to model steel yielding.

The water was modeled as a hydrodynamic material and the following Mie–Grüneisen equation of state with a linear Hugoniot relation was used

$$p = \frac{\rho_0 \cdot c_0^2 \cdot \eta}{(1 - s_1 \cdot \eta)^2} \cdot \left(1 - \frac{\Gamma_0 \cdot \eta}{2}\right) + \Gamma_0 \cdot \rho_0 \cdot E_m, \qquad u_s = c_0 + s_1 \cdot u_p.$$

A tensile pressure was made to correspond to water cavitation at room temperature. The material properties used in the simulation are listed in Table 5. The water was modeled with 3-node axisymmetric elements. Adaptive meshing was employed to prevent excessive element distortion in the water and a contact algorithm was incorporated to avoid penetration of steel surfaces. The amplitudes and overall
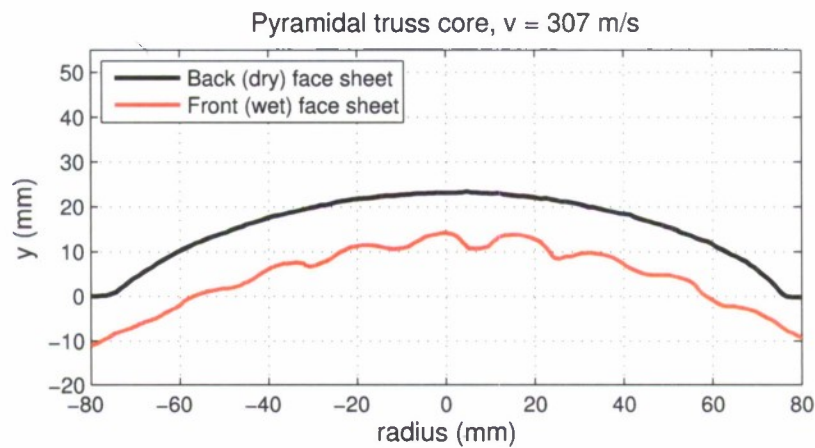
Figure 12. Postmortem profile of front and back face sheets along the diameter of the AISI 304 stainless steel panel with pyramidal truss core subjected to a nondimensional impulse of $\hat{I} = 0.925$.

Quantity	Symbol	Unit	AISI 4340 steel	AISI 4140 steel
Young's modulus	E	GPa	205	205
Poisson's ratio	ν	–	0.29	0.29
Density	ρ_0	kg/m^3	7850	7850
Yield stress	σ_0	MPa	470	1000
Hardening coefficient	K	MPa	470	1615
Hardening exponent	n	–	0	0.09

Table 4. Material properties and strain hardening coefficients for wrought AISI 4340 steel and for heat-treated AISI 4140 steel used in the numerical analyses.
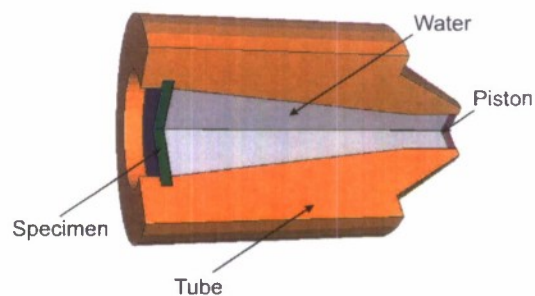
Figure 13. Schematic diagram of finite element model.

Quantity	Symbol	Unit	Water
Density	ρ_0	kg/m^3	958
Sound speed	c_0	m/s	1490
EOS coefficient	s_1	–	1.92
Grüneisen coefficient	Γ_0	–	0.1

Table 5. Material properties and parameters for the Mie–Grüneisen equation of state used for the water in the numerical analyses.

trends of pressure histories predicted by the model are in agreement with those measured in experiments [Espinosa et al. 2006].

The sandwich panels are made of stainless steel 304. The face sheets of the sandwich panel were meshed with 4-node axisymmetric elements with reduced integration. The Johnson–Cook plasticity model was adopted to model their elastic-plastic behavior. According to this model, the flow stress σ_y is given by

$$\sigma_y = \left[A + B \cdot \left(\varepsilon_p^{eq} \right)^n \right] \cdot \left(1 + c \cdot \ln \dot{\varepsilon}^* \right) \cdot \left[1 - \left(T^* \right)^m \right],$$

where

$$\dot{\varepsilon}^* \stackrel{\text{def}}{=} \frac{\dot{\varepsilon}_p^{eq}}{\dot{\varepsilon}_0}, \qquad T^* \stackrel{\text{def}}{=} \frac{T - T_{\text{room}}}{T_{\text{melt}} - T_{\text{room}}},$$

ε_p^{eq} and $\dot{\varepsilon}_p^{eq}$ are equivalent plastic strain and equivalent plastic strain rate, respectively; T is the material temperature, T_{room} is the room temperature, and T_{melt} is the melting temperature of the material; A, B,
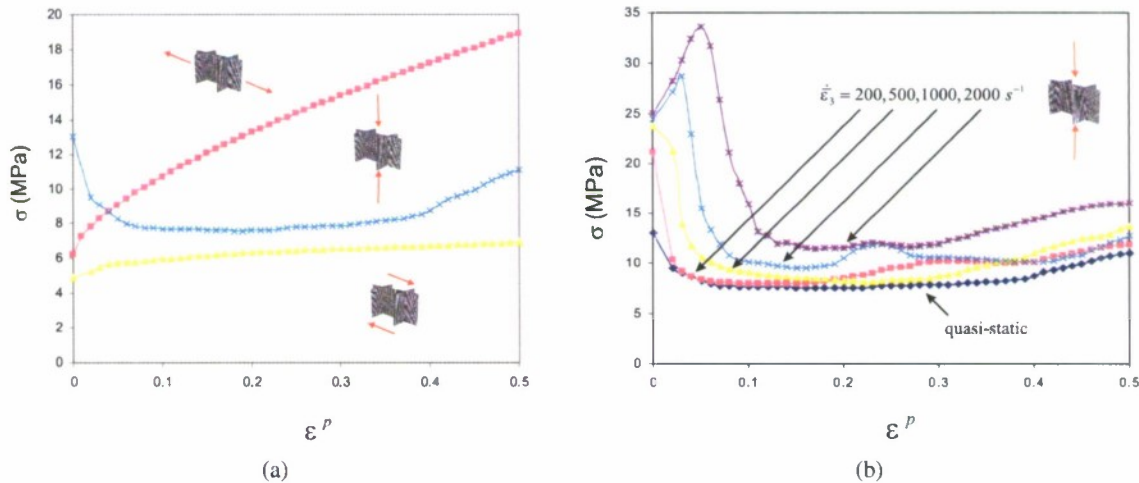
Figure 14. (a) True stress-plastic strain response of the square honeycomb core under three basic loading histories as computed using a three dimensional unit cell model. (b) Crushing response of the square honeycomb at various overall strain rates.

(a)   (b)
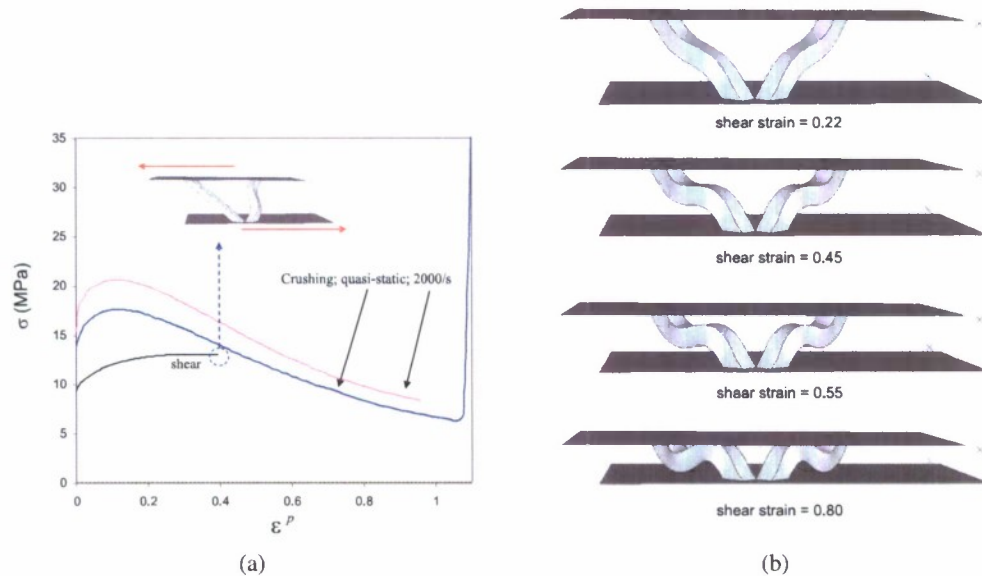
Figure 15. (a) True stress-plastic strain response of the square truss core under crushing and out of plane shearing as computed using the three dimensional unit cell model. The response of the truss core under a crushing rate of 2000/s is also depicted. Inset: deformed configuration of the truss core under out-of-plane shear at strain $= 0.4$. (b) Deformed configurations of the truss core under crushing at various level of crushing (true) strain.

n, c, $\dot{\varepsilon}_0$, and m are Johnson–Cook parameters determined by fitting experimental stress-strain curves as a function of strain rate and temperature. The material properties and the identified Johnson–Cook parameters for the AISI 304 stainless steel are listed in Table 2. The computational model of the core consists of a homogenized material using the orthotropic constitutive model developed by Xue et al. [2005]. Four-node axisymmetric elements with reduced integration were used for the core. The inputs to this constitutive model are rate-dependent stress-strain responses of the metal core under six fundamental loading histories. These inputs were calculated using full three-dimensional unit cell models of the two tested cores: square honeycomb and pyramidal truss. The unit cell calculations do not take into account any imperfection. The boundary conditions applied to the unit cell on the edges of the core webs are consistent with symmetry and periodicity. The details of the calculations are similar to those reported in [Xue et al. 2005; Vaziri and Xue 2007; Vaziri and Hutchinson 2007; Mohr et al. 2006]. The dimensions employed in the unit cell calculations were obtained from measurements on the tested panels.

Figure 14a shows the response of the square honeycomb core under crushing, out-of-plane shear, and in-plane stretching when deformed in the quasistatic regime. When the core is deformed at high strain rates, both material rate dependence and inertia effects could significantly alter its response. This effect is significant specifically under crushing where a combination of inertial resistance and delay in buckling leads to a significant enhancement in the crushing resistance of the core [Xue and Hutchinson 2005]. The response of the square honeycomb core under crushing at different strain rates are quantified in Figure
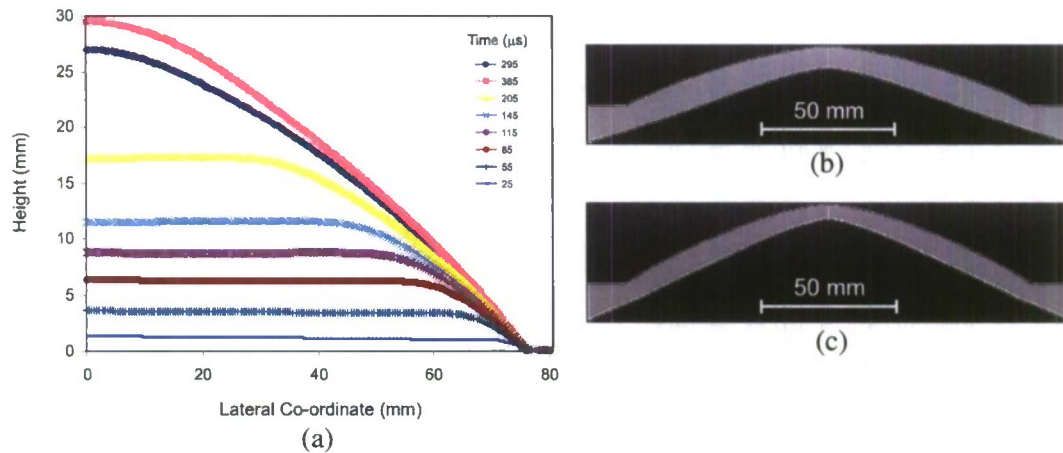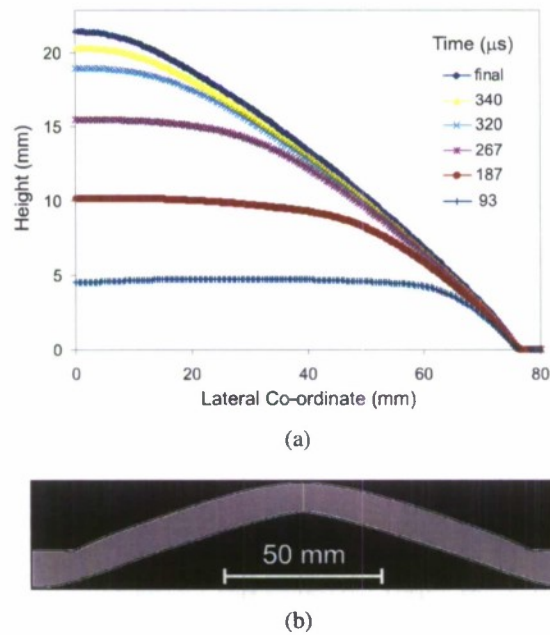
Figure 16. (a) Computed history of deformation of the dry-face sheet for the square honeycomb core sandwich panel (experimental results shown in Figure 4). (b) The final configuration of the square honeycomb core sandwich panel for the loading case $\hat{I} = 0.939$; experimental results are shown in Figure 6a. (c) The final configuration of the core sandwich panel for the loading case $\hat{I} = 1.234$; experimental results are shown in Figure 6b.

14b. These curves were directly input into the homogenized model to represent core behavior. All the calculations presented here incorporate the effect of deformation rate on core crushing. Its effect does not appear significant (see Figure 14b), in agreement with our previous studies [Xue et al. 2005; Vaziri and Xue 2007]. Similar calculations were carried out to quantify the response of the pyramidal truss core under three basic loading histories. The results of these calculations are summarized in Figure 15. For further discussion on deformation of pyramidal truss cores, see [Vaziri and Xue 2007].

In the computational model of the set up, the sandwich plate was taken to be perfectly bonded to the tube with an effective radius of 74 mm at its outer edge. The effect of the boundary condition will be discussed later. Frictionless contact was assumed at all other interfaces. The initial impulse per unit area $\bar{I}$ applied to the piston was experimentally measured. In the computational model, the impulse is simplified as a uniformly distributed velocity $v = \bar{I}/\rho h$ suddenly applied through the entire piston, where ρ and h denote the density and height of the piston.

6. Numerical results and discussion

The computed deflection histories of the dry side of the sandwich panel along its radial direction are shown in Figures 16a and 18a for the sandwich plates with square honeycomb core and pyramidal truss core. The corresponding experimental measurements are shown in Figures 4i and 9i. The maximum deflection history obtained with the FEM model is reported in Figures 17a and 19a for the sandwich plates with square honeycomb core and pyramidal truss core. Figure 19a shows an excellent agreement between numerical and experimental results. Figure 20 reports the comparison between the experimental result and the numerical prediction for the final shape of both types of sandwich structures. The difference in height between the prediction and the experimental result is less than 7% for the pyramidal truss core

(a) deflection history
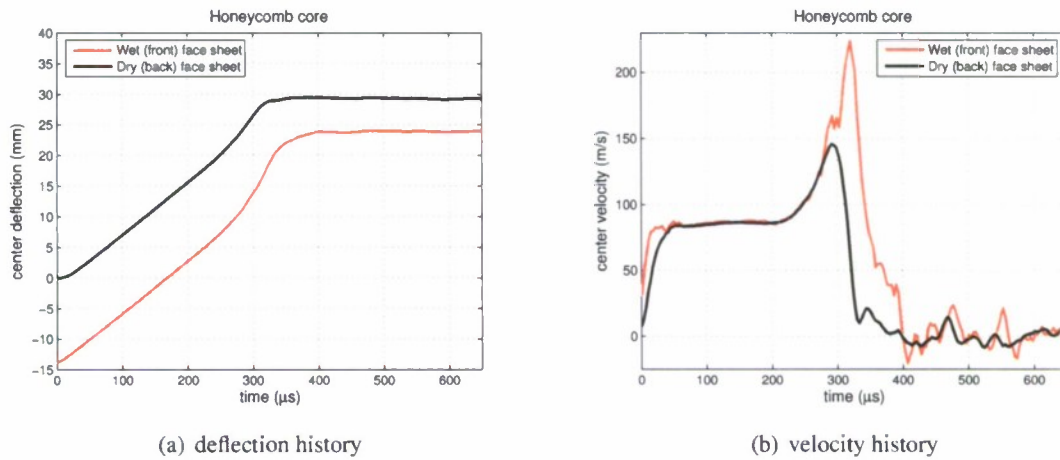
(b) velocity history

Figure 17. (a) Computed history of the maximum deflection of the dry-face and the wet face sheets for the square honeycomb core sandwich panel. (b) Computed history of the velocity of the center of the dry and wet face sheets after the Savitzky–Golay filter.

(a)

(b)

Figure 18. (a) Computed history of deformation of the dry-face sheet for the pyramidal truss core sandwich panel; experimental results are shown in Figure 9. (b) The final configuration of the pyramidal truss core sandwich panel; experimental results are shown in Figure 11.

(a) deflection history
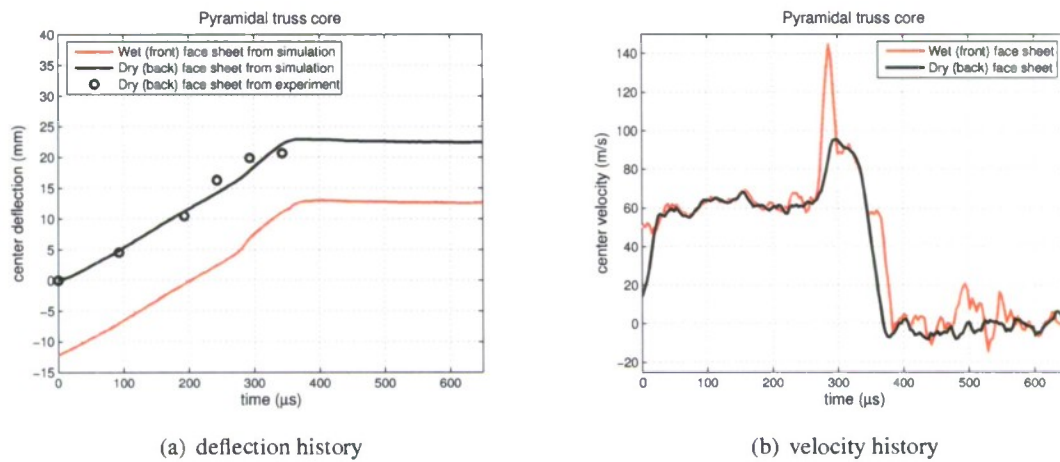
(b) velocity history

Figure 19. (a) Computed and experimental history of the maximum deflection of the dry-face and the wet face sheets for the pyramidal truss core sandwich panel. (b) Computed history of the velocity of the center of the dry and wet face sheets after the Savitzky–Golay filter.
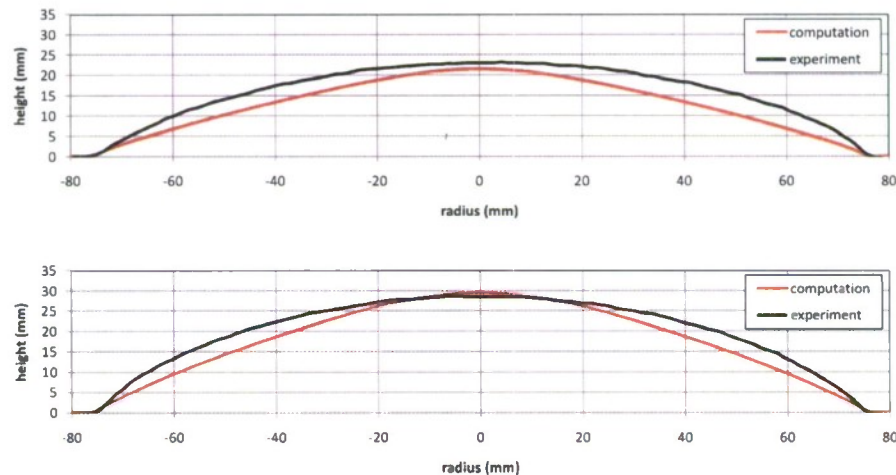
Figure 20. Comparison between the numerical prediction and the experimental result for the final shape of the pyramidal truss core sandwich (top) and the square honeycomb core sandwich (bottom).

and less than 3% for the square honeycomb. The velocity history of the center of the plate obtained with the FEM model is reported in Figure 17. Due to numerical errors of the FEM simulations, the velocity histories were noisy and so they were smoothed with a Savitzky–Golay filter on a frame of 10 points and with a polynomial of the third degree [Savitzky and Golay 1964]. The predicted deflection history profiles are in agreement with the corresponding experimental measurements. In particular, the

maximum deflection is captured very well by the computational model. A minor inconsistency between the numerical simulations and the experimental measurements is the time for the plate to attain a particular deformed shape. One possible reason is that the homogenization method fails to capture the full wave propagation process very accurately and slightly underpredicts the time interval required to achieve a given deformation. Figures 16b and 16c display the computed final deformed configuration of the sandwich panels with honeycomb cores for two impulses. Likewise, Figure 18b shows the computed final configuration for the case of pyramidal core. The results reveal a very good agreement between the experimental observations and numerical predictions, except that the crushing deformation of the sandwich panels around the edge is less in the numerical prediction. Noteworthy is that the 12 through holes machined on the panels, to achieve clamping, weaken the sandwich core locally and effectively act as imperfections. Since this feature was not accounted for in the numerical simulations, the local level of crushing observed experimentally was not reproduced by the simulations. Likewise, Figure 10 illustrates that tearing occurs on the face sheets of the sandwich panel with pyramidal truss cores in the clamped region. By contrast, the simulations did not account for fracture or rupture of the face sheets. Models capable of simulating fracture of metal sandwich plates are currently under development [Vaziri et al. 2007] and can be employed in the analysis of the experimental data in future studies. Due to the nature of the homogenization method, the numerical simulations also could not capture the local bending of the wet face due to shock loading at early stages of deformation. This local behavior is more pronounced for the panel with the truss core. Despite these limitations, the overall and maximum deflection are captured by the model in the spirit of its formulation.

7. Conclusions

A water shock tube has been used to investigate the fluid-structure interaction between water borne shock fronts and stainless steel sandwich panels with either honeycomb or pyramidal lattice cores of identical relative density. Tests have been conducted at impulse levels sufficient to initiate some of the panel failure modes. The panel deflections and back face velocity have been measured and compared with results obtained for monolithic panels of the same mass per unit area. A finite element modeling method has been used to investigate the basic deformation mechanisms of the core constituents and to predict the overall panel response to impulsive loading. We find that:

(i) The back face deflections of sandwich panels with specific mass of $14 \, \text{kg/m}^2$ subjected to impulse loading in the $1 - 2 \, \text{kPa} \cdot \text{s}$ range are approximately 30% less than those observed in solid panels of identical mass per unit area.

(ii) The difference in response partly resulted from reduced impulse acquired by the sandwich panels due to beneficial fluid-structure interactions. The simulations indicate that only a fraction of the far field impulse is transmitted to the structure.

(iii) The sandwich panels were also able to exhibit some core crushing (between 1.7 and 26.8% depending on core type and applied impulse) which also contributed to a reduction in FSI and energy dissipation.

(iv) The two core structures investigated underwent similar back (dry) face deflections. However, their front (wet) side deformation patterns were influenced by spacial distribution of nodal contacts with

the underlying core. The larger contact area for the honeycomb core resulted in slightly less face sheet stretching and tearing during the dynamic dishing of the panels.

(v) The resistance to face sheet tearing during impulse loading is clearly sensitive to the detailed design of the core-face sheet nodal contacts. Further work should explore approaches for reducing the fracture susceptibility of the various candidate topologies.

Acknowledgments

References

[ABAQUS/Explicit 6.4–1 2003] ABAQUS/Explicit 6.4–1, *User's Manual*, ABAQUS Inc., 2003.

[Biagi and Bart-Smith 2007] R. Biagi and H. Bart-Smith, "Imperfection sensitivity of pyramidal core sandwich structures", *International Journal of Solids and Structures* **44**:14-15 (2007), 4690–4706.

[Chiras et al. 2002] S. Chiras, D. R. Mumm, A. G. Evans, N. Wicks, J. W. Hutchinson, K. Dharmasena, H. N. G. Wadley, and S. Fichter, "The structural performance of near-optimized truss core panels", *International Journal of Solids and Structures* **39** (2002), 4093–4115.

[Cote et al. 2004] F. Cote, V. S. Deshpande, N. A. Fleck, and A. G. Evans, "The out-of-plane compressive behavior of metallic honeycombs", *Materials Science and Engineering A* **380** (2004), 272–280.

[Cote et al. 2007] F. Cote, R. Biagi, H. Bart-Smith, and V. S. Deshpande, "Structural response of pyramidal core sandwich columns", *International Journal of Solids and Structures* **44**:10 (2007), 3533–3556.

[Deshpande and Fleck 2001] V. S. Deshpande and N. A. Fleck, "Collapse of truss core sandwich beams in 3-point bending", *International Journal Of Solids And Structures* **38**:36–37 (2001), 6275–6305.

[Deshpande and Fleck 2005] V. S. Deshpande and N. A. Fleck, "One-dimensional response of sandwich plates to underwater shock loading", *Journal Of The Mechanics And Physics Of Solids* **53**:11 (November 2005), 2347–2383.

[Deshpande et al. 2006] V. S. Deshpande, A. Heaver, and N. A. Fleck, "An underwater shock simulator", *Proceedings of the Royal Society A: Mathematical, Physical and Engineering Sciences* **462**:2067 (2006), 1021–1041.

[Dharmasena et al. 2007a] K. P. Dharmasena, D. T. Queheillalt, H. N. G. Wadley, Y. Chen, P. Dudt, D. Knight, Z. Wei, and A. G. Evans, "Dynamic response of a multilayer prismatic structure to impulsive loads incident from water", *International Journal of Impact Engineering* (2007). Accepted.

[Dharmasena et al. 2007b] K. P. Dharmasena, H. N. G. Wadley, Z. Y. Xue, and J. W. Hutchinson, "Mechanical response of metallic honeycomb sandwich panel structures to high intensity dynamic loading", *International Journal of Impact Engineering* (2007). In press.

[Espinosa et al. 2006] H. D. Espinosa, S. Lee, and N. Moldovan, "A Novel Fluid Structure Interaction Experiment to Investigate Deformation of Structural Elements Subjected to Impulsive Loading", *Experimental Mechanics* **46**:6 (2006), 805–824.

[Fleck and Deshpande 2004a] N. A. Fleck and V. S. Deshpande, "The Resistance of Clamped Sandwich Beams to Shock Loading", *Journal of Applied Mechanics* **71**:3 (2004), 386–401.

[Fleck and Deshpande 2004b] N. A. Fleck and V. S. Deshpande, "The resistance of clamped sandwich beams to shock loading", *Journal Of Applied Mechanics-Transactions Of The ASME* **71**:3 (May 2004), 386–401.

[Hutchinson and Xue 2005] J. W. Hutchinson and Z. Y. Xue, "Metal sandwich plates optimized for pressure impulses", *International Journal Of Mechanical Sciences* **47**:4–5 (April-May 2005), 545–569.

[Lee 2005] S. Lee, *Dynamic Failure of Blast-Resistant Structures Subjected to Impulsive Loading*, Ph.D. thesis, Northwestern University, Evanston, IL, USA, December 2005.

[Lee et al. 2006] S. Lee, F. Barthelat, J. W. Hutchinson, and H. D. Espinosa, "Dynamic failure of metallic pyramidal truss core materials: Experiments and modeling", *International Journal of Plasticity* **22**:11 (2006), 2118–2145.

[Liang et al. 2007] Y. Liang, A. V. Spuskanyuk, S. E. Flores, D. R. Hayhurst, J. W. Hutchinson, R. M. McMeeking, and A. G. Evans, "The Response Of Metallic Sandwich Panels To Water Blast", *Journal of Applied Mechanics* **74**:1 (2007), 81–99.

[McShane et al. 2006] G. J. McShane, D. D. Radford, V. S. Deshpande, and N. A. Fleck, "The response of clamped sandwich plates with lattice cores subjected to shock loading", *European Journal of Mechanics — A/Solids* **25** (2006), 215–229.

[Mohr et al. 2006] D. Mohr, Z. Y. Xue, and A. Vaziri, "Quasi-static punch indentation of a honeycomb sandwich plate: Experiments and Constitutive Modeling", *Journal of Mechanics of Materials and Structures* **1**:3 (2006), 581–604.

[Qiu et al. 2003] X. Qiu, V. S. Deshpande, and N. A. Fleck, "Finite element analysis of the dynamic response of clamped sandwich beams subject to shock loading", *European Journal Of Mechanics A-Solids* **22**:6 (November-December 2003), 801–814.

[Qiu et al. 2004] X. Qiu, V. S. Deshpande, and N. A. Fleck, "Dynamic response of a clamped circular sandwich plate subject to shock loading", *Journal Of Applied Mechanics-Transactions Of The ASME* **71**:5 (September 2004), 637–645.

[Qiu et al. 2005a] X. Qiu, V. S. Deshpande, and N. A. Fleck, "Impulsive loading of clamped monolithic and sandwich beams over a central patch", *Journal Of The Mechanics And Physics Of Solids* **53**:5 (May 2005), 1015–1046.

[Qiu et al. 2005b] X. Qiu, V. S. Deshpande, and N. A. Fleck, "Impulsive loading of clamped monolithic and sandwich beams over a central patch", *Journal of the Mechanics and Physics of solids* **53** (2005), 1015–1046.

[Queheillalt and Wadley 2005] D. T. Queheillalt and H. N. G. Wadley, "Pyramidal lattice truss structures with hollow trusses", *Materials Science and Engineering A* **397** (2005), 132–137.

[Rabczuk et al. 2004] T. Rabczuk, J. Y. Kim, E. Samaniego, and T. Belytschko, "Homogenization of sandwich structures", *International Journal For Numerical Methods In Engineering* **61** (2004), 1009–1027.

[Radford et al. 2005] D. D. Radford, V. S. Deshpande, and N. A. Fleck, "The use of metal foam projectiles to simulate shock loading on a structure", *International Journal of Impact Engineering* **31** (2005), 1152–1171.

[Radford et al. 2006] D. D. Radford, N. A. Fleck, and V. S. Deshpande, "The response of clamped sandwich beams subjected to shock loading", *International Journal of Impact Engineering* **32** (2006), 968–987.

[Rathbun et al. 2004] H. J. Rathbun, Z. Wei, M. Y. He, F. W. Zok, A. G. Evans, D. J. Sypeck, and H. N. G. Wadley, "Measurement and Simulation of the Performance of a Lightweight Metallic Sandwich Structure With a Tetrahedral Truss Core", *Journal of Applied Mechanics* **71**:3 (2004), 368–374.

[Rathbun et al. 2005] H. J. Rathbun, F. W. Zok, and A. G. Evans, "Strength optimization of metallic sandwich panels subject to bending", *International Journal of Solids and Structures* **42**:26 (2005), 6643–6661.

[Rathbun et al. 2006] H. J. Rathbun, D. D. Rodford, Z. Y. Xue, M. Y. He, J. Yang, V. Deshpande, N. A. Fleck, J. W. Hutchinson, F. W. Zok, and A. G. Evans, "Performance of metallic honeycomb-core sandwich beams under shock loading", *International Journal of Solids and Structures* **43** (2006), 1746–1763.

[Savitzky and Golay 1964] A. Savitzky and M. J. E. Golay, "Smoothing and differentiation of data by simplified least squares procedures", *Analytical Chemistry* **36**:8 (1964), 1627–1639.

[Smith and Hetherington 1994] P. D. Smith and J. G. Hetherington, *Blast and ballistic loading of structures*, Butterworth-Heinemann, Oxford, November 1994.

[Taylor 1963] G. I. Taylor, *The scientific papers of G. I. Taylor*, vol. III, Chapter The pressure and impulse of submarine explosion waves on plates, pp. 287–303, Cambridge University Press, Cambridge, 1963.

[Tilbrook et al. 2006] M. T. Tilbrook, V. S. Deshpande, and N. A. Fleck, "The impulsive response of sandwich beams: analytical and numerical investigation of regimes of behaviour", *Journal of the Mechanics and Physics of Solids* **54**:11 (2006), 2242–2280.

[Vaughn and Hutchinson 2006] D. G. Vaughn and J. W. Hutchinson, "Bucklewaves", *European Journal of Mechanics A-Solids* **25**:1 (2006), 1–12.

[Vaughn et al. 2005] D. G. Vaughn, J. M. Canning, and J. W. Hutchinson, "Coupled plastic wave propagation and column buckling", *Journal of Applied Mechanics* **72**:1 (2005), 139–146.

[Vaziri and Hutchinson 2007] A. Vaziri and J. W. Hutchinson, "Metallic sandwich plates subject to intense air shocks", *International Journal of Solids and Structures* **44**:1 (2007), 2021–2035.

[Vaziri and Xue 2007] A. Vaziri and Z. Y. Xue, "Mechanical behavior and constitutive modeling of metal cores", *Journal of Mechanics of Materials and Structures* **2**:9 (2007), 1743–1760. In press.

[Vaziri et al. 2006] A. Vaziri, Z. Y. Xue, and J. W. Hutchinson, "Metal sandwich plates with polymeric foam-filled cores", *Journal of Mechanics of Materials and Structures* **1**:1 (2006), 95–128.

[Vaziri et al. 2007] A. Vaziri, Z. Y. Xue, and J. W. Hutchinson, "Performance and failure of metal sandwich plates subject to shock loading", *Journal of Mechanics of Materials and Structures* (2007). In press.

[Wadley 2006] H. N. G. Wadley, "Multifunctional periodic cellular metals", *Philosophical Transactions of the Royal Society A* **364** (2006), 31–68.

[Wadley et al. 2003] H. N. G. Wadley, N. A. Fleck, and A. G. Evans, "Fabrication and structural performance of periodic cellular metal sandwich structures", *Composite Science & Technology* **63** (2003), 2331–2343.

[Wadley et al. 2007a] H. N. G. Wadley, K. P. Dharmasena, Y. Chen, P. Dudt, D. Knight, R. Charette, and K. Kiddy, "Compressive response of multilayered pyramidal lattices during underwater shock loading", *International Journal of Impact Engineering* (2007). In press.

[Wadley et al. 2007b] H. N. G. Wadley, K. P. Dharmasena, D. T. Queheillalt, Y. Chen, P. Dudt, D. Knight, K. Kiddy, Z. Xue, and A. Vaziri, "Dynamic compression of square honeycomb structures during underwater impulsive loading", *Journal of Mechanics of Materials and Structures* (2007). In press.

[Wallach and Gibson 2001a] J. C. Wallach and L. J. Gibson, "Defect sensitivity of a 3D truss material", *Scripta Materialia* **45**:6 (2001), 639–644.

[Wallach and Gibson 2001b] J. C. Wallach and L. J. Gibson, "Mechanical behavior of a three-dimensional truss material", *International Journal of Solids and Structures* **38** (2001), 7181–7196(16).

[Wicks and Hutchinson 2001] N. Wicks and J. W. Hutchinson, "Optimal truss plates", *International Journal of Solids and Structures* **38**:30–31 (2001), 5165–5183.

[Xue and Hutchinson 2003] Z. Y. Xue and J. W. Hutchinson, "Preliminary assessment of sandwich plates subject to blast loads", *International Journal Of Mechanical Sciences* **45**:4 (April 2003), 687–705.

[Xue and Hutchinson 2004a] Z. Y. Xue and J. W. Hutchinson, "A comparative study of impulse-resistant metal sandwich plates", *International Journal of Impact Engineering* **30**:10 (November 2004), 1283–1305.

[Xue and Hutchinson 2004b] Z. Y. Xue and J. W. Hutchinson, "Constitutive model for quasi-static deformation of metallic sandwich cores", *International Journal For Numerical Methods In Engineering* **61** (2004), 2205–2238.

[Xue and Hutchinson 2005] Z. Y. Xue and J. W. Hutchinson, "Crush dynamics of square honeycomb sandwich cores", *International Journal for Numerical Methods in Engineering* **65** (2005), 2221–2245.

[Xue et al. 2005] Z. Y. Xue, A. Vaziri, and J. W. Hutchinson, "Non-uniform constitutive model for compressible orthotropic materials with application to sandwich plate cores", *Computer Modeling in Engineering & Sciences* **10**:1 (2005), 79–95.

[Zok et al. 2004a] F. W. Zok, H. Rathbun, M. He, E. Ferri, C. Mercer, R. M. McMeeking, and A. G. Evans, "Structural performance of metallic sandwich panels with square honeycomb cores", *Philosophical Magazine* **85** (2004), 3207–3234.

[Zok et al. 2004b] F. W. Zok, S. A. Waltner, Z. Wei, H. J. Rathbun, R. M. McMeeking, and A. G. Evans, "A protocol for characterizing the structural performance of metallic sandwich panels: application to pyramidal truss cores", *International Journal of Solids and Structures* **41** (2004), 6249–6271.

L. F. MORI: lapo.mori@gmail.com
Department of Mechanical Engineering, Northwestern University, Evanston, IL 60208, United States

S. LEE: sungsoo.f.lee@gmail.com
Department of Mechanical Engineering, Northwestern University, Evanston, IL 60208, United States

Z. Y. XUE: xue@deas.harvard.edu
School of Engineering and Applied Sciences, Harvard University, Cambridge, MA 02138, United States

A. VAZIRI: avaziri@deas.harvard.edu
School of Engineering and Applied Sciences, Harvard University, Cambridge, MA 02138, United States

D. T. QUEHEILLALT: dtq2j@virginia.edu
Department of Materials Science and Engineering, University of Virginia, 140 Chemistry Way, Charlottesville, VA 22904, United States

K. P. DHARMASENA: kumar@virginia.edu
Department of Materials Science and Engineering, University of Virginia, 140 Chemistry Way, Charlottesville, VA 22904, United States

H. N. G. WADLEY: haydn@virginia.edu
Department of Materials Science and Engineering, University of Virginia, 140 Chemistry Way, Charlottesville, VA 22904, United States

J. W. HUTCHINSON: jhutchin@fas.harvard.edu
School of Engineering and Applied Sciences, Harvard University, Cambridge, MA 02138, United States

H. D. ESPINOSA: espinosa@northwestern.edu
Department of Mechanical Engineering, Northwestern University, Evanston, IL 60208, United States

Appendix E

The resistance of metallic plates to localized impulse

Z. Wei[a,*], V.S. Deshpande[b], A.G. Evans[a,b], K.P. Dharmasena[c],
D.T. Queheillalt[c], H.N.G. Wadley[c], Y.V. Murty[d], R.K. Elzey[d], P. Dudt[e],
Y. Chen[e], D. Knight[e], K. Kiddy[f]

[a]Materials Department, University of California, Santa Barbara, CA 93106, USA
[b]Mechanical Engineering Department, University of California, Santa Barbara, CA 93106, USA
[c]Department of Materials Science, University of Virginia, Charlottesville, VA 22904, USA
[d]Cellular Materials International, Inc., Charlottesville, VA 22903, USA
[e]Naval Surface Warfare Center, Carderock, MD 20817, USA
[f]Naval Surface Warfare Center, Indian Head, MD 20640, USA

Abstract

The responses of metallic plates and sandwich panels to localized impulse are examined by using a dynamic plate test protocol supported by simulations. The fidelity of the simulation approach is assessed by comparing predictions of the deformations of a strong-honeycomb-core panel with measurements. The response is interpreted by comparing and contrasting the deformations with those experienced by the same sandwich panel (and an equivalent solid plate) subjected to a planar impulse. Comparisons based on the center point displacement reveal the following paradox. The honeycomb panel is superior to a solid plate when subjected to a planar impulse, but inferior when localized. The insights gained from an interpretation of these results are used to demonstrate that a new design with a doubly-corrugated soft core outperforms solid plates both for planar and localized impulses.
Published by Elsevier Ltd.

1. Introduction

Many of the issues that affect the dynamic response of metallic sandwich panels have been established for a planar blast wave impinging on a plate at zero obliquity (e.g. Xue and Hutchinson, 2004; Deshpande and Fleck, 2005; Hutchinson and Xue, 2005; Deshpande et al., 2006; Tilbrook et al., 2006; Dharmasena et al., 2007a; Liang et al., 2007; Wadley et al., 2007; Wei et al., 2007a, b). Analytic expressions derived for the fluid/structure interaction (FSI) (Deshpande and Fleck, 2005; Liang et al., 2007) predict the time evolution of the

*Corresponding author. Materials Department, University of California, Santa Barbara, CA 93106, USA. Tel.: +1 805 893 5871; fax: +1 805 893 8486.
E-mail address: zhensong@engr.ucsb.edu (Z. Wei).

face velocities and the momentum acquired by the panel. The analytic formulae have been validated by comparison with numerical simulations and with experimental measurements on panels subjected to dynamic loads. The formulae predict the most important response metrics. These include the center displacements of the back face, the reaction forces induced at the supports and the plastic strains in the face sheets. The latter allow estimates to be made of the occurrence of face sheet tearing. The intent of this article is to explore the corresponding situation in the near-field of a localized blast source with spherically-expanding wave front and thereupon, establish a simulation procedure that decouples determination of the impulse from its imposition onto the structure. Such decoupling has the advantages that it reduces the simulation time while also allowing access to the wide range of material models available in commercial finite element codes such as ABAQUS/ Explicit (ABAQUS Inc., 2006).

To provide context we recall that the impulsive response of sandwich panels can span a range between soft and strong (Tilbrook et al., 2006; Liang et al., 2007). Soft-cores crush extensively following application of an impulse to the front face. In this situation, the back face displacement arrests while the front face is still in motion. Strong-cores exhibit minimal crushing and both faces acquire a common velocity before arresting. For plane waves, the best combination of performance metrics arises for soft-core designs with unclamped front faces. It will be shown that the requirements differ for localized loadings. To validate the numerical procedures, measurements are performed utilizing the test fixture shown in Fig. 1a, incorporating a panel with a triangular honeycomb core fabricated from a super-austenitic stainless steel (Fig. 1b). In this test, the panel is
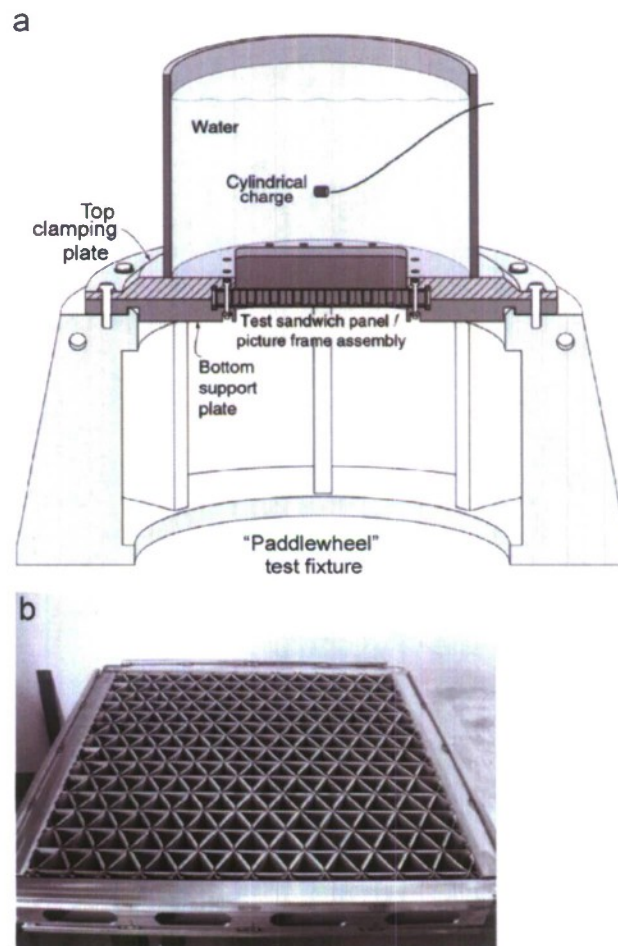
Fig. 1. (a) The configuration used for the paddle wheel test. (b) The triangular honeycomb sandwich panel used for the measurements (the front face sheet is not shown).

rigidly supported around its perimeter and subjected to a localized impulse from a blast source close to the center of the plate.

The article is organized in the following manner. The measurements are summarized. The calculations of the blast source pressure and velocity fields are obtained using the dynamic system mechanics analysis simulation (DYSMAS) code, followed by ABAQUS/Explicit calculations of the response of the panel. Comparisons between the calculations and the measurements are used to assess the fidelity of the simulation approach. Calculations are performed for solid plates as well as for several sandwich designs to establish a pathway towards configurations that outperform solid plates.

2. Experimental details

The sandwich panels were fabricated from a super-austenitic stainless steel alloy by CMI Inc. (Charlottesville, Virginia). The triangular honeycomb core was fabricated using an interlocking assembly approach proposed originally by Dharmasena et al. (2007b) (Fig. 2). Briefly, a series of 50.8 mm spaced triangular notches and narrow rectangular slots were laser cut into 60.8 mm wide, 0.76 mm thick strips. One pattern (shape #1 in Fig. 2) had slots along a single edge. The other (shape #2) had slots along both. Each strip was bent at 90° along the two lengthwise edges to provide ~5 mm surface tabs for attachment of the core to the top and bottom faces. The strips were arranged at 60° and assembled to create a core having relative
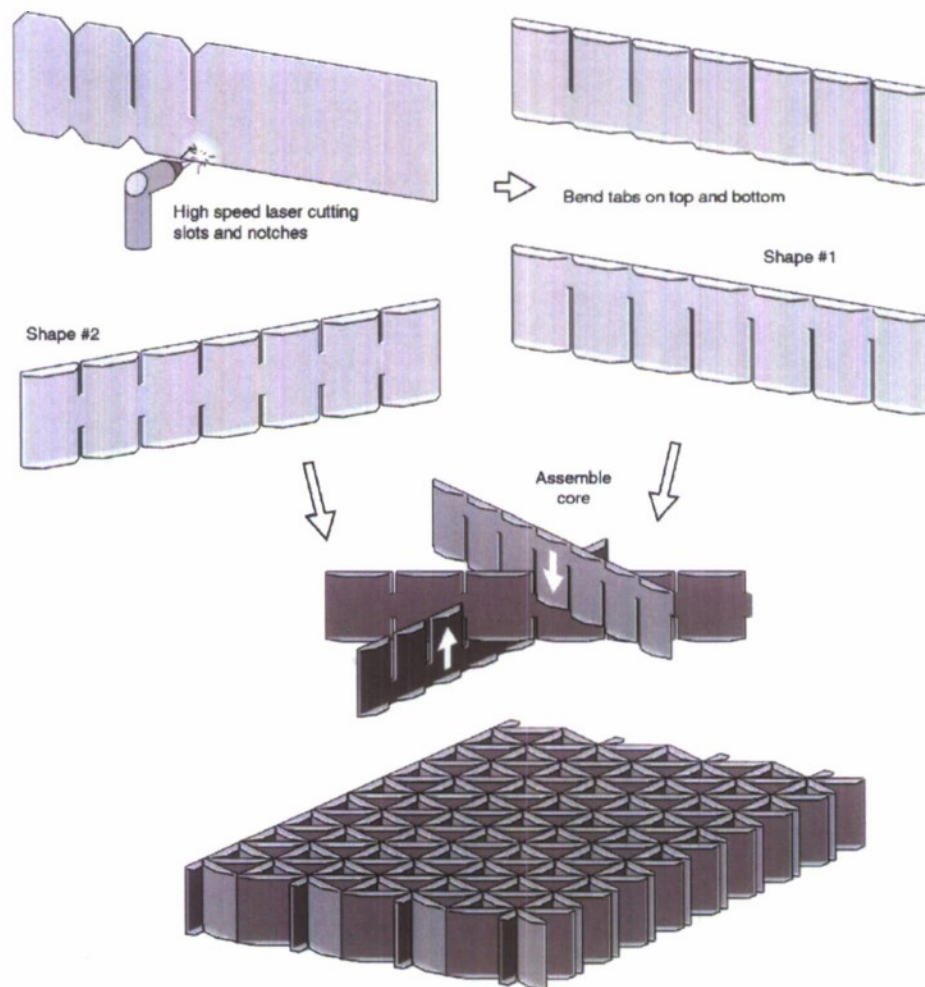
Fig. 2. Cutting, bending and assembling operations used to fabricate triangular honeycomb cores.

density (ignoring the face attachment tabs):

$$\bar{\rho} = 2\sqrt{3}\left(\frac{b}{l}\right),\tag{1}$$

where b is the thickness of the web and l is the cell size (node spacing). For the chosen design (with $b = 0.76$ mm and $l = 50.8$ mm), the relative density $\bar{\rho} = 0.052$. The assembled core with dimensions $0.64 \times 0.64 \times 0.051$ m was mounted in a picture frame with 50.8×50.8 mm hollow tube edge members. The core was metallurgically bonded to 0.71 m $\times 0.71$ m $\times 1.52$ mm faces by spraying with braze powder (Wall Colmonoy Nicrobraz 31 alloy), assembling, installing in a vacuum system (Solar Atmospheres, Souderton, PA) at 0.13 Pa and imposing the following thermal cycle: (i) holding at $550\,°C$ for ~30 min to remove the polymer binder mixed with the braze alloy; (ii) equilibrating at $925\,°C$ for 30 min; and (iii) bonding at $1155\,°C$ for 60 min, before cooling to ambient. After brazing, 24 holes were drilled through the edges, for attachment to the test fixture. The as-brazed panel with a core thickness of 50.8 mm had mass/area equivalent to a 5.7 mm thick solid steel plate.

For testing purposes, the four edges of the panel were rigidly clamped between two plates with a series of through-bolts (Fig. 1a). The test fixture was submersed in water and a large localized impulsive load created by the detonation of a small explosive charge centered above the test plate at a pre-selected standoff. Both faces of the panel suffered significant displacement, accompanied by localized buckling of some of the core members (Fig. 3). The front face deformed around the core members with some tearing at the nodes near the center (Fig. 4). The back face exhibited much less localized deformation (Fig. 5).
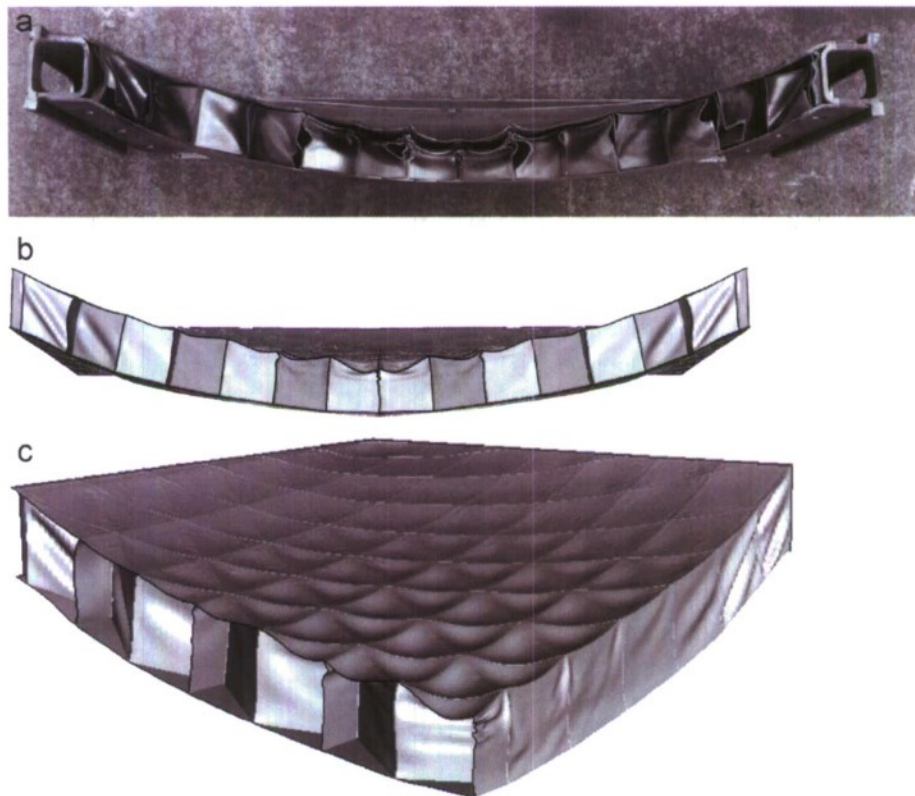
Fig. 3. The deformations of the sandwich panel. (a) A cross-section through the center of the panel. (b) The corresponding cross-section obtained by simulation. (c) An inclined view of a quarter of the panel.
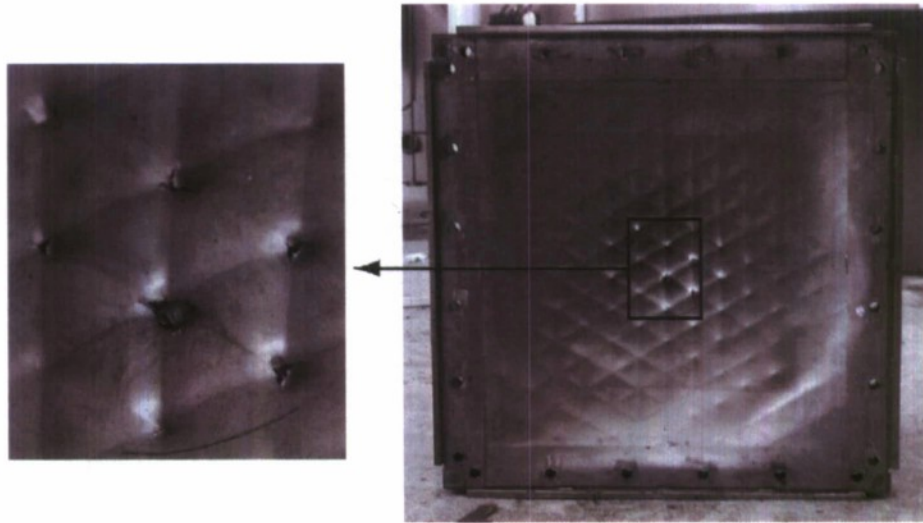
Fig. 4. Plan view of the front face after testing and high-resolution view of the center revealing the deformation of the face around the core members and the tearing of the face at the node intersections.

Fig. 5. Plan view of the back face after testing revealing minimal localized deformations around core members around the center.

3. Impulsively loaded sandwich panels

3.1. Planar impulsive loading

3.1.1. Time scales and velocities

For plane waves characterized by an exponentially-decaying impulse, with maximum pressure, p_0, and time constant, t_0 (impulse per area, $I_0 = p_0 t_0$) the front face rapidly accelerates to a maximum velocity, $\hat{v}_{peak}$, just before cavitation in the water, which commences, at time $t = t_c$. Thereafter, the core imposes a push-back stress, causing the front face to decelerate and the back face to accelerate in a manner governed by the

dynamic strength of the core, σ_{YD}^c. For a strong core, the front and back face velocities converge to a common velocity, v_{common}. This happens at time t_{II}. Thereafter, both faces decelerate together and arrest at time, t_{III}.

For a strong core, the back face velocity attains a maximum velocity at t_{II} (Tilbrook et al., 2006):

$$v_b = \frac{\sigma_{YD}^c}{m_b} t_{II},$$

(2)

where m_b is the mass of the back face while the dynamic strength of the honeycomb core is (Xue and Hutchinson, 2006):

$$\sigma_{YD}^c = \bar{\rho}\sigma_{YD}(\dot{\varepsilon}).$$

(3)

Here σ_{YD} is the dynamic yield strength of the material in the core at the strain rate, $\dot{\varepsilon} \approx \hat{v}_{peak}/H_c$ (H_c is the core thickness). The back face decelerates as plastic hinges propagate along its length and arrest at a time (Tilbrook et al., 2006):

$$t_{III} \approx L\sqrt{\frac{\rho}{\sigma_Y}},$$

(4)

where ρ is the density of the material comprising the face, σ_Y its yield strength at low strain-rates and L is the half-span of the beam. The average reaction force at the supports RF is related to the total momentum imparted from water to the panel, I ($\approx I_0$ in most cases), by

$$RF = \frac{I}{t_{III}}.$$

(5)

3.1.2. Numerical simulations

For plane-waves it has been possible to conduct successful simulations of the responses of the panel and of the water by using the commercial finite element code ABAQUS/Explicit (Dharmasena et al., 2007a; Liang et al., 2007; Wei et al., 2007a, b). In these investigations, the input to the ABAQUS simulations is the pressure versus time history created in the water by the explosion calculated using the code DYSMAS (Dharmasena et al., 2007a; Wei et al., 2007a, b). A similar DYSMAS–ABAQUS procedure is adopted in this study.

3.2. Localized impulsive loading

3.2.1. Time scales and pressures

A synopsis of the main characteristics of a shock wave resulting from an underwater impulsive source (ascertained over decades by means of large-scale experiments and modeling, e.g. Cole, 1948; Swisdak, 1978) underpins the ensuing assessments. The impulse is transmitted through the surrounding water by the propagation of a spherical shock at near the sonic speed (see Fig. 6a). Upon arrival at a fluid element radial distance r from a point source, the pressure rises (almost instantaneously) to a peak p_0. Subsequently, it decreases at nearly exponential rate, with a time constant t_0 (of order milliseconds): $p = p_o e^{-t/t_0}$, where t is the time measured from the instant of arrival of the blast wave. For blast-created impulses, the magnitude of the shock pressure and decay constant depend upon the mass and type of explosive material as well as r. The experimental data and physical models (Cole, 1948; Swisdak, 1978) support the use of simple power-law scaling between the mass M of explosive, the radial distance r, p_0 and t_0. For example, for an underwater TNT explosion, the peak pressure (in MPa) scales as (Swisdak, 1978):

$$p_0 = 52.4\left(\frac{M^{1/3}}{r}\right)^{1.13}.$$

(6)

where M is in kilograms and r in meters. The time constant t_0 (in ms) scales as:

$$t_0 = 0.084 M^{1/3}\left(\frac{M^{1/3}}{r}\right)^{-0.23}.$$

(7)

These relations have been validated for wide domains of M and r.
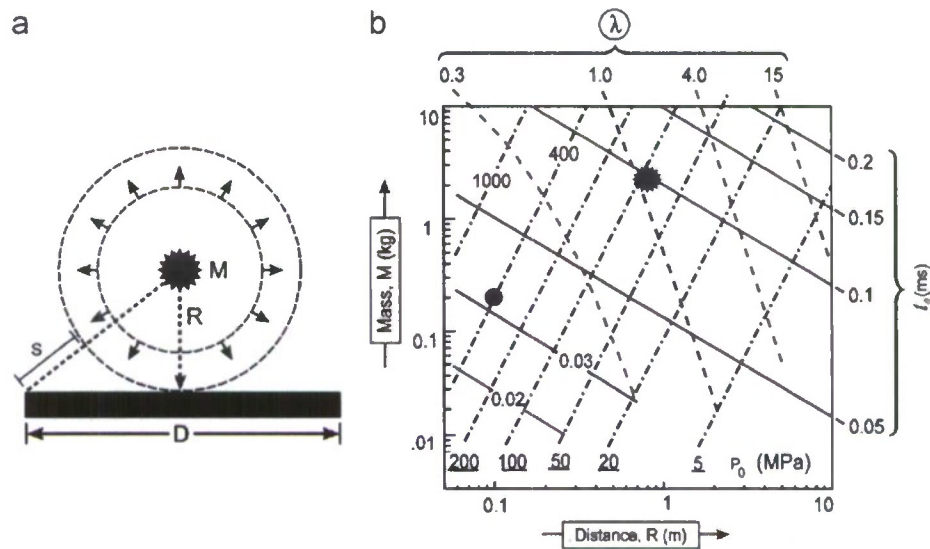
Fig. 6. (a) Schematic of a circular panel subject to a spherical blast. (b) Underwater explosion map for spherical blasts with axes of the explosive mass M and stand-off R. Contours of constant peak pressure p_0 and decay time t_0 are plotted on the map. Also included are contours of the blast planarity measure λ for a circular panel of diameter $D = 0.64\,\text{m}$. The blast investigated experimentally in this study is marked by the solid circle, while the star denotes an equivalent "planar" blast due to a point source.

3.2.2. Localized versus planar loading

In order to quantify the degree of "planarity" of the impulse loading of a sandwich panel, we define a planarity measure:

$$\lambda \equiv \frac{c_w t_0}{s}, \tag{8}$$

where s is the additional distance that the blast wave has to travel before it impinges onto the edge of the panel. It is defined in Fig. 6a and given as:

$$s \equiv R\left(\sqrt{\left(\frac{D}{2R}\right)^2 + 1} - 1\right). \tag{9}$$

where R is the standoff distance of the panel from the point explosive charge ($r = R$ when the blast wave impinges at the center of the panel) and D the span of the panel. We interpret λ as the ratio of the decay constant t_0 to the time delay for the blast to impinge on the edge after reaching the mid-span. Here, situations with $\lambda < 1$ are considered non-planar (the incident blast pressure at the mid-span has dropped below $0.37p_0$ before the blast wave impinges on the edge). Conversely, cases with $\lambda \geqslant 1$ are deemed planar.

A map with explosive mass M and distance R as coordinates (Fig. 6b) is used to display contours of the blast planarity measure λ for a circular panel, diameter $D = 0.64\,\text{m}$ (a representative size for the panel tested here). Also included are contours of constant p_0 and t_0.

4. The simulation scheme

The time variation of the predicted pressure wave (using DYSMAS) created by the source at a stand-off $R = 0.102\,\text{m}$ is depicted in Fig. 7. Using this pressure history we estimate the source to correspond to $M \approx 0.2\,\text{kg}$ of TNT using published nomographs for explosions in water (Swisdak, 1978). Prior to the pressure front contacting the panel, the wave is spherically symmetric. The pressure and velocity profiles in the water at two times prior to impact are summarized in Fig. 8a and b. The particle velocity increases with distance from the wave front, attains a maximum, and decreases to zero at the center of the source, albeit in a non-monotonic manner. The temporal characteristics of the pressure shown in Fig. 8c reveal a scaling:
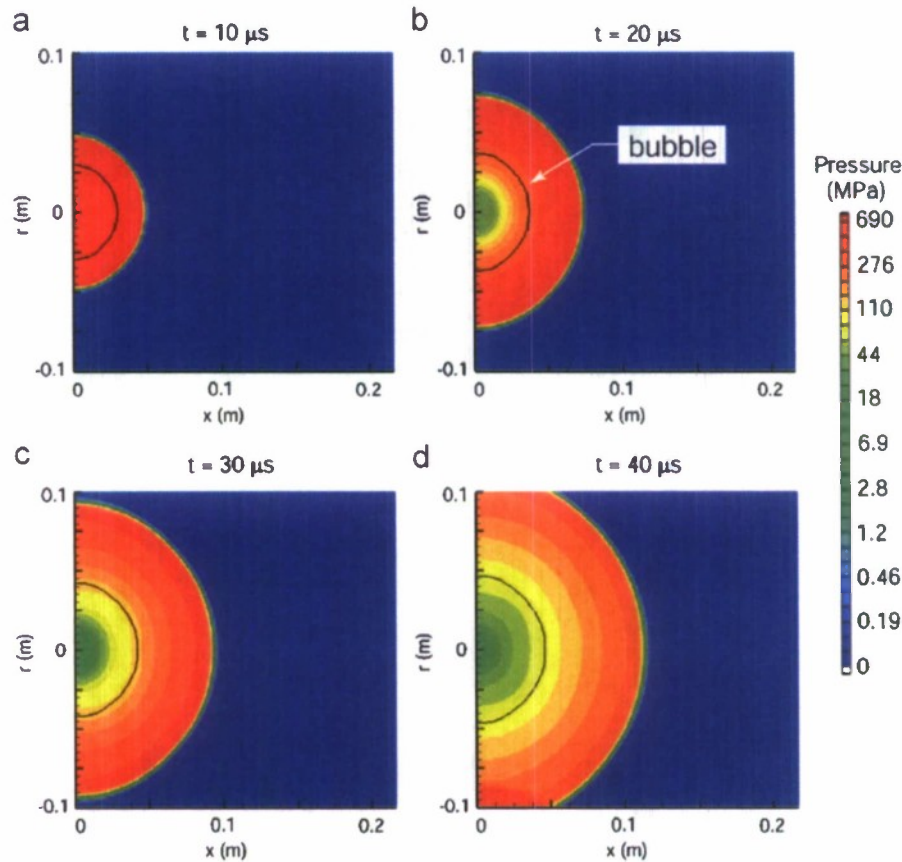
Fig. 7. DYSMAS simulation of the propagation of the blast wave generated by a spherical charge at selected times t after the detonation: (a) $t = 10\,\mu s$, (b) $t = 20\,\mu s$, (c) $t = 30\,\mu s$ and (d) $t = 40\,\mu s$.

$p(r/R)^{3/2} \sim \exp[-t(r/R)^{1/2}]$. The scaling differs from that used for point charges (Eqs. (6) and (7)), presumably because of the finite source size and its proximity to the panel. The approach that most faithfully reproduces the FSI effect parameterizes the spatial variation of the pressure and velocity at times preceding contact (Fig. 8a and b) and uses these to set up the initial pressure and velocity fields in the water for the ABAQUS analysis. That is, the potential and kinetic energy are transferred from DYSMAS to ABAQUS through the pressure and velocity fields, respectively. The higher pressures in the reflected wave then become an output of the calculation. FORTRAN programming has been used to facilitate the transfer process.

Due to the symmetry, only one-quarter of the sandwich panel need be modeled. For computational efficiency, shell elements with reduced integration (S4R) are used for the panel. Eight-noded solid elements (C3D8R), coupled with linear equation of state, are used to model the water. The mesh is depicted in Fig. 9. The general contact algorithm in ABAQUS/Explicit was used. The constitutive laws used for the stainless steel and water have been described elsewhere (Xue and Hutchinson, 2006; Liang et al., 2007), but are summarized in Appendix A for completeness.

To adequately simulate the dynamic response of the core members it has often been necessary to incorporate geometric imperfections. However, due to the very large number of degrees of freedom in the model, only the first 50 eigen-modes could be extracted from a modal analysis. These modes depicted in Fig. 10a do not include the short-wavelength modes that are critical to accurate predict the dynamic collapse response of honeycombs (McShane et al., 2007). Thus, instead of selecting one of these modes, a short-wavelength imperfection is introduced into the core member at the center of symmetry having amplitude equal the member thickness (Fig. 10b). The premise is that all other members will buckle in the appropriate manner because of the bending moments generated in these members.
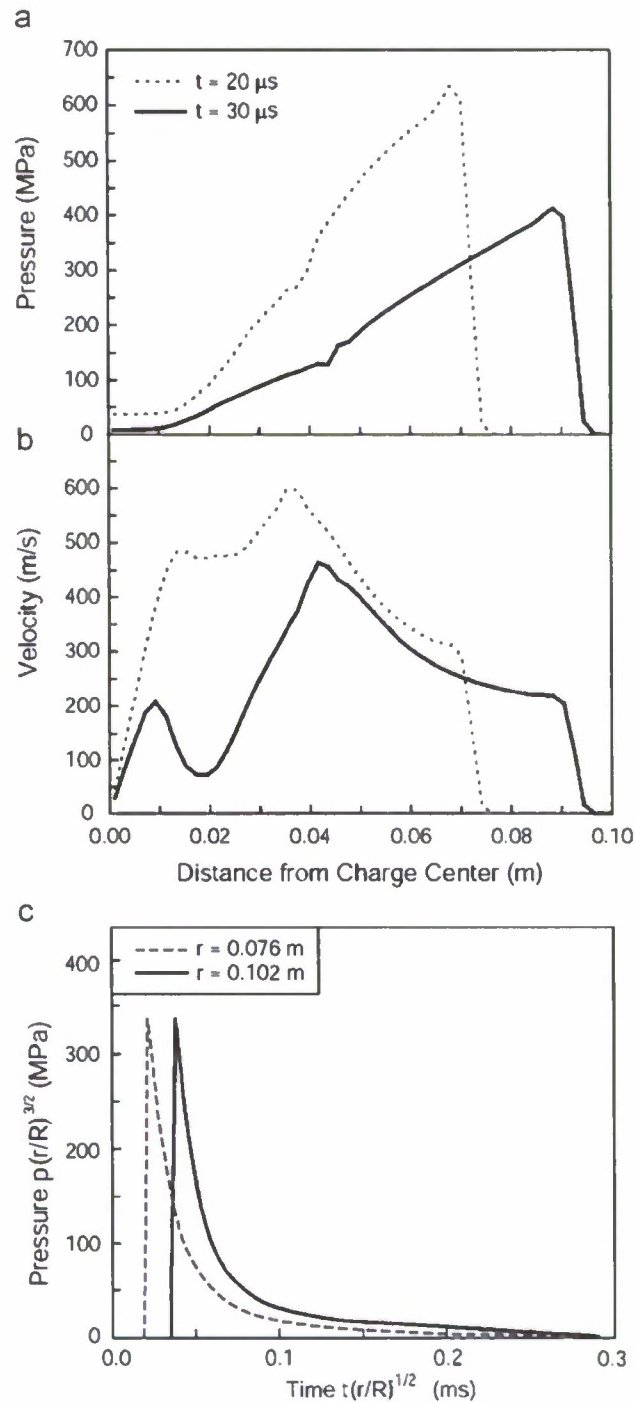
Fig. 8. Spatial response profiles in the water at two times t prior to the wave impinging on the panel: (a) pressure and (b) velocity. (c) The temporal characteristics of the pressure wave.

5. Simulation results for honeycomb core sandwich panel

The deformations experienced by the panel are depicted in Fig. 3. In this figure, the simulated shapes (Fig. 3b and c) are compared with the cross section of the tested panel (Fig. 3a). The close similarity is
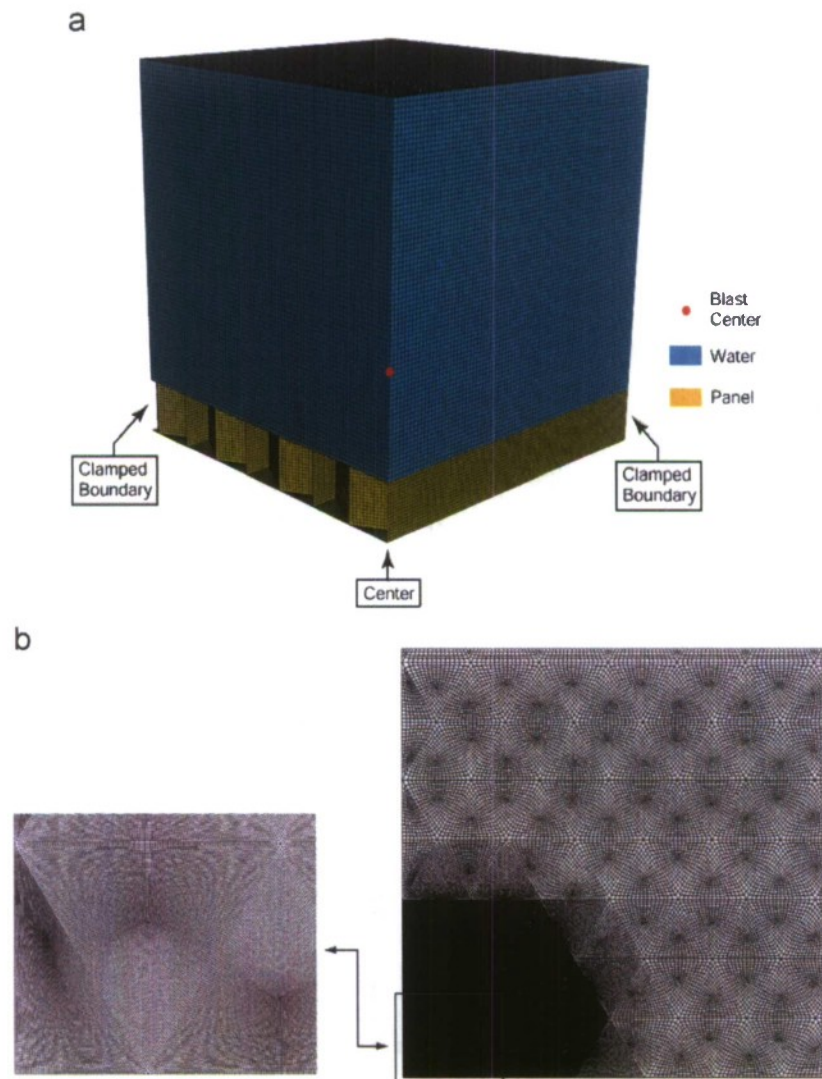
Fig. 9. The finite element mesh used for simulations: (a) the water column and (b) the front face adjacent to the center of the configuration.

apparent. For computation tractability, a rupture criterion has not been included in the ABAQUS model. Instead, the equivalent plastic strain ε_e^{pl} distribution in the front face around the centermost unit cell of the core is used as a surrogate (Fig. 11). The large plastic strains occur at two types of locations near the center of the panel: one around the nodes, and the other along the core member edges. The strains at those locations have a maximum of about 70% and exceed the ductility of the alloy: the tensile ductility of the stainless steel is approximately 50% (Nemat-Nasser et al., 2001). However, face tearing only occurred around the nodes in the experiment (Fig. 4). This discrepancy is attributed to the tabs on the core members (Fig. 2) that were not modeled in the simulation, which reduce the stress concentration and prevent large plastic strains along core member edges.

The velocities acquired by the front and back faces at the panel center (Fig. 12) have typical strong-core characteristics. Namely, with minimal core crushing, the faces acquire a common velocity after about 0.1 ms and (following some oscillations) decelerate together and arrest after about 1.5 ms. After arresting there are elastic reverberations. The maximum velocity acquired by the front face, $\hat{v}_{peak} = 225\,\mathrm{ms}^{-1}$ is appreciably higher than that found in previous planar wave assessments (Liang et al., 2007; Wei et al., 2007a, b) because of

a
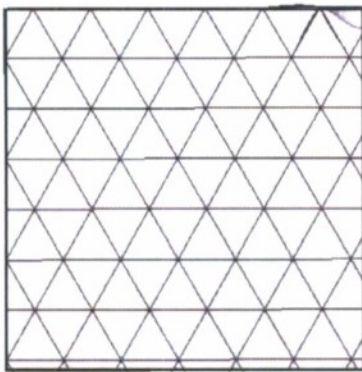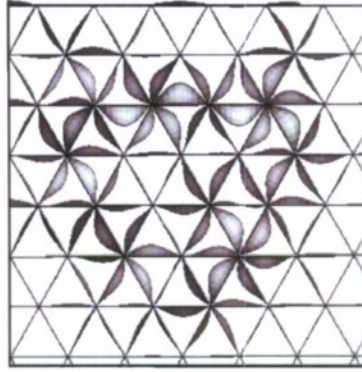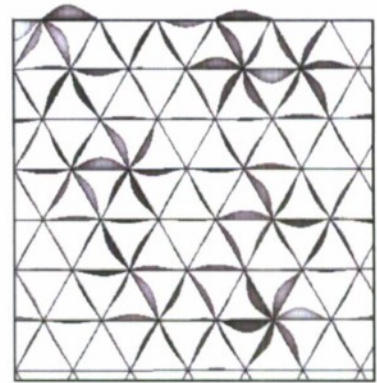
mode 1   mode 10   mode 20
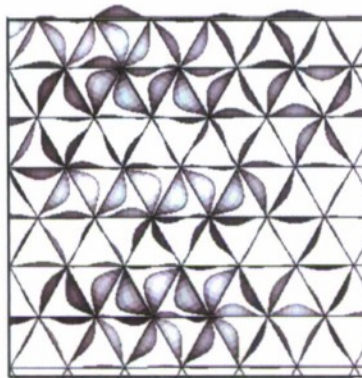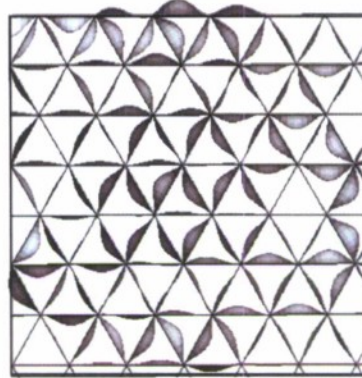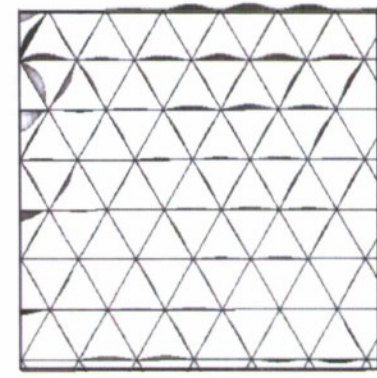
mode 30   mode 40   mode 50

b
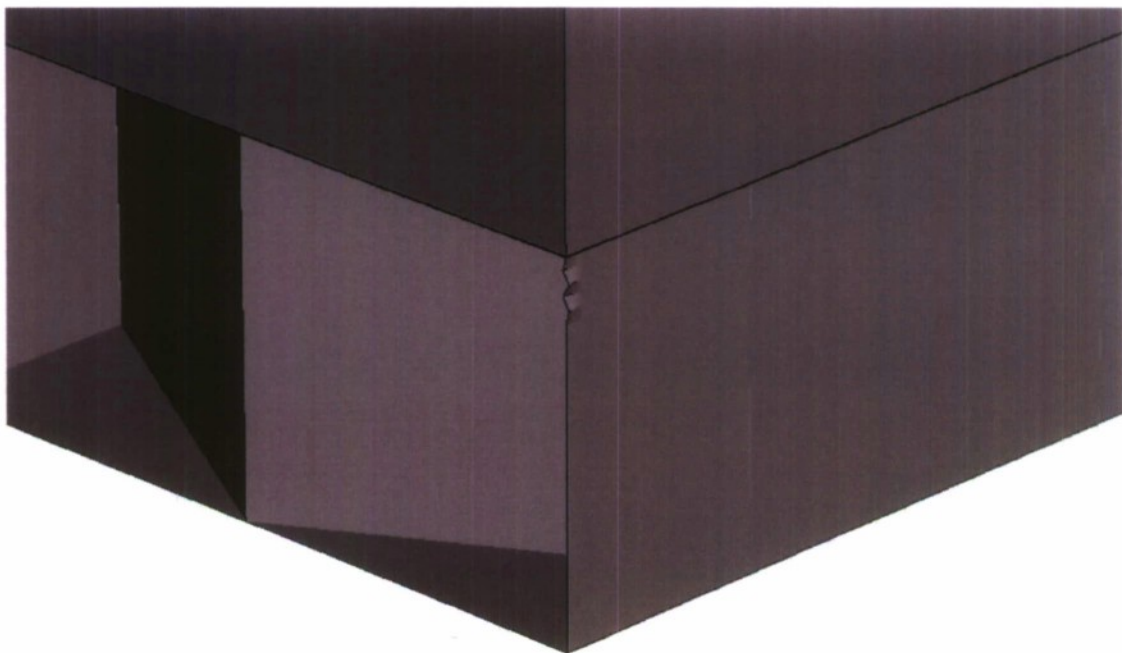
Fig. 10. (a) Selected eigen-modes for the triangular honeycomb core. (b) The short wavelength geometric imperfection introduced in the core member at the center of symmetry.
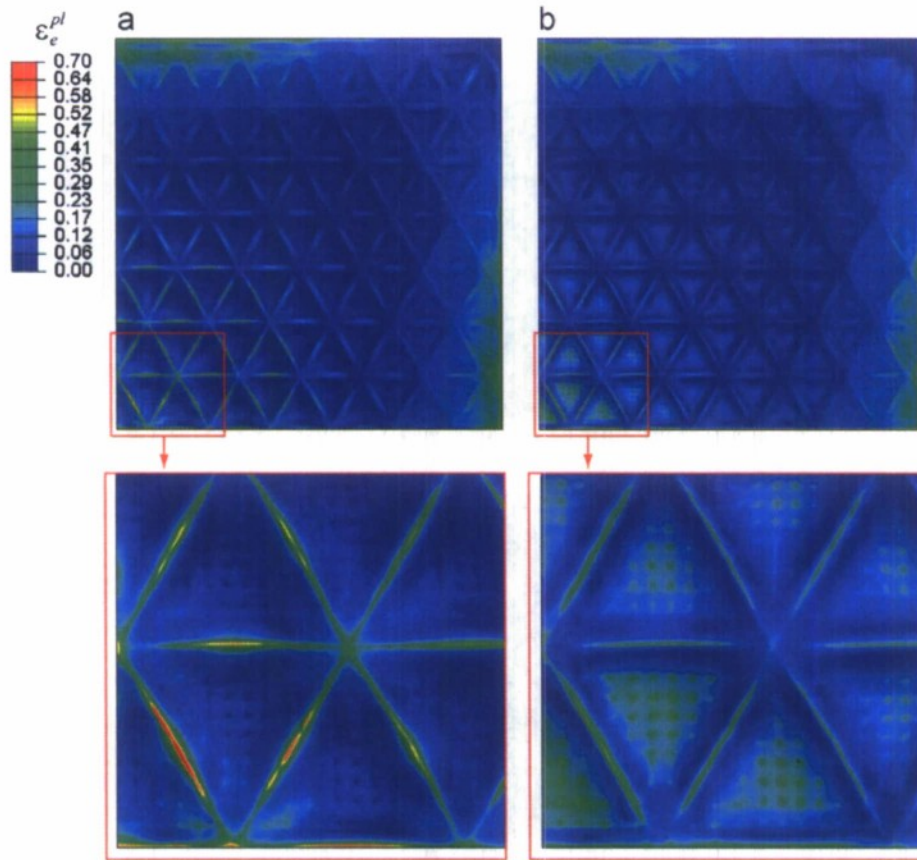
Fig. 11. The equivalent plastic strain distribution of the front face on (a) the wet surface and (b) dry surface.

the larger (albeit localized) pressure. The constancy of the acceleration of the back face at its center, prior to attaining a common velocity, suggests that the dynamic strength of the core can be estimated from Eq. (2). The ensuing estimate, $\sigma_{YD} \approx 15\,MPa$ (along with Eq. (3) and $\bar{\rho} = 0.052$) would infer a dynamic yield strength, $\sigma_{YD} \approx 290\,MPa$ at strain-rate (based on the front face velocity, Fig. 12), $\dot{\varepsilon} \approx 4 \times 10^3\,s^{-1}$. The inference is that, despite the localized nature of the impulse, the back face velocity at the center can still be estimated from Eq. (2). Moreover, the duration of the deformation ($\sim$1.60 ms) is close to that expected for plastic hinge propagation time along the back face, t_{III} ($\sim$1.65 ms calculated from Eq. (4)), despite a seemingly different deformation sequence.

The pressure wave propagation sequence in the water (Fig. 13) reveals the magnitude of the reflected wave, as well as the formation and expansion of the cavitated regions (delineated by domains where the pressure in the water is zero). The source creates a spherically-expanding cavitation front. The reflection creates another front propagating in the opposite direction (away from the panel). This front initiates at a stand-off distance ($x_e = 15\,mm$) from the panel, at times greater than 30 μs, causing an uncavitated layer of water to attach to the panel. At 60 μs these cavitation fronts converge along the center-line. Thereafter, the complexity of the velocity field eludes simple description.

6. Comparative responses

6.1. Equivalent impulses

The source pressure and duration in the test inferred from the calculations (Fig. 8) are used to infer the equivalent mass of TNT from (Swisdak, 1978) and the data superimposed on the nomograph (marked as
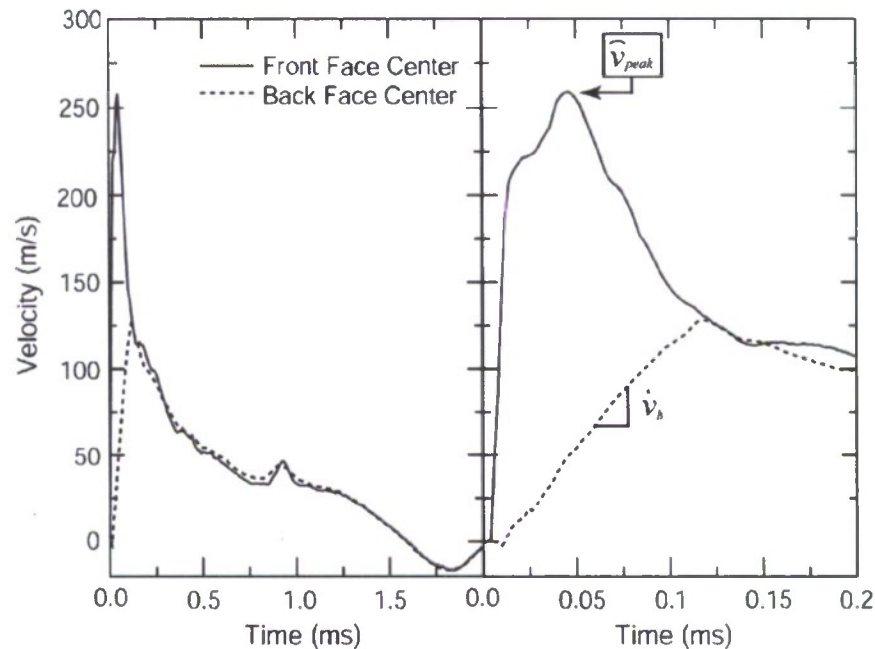
Fig. 12. The time variation of the velocities acquired by the front and back faces at the panel center.

a solid circle in Fig. 6b) to affirm that the source in this test is truly localized ($\lambda < 0.3$). Note, however, that the decay time ($t_0 \approx 0.03$ ms) exceeds that found from the DYSMAS calculations ($t_0 \approx 0.02$ ms; see Fig. 8c), again presumably because of the close proximity of the blast source. The velocity and pressure characteristics for the spherical wave front (Fig. 8a and b) indicate that it is equivalent to a planar uniform source with the free field impulse, $I_0 \approx 6$ kPa s. In order to gauge the performance of the same panel subjected to an "equivalent" planar impulse, we use the same free field impulse and explore two options: (i) an impulse with essentially the same duration ($t_0 \approx 0.02$ ms) as that in the test and peak pressure of about 300 MPa. Such a planar source cannot be ascribed to a local (point) event because of the small λ. However, this could be envisioned as an equivalent impulse emanating from a thin-sheet-explosive described in previous studies (Dharmasena et al., 2007a; Wadley et al., 2007; Wei et al., 2007a, b); and (ii) a point source blast with $t_0 = 0.1$ ms consistent with a previous investigation (Liang et al., 2007) and peak pressures of about 60 MPa. This corresponds to source at a stand-off $R \approx 1$ m and indicated by the star in Fig. 6b. This source gives, $\lambda \approx 2$ (Fig. 6b), satisfying the planarity requirement associated with a point blast source.

6.2. Deformations

Comparison of the permanent deformations of the solid plate reveal major differences between the response to the two "equivalent" blast sources as well as non-intuitive differences between the planar and localized cases (Figs. 14 and 15a and b). Given the small deflection found for the "equivalent" source using the lower pressure (giving a planar blast wave), we assert that this is not the relevant comparison. The ensuing comparison is thus restricted between the local and the planar impulse with $p_0 = 300$ MPa and $t_0 = 0.02$ ms.

For the planar impulse, the panel assumes a conical shape with maximum deflection at the center (Fig. 15b). Conversely, the local impulse results in a planar segment at the center (Fig. 15a). The difference is briefly explained as follows: elastic wave reflections from the supports interfere with the propagation of plastic hinges and prevent the formation of the conical shape. The corresponding deformations experienced by the honeycomb core panel are plotted on the same figure and are almost identical.

A plot of the maximum deflections from all of the calculations (Fig. 15a–d) demonstrates two important effects: (i) For planar impulse, the center deflection of the back face is less than that for the center of the solid plate. Moreover, the reduction in deflection is consistent with that reported previously for honeycomb cores
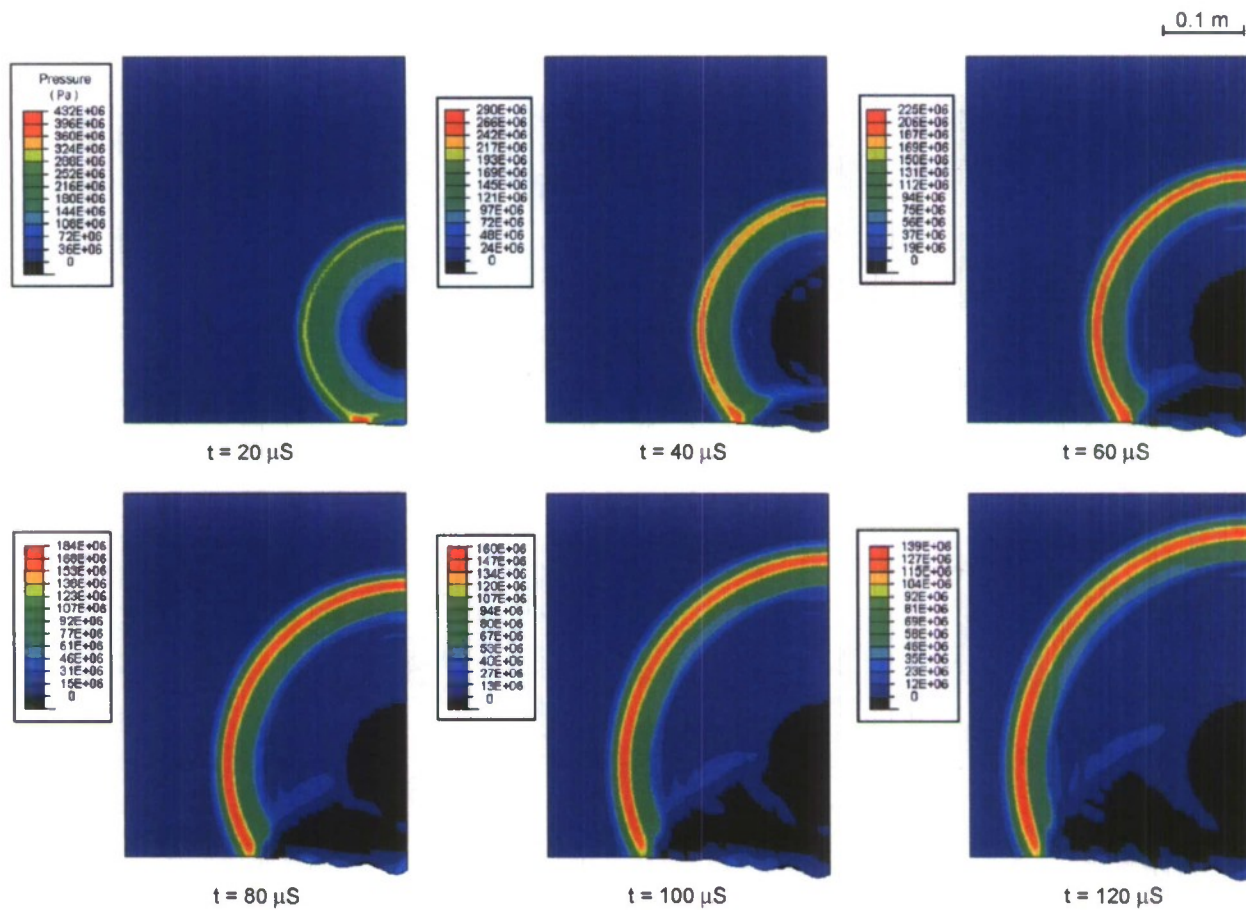
Fig. 13. The propagation sequence of the pressure wave in the water, indicating the reflected wave as well as the formation and expansion of the cavitated regions. The contours signify the pressure, with black being zero (the black domains contain the cavitated water). *Note*: The (blue) region of non-cavitated water attached to the front face has thickness, 15 mm.
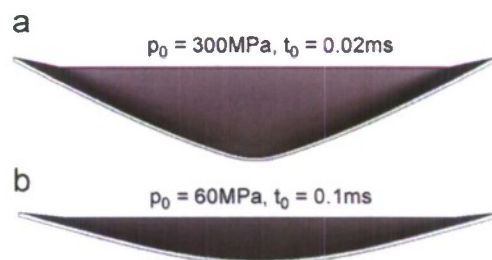

Fig. 14. Comparison of deformed shapes of the monolithic plate subject to two "equivalent" planar uniform water blasts: (a) $p_0 = 300$ MPa and $t_0 = 0.02$ ms and (b) $p_0 = 60$ MPa and $t_0 = 0.1$ ms.

with similar relative density (Xue and Hutchinson, 2004; Liang et al., 2007). (ii) Conversely, for localized impulsive source, the center of the panel deflects more than the solid plate.

6.3. Impulse and reaction force

The temporal variation of the reaction force at the peripheral support and the momentum transfer are plotted in Fig. 16. Note that the rate of change of momentum is nearly constant for the local source, resulting
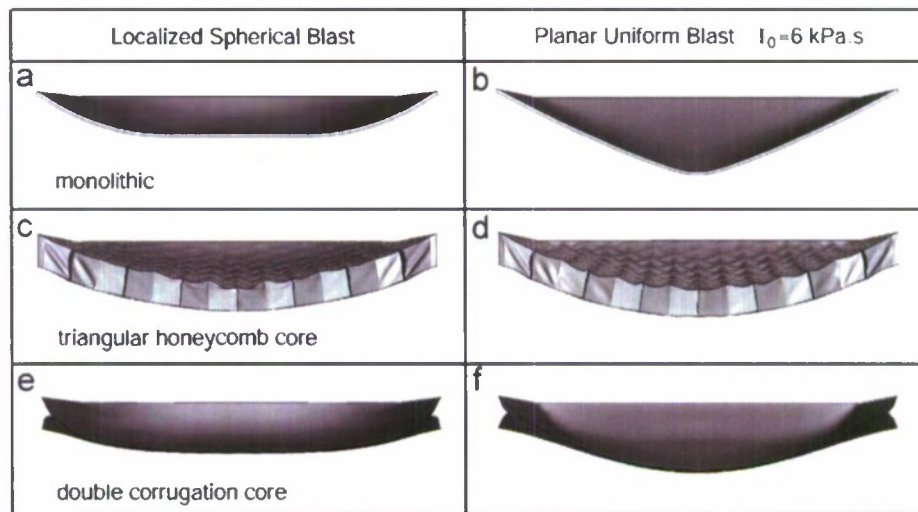
Fig. 15. Comparisons of deformed shapes of the monolithic plate, triangular honeycomb core and doubly-corrugated core sandwich panels subject to localized spherical and planar uniform water blasts.

in an essentially constant reaction force, spread over a relatively long time. This response differs from the plane wave situation wherein the reaction force exhibits a large initial peak with short duration (Liang et al., 2007). The following consequences ensue: (i) the flat response for the local source eliminates any benefit from the sandwich; and (ii) the local source generates relatively small transmitted force because the spreading of the impulse increases the duration of the response.

6.4. Plastic strains

The maximum equivalent plastic strains in the front and back faces are compared with that found in the solid plate for both localized spherical and planar uniform sources (Table 1). The maximum equivalent plastic strain in the front face is much larger than that in the monolithic plate, while the maximum equivalent plastic strain in the back face is nearly equal to that in the monolithic plate.

The implication of the foregoing set of results is that the significant benefits of the honeycomb core panel over a solid plate apparent for planar sources are completely eliminated for local impulses.

7. Designs that enhance performance

Given the disappointing performance of the strong honeycomb core, we have explored a soft core to assess whether panels with the appropriate core design can be an attractive option for resisting localized blast. The choice is the doubly-corrugated core with relative density, $\bar{\rho} = 2\%$ (Fig. 17). The overall sandwich panel dimensions are the same as for the honeycomb panel analyzed above with the core and face-sheet dimensions included in Fig. 17b. The results are superposed in Table 1 and Figs. 15 and 16. Note that the core indeed crushes at its center indicative of a soft response. The consequence is a back face deflection substantially smaller than the solid plate (Fig. 15). The initial reaction force is also lower but increases subsequently to a similar level (Fig. 16). This late stage elevation is attributed to slapping of the front face into the back face: a problem that can be eliminated by using either a slightly greater core thickness or larger relative density. The maximum equivalent plastic strain in the front face is much larger than that in the monolithic plate. However, the maximum equivalent plastic strain in the back face is much lower (Table 1).

Thus, we see that a suitably well-designed soft core sandwich panel can outperform an equal mass monolithic panel even under localized blast loading conditions. However, such soft-core panels suffer from the drawback that they undergo face sheet slap for high values of the blast impulse that significantly degrades their performance as discussed in previous studies (e.g. Hanssen et al., 2002; Nesterenko, 2003; Yen et al., 2005;
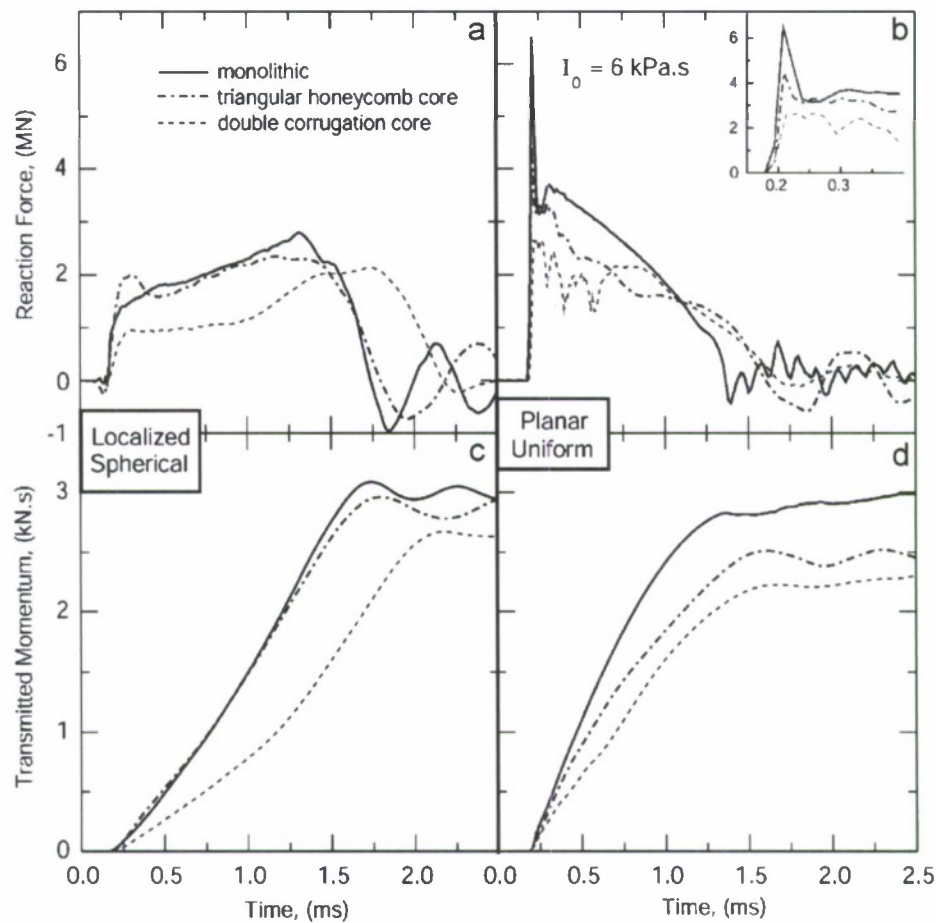
Fig. 16. Comparisons of reaction force and corresponding transmitted momentum of the monolithic plate, triangular honeycomb core and doubly-corrugated core sandwich panels subject to localized spherical and planar uniform water blasts.

Table 1

Maximum equivalent plastic strain in the monolithic plate as well as the front and back faces of the triangular honeycomb and doubly-corrugated core panels

	Localized spherical	Planar uniform, $I_0 = 6$ kPa s
Monolithic	0.37	0.29
Triangular honeycomb core		
Front face	0.80	0.56
Back face	0.40	0.30
Doubly-corrugated core		
Front face	0.89	0.77
Back face	0.16	0.17

Tilbrook et al., 2006) and thus are useful only over a limited range of blast impulses. Moreover, soft-core panels typically have a poor quasi-static indentation resistance and thus such panels may be unsuitable under normal service conditions. A combined quasi-static and dynamic optimization needs to be performed to design optimal cores over a wide range of loading scenarios.
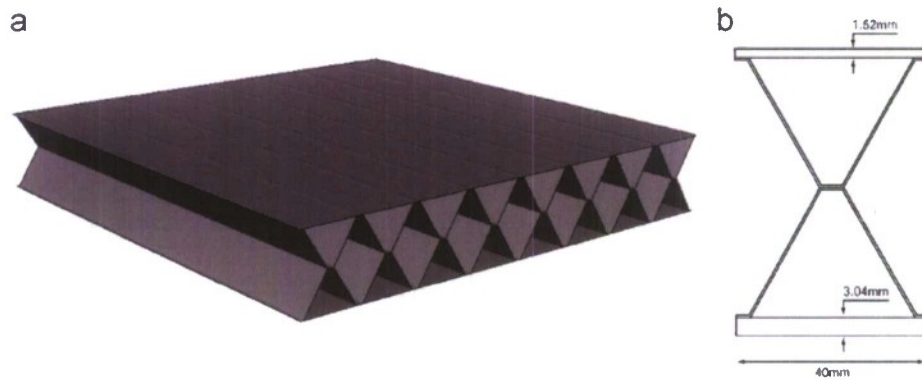
Fig. 17. Schematics of (a) the doubly-corrugated core sandwich panel and (b) its unit cell. The dimensions used in the simulation model are indicated.

It is worth emphasizing here that the conclusions of this study relate to a rather limited blast-loading scenario as marked by the solid circle in the blast nomograph in Fig. 6b. A larger set of experiments and simulations need be carried to scope out the nomograph in order to draw broader conclusions.

8. Concluding remarks

The resistance of metallic sandwich panels to localized spherical impulsive sources has been examined with the objective of devising and implementing a simulation capability amenable to the discovery of panel configurations that impart the best combination of performance metrics. The simulation protocol uses the output from a hydro-code characterization of the blast wave as input to ABAQUS/Explicit. Experiments on a triangular honeycomb core sandwich panel have been used to assess the fidelity. The accurate duplication of the deformations (both global and local) provides confidence in the approach. Thereafter, the code has been used to compare and contrast various features governing the response of panels to localized and planar impulses in water.

(i) The responses of monolithic plates subject to local and planar impulses have been compared and shown to be quite different. For the planar case, the plate assumes a conical shape with maximum deflection at the center. Conversely, the localized case results in a planar segment around the center.
(ii) For planar sources, the maximum deflections of both the (strong) triangular honeycomb and (soft) doubly-corrugated core panels are less than that for the solid plate having the same mass/area. The maximum reaction force at the supports is similarly reduced. The benefits of the sandwich designs are consistent with those demonstrated in previous studies (Xue and Hutchinson, 2004; Liang et al., 2007).
(iii) For localized sources, the situation differs. The deflection of the strong honeycomb core panel now exceeds that for the monolithic plate. However the soft doubly-corrugated core panel exhibits much smaller deflection. Thus, a dependence of the response on core softness again emerges, but the characteristics differ from those found for planar blast. Continuing assessments will pursue designs that provide the best performance subject to localized loading.
(iv) The reaction forces for local source case are not that sensitive to the design and thus appear to be a second order performance metric.

Appendix A. Material models for water and stainless steel

In the FE computations, the water is considered to be linear elastic under compression but has zero tensile strength and zero shear modulus (Liang et al., 2007). The pressure p in the water is then given by $p = -c_w^2 \rho_w \varepsilon_V$, where the sound speed in water $c_w = 1500 \, \text{ms}^{-1}$, the water density $\rho_w = 1000 \, \text{kg m}^{-3}$ and ε_V is the volumetric strain. When $\varepsilon_V \geqslant 0$, cavitation means that all stresses in the water become zero.

In the FE calculations, the monolithic plates and sandwich panels are assumed to be made from a von-Mises material with properties representative of stainless steel. Thus, the material is taken to have a relatively high strain hardening capacity and moderate strain rate dependence. The uniaxial tensile true stress versus strain ($\sigma - \varepsilon$) behavior is represented by the rate-dependent bilinear relation (Xue and Hutchinson, 2006):

$$\sigma = \begin{cases} E\varepsilon, & \varepsilon \leqslant \dfrac{k\sigma_Y}{E} \\ k\sigma_Y + E_t\left(\varepsilon - \dfrac{k\sigma_Y}{E}\right), & \varepsilon > \dfrac{k\sigma_Y}{E} \end{cases} \tag{A1}$$

Here E is the Young's modulus, E_t is the linear strain hardening rate and σ_Y is the quasi-static yield strength. Rate-dependence is tied to the plastic strain rate, $\dot{\varepsilon}_p \equiv \dot{\varepsilon} - \dot{\sigma}/E$, through the factor $k \equiv 1 + (\dot{\varepsilon}_p/\dot{\varepsilon}_0)^m$ which elevates the flow stress. Here $\dot{\varepsilon}_0$ and m are material parameters determined by experiment. The following choice of material parameters used in all the computations in this paper: $E = 200 \, \text{GPa}$, $\sigma_Y = 305 \, \text{MPa}$, $E_t = 1.9 \, \text{GPa}$, $\dot{\varepsilon}_0 = 4916 \, \text{s}^{-1}$, $m = 0.154$, density $\rho = 8000 \, \text{kg m}^{-3}$, and elastic Poisson's ratio $v = 0.3$.

References

ABAQUS Inc. 2006. ABAQUS Analysis User's Manual, Version 6.5.

Cole, R.H., 1948. Underwater Explosions. Princeton University Press.

Deshpande, V.S., Fleck, N.A., 2005. One-dimensional shock response of sandwich plates. J. Mech. Phys. Solids 53, 2347–2383.

Deshpande, V.S., Heaver, A., Fleck, N.A., 2006. An underwater shock simulator. Proc. R. Soc. A 462, 1021–1041.

Dharmasena, K.P., Queheillalt, D.T, Wadley, H.N.G., Chen, Y., Dudt, P., Knight, D., Wei, Z., Evans, A.G., 2007a. Dynamic response of a multilayer prismatic structure to impulsive loads incident from water. Int. J. Impact Eng. (in press).

Dharmasena, K.P., Queheillalt, D.T., Wadley, H.N.G., Dudt, P., Chen, Y., Knight, D., 2007b. The dynamic compressive response of periodic cellular metals subjected to underwater impulsive loading (in preparation).

Hanssen, A.G., Enstock, L., Langseth, M., 2002. Close-range blast loading of aluminum foam panels. Int. J. Impact Eng. 27, 593–618.

Hutchinson, J.W., Xue, Z., 2005. Metal sandwich plates optimized for pressure impulses. Int. J. Mech. Sci. 47, 545–569.

Liang, Y., Spuskanyuk, A.V., Flores, S.E., Hayhurst, D.R., Hutchinson, J.W., McMeeking, R.M., Evans, A.G., 2007. The response of metallic sandwich panels to water blast. J. Appl. Mech. 74, 81–99.

McShane, G.J., Radford, D.D., Deshpande, V.S., Fleck, N.A., 2007. The dynamic compressive response of square-honeycombs. J. Appl. Mech. 74, 658–667.

Nemat-Nasser, S., Guo, W.G., Kihl, D.P., 2001. Thermomechanical response of AL-6XN stainless steel over a wide range of strain rates and temperatures. J. Mech. Phys. Solids 49, 1823–1846.

Nesterenko, V.F., 2003. Shock (blast) mitigation by "soft" condensed matter. MRS Symp. Proc. 759, 4.3.1–4.3.12.

Swisdak, M.M., 1978. Explosion effects and properties: part II. Explosion effects in water. Naval Surface Warfare Center Report, NSWC/WOL TR 76-116.

Tilbrook, M.T., Deshpande, V.S., Fleck, N.A., 2006. The impulsive response of sandwich beams: analytical and numerical investigation of regimes of behavior. J. Mech. Phys. Solids 54, 2242–2280.

Wadley, H.N.G., Dharmasena, K.P., Chen, Y., Dudt, P., Knight, D., Charette, R., Kiddy, K., 2007. Compressive response of multilayered pyramidal lattices during underwater shock loading. Int. J. Impact Eng. (in press).

Wei, Z., Dharmasena, K.P., Wadley, H.N.G., Evans, A.G., 2007a. Analysis and interpretation of a test for characterizing the response of metallic sandwich panels to water blast. Int. J. Impact Eng. 34, 1602–1618.

Wei, Z., He, M.Y., Evans, A.G., 2007b. Application of a dynamic constitutive law to multilayer metallic sandwich panels subject to impulsive loads. J. Appl. Mech. 74, 636–644.

Xue, Z.Y., Hutchinson, J.W., 2004. A comparative study of impulse-resistant metal sandwich plates. Int. J. Impact Eng. 30, 1283–1305.

Xue, Z., Hutchinson, J.W., 2006. Crush dynamics of square honeycomb sandwich cores. Int. J. Num. Method Eng. 65, 2221–2245.

Yen, C.F., Skaggs, R., Cheeseman, B.A., 2005. Modeling of shock mitigation by sandwich structures for blast protection. In: Proceedings of the International Conference on Structural Stability and Dynamics, Kissimmee, Florida.

Appendix F

Dynamic Response of a Multilayer Prismatic Structure to Impulsive Loads Incident from Water

Kumar Dharmasena*, Doug Queheillalt and Haydn Wadley
Department of Materials Science
University of Virginia,
Charlottesville, Virginia 22904
Yungchia Chen, Philip Dudt and David Knight
Naval Surface Warfare Center,
Carderock, Maryland 20817
Zhensong Wei and Anthony Evans
Materials Department, University of California at Santa Barbara,
Santa Barbara, California 93106

Abstract

The dynamic crush response of a low relative density, multilayered corrugated core is investigated by combining insights from experiments and 3D finite element simulations. The test structures have been fabricated from 304 stainless steel corrugations with 0°/90° lay-up orientation and bonded by means of a transient liquid phase method. Characterization of the dynamic crushing of these structures has revealed that at low rates, interlayer interactions induce a buckling-dominated soft response. This softness is diminished at high rates by inertial stabilization and the response of the structure transitions to yield-dominated behavior. Unidirectional dynamic crushing experiments conducted using a dynamic test facility reveal a soft response, consistent with lower rate crushing mechanisms. The 3D simulation predictions of crushing strain, pulse amplitude/duration and impulse delivery rate correspond closely with the measurements. The application of core homogenization schemes has revealed that by calibrating with a multilayer unit cell, high fidelity continuum level predictions are possible. Moreover, even simplified hardening curves based on equivalent energy absorption provide remarkably accurate predictions of the crush strains and the impulse transmitted through the core. The multilayered structures investigated here significantly reduced the transmitted pressures of an impulsive load.

*Corresponding author
E-mail: kumar@virginia.edu

1. INTRODUCTION

Metallic sandwich panels with thin faces and low relative density cellular cores are being investigated for their resistance to high intensity, localized, impulsive loads impinging from water [1-8]. Recent assessments have indicated a major effect of the dynamic strength of the core upon the rate at which the impulse is transmitted through the panel core to the dry face: with consequent influence on the transmitted pressure [6,8]. Two observations now appear unequivocal: (i) Panels with strong cores subject to an incident impulse, I_0, cause complete reflection and acquire an impulse, $2I_0$ [8]. (ii) Reducing the core strength to a level that allows permanent crushing enables the transmitted impulse and pressure to be appreciably reduced [6,7]. For example, in a multilayered pyramidal lattice structure, the transmitted stress has been measured to be over an order of magnitude smaller than the pulse pressure in the water [6,7]. This was accomplished by an increase in the rise time of the transmitted impulse time history. While complete explanations are not yet forthcoming, assessments of the response of sandwich panels to impulsive loads have revealed that "soft core" designs exhibit performance superior to those with "strong cores" [5-10]. Multilayers offer the potential for successive layer-by-layer crushing tailored to satisfy the preferred level of softness [6,7].

The intent of the present article is to explore a new multilayer core with potential for an unprecedented softness. The core has a topology comprising several layers of orthogonally-oriented corrugations with thin intervening sheets, as depicted on Figure 1. The protocol used in a prior assessment of a multilayer pyramidal truss core is followed here [6,7]. Initially, the quasi-static response of the configuration is characterized using measurements and numerical simulations. Thereafter, dynamic characterization is conducted. This is achieved by combining experimental measurements of the crush response of the core to high intensity impulse loading in water by using a "Dynocrusher" test facility [6,8], Figure 2, with 3D numerical simulations performed using ABAQUS Explicit [11]. By fully-meshing the entire core, results are obtained that facilitate interpretation of the measurements. They also provide insight about the momentum transfer and the phenomena governing the pressure transmitted by the core during crushing.

A secondary objective of the study is an assessment of a continuum constitutive law (including the preferred meshing scheme) for the dynamic crush response of the core. Such a representation will be required for simulations of large structures and platforms. To ascertain their fidelity, the continuum predictions are compared with the measurements and 3D simulations. Relatively simple models are shown capable of remarkably accurate prediction of the impulsive load mitigation characteristics of the core topology.

2. FABRICATION

A plate folding method was used to fabricate the corrugated layers in the core structure shown in Figure 1. The individual corrugations were made by bending a 0.6mm

2

thick 304 stainless sheet to create a structure with a 90° corrugation angle and a fold period of 4.1cm. The ridges were coated with a brazing paste (Wall Colmonoy Nicrobraz 51 alloy) and stacked to form a $0^\circ/90^\circ$ laminate using 1 mm thick intervening sheets to form the multilayer core structure shown in Figure 1(a). Two, 4.8mm thick, 304 stainless steel face sheets were also placed on the top and bottom of the structure prior to vacuum brazing. The brazing process cycle included a step to volatilize the polymer components ($550^\circ C$ for 20 minutes), followed by brazing at $1050^\circ C$ for 60 minutes at a base pressure $\sim 10^{-4}$ Torr.

An electro-discharge machining method was used to cut 20 cm diameter, 9.5 cm high cylindrical test samples from the brazed structure. An example of one of the test structures is shown on Figure 1(b). The core thickness was 8.5 cm. The relative density of a single corrugation layer is:

$$\bar{\rho} = \frac{2t_w}{(l\sin 2\omega + 2t_w \cos\omega)} \tag{1}$$

where t_w is the corrugation web thickness, l the length of the corrugation and ω the angle between the corrugated web and the interlayer or face sheet. For the multilayer sample with interlayer sheets, thickness t_{il}, the relative density becomes:

$$\bar{\rho} = \frac{2(t_w + t_{il}Cos\omega)}{lSin2\omega + 2(t_w + t_{il})Cos\omega} \tag{2}$$

The measured relative density of the core (including the interlayer sheets) of the fabricated sample with a corrugation angle of 45° was, $\bar{\rho} = 8.4$ % of which ~50% was within the corrugated layers and the remaining ~50% in the interlayer sheets.

The tensile stress/strain response of 304 stainless steel in the brazed condition is essentially bi-linear up to a strain of about 20%, and adequately represented by:

$$\sigma = \begin{cases} E\varepsilon & \varepsilon \leq \dfrac{k\sigma_y}{E} \\[2ex] k\sigma_y + E_t\left(\varepsilon - \dfrac{k\sigma_y}{E}\right) & \varepsilon > \dfrac{k\sigma_y}{E} \end{cases} \tag{3}$$

with Young's modulus, $E = 203 GPa$, constant tangent modulus, $E_t = 2.4 GPa$, and yield strength $\sigma_y = 180 MPa$ [9,12-14]. The rate-dependence is tied to the plastic strain-rate, $\dot{\varepsilon}_p$, through the factor, k, elevating the flow stress: $k = 1 + (\dot{\varepsilon}_p / \dot{\varepsilon}_o)^m$, with the reference strain rate, $\dot{\varepsilon}_0 = 4920 s^{-1}$, and rate exponent, $m = 0.15$[15]. The material has density $\rho = 8 Mg / m^3$ and Poisson ratio, $v = 0.3$.

3

3. QUASI-STATIC COMPRESSION

3.1. Measurements

One of the test structures was loaded in uniaxial compression at an effective strain rate of $5 \times 10^{-4} s^{-1}$, Figure 3(a). The structure had a peak strength, $\sigma_{max} \approx 3.4$ MPa corresponding to a dimensionless strength, $\sigma_{max} / \sigma_y \bar{\rho} = 0.22$. This is appreciably lower than that expected for yielding for which, $\sigma_{max} / \sigma_y \bar{\rho} = 0.5$ [16]. Visual observations indicated that the peak strength coincides with the onset of elastic buckling of the uppermost layer. When the strain was sufficient to cause contact between the core members and the faces, hardening of the first layer occurred, followed by a second buckling event in an adjoining layer at the strain marked by the second arrow in Figure 3(a). The strains at the onset of buckling in the two other layers are also indicated by arrows. In each case, buckling was preceded by a small stress peak. The average flow stress during large-scale compression was $\sigma_{pl} \approx 2 MPa$. At a strain approaching 65%, the onset of densification of the fourth layer caused rapid hardening. An image taken just after the fourth buckling event, Figure 3(b), indicates the deformation patterns. The bottom layer reveals the deformation soon after the onset of buckling. The second layer illustrates contact between the interlayer and the plastically deformed core members.

3.2. Finite Element Simulations

The test was analyzed using ABAQUS/Explicit Version 6.5 [11]. Due to the symmetry, only one-quarter of the structure was modeled, Figure 4(a). Symmetry boundary conditions were applied to the nodes on the x-z plane (at y = 0) and on the y-z plane (at x = 0). Shell elements with reduced integration (S4R) were used to increase the computational efficiency. A constant velocity of 1 mm/s was applied in the downward z-direction to the top of the exterior plate (selected based on an eigen-value analysis to ensure a quasi-static response). The mesh, Figure 4(a) was constructed based on a previous study of corrugated structures [17]. The general contact algorithm in ABAQUS/Explicit was used to model contact between the interlayer sheets and the core members as the structure crushes. The sample at 35% strain, Figure 4(c), reveals a deformation pattern similar to that observed within the test, Figure 3(b).

The stress/strain curve, when superimposed on the measurements, Figure 3(a), indicates that the calculated and measured levels of the initial stress peak coincide closely. The ensuing response is also similar: albeit with differences in detail. The deformation pattern corresponding to the initial stress peak indicates that hard points at intersections of the under and overlying layers nucleate elastic buckling, Figure 4(b), before yielding. This affirms that the stress peak coincides with the elastic buckling of the first layer. To further confirm the role of the intersections, another simulation was performed with much thicker interlayer sheets. In this case, the stress peak is much larger and coincident with that expected for yielding. In summary, the strong interlayer interaction caused by thin interlayer sheets and 90^0 layer-by-layer rotation, has a major

4

influence on the performance of this core. Consequently, under these conditions, the core is softer than many other multilayer counterparts [6].

4. DYNAMIC MEASUREMENTS

4.1. Test Method. An underwater explosive test method schematically illustrated in Figure 2 was used to investigate the dynamic crushing. A detailed description of the measurement is provided elsewhere [6,8]. The test specimens were fitted into a thick, high strength steel cover plate with a central opening and positioned on four 3.8 cm diameter, 12 cm long HY-100 steel columns. Strain gauges were attached to each column to enable their averaged output to be converted into a measure of the pressure transmitted to the back face. A 0.9m diameter cardboard cylinder was placed above the specimen and filled with water. A 200 x 200 x 1 mm thick explosive sheet was positioned at a distance of either 25.4 or 10 cm from the top surface of the test sample. The explosive sheet was center detonated and the back face pressure recorded as a function of time after detonation. The long and short stand-off tests are henceforth referred to as the low and high impulse cases, respectively.

4.2. Calibration Tests. The test system was calibrated by replacing the sandwich panels with a solid aluminum cylinder having identical outer dimensions and measuring its dynamic response, Figure 5. The stress-strain response of the HY-100 steel columns on to which the strain gages were mounted (Figure 2) was initially obtained under quasi-static loading conditions. For HY-100 which has low strain rate sensitive hardening behavior, the initial quasi-static test provides an acceptable strain – load calibration correlation to be used for the dynamic loading of the columns when the test panels are impulsively loaded. The strain gage measurements with the solid cylinder were performed at two standoff distances, 25.4 cm and 10 cm and were found to be repeatable and consistent for each of the four load columns. As observed in Figure 5, the 0.25m standoff test (low impulse load) resulted in a back face pressure peak of 28MPa, while the high impulse load corresponding to the closer standoff of 0.1m, resulted in a measurement 52MPa. In both cases, the pulse width was about 0.3 ms. The transmitted impulses corresponding to the long and short standoff cases were 5 and 11.8kPa.s, respectively. The oscillatory behavior exhibited by the wave-forms is caused by elastic reverberations within the test system, Appendix I.

4.3. Dynamic Crush Response. The back-side pressure waveforms for the multilayers are plotted in Figure 6. The peak pressures are much lower than those obtained with the calibration block. They decreased by about a factor of ~6: from 28 to 5MPa for the low impulse, Figure 6(a), and from 52 to 8MPa at high impulse, Figure 6(b). The impulses increased to their plateau levels in about 2ms, Figures 6(c) and (d), compared to ~0.3 ms for the solid samples. The average pressures acting on the back face, estimated by dividing the impulse by the rise time, were 4.0 and 2.3MPa respectively. The corresponding crush strains were ~25% and ~65%.

5. DYNAMIC FINITE ELEMENT SIMULATIONS

5.1. Methodology

To simulate the dynamic tests, a water column, a quarter of the specimen tray and one gage column were incorporated into an all-shell model, Figure 7. The representation used for the water has been described elsewhere [4]. The solid components used 8-node solid elements with reduced integration (C3D8R) [11]. The finite element mesh (not depicted in Figure 7 for clarity) was constructed based on a previous study of corrugated structures [4]. Frictionless general contact was implemented throughout with the specimen tray and gage column "tied" together. A spring and a dashpot were introduced beneath the column to address the elasticity and energy absorption of the base. The coefficients of the dashpot and spring were calibrated using the reference test [6, 8]. For simulation purposes, the impulse was regarded as planar with a time dependence given by $p(t) = p_0 \exp(-t/t_0)$ [7]. The incident peak pressures, p_0, were 110 and 260MPa for the low and high impulse cases, with the pulse decay time $t_0 = 0.02\,ms$ in both cases. These pressures have been ascertained using hydrocode simulations and pressure gauge measurements [6, 8].

5.2. Dynamic Core Strength

Unit cell calculations have been used to estimate the dynamic strength of the core. These calculations were performed with shell elements used to model the core members and interlayer sheets, and mass-less rigid elements adopted for the top and bottom faces to capture the face/core contact without introducing extra inertia. Equal and opposite uniform velocities were applied to the top and bottom faces. In this situation, the center of mass of the core is stationary, minimizing the inertia of the core members and interlayer sheets. The stress/strain curve of the corrugated multilayer structure, Figure 8(b), at a strain rate of 1000 /s (for the high impulse), exhibits features equivalent to those analyzed previously for I-cores [18], Figure 8(a). Beyond a strain-rate of about 200 /s, the curves exhibit two levels of dynamic strength. The initial strength is large. It exceeds that in quasi-static compression because of inertial stabilization against buckling [18,19]. This dynamic peak strength is given by: $\sigma_{YD}^c / \sigma_Y \bar{\rho} \approx 0.5$, where σ_Y is the dynamic yield strength at an effective strain-rate, $\dot{\varepsilon}'_{eff} = v/h_c$ (where v is the initial face velocity and h_c the height of one corrugation layer). Beyond a time, $t_{pulse} = h_c/c_{pl}$ (where c_{pl} is the plastic wave velocity in the core members), the strength drops to a much lower, steady-state level. This level is also rate-dependent and is given by:

$$\frac{\sigma_{ss}}{\bar{\rho}\sigma_y} \approx 0.2 + 0.005\sqrt{\frac{\dot{\varepsilon}_{eff}}{\dot{\varepsilon}_u}} \tag{4}$$

where σ_y is the quasi-static yield strength, $\dot{\varepsilon}_u = 1$ s^{-1}, and $\dot{\varepsilon}_{eff} = v/H_c$ is the overall effective stain rate (where H_c is the total core height). These dynamic strength characteristics will be used later to interpret the transmitted pressure as well as the rate of change of transmitted impulse.

The dynamic strength at higher rates, being yield-controlled, is essentially the same as that found for other cores at equivalent relative density. Namely, the high rate response of the corrugated multilayer core is indistinguishable from other cores.

5.3. Dynocrusher Simulations

The deformed structures obtained by simulating the Dynocrusher tests are compared with images of the tested panels in Figure 9. The predicted deformation patterns are consistent with the experiments. The predicted crushing strains (25% and 65% for the lower and higher impulses) are also in excellent agreement with measured values. The calculated values of the transmitted momentum, Figures 6(c) and 6(d) are almost the same as those found experimentally, for both high and low impulse, at times up to about 1.5ms after the impulse arrives. Thereafter, the measured impulse continues to increase by about 15%, whereas the calculated values remain invariant, Figures 6(c),(d). This discrepancy is consistent with that found in a previous study of multilayer pyramidal cores [6, 8] and relates to extra momentum contained in the water column not duplicated in the simulations. The additional momentum is attributed to a second pressure peak when the cavitated water coalesces. The calculated values of the transmitted pressures are presented as the average within the column cross-section at the vertical location of the strain gauges. The ensuing pressure/time curves (Figure 6(a), (b)) are in broad agreement with the measurements, but the stress oscillations differ. Oscillations similar to those found experimentally emerge when the stresses are ascertained at the column surface, where the gauges are located (Appendix 1), and consistent with a simple mass/spring model. The absence of oscillations in tests conducted on the higher strength cores is attributed to the shorter duration of the transmitted pressure, which is on the same order as the oscillation period.

6. CONSTITUTIVE LAW AND CALIBRATION SCHEMES

While several constitutive laws have been developed for the homogenization of sandwich structures [20-26], none provides an approach for multilayer sandwich structures with strong interlayer interaction. Because of the unknown importance of this interaction, three calibration schemes are assessed, Figure 10. In Scheme 1, a single element is used through the entire core, Figure 10(a); for scheme II, multiple elements are inserted through the core, Figure 10(b). In these two schemes, calibration is based upon the multilayer unit cell so that interlayer interactions are implicitly included. In Scheme III a single element within each layer is used, but it is calibrated by calculations conducted for a uni-layer unit cell, Figure 10(c). The interlayer sheets are explicitly modeled in this scheme. The velocities and transmitted pressure wave forms calculated using the three continuum models are compared in Figures 11 and 12 with the full 3-D simulations

Low Impulse. Comparisons of the three schemes, Figures 11 and 12, indicate that I and II provide more consistent results than III. Moreover, II provides the best correlations with the velocity, Figure 11, and pressure, Figure 12 peaks. It is concluded

7

that to adequately capture the interlayer interaction, multilayer unit cells should be used for calibration (scheme II).

High Impulse. At the high impulse, scheme II is still the best, but the other two are almost as good because dynamic effects suppress the interlayer interaction. In summary, for multilayer panels with strong interlayer interaction, the fidelity of the continuum calculations is enhanced by calibrating using multilayer unit cells.

Provided that the most appropriate calibration has been chosen, the good comparison between the continuum results and the fully-meshed calculations provides a high level of confidence in the application of the continuum methodology when large scale calculations are envisaged. The merits of a simplified version of the constitutive law are examined in Appendix II. This version has wider applicability to alternative, commercial dynamic codes, such as LS-DYNA [27].

7. DISCUSSION

The results obtained in the Dynocrusher tests and the associated simulations are most relevant to the response of a sandwich structure in the vicinity of the stationary supports. In particular, the rate of change of the transmitted momentum, $\dot{\beta}$, correlates directly with the reaction forces imparted to the supports [4, 5, 10]. The transmitted pressures also provide a measure of the dynamic strength of the core, which, in turn, governs the acceleration of the back face of a sandwich panel suspended between rigid supports. Normalizing these quantities with the pressure in the incident impulse, p_0, provides a basis for comparison with fundamental models. To construct comparisons, a dynamic core strength must be chosen. The steady-state strength, σ_{ss} as defined by equation (4) has been chosen.

This can be rationalized by invoking an analytic expression for the rate at which the impulse is transmitted to the back face [5, 10]. Because the duration of the initially large push back stress is so small, $t_{pulse} \approx 0.2ms$, Figure 8, its influence on the impulse rate is insignificant. Namely, the impulse is dominated by the lower, steady-state, crushing stress and given by [5]:

$$\dot{I}_{tot} \approx \sigma_{ss} \tag{5}$$

with σ_{ss} given by (4) with $\dot{\varepsilon}_{eff} = \hat{v}_{wet}/H_c$, where $\hat{v}_{wet}$ the peak wet face velocity. The influence of the incident impulse is manifest in this velocity, as ascertained from the response of the wet face at the instant the water cavitates [4, 10]. It is given by:

$$\hat{v}_{wet} = \frac{2p_0}{\rho_w c_w} \beta^{\frac{1}{1-\beta}}, \tag{6}$$

where β is the fluid-structure interaction parameter, $\beta = \rho_w c_w t_0 / m_{wet}$ in which ρ_w and c_w are the density of the water and its sound speed, respectively and m_{wet} is the mass per unit area of the face. Combining (4), (5) and (6) gives:

8

$$\dot{I}_{tot} \approx \sigma_y \overline{\rho} \left[0.2 + 0.005 \left(\frac{2p_0}{\rho_w c_w H_c \dot{\varepsilon}_u} \beta^{\frac{1}{1-\beta}} \right)^{1/2} \right] \tag{7}$$

Recall that σ_y is the quasi-static yield strength of the material used in the core and $\dot{\varepsilon}_u = 1/s$. The total transmitted impulse is [10]:

$$I_{tot} \approx m_{wet}\hat{v}_{wet} + \rho_w \int_{-H_w}^{0} v_r(z)dz \tag{8}$$

where H_w is the height of water column, and v_r the residual velocity of the cavitated water [10]:

$$v_r(z) = \frac{2p_0}{\rho_w c_w} \left\{ \frac{1}{2\beta} \left[(1-\beta)e^{\frac{2\beta z}{c_w t_0}} + (1+\beta)e^{\frac{2(\beta-1)z}{c_w t_0}} \right] \right\}^{\frac{1}{\beta-1}} \tag{9}$$

The analytic estimates of transmitted impulse and its rate, calculated from the above equations, are superposed on Figures 6(c) and (d). Evidently, there is reasonable consistency of the analytic estimates with the experiments and the 3D simulations.

This calculation approach for the transmitted impulse and rate can be extended to a multilayer pyramidal core topology [6,7] and a square honeycomb core topology [8] using the following steps. The measurements of the impulse rate for each core (multilayer triangular corrugation, multilayer pyramidal and square honeycomb) are used to obtain β (e.g. Figure 6 for the triangular corrugation core). The intent is to cross plot β against the steady-state crush stress, σ_{ss}. Because of the ringing effects in the support columns described in Appendix I, the measured pressures do not give σ_{ss} values with sufficient fidelity. Consequently the unit cell simulations are used, with the results for σ_{ss} expressed in the form of equation (4) and its analog for the other cores (Appendix III). The results of β vs. σ_{ss} are plotted on Figure 13 for the multilayer triangular corrugated, multilayer pyramidal, and square honeycomb topologies. It is apparent that the approach provides a meaningful correlation between the impulse delivered and the core strength properties. Moreover the slope of the best fit line is unity as expected from (5). Such a correlation could be used for the preliminary design of other cores.

8. CONCLUSIONS

The performance of multilayer corrugated cores subject to impulsive load has been investigated by a combination of quasi-static and dynamic experiments, as well as fully-meshed and continuum simulations. When the cores contain thin interlayer sheets and 90^0 layer-by-layer rotations, strong interlayer interaction effects have been identified at low rates. This interaction causes the response to be buckling-dominated, rendering these cores softer than all others previously examined. These interactions become

9

relatively insignificant at high-rates, because inertial stabilization causes the response to become yield (rather than buckling)-controlled. At these rates, the dynamic strength is essentially the same as all other cores, at equivalent relative density.

The pressures transmitted through the multilayer corrugated core subject to impulsive loads are slightly lower than those measured for multilayer truss cores at comparable relative density [6]. The rate at which the impulse is transmitted from the water to the back face is also smaller. Namely, at the strain-rates induced by the impulse, these cores respond in a relatively soft manner.

The pressure profiles and crushing strains obtained by 3D simulation correlate closely with those determined by experiment. The stress oscillations correlate when the stresses are calculated at the surfaces of the columns.

Core homogenization schemes have been investigated. The assessment has revealed that by calibrating with a multilayer unit cell, high fidelity continuum level predictions are possible. Moreover, even simplified hardening curves based on equivalent energy absorption provide remarkably accurate predictions. Consequently, these schemes have potential for generating accurate predictions within large-scale simulations.

Finally, a correlation has been found between the transmitted impulse rate and the dynamic strength. The correlation has been extended to several core topologies previously tested in the "dynocrusher" facility.

Appendix I: Reverberations in the Supporting Columns

The objective is to elaborate on the strains at the surface-mounted gauges. An example of the distribution of stress calculated at one of the gauge locations is presented on Figure A1. Evidently, the stresses vary substantially with location, varying from one side to the other, indicative of flexural waves. Plots of the temporal dependence of the stress at one location around the surface [marked as (a) on Figure A1] indicate the stress oscillations associated with these waves (Figure A2). Moreover, superposing onto the measurements indicates close correspondence. To characterize the oscillations, a simple mass-spring model is invoked. The free oscillation period of the system is

$$T = 2\pi\sqrt{m/k}, \tag{A1}$$

where m and k are the mass and stiffness respectively. The mass includes that of the sample m_s, the specimen tray m_t and the four gage columns m_g,

$$m = m_s + m_t + m_g, \tag{A2}$$

while the stiffness comprises the base structure k_2 in series with the four gage columns k_1,

$$k = \frac{k_1 k_2}{k_1 + k_2}, \tag{A3}$$

Here, $k_1 = 4EA/L$, where E is the Young's Modulus of the material, with A and L the cross-section area and length of a gage column, respectively. The stiffness of the base

10

structure was obtained by a calibration conducted using the reference test [7]. These equations predict an oscillation period, 0.74ms, almost the same as the measured peak separation, 0.75ms.

Appendix II: Simplified Continuum Representation

While the detailed hardening and softening features of the stress/strain curves obtained from unit cell calculations can be input to foregoing continuum models, it is often inconvenient. Moreover, for some codes, such as LS-DYNA, it is not possible, because the hardening curves at different strain rates must be self-similar [27]. Thus, the possibility of using simplified hardening curves is examined (Figure B1), using elastic/perfectly-plastic representations, constructed by enforcing equivalent plastic dissipation. For example, on Figure B1a, the constant stress in the simplified curve is based on the average for the detailed curve prior to densification. Using these simplified curves (Figure B1b), the scheme II continuum simulations were repeated. The results are summarized on Figure B2. The comparisons reveal that the face velocities are slightly higher (Figure B2e,f), causing somewhat larger core crushing strains (Figure B2a,b), with corresponding reductions in the pulse durations. Oscillations in the transmitted pressure and the initial peaks are no longer reproduced (Figure B2c,d). Nevertheless, the simplified approach appears to work remarkably well, and can be more conveniently used.

Appendix III: Dynamic core strength calculation

For the triangular corrugation core topology structure, the dynamic core strength is calculated using equation (4) in Section 5.2. In Figure 13, the strength for the pyramidal core structure is calculated from [7],

$$\frac{\sigma_{ss}}{\bar{\rho}\,\sigma_y} \approx 0.035\sqrt{\frac{\dot{\varepsilon}_{eff}h_c}{\dot{\varepsilon}_u h_0}} \tag{A4}$$

with $h_0 = 0.1m$. For the square honeycomb structure, the strength is calculated from [23],

$$\frac{\sigma_{ss}}{\bar{\rho}\,\sigma_y} \approx 1 \tag{A5}$$

Acknowledgements

References

[1]. Hutchinson JW, Xue Z. Metal sandwich plates optimized for pressure impulses. Int. J. Mechanical Sciences 2005; 47: pp. 545-569.

[2]. Deshpande VS, Fleck NA. One-dimensional shock response of sandwich plates. Journal of Mechanics and Physics of Solids 2005;53: pp. 2347-2383.

[3]. Deshpande VS, Heaver A, Fleck NA. An underwater shock simulator, Proc. Royal Society A, 2006; 462: pp. 1021-1041.

[4]. Liang Y, Spuskanyuk AV, Flores SE, Hayhurst DR, Hutchinson JW, McMeeking, RM, Evans AG. The response of metallic sandwich panels to water blast. J. Appl. Mech. 2007; 74 : pp.81-99.

[5] Tilbrook MT, Deshpande VS, Fleck NA. The impulsive response of sandwich beams: Analytical and numerical investigation of regimes of behaviour. Journal of the Mechanics and Physics of Solids, 2006; 54: pp. 2242-2280.

[6] Wadley HNG, Dharmasena KP, Chen Y, Dudt P, Knight D, Charette R, Kiddy K. Compressive response of multilayered pyramidal lattices during underwater shock loading. Int. J. Impact Engng. 2008; 35: pp. 1102-1114.

[7] Wei Z, Dharmasena KP, Wadley HNG. and Evans AG Analysis and interpretation of a test for characterizing the response of sandwich panels to water blast. Int. J. Impact Engng. 2007; 34: pp. 1602-1618.

[8] Wadley HNG, Dharmasena KP, Queheillalt DT, Chen Y, Dudt P, Knight D, Kiddy, K, Xue Z, Vaziri A. Dynamic Compression of Square Honeycomb Structures during Underwater Impulsive Loading, Journal of Mechanics of Materials and Structures, 2007; 2(10):pp. 2025-2048.

[9] Rathbun HJ, Radford DD, Xue Z, He MY, Yang J, Deshpande V, Fleck NA, Hutchinson JW, Zok FW, Evans AG. Performance of metallic honeycomb-core sandwich beams under shock loading. Int. J. Solids Struct. 2006; 43: pp. 1746-1763.

[10] McMeeking RM, Spuskanyuk AV, He MY, Deshpande VS, Fleck NA, Evans, AG. An analytic model for the response to water blast of unsupported metallic sandwich panels, Int. J. Solids and Structures, 2008; 45: pp. 478-496.

[11] ABAQUS Analysis User's Manual, Version 6.5. ABAQUS, Inc., 2005.

[12] Zok FW, Waltner SA, Wei Z, Rathbun HJ, McMeeking RM, Evans AG. A protocol for characterizing the structural performance of metallic sandwich panels: application to pyramidal truss cores. Int. J. Solids Struct. 2004; 41(22-23): 6249-6271.

[13] Zok FW, Rathbun HJ, He MY, Ferri E, Mercer C, McMeeking RM, Evans AG. Structural performance of metallic sandwich panels with square honeycomb cores. Philosophical Magazine, 2005; 85: 3207-3234.

[14] Mori L.F, Lee S, Xue Z, Vaziri A, Queheillalt DT, Dharmasena KP, Wadley HNG, Hutchinson JW, Espinosa HD. Deformation and Fracture Modes of Sandwich Structures subjected to Underwater Impulsive Loads. Journal of Mechanics of Materials and Structures 2007; 2(10); pp.1981-2006.

[15] Dharmasena KP, Wadley HNG, Xue Z, Hutchinson JW. Mechanical Response of Metallic Honeycomb Sandwich Panel Structures to High Intensity Dynamic

Loading, *International Journal of Impact Engineering*, 2008; 35: pp. 1063-1074.

[16] Rathbun HJ, Zok FW, Evans AG. Strength optimization of metallic sandwich panels subject to bending, *International Journal of Solids and Structures*, 2005; 42: 6643-6661.

[17] Valdevit L, Wei Z, Mercer C, Zok FW, Evans AG. Structural Performance of Near-Optimal Sandwich Panels with Corrugated Cores, *International Journal of Solids and Structures*, 2005; 43: 4888-4905.

[18] Ferri E, Antinucci E, He MY, Hutchinson JW, Zok FW, Evans AG. Dynamic Buckling of impulsively loaded prismatic cores. Journal of Mechanics of Materials and Structures, 2006; 1(8): pp. 1345-1366.

[19] Vaughn DG, Canning JM, Hutchinson JW. Coupled plastic wave propagation and column buckling. J. Appl. Mech. 2005; 72: 139-146.

[20] Desphande VS, Fleck NA, Ashby MF. Isotropic constitutive models for metallic foams. J. Mech. Phys. Solids. 2000; 48:1253-1283.

[21] Mohr D, Doyoyo M. Large plastic deformation of metallic honeycomb: orthotropic rate-independent constitutive model. Int. J. Solids Struct. 2004; 41:4435-4456.

[22] Rabczuk T, Kim JK, Samaniego E, Belytschko T. Homogenization of sandwich structures. Int. J. Numer. Meth. Engng. 2004; 61:1009-1027.

[23] Xue Z, Hutchinson JW. Crush dynamics of square honeycomb sandwich cores. Int. J. Numer. Meth. Engng. 2006; 65:2221-2245.

[24] Xue Z, Vaziri A, Hutchinson JW. Non-uniform hardening constitutive model for compressible orthotropic materials with application to sandwich plate cores. Comp. Modeling in Engng. & Sci. 2005; 10:79-95.

[25] Xue Z, Hutchinson JW. Constitutive model for quasi-static deformation of metallic sandwich cores. Int. J. Numer. Meth. Engng. 2004; 61:2205-2238.

[26] Wei Z, He MY, Evans AG. Application of a dynamic constitutive law to multilayer metallic sandwich panels subject to impulsive loads. J. Appl. Mech. 2006; 74:636-644.

[27] Livermore Software Technology Corporation (1998): LS-DYNA theoretical manual.
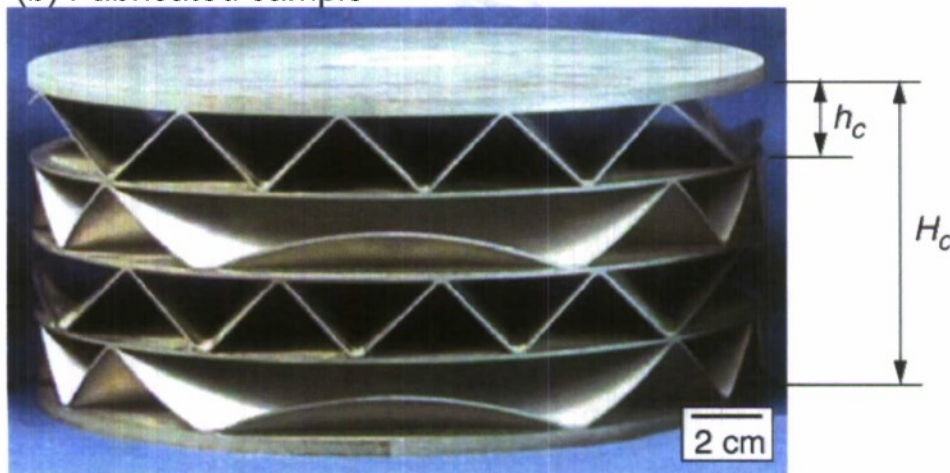
FIGURE CAPTIONS

Figure 1. (a) Topology of a multi-layer corrugated core. (b) An optical image of stainless steel test specimen.

Figure 2. Schematic representation of "dynocrusher" test. The strain measured on the gauge columns was converted to stress using data collected during quasi-static compression of the columns.
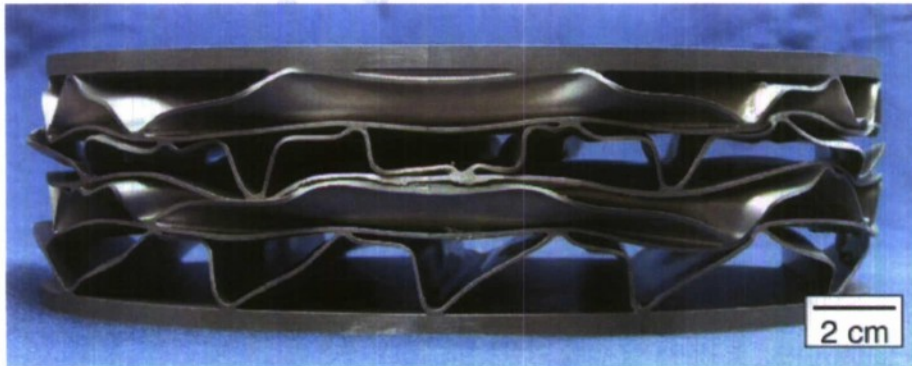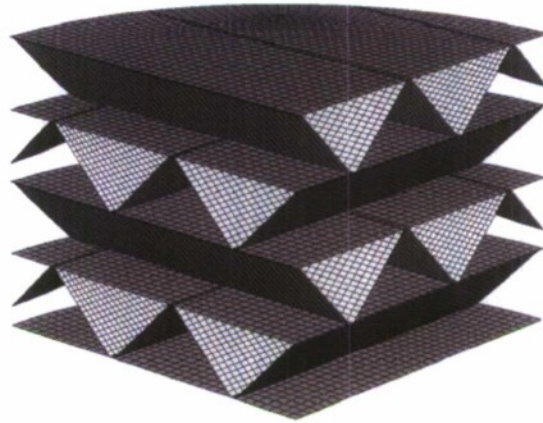
Figure 3. (a) Quasi-static compressive stress/strain response. (b) Deformed shape at 35% strain.

Figure 4(a). The 3-D finite element model used for the simulations (quarter based on symmetry). (b) Premature localized buckling shown on the deformed panel corresponding to the peak stress in Figure 3a. (c) Deformed shape at 35% strain as a comparison with figure 3b.

Figure 5(a),(b) Transmitted pressure and (c),(d) impulse responses of the reference solid cylinder for low and high impulse loading respectively.
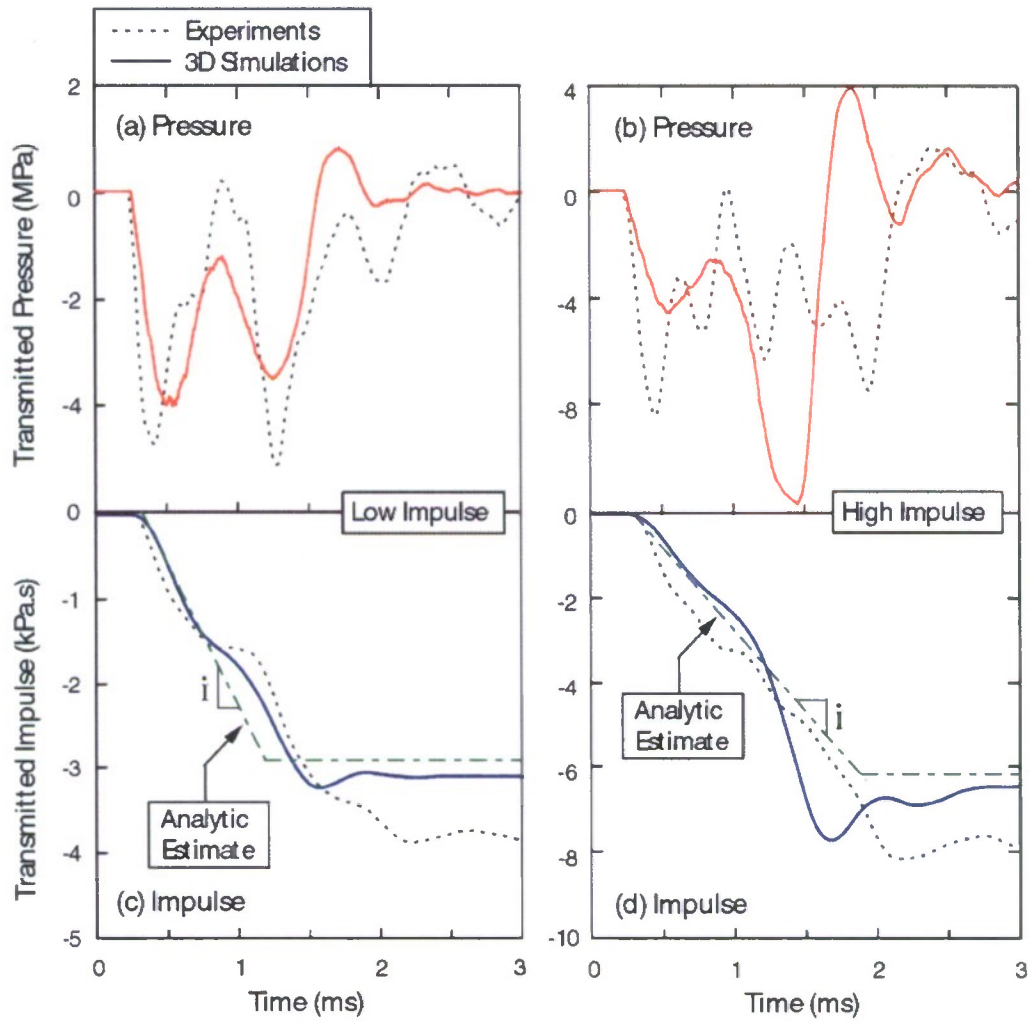
Figure 6. A comparison between measurements and simulations of the transmitted pressure and impulse for the multilayer corrugated core at the two impulse levels. Also shown are the analytic estimates of the transmitted impulse.
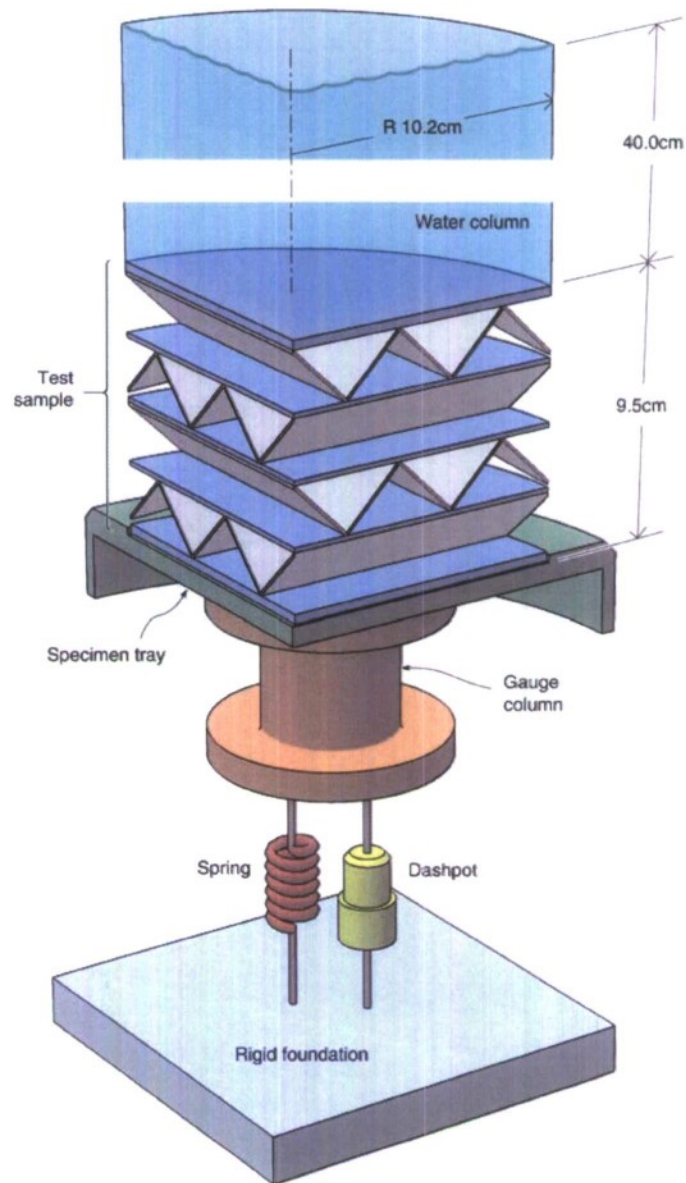
Figure 7. The 3-D finite element model of the Dynocrusher test, including a water column, support gage column, and spring-dashpot to represent the response of the base.
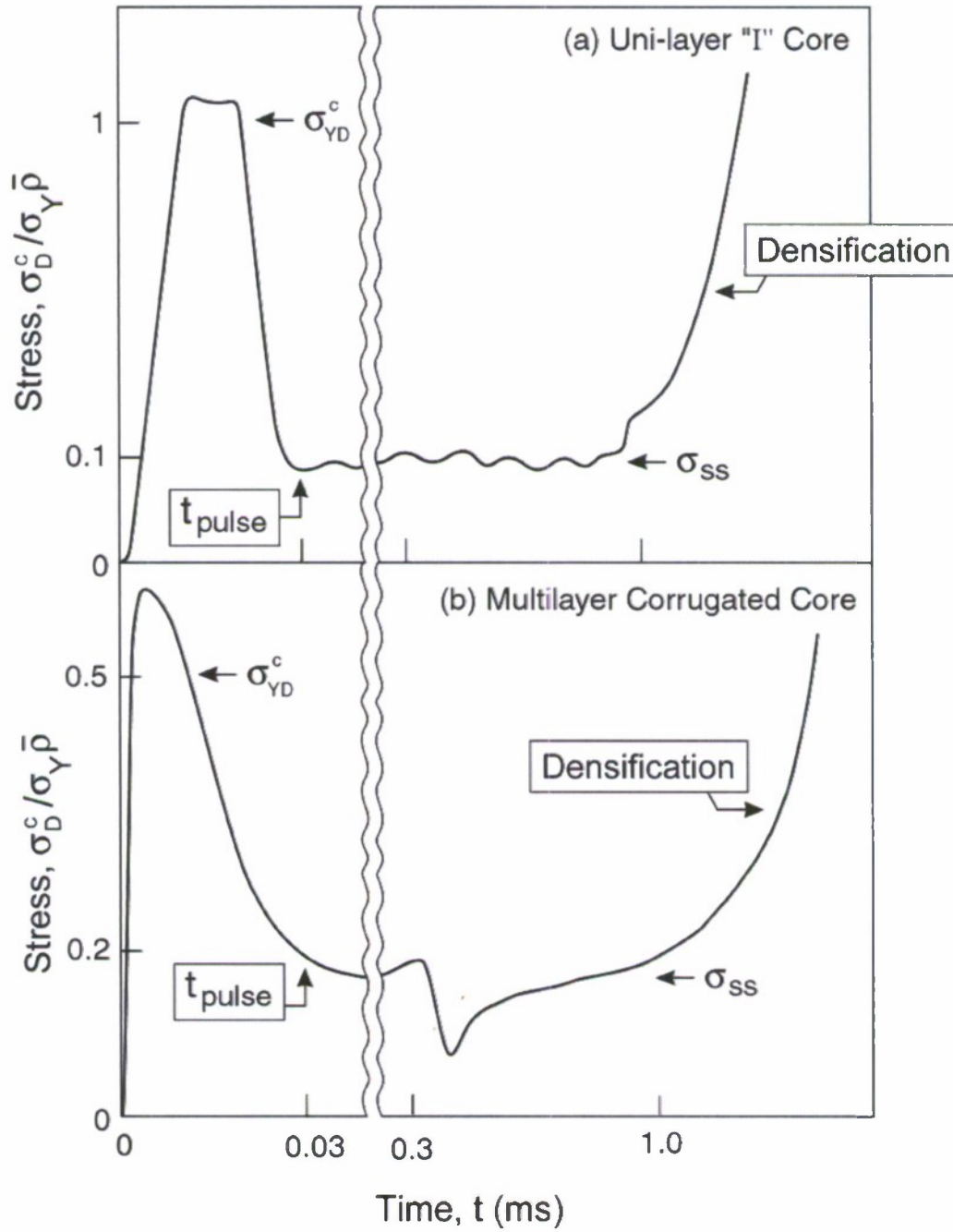
Figure 8. Time varying stress response of (a) a single layer I-core (b) a multilayer corrugated core.
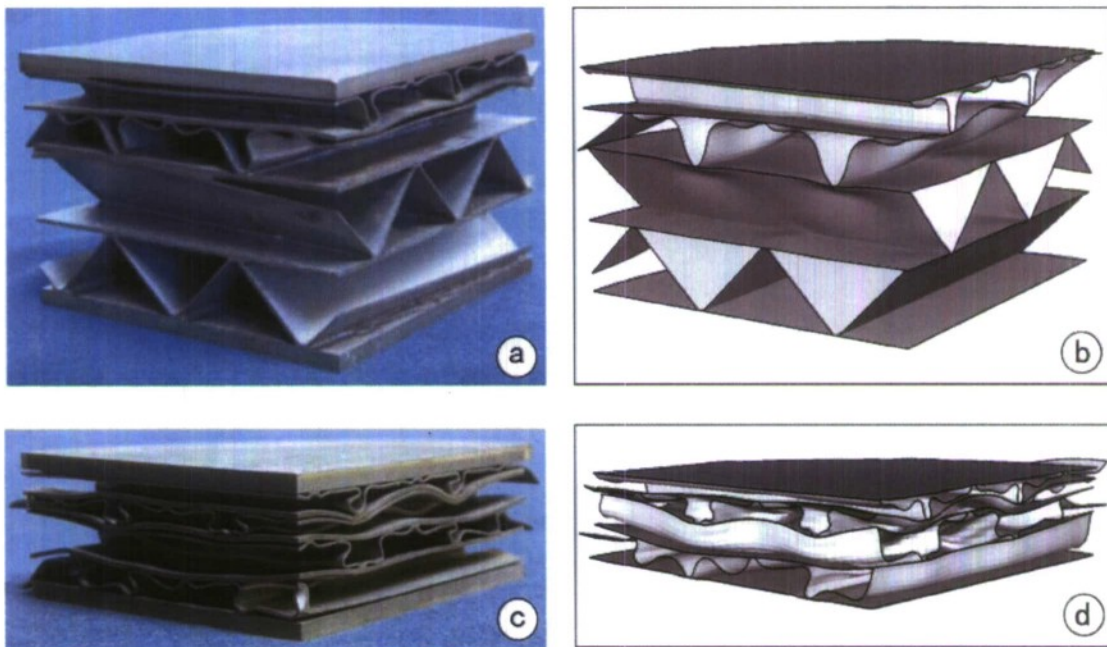
Figure 9. (a) Sandwich panel after the low impulse test. (b) Predicted deformation following the low impulse exposure. (c) Sandwich panel tested at the high impulse. (d) Predicted deformation after the high impulse exposure.
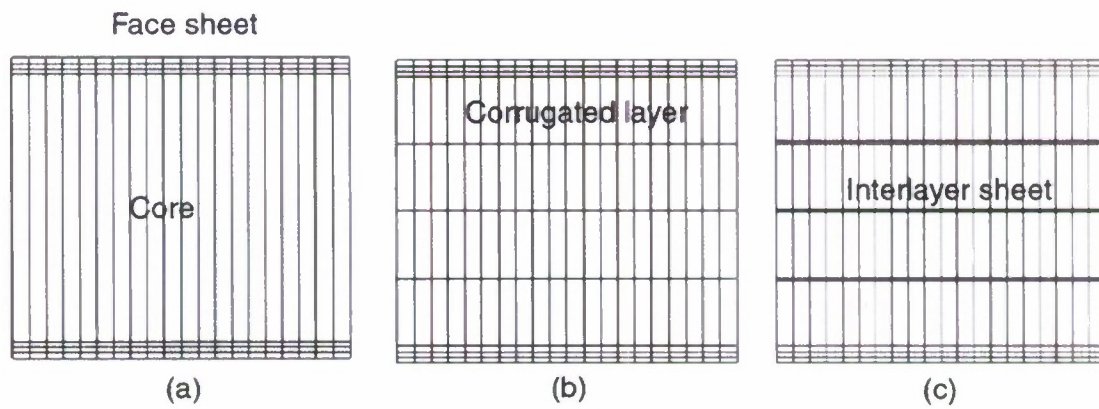
Figure 10. The finite element meshes used for the three schemes used to predict the dynamic response: (a) Scheme I, (b) scheme II, (c) scheme III.
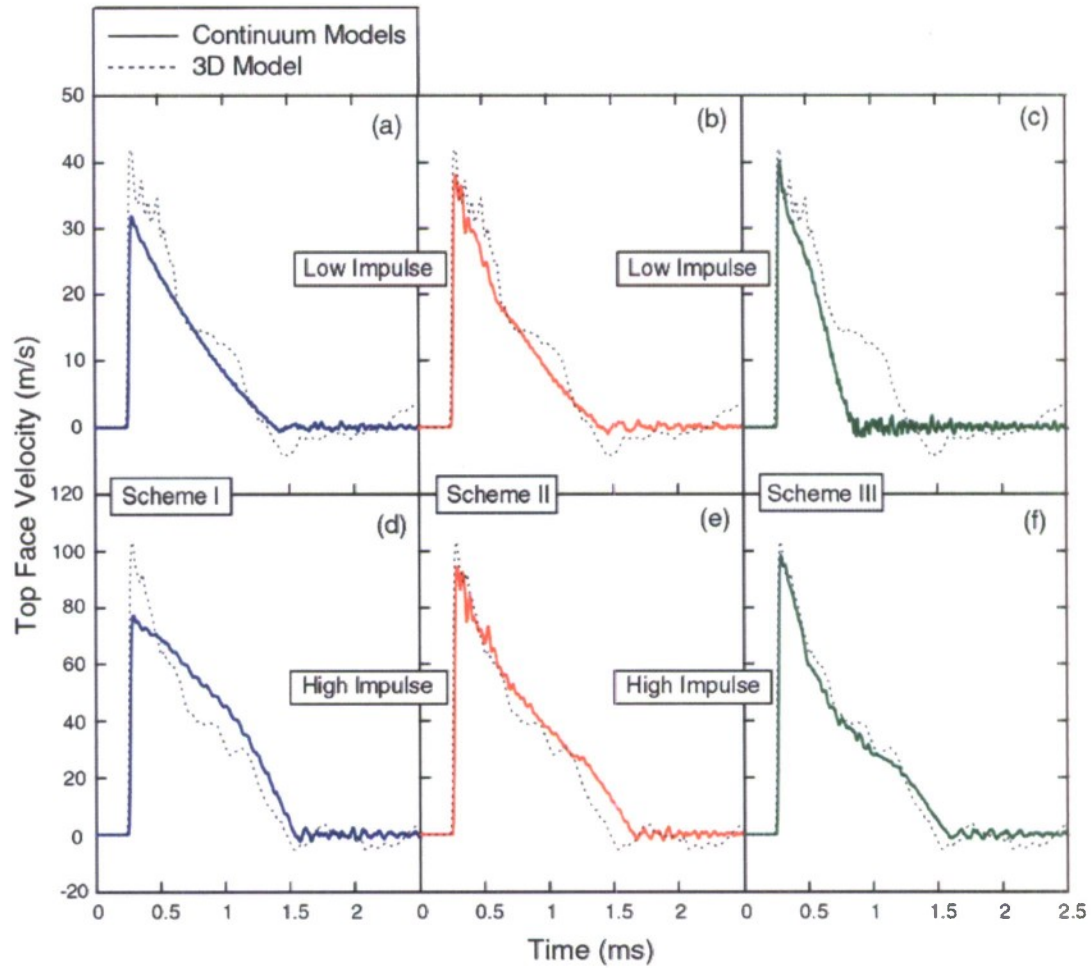
Figure 11. The temporal variation in the velocity of the wet face predicted by the three continuum schemes relative to that predicted by the 3D simulation at the same levels of impulse.
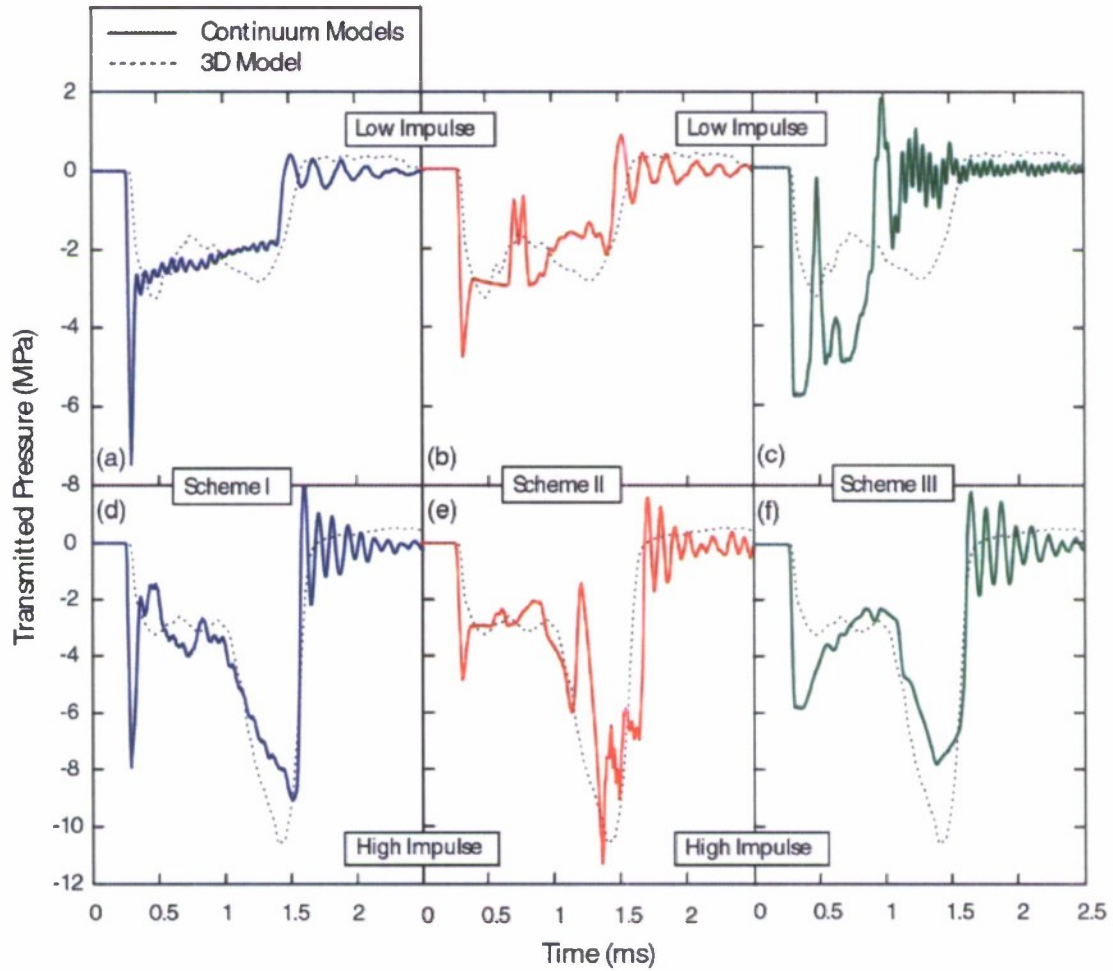
Figure 12. The temporal variation in the transmitted pressure predicted by the three continuum schemes relative to that predicted by the 3D simulation at the same levels of impulse.
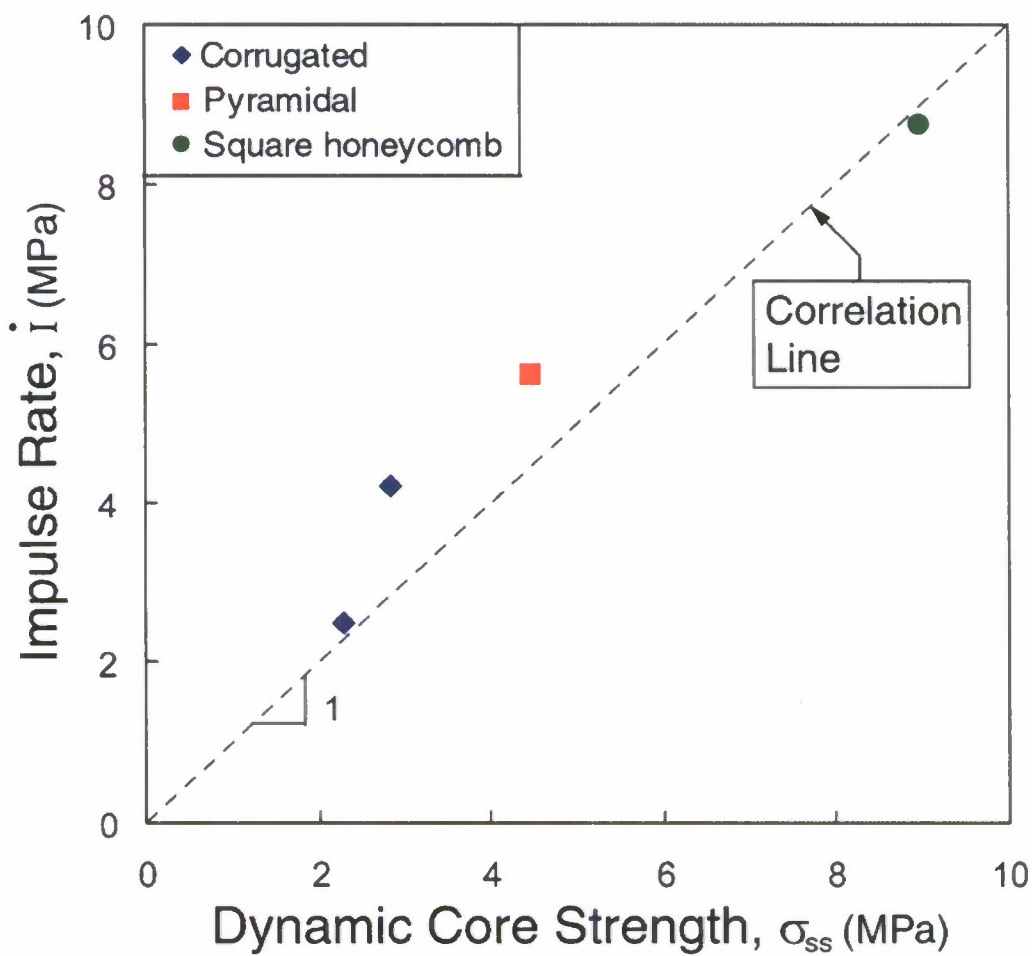
Figure 13. The correlation between the impulse transfer rate and the dynamic core strength plotted for three topologies.
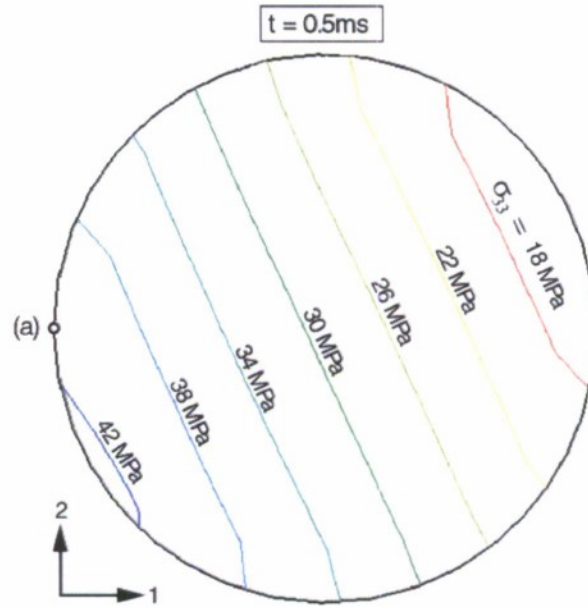
Figure A1. Normal stress contours on the cross-section of the gage column. The even-varying stress from one side to the other indicates flexural waves.

Figure A2. The temporal dependence of the stress measured through one position around the surface [marked as (a) on figure A1].

Figure B1. (a) Illustration of constructing simplified curves by enforcing equivalent plastic dissipation. (b) Simplified stress/strain curves at different strain rates.

Figure B2. The temporal variations in the core crushing strain, transmitted pressure and top face velocity predicted by using the simplified curves (figure B1b) relative to that predicted by using an original curve (Figure B1a).

(a) Design Structure
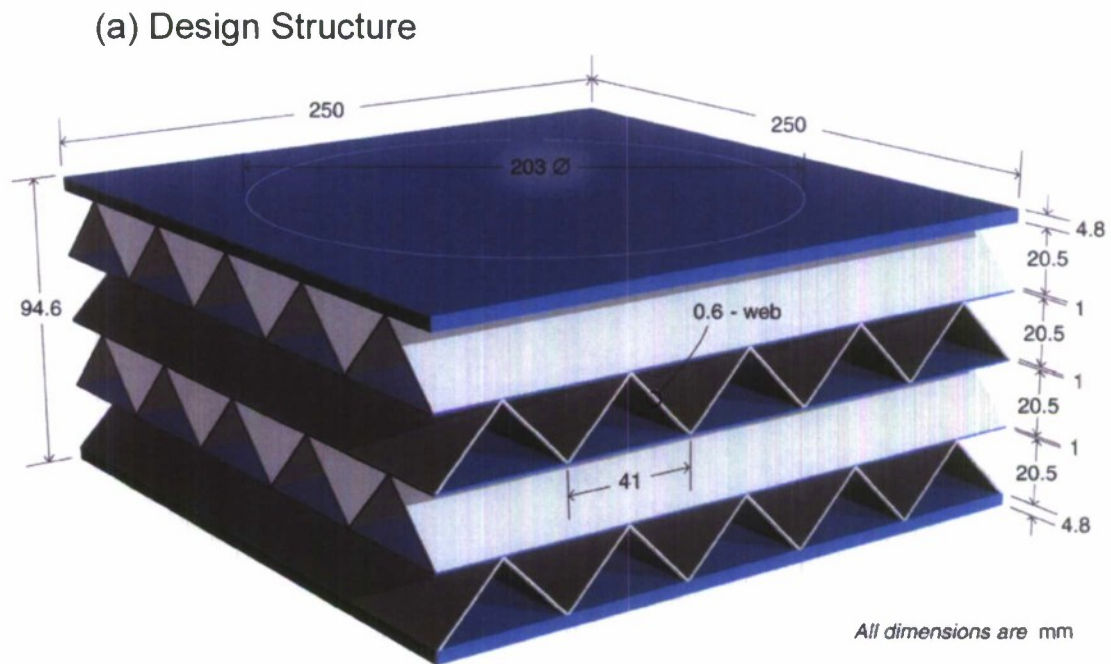
(b) Fabricated sample

Figure 1. (a) Topology of a multi-layer corrugated core. (b) An optical image of a stainless steel test specimen.

1
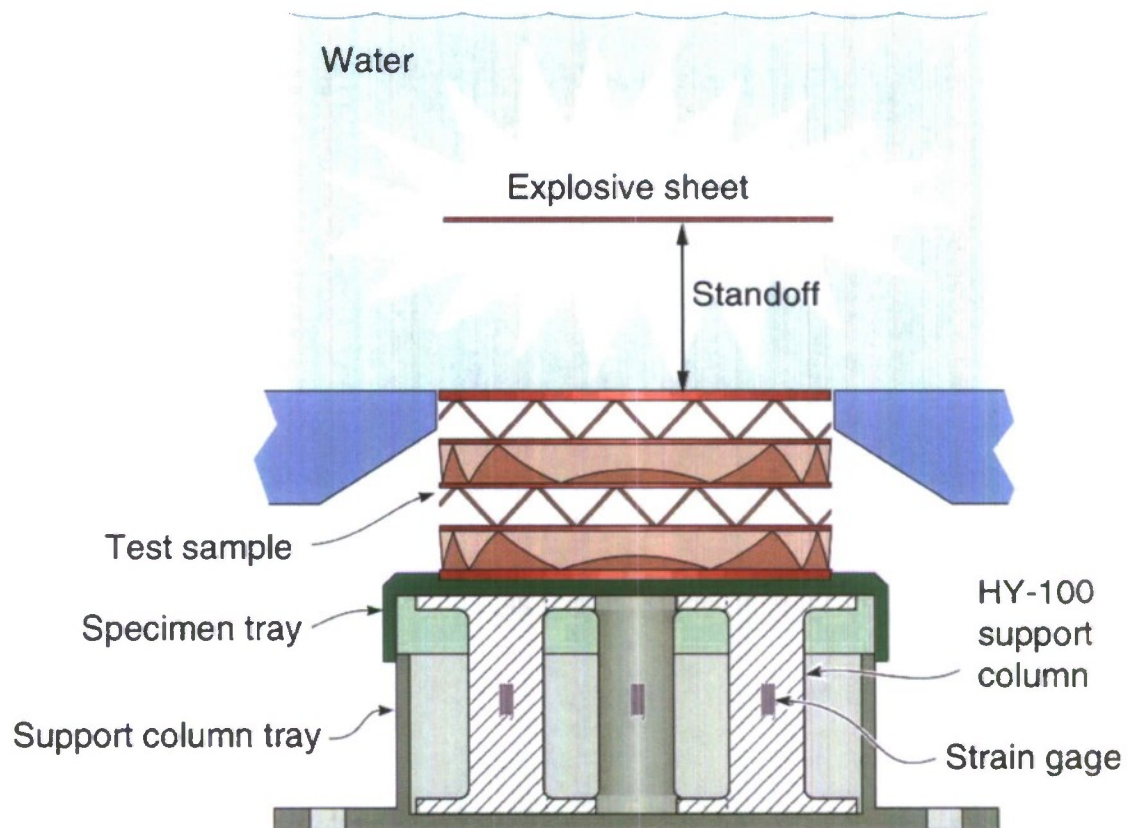
Figure 2. Schematic representation of the "dynocrusher" test. The strains measured on the gauge columns were converted stresses using data collected during quasi-static compression of the columns.

(a) Quasi-static Compressive Response
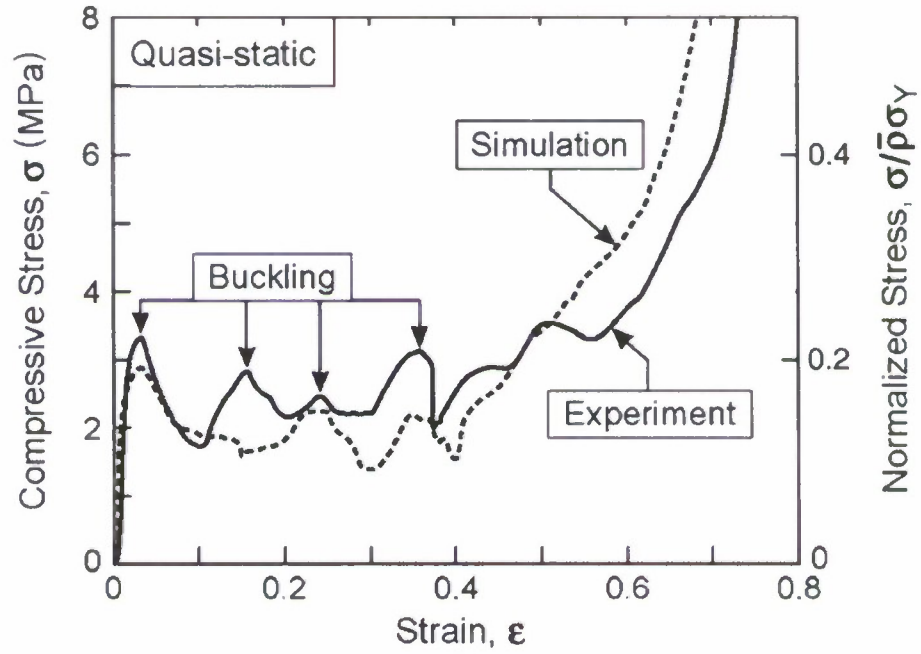
(b) Partially Crushed Structure

Figure 3. (a) Quasi-static compressive stress-strain response. (b) Deformed shape at 35% strain.

3

(a) 3-D Finite Element Model

(b) Initial Buckling Phase

(c) Buckling at 35% Crush Strain

Figure 4. (a) The 3-D finite element model used for the simulations (quarter based on symmetry). (b) Premature localized buckling shown on the deformed panel corresponding to the initial peak stress in Figure 3(a). (c) Deformed shape at 35% strain as a comparison with Figure 3(b).

4

Figure 5. (a),(b) Transmitted pressure and (c),(d) impulse responses of the reference solid cylinder for low and high impulse loading respectively.

Figure 6. A comparison between measurements and simulations of the transmitted pressure and impulse for the multilayer corrugated core at the two impulse levels. Also shown are the analytic estimates of the transmitted impulse.

Figure 7. The 3-D finite element model of the "Dynocrusher" test, including a water column, support gage column, and spring-dashpot to represent the response of the base.

Figure 8. Time varying stress response of (a) a single layer I-core (b) a multilayer corrugated core.

Figure 9. (a) Sandwich panel after the low impulse test. (b) Predicted deformation following the low impulse exposure. (c) Sandwich panel tested at the high impulse. (d) Predicted deformation after the high impulse exposure.

Face sheet

Figure 10. The finite element meshes used for the three schemes used to predict the dynamic response: (a) Scheme I, (b) scheme II, (c) scheme III.

Figure 11. The temporal variation in the velocity of the wet face predicted by the three continuum schemes relative to that predicted by the 3D simulation at the same levels of impulse.

11

Figure 12. The temporal variation in the transmitted pressure predicted by the three continuum schemes relative to that predicted by the 3D simulation at the same levels of impulse.

Figure 13. The correlation between the impulse transfer rate and the dynamic core strength plotted for three topologies.

Figure A1. Normal stress contours on the cross-section of the gage column. The even-varying stress from one side to the other indicates flexural waves.

Figure A2. The temporal dependence of the stress measured through one position around the surface [marked as (a) on figure A1].

14

Figure B1. (a) Illustration of constructing simplified curves by enforcing equivalent plastic dissipation. (b) Simplified stress/strain curves at different strain rates.

Figure B2. The temporal variations in the core crushing strain, transmitted pressure and top face velocity predicted by using the simplified curves (Figure B1b) relative to that predicted by using an original curve (Figure B1a).

16

Dynamic Compression of Metallic Sandwich Structures During Planar Impulsive Loading in Water

K.P. Dharmasena*, D.T. Queheillalt, H.N.G. Wadley
Department of Materials Science & Engineering
University of Virginia
Charlottesville, VA 22904, USA.

P. Dudt, Y. Chen, D. Knight
Naval Surface Warfare Center
Carderock, MD 20817, USA.

A.G. Evans
Department of Mechanical Engineering
University of California Santa Barbara
Santa Barbara, CA 93106, USA.

V.S. Deshpande
Department of Engineering
University of Cambridge
Cambridge, CB2 1PZ, UK

Abstract

The compressive response of rigidly supported stainless steel sandwich panels subject to a planar impulsive load in water is investigated. Five core topologies that spanned a wide range of crush strengths and strain-dependencies were investigated. They included a (i) square honeycomb, (ii) triangular honeycomb, (iii) multi-layer pyramidal truss, (iv) triangular corrugation and (v) diamond corrugation, all with a core relative density of approximately 5%. Quasi-statically, the honeycombs had the highest peak strength, but exhibited strong softening beyond the peak strength. The truss and corrugated cores had significantly lower strength, but a post yield plateau that extended to beyond a plastic strain of 60% similar to metal foams. Dynamically, the transmitted pressures scale with the quasi-static strength. The final transmitted momentum increased slowly with core strength (provided the cores were not fully crushed). It is shown that the essential aspects of the dynamic response, such as the transmitted momentum and the degree of core compression, are captured with surprising fidelity by modeling the cores as equivalent metal foams having plateau strengths represented by the quasi-static peak strength. The implication is that, despite considerable differences in core topology and dynamic deformation modes, a simple foam-like model replicates the dynamic response of rigidly-supported sandwich panels subject to planar impulsive loads. It remains to ascertain whether such foam-like models capture more nuanced aspects of sandwich panel behavior when locally loaded in edge clamped configurations.

*Corresponding author
(E-mail: kumar@virginia.edu)

1. Introduction

Metallic sandwich panels offer significant advantages over equivalent mass per unit area monolithic plates when exposed to underwater impulsive loading [1-3]. These benefits arise from two main factors: (i) the enhanced bending strength of sandwich panels over monolithic plates of equal mass per unit area and (ii) reduced momentum transfer from the water to the sandwich structure due to the low inertia of a thin (light), impulsively loaded face sheet supported by a crushable core. This study investigates dynamic core compression and the associated fluid-structure interaction (FSI) occurring at the wet face/fluid interface. The assessment is conducted for three classes of cellular topology: honeycombs, prismatics and trusses [4]. These classes differ in the following sense. (a) Honeycombs offer high crush resistance and (when square or triangular) also have high in-plane stretch strength, but are not amenable to additional functionalities, such as active cooling [5, 6]. (b) Trusses have an open architecture suitable for multi-functionality, but have low in-plane strength. (c) Prismatics have intermediate crush and stretch performance, and benefit from ease of manufacture. When subjected to impulsive loads, the honeycombs are most resistant to crushing and thus, transmit large stresses to the back face of the sandwich panel, with deleterious consequences for the governing metrics: notably, back face deflection, reaction forces at the supports and face tearing [7-9]. The trusses and prismatics, which are more susceptible to crushing, offer performance benefits in terms of impulsive load resistance [7,8,10,11]. However, a unified perspective on the role of core topology has yet to emerge. Attaining such a perspective is the primary objective of this article.

The crush dynamics and associated the FSI are investigated using a dynamic ("Dyno") crush test facility [9-12] that employs an explosive sheet to generate an underwater, planar impulse that impinges onto the test structure. In such tests, the impulse in the water causes the pressure to rise to a peak, p_0, almost instantaneously. The pressure subsequently decreases at nearly exponential rate, with a time constant θ of order milliseconds such that,

$$p = p_0 \exp\left(-t / \theta\right), \tag{1}$$

where t is measured from the instant of impulse arrival. Damped oscillations of the gas bubble containing the explosive products leads to secondary impulses, but these generate smaller pressures, and are much less damaging.

When the impulse impinges onto a rigid plate at normal incidence it imparts an impulse I_0 :

$$I_0 \equiv 2 \int_0^\infty p_0 e^{-t/\theta} dt = 2 p_0 \theta . \tag{2}$$

The factor of two arises due to full reflection of the pressure wave. If, instead, the pressure-wave impacts a free-standing plate of areal mass m, it sets the plate in motion, causing the reflected wave to become tensile. The ensuing net pressure in the fluid drops to zero and cavitation sets in. The momentum per unit area I_{trans} transmitted into the structure is then:

$$I_{trans} = \xi I_0 \tag{3a}$$

2

where,

$$\xi \equiv \psi^{\psi/(1-\psi)} \tag{3b}$$

and $\psi \equiv \rho_w c_w \theta / m$.

For a sandwich panel, these results are modified by the push-back stress exerted on the wet face by the core as it crushes. This effect has been examined at two levels. (i) Simplified models that endow the core with a fixed dynamic strength without explicitly modeling the core topology or the crushing dynamics. One such model indicates that the transmitted momentum becomes [2]:

$$\frac{I}{I_0} = \psi^{\psi/(1-\psi)} + 0.63(1 - \psi^{\psi/(1-\psi)})\frac{\sigma_p}{p_0} \tag{4}$$

where σ_p is the core strength.(ii) Detailed finite element (FE) analysis of the response [13-15]. It has yet to be ascertained whether the simplified models suffice to capture the response or whether the details are important. An additional aim of this paper is to present a detailed experimental/numerical investigation that addresses this issue.

The outline of the paper is as follows. The manufacture of the various cores is described, simple analytical formulae for their static strength are presented and measurements reported. The dyno-crusher apparatus is briefly described and the dynamic measurements detailed. Thereafter, a numerical model is developed based upon the crushing of an equivalent mass and strength foam core, and the predictions compared with the measurements. These comparisons are used to draw conclusions regarding the explicit roles of core topology and strength.

2. Sandwich panel manufacture and core properties

Circular sandwich panels with a diameter $D = 203$ mm and core thickness $c \approx 90$ mm, were manufactured from 304 stainless steel. The panels had two identical stainless steel faces with thickness $h = 5$ mm. Five different core topologies were produced (Figs. 1, 3 and 4) by vacuum brazing core/face assemblies using a Ni-Cr-P powder (Wall Colmonoy Nicrobraz 51 alloy) for 1h at 1050°C. Estimates of the core strengths are presented below in terms of the solid material's Young's modulus E_s, Poisson's ratio ν and yield strength, σ_Y.

Square-honeycombs (Fig. 1a) were manufactured from steel sheets, with a thickness $t = 0.76$ mm. The sheets were cropped into rectangles with height $c = 89$ mm and length 250 mm. Cross-slots (width $\Delta t = 0.76$ mm and spacing $l = 31$ mm) were laser cut into the rectangles to depth $c/2$ and assembled as detailed elsewhere [4,9,16]. These cores had a relative density $\bar{\rho} \approx 0.05$. The quasi-static peak strength σ_p of such cores is elastic buckling governed at low relative densities and yielding dominated at higher densities such that [16]:

3

$$\sigma_p = \begin{cases} \dfrac{\pi^2}{12\left(1-\nu^2\right)} E_s \bar{\rho}^3 & \bar{\rho} < \dfrac{1}{\pi}\sqrt{12\varepsilon_Y(1-\nu^2)} \\[12pt] \bar{\rho}\sigma_Y & \text{otherwise} \end{cases} \tag{5}$$

where the yield strain. $\varepsilon_Y \equiv \sigma_Y / E_s$ and $\bar{\rho}$ is the relative density. For a square honeycomb (see unit-cell in Fig.1a),

$$\bar{\rho} \approx \frac{2t}{l} \tag{6}$$

Triangular-honeycombs (Fig. 1b) were fabricated from the same steel sheets, cropped into rectangles with height $c = 89$ mm and length 250 mm. In one set of the rectangles (labeled shape #1 in Fig. 2a) cross slots having width $\Delta t = 0.76$ mm and spacing $l = 51$ mm were laser cut to a depth $2c/3$, while in another, slots of depth $c/3$, spaced 51 mm apart, were cut from both ends (shape #2 in Fig. 2a). The sheets were assembled (Fig. 2b) into equilateral triangular cells of side $l = 51$ mm forming the core for the samples used here (Fig. 2c). For the unit-cell shown in Fig 1b,

$$\bar{\rho} \approx \frac{2\sqrt{3}t}{l} \tag{7}$$

These cores also have a relative density, $\bar{\rho} \approx 0.05$.

Multi-layer pyramidal truss cores were manufactured by laser cutting a diamond pattern into a flat sheet with a thickness $t = 1.52$ mm, leaving a series of intersecting square-section ligaments each 1.52×1.52 mm in cross section and length $l = 17$mm. The perforated sheets were folded along ligament node rows to generate pyramidal trusses having inclination, $\omega = 45°$, with respect to the horizontal plane (Fig. 3). The core comprised 7 pyramidal layers, each separated by solid sheets with thickness, $t_s = 0.76$ mm. They were assembled to create the unit cell geometry shown in Fig 3 and brazed. The total relative density of a multilayered pyramidal core (including the sheets separating the core layers) is given by:

$$\bar{\rho} \approx \frac{\sqrt{2}(4wt + t_s l)}{l(l + \sqrt{2}t_s)} \tag{8}$$

where l is the length of the truss and $w \times t$ is the truss cross-section. For the unit-cell shown in Fig. 3 $\bar{\rho} \approx 0.09$ with the contribution of just the trusses ~5%. The compressive strength is again governed by elastic buckling at low $\bar{\rho}$ and by yielding otherwise. In this configuration, to account for the constraints of the intervening sheets in an approximate manner we regard the trusses as simply supported at one end and clamped at the other. The strength then becomes

4

$$\sigma_p = \begin{cases} \dfrac{\sqrt{2}\pi^2}{3}\left(\dfrac{t}{l}\right)^3 E_s & \dfrac{t}{l} < \dfrac{6\varepsilon_Y}{\pi^2} \\[3mm] 2\sqrt{2}\left(\dfrac{t}{l}\right)^2 \sigma_Y & \text{otherwise} \end{cases} \tag{9}$$

Note that the intermediate sheets are assumed not to explicitly contribute to the uniaxial compressive strength.

Multilayer triangular corrugated cores were manufactured by folding the $t = 0.76$ mm sheets into corrugations of side $l = 30.5$ mm and angle $\omega = 45°$ (Fig. 4a). For a single-layer corrugation, the relative in the limit $l \gg t$ is given by:

$$\overline{\rho} \approx \frac{2t}{l\sin 2\omega}. \tag{10}$$

Four such sheets were stacked into a $0-90°$ layup separated by intermediate sheets of thickness $t_s = 0.76$ (Fig. 4a). This multi-layered core had a relative density, $\overline{\rho} \approx 0.07$ including the mass of the intermediate sheets. Estimates of the strength are again obtained by regarding the members as built-in at one end and simply-supported at the other, whereupon,

$$\sigma_p = \begin{cases} \dfrac{\pi^2}{6}\left(\dfrac{t}{l}\right)^3 E_s & \dfrac{t}{l} < \dfrac{1}{\pi}\sqrt{6\varepsilon_Y} \\[3mm] \left(\dfrac{t}{l}\right)\sigma_Y & \text{otherwise} \end{cases} \tag{11}$$

Diamond corrugated cores were manufactured in a similar manner but with a different stacking sequence (Fig. 4b). Two corrugations were stacked to form diamond-shaped cells. The diamonds were then stacked in a $0-90°$ layup separated by an intermediate sheet of thickness $t_s = 0.76$ mm as shown in Fig. 4b. Similar to the triangular corrugation, the diamond corrugation also had cells of side $l = 30.5$ mm and made from a $t = 0.76$ mm steel sheet with $\omega = 45°$. The relative density of the core including the intermediate sheets is $\overline{\rho} \approx 0.06$. In this configuration, member rotation is less constrained such that they are simply supported at both ends giving the quasi-static strength:

$$\sigma_p = \begin{cases} \dfrac{\pi^2}{12}\left(\dfrac{t}{l}\right)^3 E_s & \dfrac{t}{l} < \dfrac{1}{\pi}\sqrt{12\varepsilon_Y} \\[3mm] \left(\dfrac{t}{l}\right)\sigma_Y & \text{otherwise} \end{cases} \tag{12}$$

3.   Quasi-static Measurements

The quasi-static compressive responses were measured in a screw driven test machine at a nominal strain rate of 5×10^{-4} s^{-1} [17]. The stress was ascertained from the load cell, while the average compressive strain was deduced from laser interferometer

measurements of the relative approach of the two faces. The measured responses are plotted on Fig. 5. The honeycombs (Fig. 5a) display a high initial strength σ_p followed by a strongly softening response prior to densification as the strain exceeded 60%. Recalling from (5) that cores with $\bar{\rho} \approx 0.05$ reside close to the transition between elastic buckling and yielding. We attribute the peak to elastic buckling and the softening to post-buckling plasticity. The reduced strength of the triangular honeycombs is attributed to manufacturing defects introduced where the three separate sheets intersect at the nodes. The multilayer cores (Fig. 5b) crush at almost constant stress with small fluctuations as successive layers collapse, reminiscent of the response of metal foams. The increase in stress at a nominal strain around 60% is caused by contact of the core members (i.e. densification). Comparisons between the measurements and the estimates (Section 2) are included in Table 1, where we have taken the properties of 304 stainless steel in its as-brazed state as $E_s = 210\,\text{GPa}$, $\nu = 0.3$ and $\sigma_Y = 220\,\text{MPa}$ [9-11,18]. Reasonable agreement is obtained in all cases: albeit that the predictions (which do not account for imperfections) slightly overestimate the measurements.

4. Dynamic Measurements

Apparatus: The samples were rigidly back supported by a set of strong pedestals to which strain gages were attached for transmitted pressure measurements. A cardboard cylinder was then placed around the samples and this was filled with water. Some essential information about the experimental set-up is provided (Fig. 6), with details given elsewhere [9-12]. The base of the cardboard cylinder containing the water comprises a thick steel plate with a central hole. The circular test panel was aligned such that the wet face was flush with the annular plate. The dry face was supported on a specimen tray, mass 2.5 kg, and four 2 cm long HY-100 steel columns each 3.8 cm in diameter. The four columns were instrumented with axial strain gauges to provide temporal measurements of the loads transmitted through the core. The planar impulses were generated by detonation of an explosive sheet (Detasheet), diameter 203 mm and thickness 1 mm, placed at a stand-off, $H = 0.1\,\text{m}$ from the wet face.

The temporal dependence of the free field pressure p has been calculated using the DYSMAS hydrocode [14]. It is plotted in Fig. 7, where $t = 0$ is the time at which the pressure pulse reaches the front face of the test panel (at a stand-off, $H = 0.1\,\text{m}$). This pressure is well-approximated by relation (1), with peak pressure $p_0 = 260\,\text{MPa}$ and decay constant $\theta = 0.023\,\text{ms}$ as illustrated in Fig. 7. The impulse per unit area for such a wave incident on a *stationary* rigid plate is given from Eq. (2) as, $I_0 \approx 12\,\text{kPa.s}$.

Calibration: The fidelity of the apparatus was assessed by first conducting a test using a 6061-T6 solid aluminum cylinder with diameter, $D = 203\,\text{mm}$ and height 100 mm. The temporal variation of the transmitted pressure p_t (over the area $A \equiv \pi D^2 / 4$ of the cylinder) of the sandwich panel and the corresponding areal impulse,

6

$$I = \int_0^t p_t \, dt \qquad (13)$$

are plotted in Figs. 8a and 8b, respectively. These figures identify three metrics: the peak pressure, $p_{\max}$ as well as the time, t_{ss}, before the impulse attains steady-state, I_{ss}. Note that the peak pressure is considerably below the value, $2p_0 = 520\,\mathrm{MPa}$, expected from an acoustic analysis of impulse reflection at a rigid structure – water interface (2). However, the steady-state transmitted impulse, $I_{ss} \approx 11.5\,\mathrm{kPa.s}$, is consistent with the acoustic prediction (2). This happens because of signal dispersion and wave reflection within the aluminum block and measurement columns reduces the measured pressures as discussed in [14] but does not significantly affect the measured transmitted momentum.

Crush response of sandwich panels: The temporal variation of the transmitted pressure for the five cores is reported in Figs. 9. While there is some ambiguity regarding the pressure histories (because of wave dispersion and reflection), the following sequence in peak pressure (from highest to lowest) is clear: honeycomb > truss > triangular corrugation. The diamond corrugation, which initially transmits a low pressure, undergoes sufficient crushing that core fully crushes permitting transmission of large stresses. This effect is analogous to the case of an air core sandwich, in which the wet face "slaps" into the dry face, resulting in the sudden increase in the pressure at $t_{slap} \approx 1.5\,\mathrm{ms}$ as indicated in Fig. 9e. These dynamic strengths rank in the same order as the quasi-static strengths (Fig. 5).

The impulse waveforms are shown in Fig. 10. The steady-state impulse I_{ss} (Fig. 10) varies only slightly with core topology. In order to provide meaningful comparisons with the ensuing simulations, the relationships between the core strength (Table I) and (i) the core crushing strain, $\varepsilon_c^f \equiv \Delta c / c$ (where Δc is the final reduction in the core thickness), (ii) the time t_{ss} and (iii) the steady-state impulse, I_{ss}, are plotted in Fig. 11 (the time t_{ss} is defined as the time corresponding to the knee prior to the plateau in the I versus time curves and I_{ss} as average value of I over the range $t_{ss} \leq t \leq 2\,\mathrm{ms}$ as indicated in Fig. 10). Note that, while ε_c^f increases with decreasing σ_p, the time t_{ss} has a maximum at $\sigma_p \approx 4\mathrm{MPa}$ just prior to the onset of face-sheet slap. Moreover, the measurements plotted in Fig. 11c suggest a small drop in I_{ss}/I_0 as σ_p decreases. This indicates that the momentum transferred to sandwich structures *supported by a rigid foundation* is a weak function of core strength over the practical ranges of core strengths considered here. The transmitted momentum as predicted by Eq. (4) (with m interpreted as the areal mass of the wet face sheet) is included in Fig. 11c. The simplified model significantly under-predicts the transmitted momentum due to the fact that it does not accurately account for the re-loading of the sandwich panel after first cavitation in the water column. We note that over this practical range of cores strengths, I_{ss}/I_0 is about 25% less than the impulse transmitted into a rigid stationary structure. This result contrasts with the results obtained for free standing sandwich panels as discussed in Section 1 [1-3].

To reveal the final deformations, the panels were sectioned along two perpendicular diametrical planes (Fig. 12). For the honeycombs, the majority of the deformation occurs adjacent to the wet face while the deformation is more diffuse for the other cores. We surmise that their deformation started adjacent to the wet face and spread through the core. Recall that, for the diamond cores, a sudden increase in the transmitted pressure and momentum were measured at $t \approx 1.5$ ms, attributed to "slapping". This slap mechanism is evident in Fig. 12e where the sheets between adjacent layers of the core are in contact with each other and the wet face.

5.   Simulation

A simplified one-dimensional finite element (FE) model is presented (Fig. 13). It comprises a sandwich panel and a fluid column of height H_w. In order to rationalize and unify the foregoing responses, the crushing dynamics of the cores are simulated using a simplified (foam), model wherein the quasi-static response is represented by a plateau collapse stress, equated to σ_p (Fig. 5 and Table I) and a (logarithmic) densification strain is taken as $\varepsilon_D = -\ln(2\bar{\rho})$. The sandwich panel has identical faces, thickness h, and a core thickness, c. The faces are elastic with Young's modulus $E_f = 210$ GPa and density $\rho_f = 8000\,\text{kgm}^{-3}$, representative of steel. The main simplification is that the core is modeled as a compressible foam (in a 1D setting) with a density ρ_c. Such a model accounts for the shock wave propagation in the compressible sandwich cores (and thus the differences between the stresses exerted by the core on the wet and dry faces of the sandwich panel). However, the model does not model the enhanced dynamic strengths of the core due to micro-inertial stabilization of the struts of the core against buckling. The subsequent comparisons with measurements shall demonstrate that including this effect is not critical in modeling the compression of sandwich panels in the Dyno-crusher set-up.

The foam model is analyzed as follows. The total logarithmic strain rate $\dot{\varepsilon}$ is written as the sum of an elastic strain rate $\dot{\varepsilon}_e$ and a plastic strain rate $\dot{\varepsilon}_p$, resulting in a stress level σ.

$$\dot{\varepsilon} = \dot{\varepsilon}_e + \dot{\varepsilon}_p \text{sign}(\sigma) \tag{14}$$

The elastic strain rate is related to the stress rate by:

$$\dot{\varepsilon}_e = \frac{\dot{\sigma}}{E_c} \tag{15}$$

where E_c is the Young's modulus of the core. An overstress visco-plastic model [19] governs the plastic strain rate,

$$\dot{\varepsilon}_p = \begin{cases} \left(\dfrac{|\sigma| - \sigma_p}{\eta} \right), & \text{if } |\sigma| \ge \sigma_p \text{ and } \varepsilon_p < \varepsilon_D \\ 0 & \text{otherwise,} \end{cases} \tag{16}$$

where the viscosity η is chosen to give a shock width [19]:

$$l_s = \frac{\eta \varepsilon_D}{\rho_c \Delta v} = \frac{c}{10} \qquad (17)$$

where Δv is the velocity jump across the shock. With $l_s = c/10$ we ensure that the viscosity η plays no role in the overall structural response other than regularizing the numerical problem to obtain a shock of finite width. We employ the estimate $\Delta v = p_0 \theta / (\rho_f h)$ based upon a free-standing front face, with fluid-structure interaction effects neglected. Because large gradients in stress and strain occur over the shock width a mesh size $c/10$ is chosen to resolve these gradients accurately. Calculations are presented for strengths in the range $1\,\text{MPa} \le \sigma_p \le 15\,\text{MPa}$ and two relative densities $\bar{\rho} = 0.05$ and 0.1 corresponding to $\rho_c \equiv \bar{\rho}\rho_f = 400\,\text{kgm}^{-3}$ and $800\,\text{kgm}^{-3}$ (i.e. cellular cores constructed from steel with $\rho_f = 8000\,\text{kgm}^{-3}$). The Young's modulus of the core material is taken to be $E_c = \bar{\rho}E_f$ (the response is insensitive to this choice).

The water is modeled as a one-dimensional column of height H_w (Fig. 13) and thus we neglect the bursting of the cardboard cylinder containing the water. This is rationalized by noting that the entire event comprising the transmission of the blast momentum and core crushing is completed well before the constraint on the water column is lost. Following Bleich and Sandler [20], the fluid medium is modeled as a bilinear elastic solid with density $\rho_w = 1000\,\text{kgm}^{-3}$ and modulus $E_w = 1.96\,\text{GPa}$, giving a wave speed $c_w = \sqrt{E_w/\rho_w} = 1400\,\text{ms}^{-1}$, representative of water. The stress σ, logarithmic strain ε relationship is taken to be:

$$\sigma = \begin{cases} E_w \varepsilon & \varepsilon \le 0 \\ 0 & \text{otherwise} \end{cases} \qquad (18)$$

so that the water is incapable of sustaining tensile stress.

A pressure history,

$$p = p_0 e^{-t'/\theta} \qquad (19)$$

is applied to the top of the fluid column (Fig. 13), with time t' measured from the instant of application of the pressure. The time t is measured from the instant that the impulse impinges on the structure. The two are related by $t' = t + (H_w/c_w)$. The height H_w of the water column is taken to be sufficiently large that the reflected wave does not reach the top over the duration of the calculations. Namely, the column can be considered semi-infinite. All calculations take $p_0 = 260\,\text{MPa}$ and $\theta = 0.023\,\text{ms}$ consistent with the impulses generated in the experiments.

The calculations were conducted using an updated Lagrangian scheme with the current configuration at time t serving as the reference. The coordinate x denotes the position of a material point in the current configuration with respect to a fixed Cartesian frame, and u is the displacement of that material point. The principle of virtual work (neglecting effects of gravity) for a volume V and surface S is written in the form:

9

$$\int_V \sigma \delta\varepsilon \, dV = \int_S T \delta u \, dS - \int_V \rho \frac{\partial^2 u}{\partial t^2} \delta u \, dV \tag{20}$$

where σ is the Cauchy stress, $\varepsilon \equiv \partial u / \partial x$ is the strain, T is the traction on the surface S of the current configuration and ρ is the density of the material in the current configuration.

A discretization based on linear, one-dimensional elements is employed. When this discretization is substituted into the principle of virtual work (20) and the integrations carried out, the discretized equations of motion are obtained as:

$$\mathbf{M}\frac{\partial^2 \mathbf{U}}{\partial t^2} = \mathbf{R} \tag{21}$$

where $\mathbf{U}$ is the vector of nodal displacements, $\mathbf{M}$ is the mass matrix and $\mathbf{R}$ is the nodal force vector. A lumped mass matrix is used in (21) instead of a consistent mass matrix since this is preferable for both accuracy and computational efficiency [21]. An explicit time integration scheme, based on the Newmark β-method with $\beta = 0$, is used to integrate equation (21) to obtain the nodal velocities and displacements. The sandwich panel geometry in the simulations was chosen to match the experiments, i.e. a face sheet thickness $h = 5\,\mathrm{mm}$ and a core depth $c = 90\,\mathrm{mm}$. Typically, there are 40,000 one-dimensional elements in the fluid, 2000 in the core and 200 in each face sheet. In order to simulate the supporting structures, the constraint $u \le 0$ was imposed on the outside of the dry sheet, i.e. the dry face could loose contact with the support but not move beyond $x = 0$ as sketched in Fig. 13.

5.1 *Predictions and comparisons with measurements*

The predicted temporal variations of the wet face velocity v_w for the $\bar{\rho} = 0.1$ sandwich panels are plotted in Fig. 14a for selected values of the core strength, σ_p. The velocity rises rapidly and attains a peak independent of core strength. Thereafter, for an extended period, the wet face decelerates at a rate that increases with increasing σ_p. But for the lower σ_p ($\sigma_p \le 2\,\mathrm{MPa}$) the core undergoes full densification, resulting in a sudden deceleration, at $t \approx 1.2\,\mathrm{ms}$, followed by elastic vibrations. The temporal variations of the core compression strains,

$$\varepsilon_c(t) \equiv \frac{1}{c}\int_0^t v_w \, dt \tag{22}$$

and of the impulse I transferred to the rigid supports are plotted in Figs. 14b and 14c, respectively. The key observations are as follows: (i) The final core compression ε_c^f increases with decreasing σ_p, with full densification $\varepsilon_c^f = 1 - 2\bar{\rho}$ attained when $\sigma_p \le 2\,\mathrm{MPa}$; (ii) Prior to densification (or arrest of the wet face), the rate of impulse transfer $\dot{I} \approx \sigma_p$; (iii) The final impulse transferred to the supports I_{ss} decreases slowly with core strength for $\sigma_p > 3\,\mathrm{MPa}$, but rises for lower strengths due to slapping; (iv) The

10

time t_{ss} at which the steady-state impulse is attained coincides with the end of core compression (and the time when the wet face comes to rest).

The predicted variations of ε_c^f, t_{ss} and I_{ss} with σ_p are superimposed on Fig. 11. Note that there is almost no affect of the core relative density between 0.05 and 0.1. The general features are consistent with the measurements, but with some discrepancies. In particular, the increase in the transmitted momentum predicted when $\sigma_p < 3\,\text{MPa}$ is not evident in the measurements. Nevertheless, given the simplicity of the model, it captures the essence of dynamic crushing remarkably well, even for honeycombs that have extreme strain-dependence of their crushing strength. This is contrasted with the prediction of the simplified analytical model, Eq. (4) which is non-conservative, and significantly under-predicts the transmitted momentum.

6. Concluding remarks

The response of rigidly supported sandwich panels to a planar water borne impulse is investigated using a dyno-crusher apparatus. Honeycomb, truss and prismatic core topologies have been studied in an attempt to understand the effect of topology. All of the cores had the same overall dimensions and a relative density of approximately 5%. The measured quasi-static compressive responses revealed that, while the honeycombs had high initial strength, their post peak response was strongly softening. The truss and corrugated cores had a lower strength, with a long plateau, similar to metal foams. The dyno-crusher measurements reveal that while the transmitted pressures and core compression scale with the static core strength, the final transmitted momentum is weakly affected. The use of a crushable core in a fully back supported test configuration reduces the transmitted impulse by about 25% compared to that transmitted through a rigid, fully supported block.

Simulations conducted by modeling the cores as a foam capture the major experimental trends in the transmitted momentum and core compression, implying that the static core strength is the primary variable governing dynamic crushing. It has yet to be ascertained whether such foam-like models capture more nuanced aspects of sandwich panel behavior in clamped configurations such as the soft/strong transition, face tearing and reaction forces.

References

[1]   Fleck NA and Deshpande VS. The resistance of clamped sandwich beams to shock loading. Journal of Applied Mechanics 2004; 71:386-401.

[2]   Hutchinson JW and Xue Z. Metal sandwich plates optimized for pressure impulses. International Journal of Mechanical Sciences 2005; 47:545-569.

[3]   McShane GJ, Deshpande VS and Fleck NA. The underwater blast resistance of metallic sandwich beams with prismatic lattice cores. Journal of Applied Mechanics 2007; 74:352-364.

[4]   Wadley HNG. Multifunctional periodic cellular metals. Philosophical Transactions of the Royal Society A 2006: 364: 31-68.

[5]   Queheillalt DT, Carbajal G, Peterson GP and Wadley HNG. A Multifunctional Heat Pipe Sandwich Panel Structure. Journal of Heat and Mass Transfer, 51, pp. 312-326.

[6]   Tian J, Lu TJ, Hodson HP, Queheillalt DT and Wadley HNG. Cross Flow Heat Exchange of Textile Cellular Metal Core Sandwich Panels. International Journal of Heat and Mass Transfer 2007; 50:2521-2536.

[7]   Liang Y, Spuskanyuk AV, Flores SE, Hayhurst DR, Hutchinson JW, McMeeking RM and Evans AG. The response of metallic sandwich panels to water blast. Journal of Applied Mechanics 2007; 74:81-99.

[8]   Tilbrook MT, Deshpande VS and Fleck NA. The impulsive response of sandwich beams: Analytical and numerical investigation of regimes of behaviour. Journal of the Mechanics and Physics of Solids 2006; 54:2242-2280.

[9]   Wadley HNG, Dharmasena KP, Queheillalt DT, Chen Y, Dudt P, Knight D, Kiddy K, Xue Z and Vaziri A. Dynamic compression of square honeycomb structures subjected to impulsive underwater loading. Journal of Mechanics of Materials and Structures, 2007; 10(2), 2025-2048

[10]   Wadley HNG, Dharmasena KP, Chen Y, Dudt P, Knight D, Charette R and Kiddy K. Compressive response of multilayered pyramidal lattices during underwater shock loading. International Journal of Impact Engineering, 2008; 35:1102-1114.

[11]   Dharmasena KP, Queheillalt DT, Wadley HNG, Chen Y, Dudt P, Knight D, Wei Z and Evans AG. Dynamic response of a multilayer prismatic structure to impulsive loads incident from water. International Journal of Impact Engineering, doi:10.1016/j.ijimpeng.2008.06.002.

[12]   Knight, D., Y-C. Chen, W.Lewis, and P. Dudt, "Comparison of Explosive-Loaded Periodic Cellular Structures using a Dynocrusher Device," Naval Surface Warfare Center, Carderock Division Report NSWCCD-66-TR-2005/23 (Oct.2005).

 [13]   Deshpande VS and Fleck NA. One-dimensional response of sandwich plates to underwater shock loading. Journal of the Mechanics and Physics of Solids 2005; 53:2347-2383.

[14]   Wei Z, Dharmasena KP, Wadley HNG and Evans AG. Analysis and interpretation of a test for characterizing the response of metallic sandwich panels to water blast. International Journal of Impact Engineering 2007; 34:1602-1618.

[15]   Mori LF, Lee S, Xue Z, Vaziri A, Queheillalt DT, Dharmasena K.P, Wadley HNG, Hutchinson JW and Espinosa HD. On the behavior of sandwich structure subjected to under water impulse loads. Journal of Mechanics of Materials and Structures 2007; 2(10), 1981-2006.

[16]   Cote F, Deshpande VS, Fleck NA and Evans AG. The out-of-plane compressive behavior of metallic honeycombs, Materials Science and Engineering A, 2004; 380:272-278.

[17]. Chen, Y-C. and P. Dudt, "Evaluation of Stainless Steel Periodic cellular Materials under Quasi-Static Loading Conditions," Naval Surface Warfare Center, Carderock Division Report NSWCCD-66-TR-2005/05 (March 2005).

[18]   Cote F, Deshpande VS, Fleck NA and Evans AG. The compressive and shear responses of corrugated and diamond lattice materials. International Journal of Solids and Structures 2006; 43:6220-6242.

[19]   Radford DD, Deshpande VS and Fleck NA. The use of metal foam projectiles to simulate shock loading on a structure. International Journal of Impact Engineering 2005; 31:1152-1171.

[20]   Bleich HH and Sandler IS. Interaction between structures and bilinear fluids, International Journal of Solids and Structures, 1970; 6:617–639.

[21]   Krieg RO and Key SW. Transient shell response by numerical time integration, International Journal of Numerical Methods in Engineering, 1973; 7:273–286.

Tables

Core topology	Measured peak strength (MPa)	Analytical prediction σ_p (MPa)
Square honeycomb	11.5	10.8
Triangular honeycomb	8.4	10.8
Multi-layer pyramidal truss	3.9	4.9
Triangular corrugation	3.4	4.6
Diamond corrugation	2.4	2.3

Table 1: Comparison between the measured values and predictions of the initial peak quasi-static strengths of the five core topologies investigated in this study. The properties of stainless steel were taken as $E_s = 210\,\text{GPa}$, $\nu = 0.3$ and $\sigma_Y = 220\,\text{MPa}$.
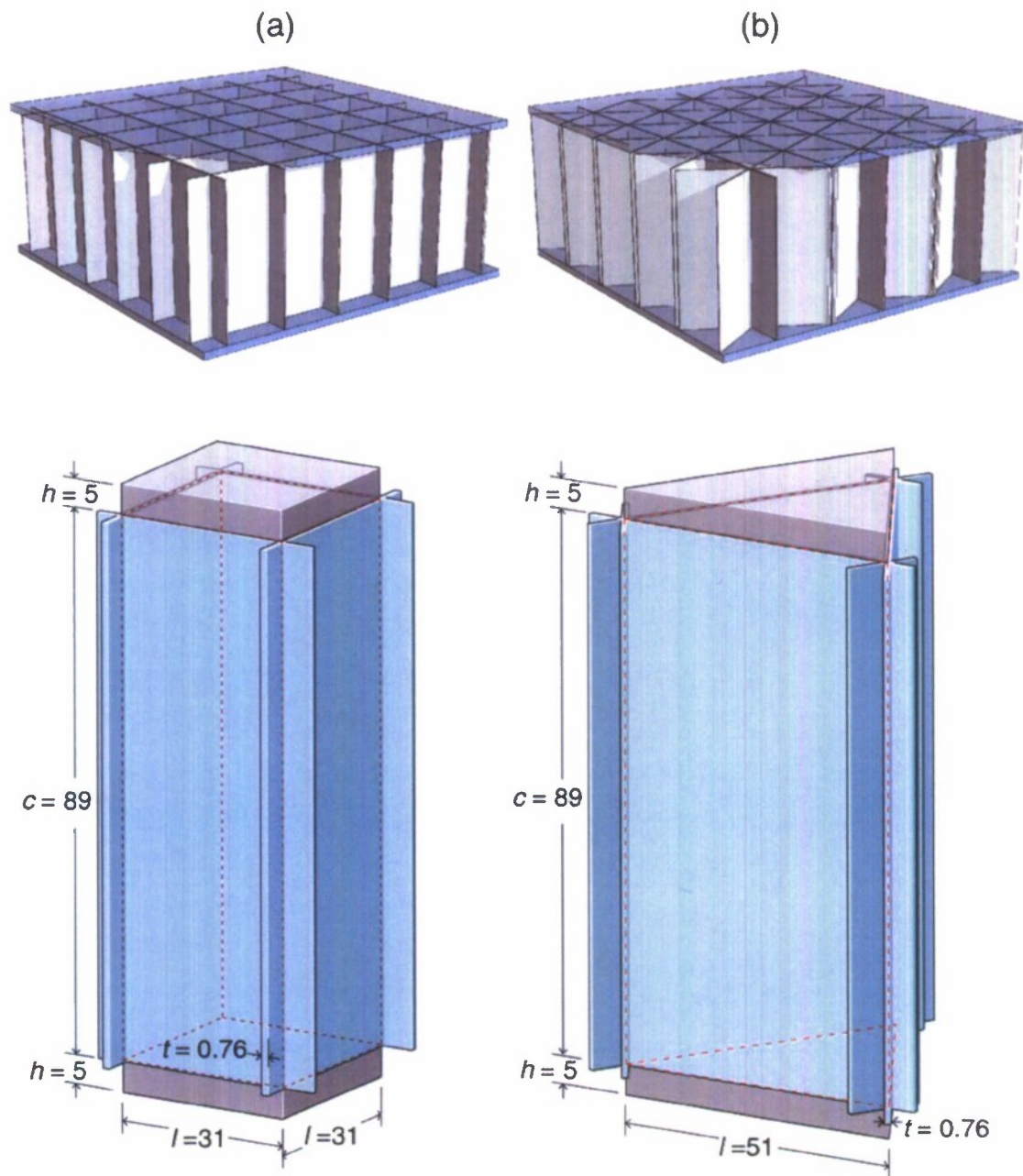
Figure 1: Sketches of the (a) square-honeycomb and (b) triangular honeycomb sandwich cores. The unit cells of the core with all relevant core dimensions marked in mm are also included.
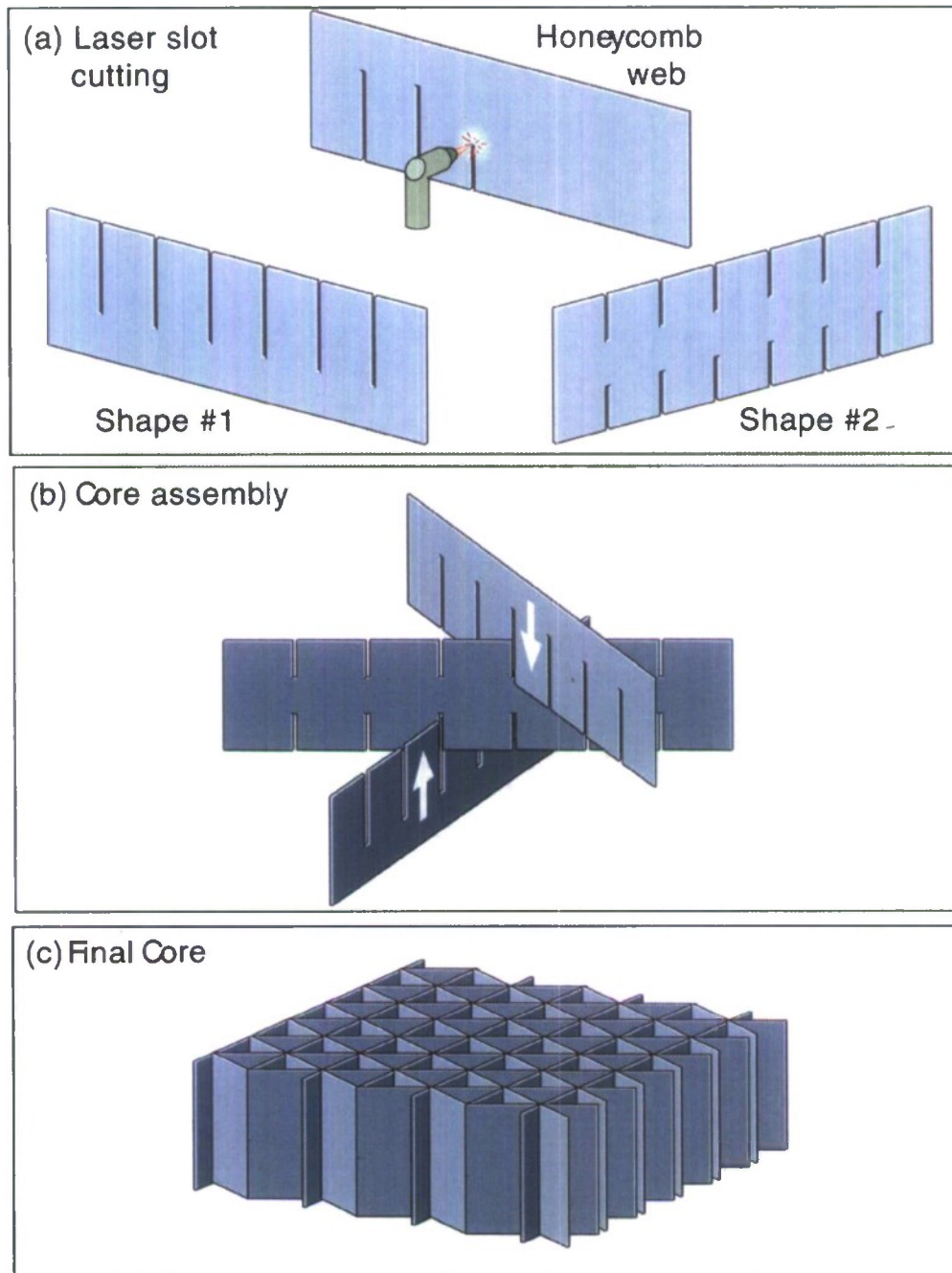
Figure 2: Sketch illustrating the manufacturing route of the triangular honeycomb. (a) The 2 shapes of slotted sheets employed, (b) the slotting together of the constituent elements and (c) the assembled triangular honeycomb core.
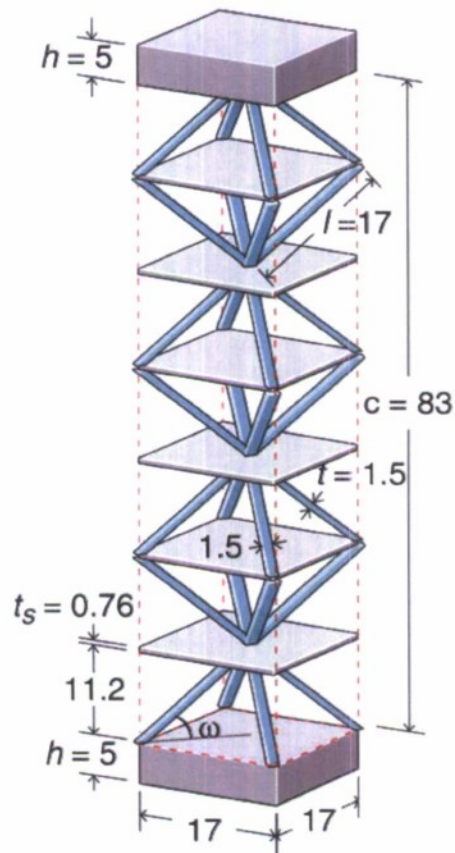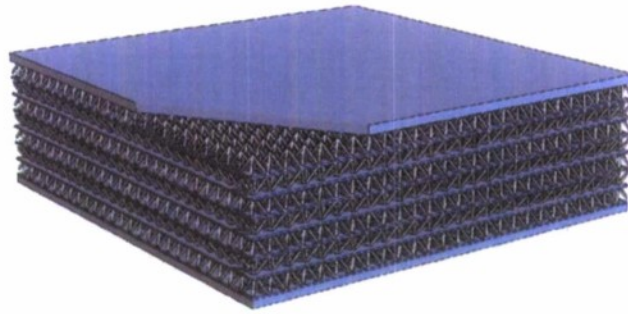
Figure 3: Sketch of the multi-layer pyramidal truss sandwich core. The unit cell of the core with all relevant core dimensions marked in mm is also included
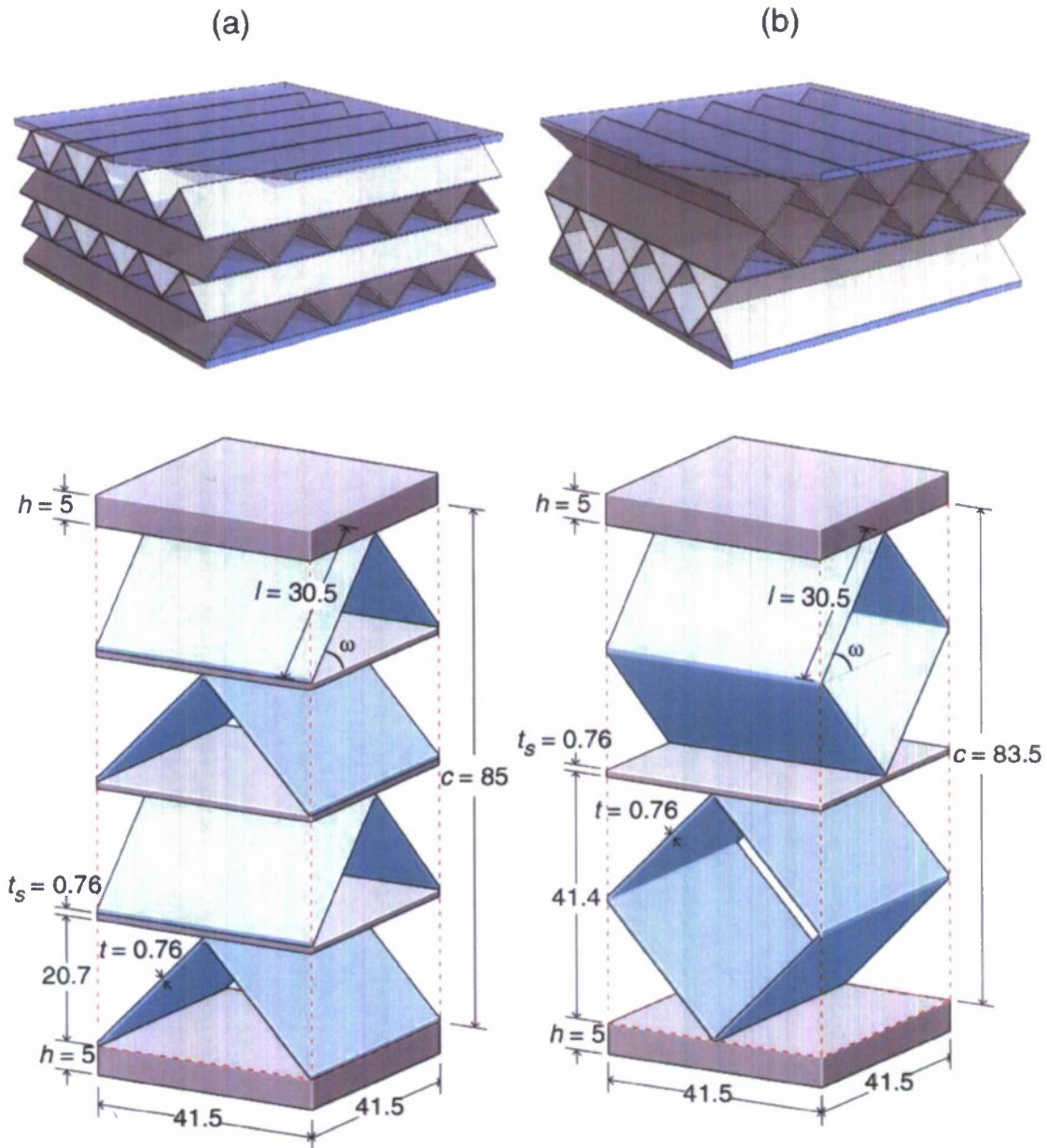
Figure 4: Sketches of the (a) triangular corrugation and (b) diamond corrugation sandwich cores. The unit cells of the core with all relevant core dimensions marked in mm are also included.
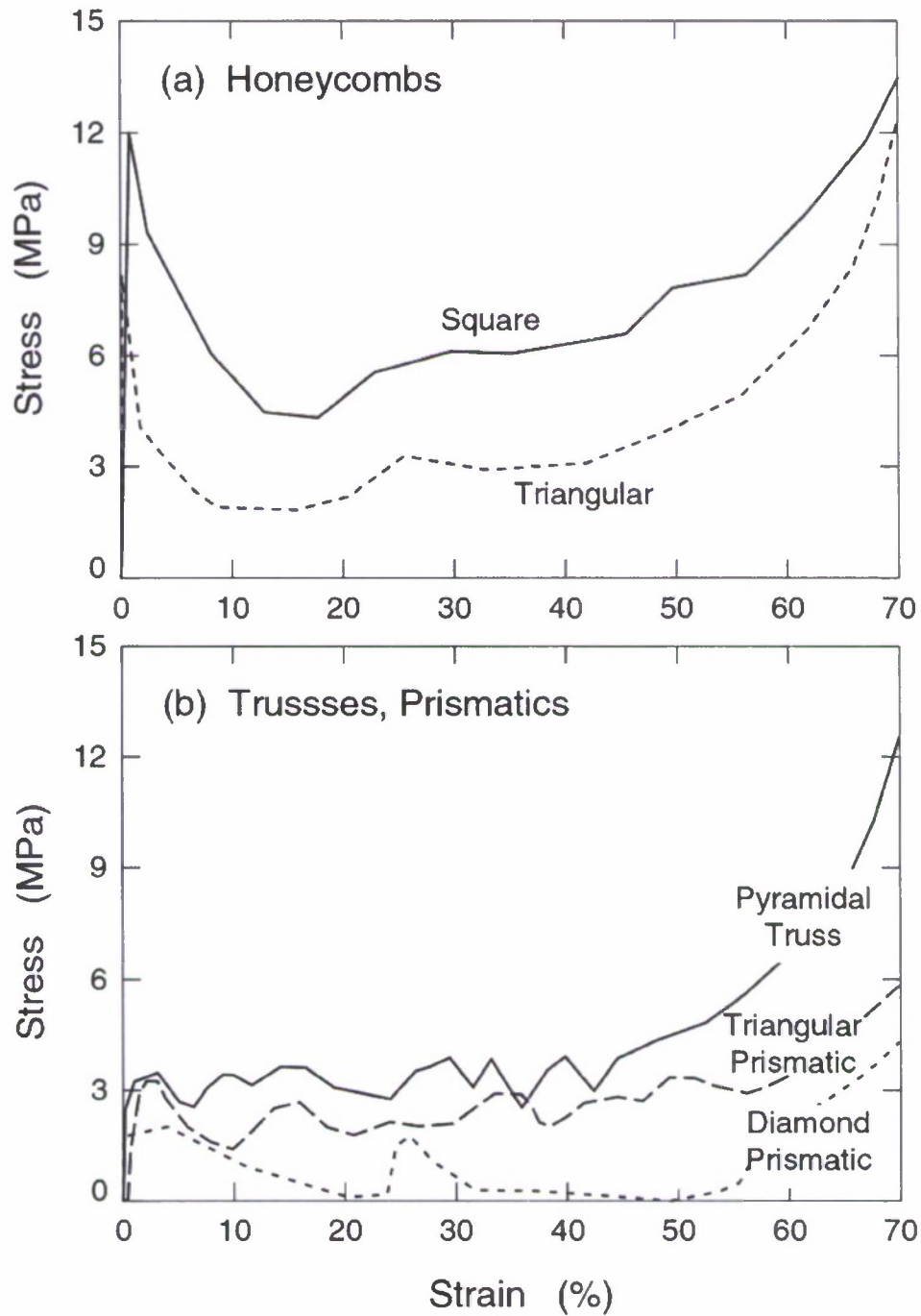
Figure 5: Measured quasi-static compressive nominal stress versus nominal strain responses of the (a) square and triangular honeycomb cores and (b) the prismatic corrugation and pyramidal truss cores.

All dimensions in mm

Φ900

203 x 203 *DETASHEET* explosive sheet

Detonator

Blast wave propagation

Water

H

Cover plate

Gage columns (4)

Gage column tray

Specimen tray

Strain gage

Support frame

Base

All dimensions in mm

Φ203

Test sample

~100

10

58.5

117

10

Φ38

470

HY-100 steel columns

Strain gage

HY-100 steel base
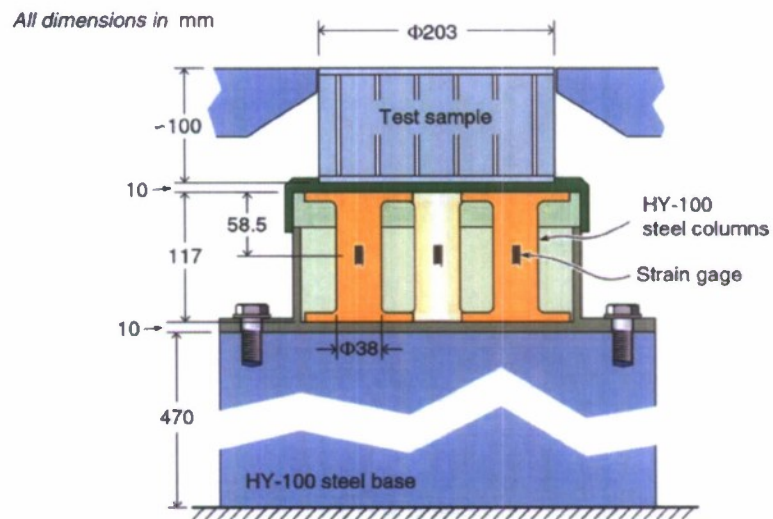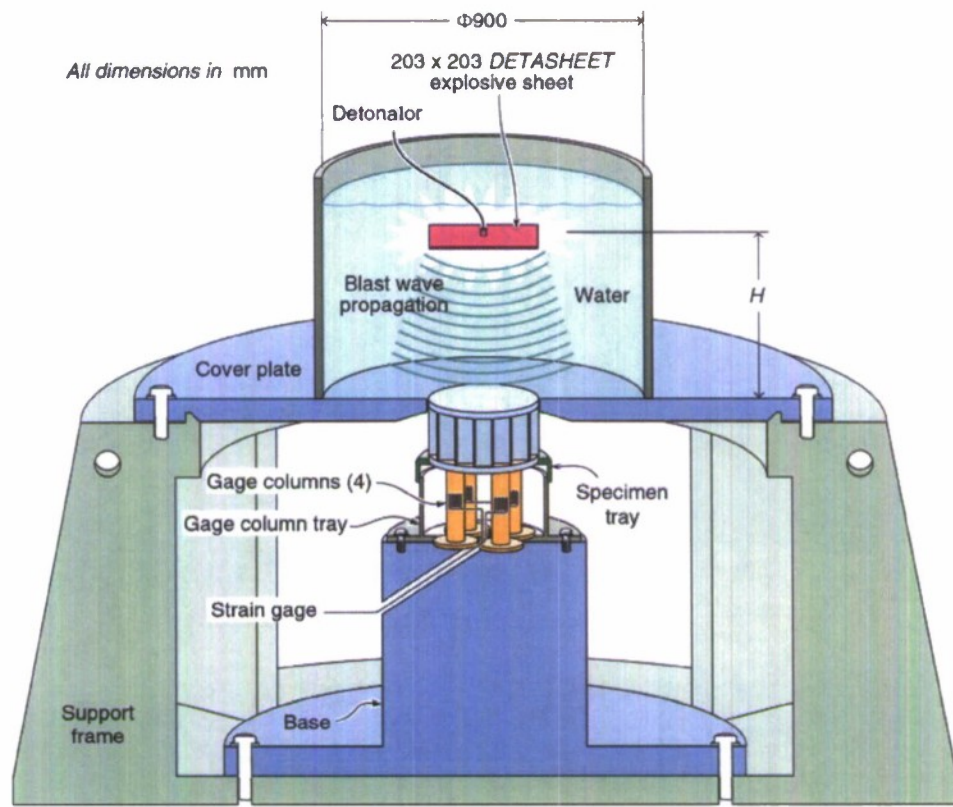
Figure 6: Sketch of the dyno-crusher apparatus with key dimensions marked. The inset shows a detailed view of the specimen and four strain gauged columns used to measure the blast loads transmitted through by the sandwich panel.
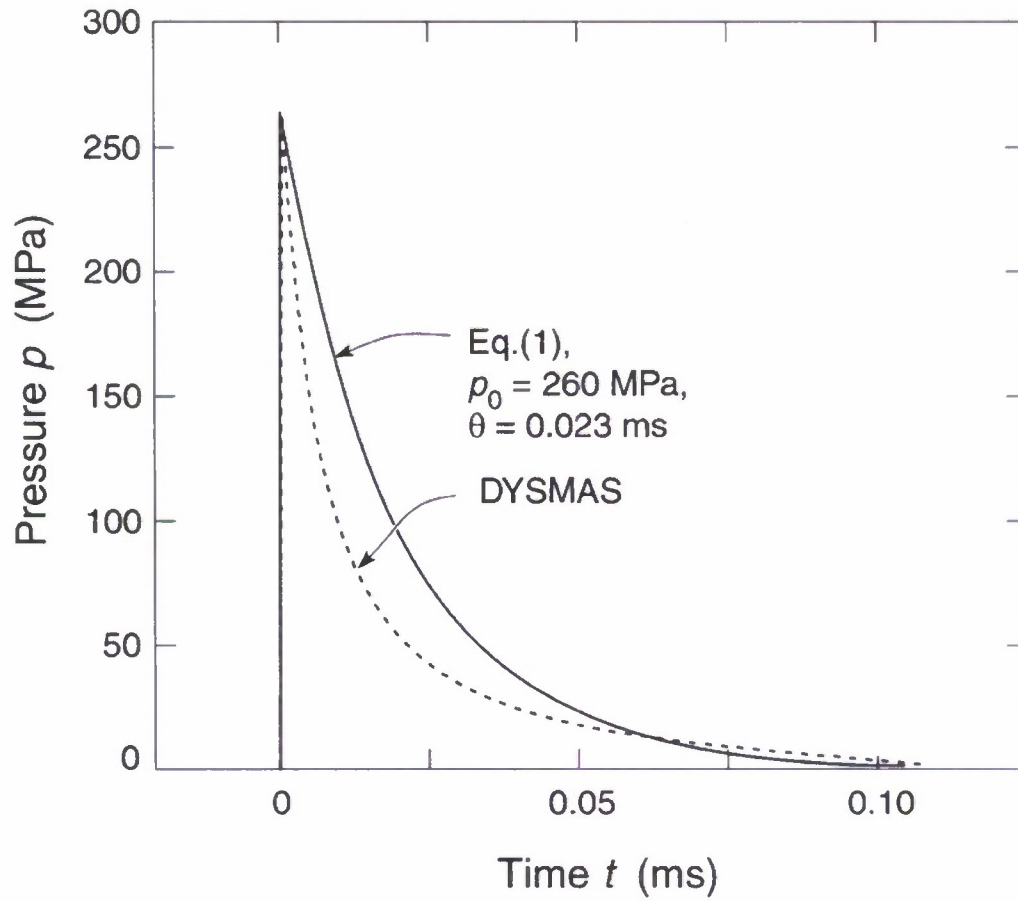
Figure 7: A DYSMAS prediction of the free field pressure p versus time t history generated by the denotation of the explosive sheet. The prediction is shown for a point located at a stand-off of $H = 0.1\,\mathrm{m}$ from the explosive sheet and $t = 0$ is defined as the time at which the pressure pulse reaches the measurement location. For comparison, the exponential pressures pulse given by Eq. (1) with the choices $p_0 = 260\,\mathrm{MPa}$ and $\theta = 0.023\,\mathrm{ms}$ is also included.
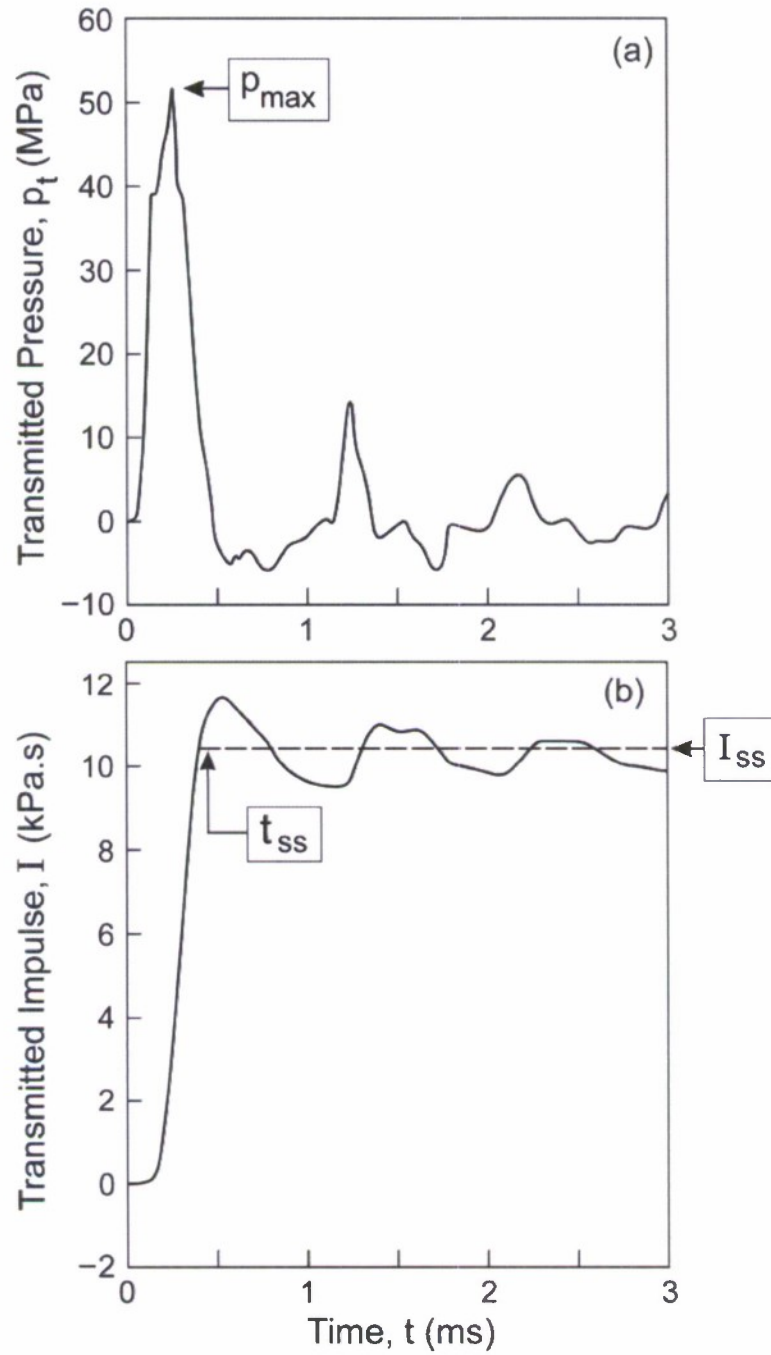
Figure 8: The measured temporal variations of the transmitted (a) pressure σ and (b) impulse I for blast loading of a reference solid Al cylinder. Time $t = 0$ is defined as the time when the blast wave impinges on the wet face of the cylinder.
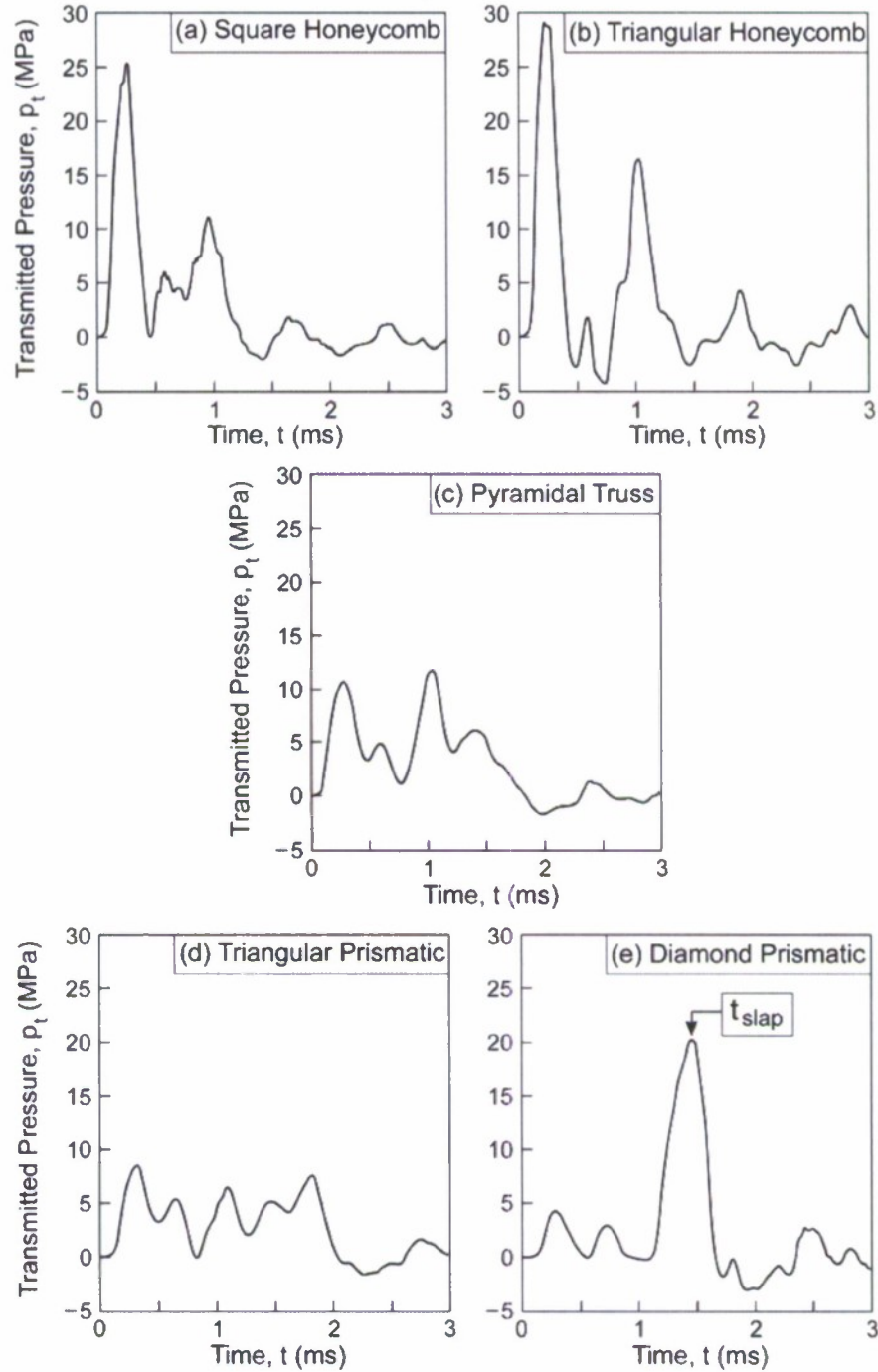
Figure 9: The measured temporal variations of the transmitted pressure p_t for the five sandwich cores investigated here. (a) square-honeycomb, (b) triangular honeycomb, (c) multi-layer pyramidal truss, (d) triangular corrugation and (e) diamond corrugation. Time $t = 0$ is defined as the time when the blast wave impinges on the wet face of the sandwich panels.
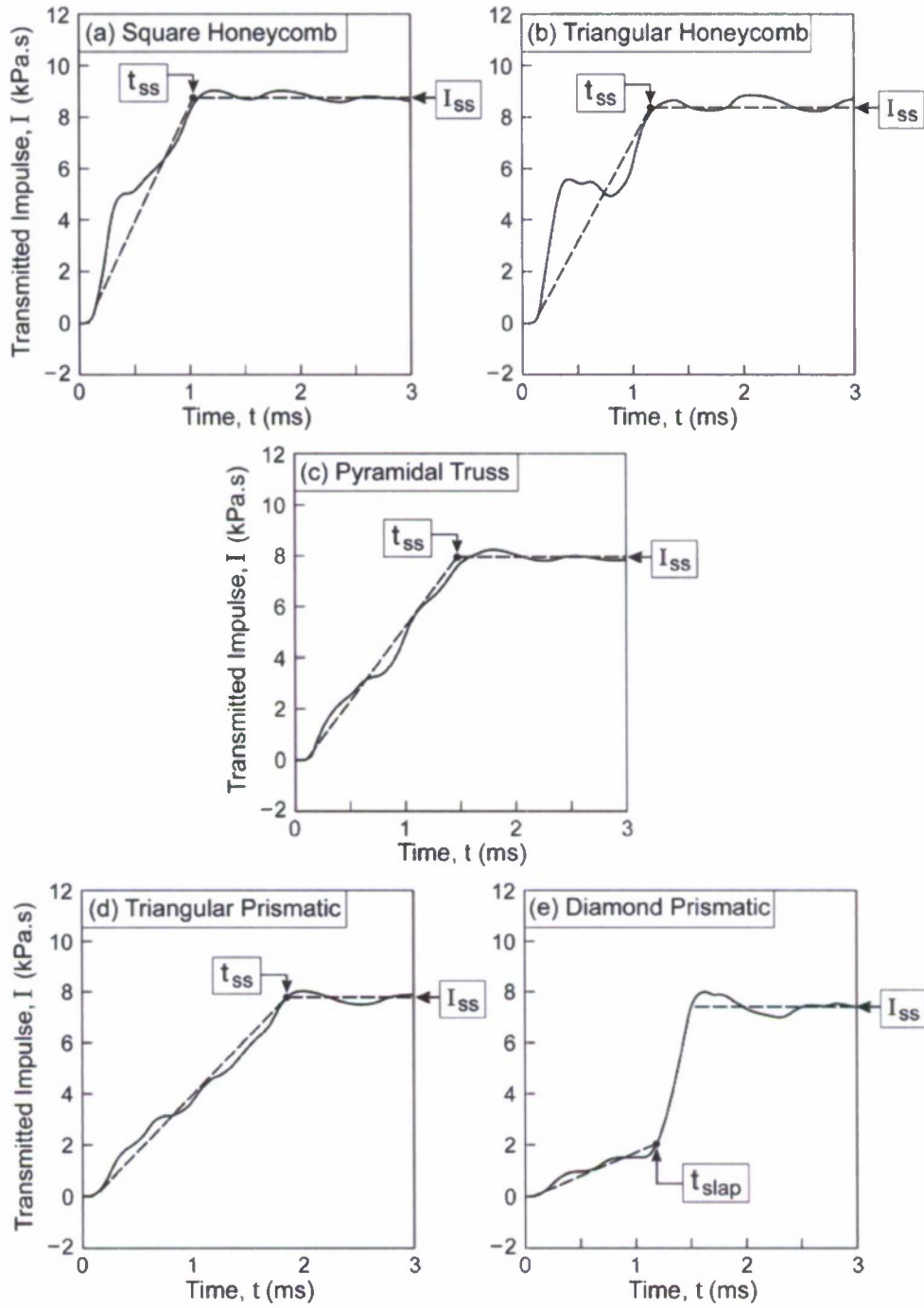
Figure 10: The measured temporal variations of the transmitted impulse I for the five sandwich cores investigated here. (a) square-honeycomb, (b) triangular honeycomb, (c) multi-layer pyramidal truss, (d) triangular corrugation and (e) diamond corrugation. Time $t = 0$ is defined as the time when the blast wave impinges on the wet face of the sandwich panels.
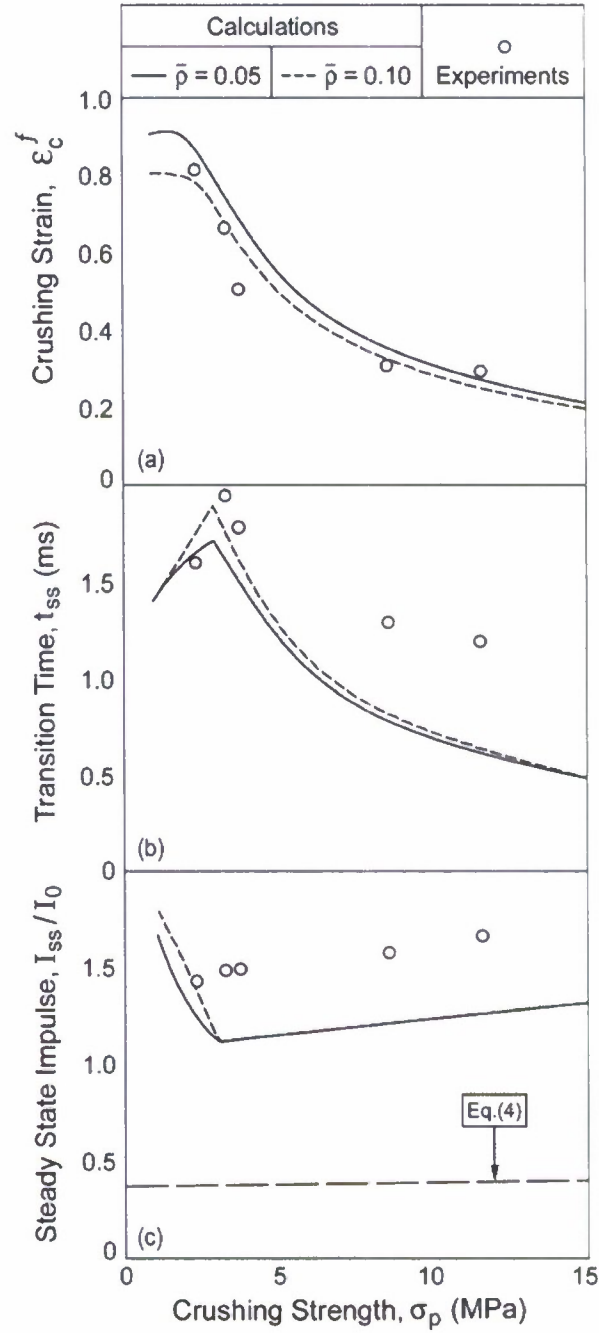
Figure 11: The measured (a) final core compression ε_c^f, (b) time t_{ss} corresponding to the knee prior to the plateau in the impulse versus time curves and (c) the steady-state transmitted impulse I_{ss} for the five cores tested here. The measured values are plotted against the analytical estimates of their respective static core strengths σ_p from Table 1. Also included are FE predictions for two choices of the core relative densities $\bar{\rho} = 0.05$ and 0.1 and the analytical prediction of the transmitted momentum, Eq. (4).
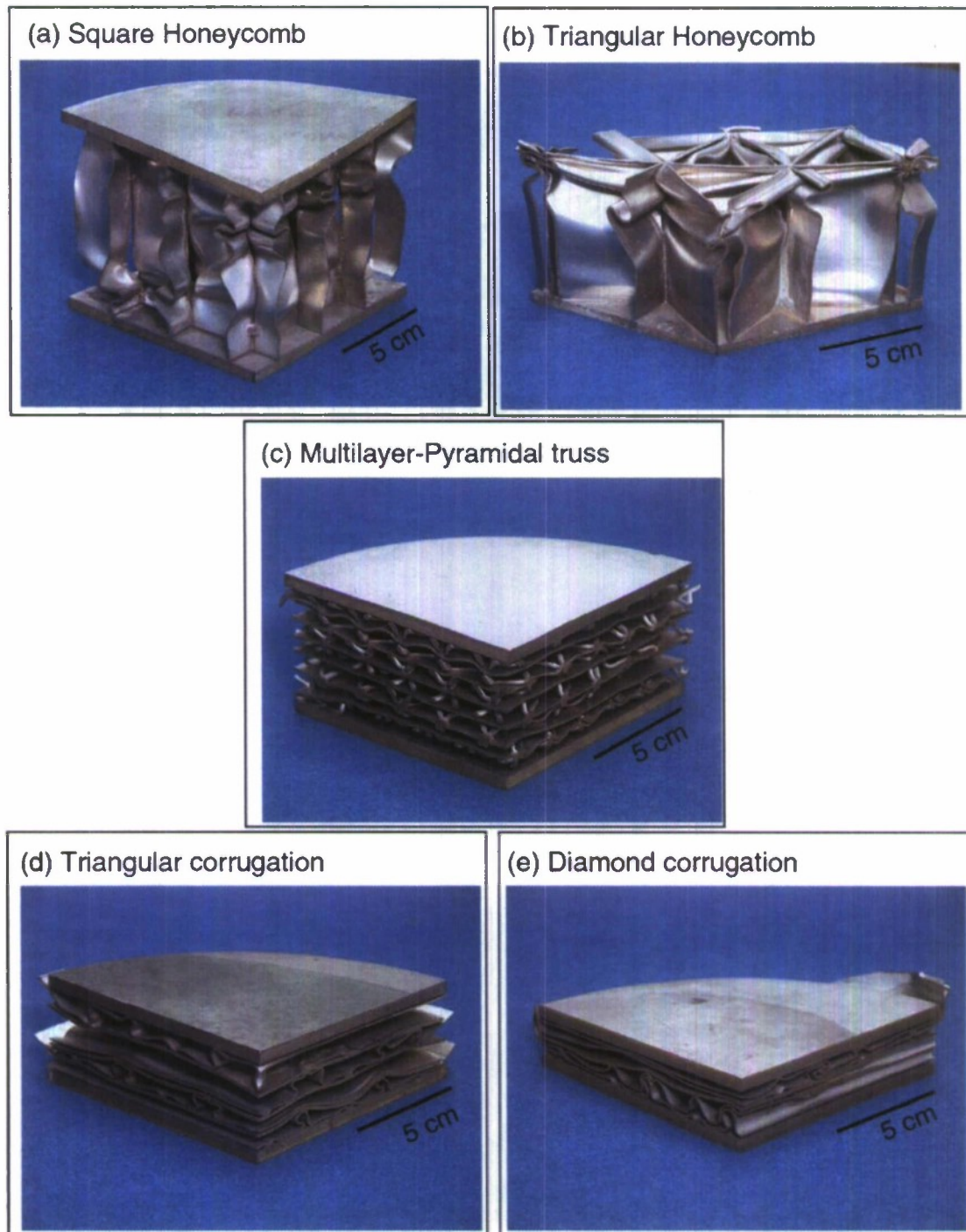
Figure 12: Photographs of the dynamically tested sandwich panels. The panels are sectioned along two orthogonal diametrical planes. (a) square-honeycomb, (b) triangular honeycomb, (c) multi-layer pyramidal truss, (d) triangular corrugation and (e) diamond corrugation.
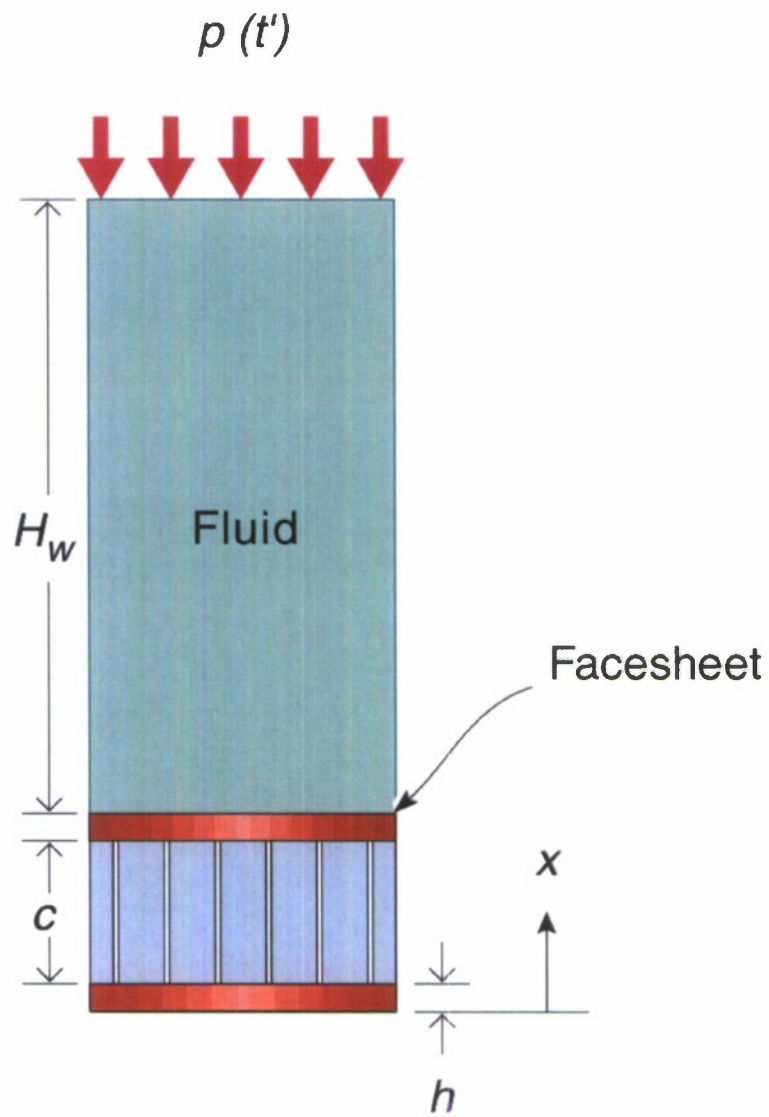
Figure 13: Sketch of the one-dimensional boundary value problem analyzed to investigate the response of the sandwich panels in the "dynocrusher" tests.
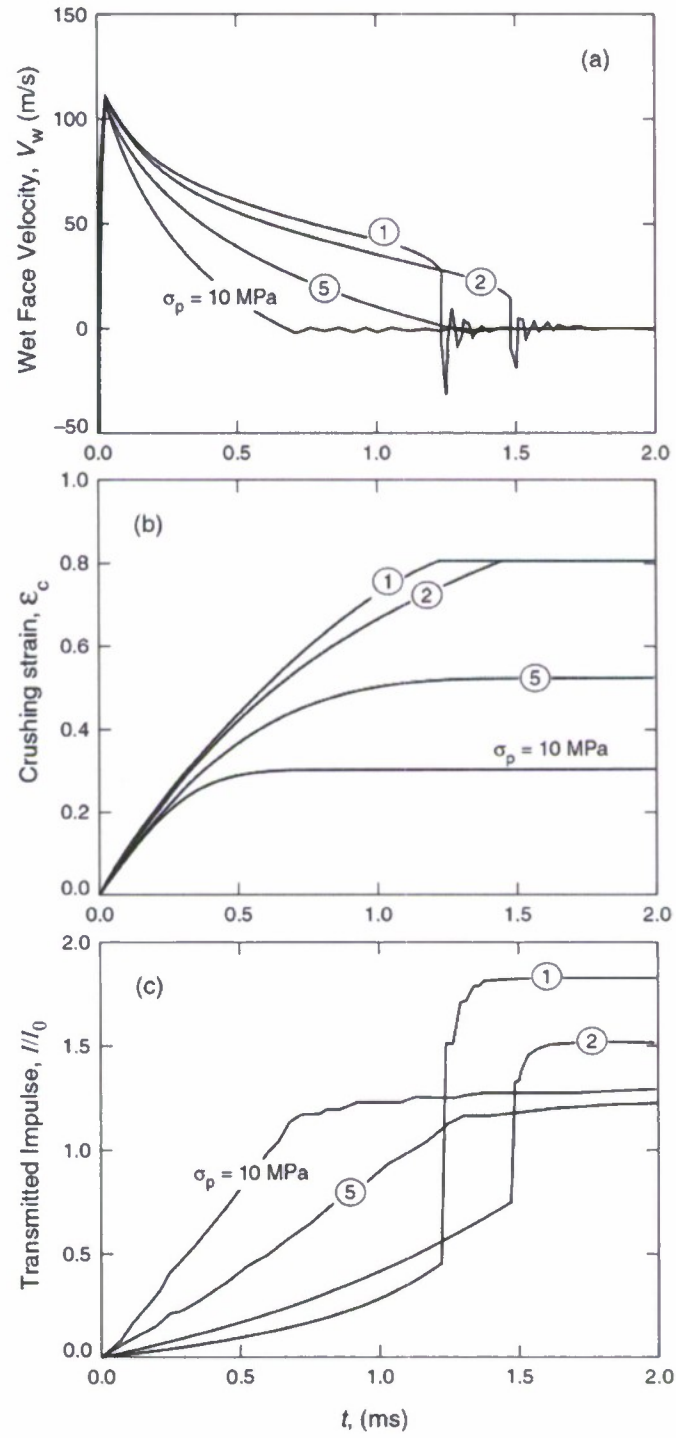
Figure 14: FE predictions of the temporal variations of (a) the wet face velocity v_w, (b) core compression ε_c and (c) areal impulse I transferred to the rigid supports for selected values of the core strength σ_p of the $\bar{\rho} = 0.1$ sandwich cores.

28

SSM Shipyard Fabrication Tiger Team Report

Jack Goeller and John McNelia (ATR Corp)
Phil Dudt and Rob Michaelson (NSWC/Carderock)
Ken Kiddy (NSWC/Indian Head)
Y Murty, Kerry Elzey and Harry Burns (CMI)
Michelle Riley (Bath Iron Works)
Tony Evans (UCSB)
Kumar Dharmasena, Phil Parrish and Haydn Wadley (UVA)

8/22/2005

A tiger team was commissioned by Ed Johnson during the SSM annual meeting in Dec. 2004. The objective was to investigate the detail issues that would be encountered with full scale fabrication and shipyard integration of the blister protection concept being developed under the SSM program. The working team members were drawn from NSWC-CD, ATR, CMI, Bath Iron Works, the University of Virginia and UCSB. Between February and May 2005 the team met on numerous occasions via telecom conferences and exchanged views and finally came to a consensus resolution. This report summarizes the outcome of the Tiger Team's efforts to date.

Charge to the Tiger team

The Tiger Team was tasked to develop concepts for the full-scale fabrication of a blast protection blisters compatible with shipyard construction practices.

Issues that were addressed included:

1)   Methods of blister attachment to the hull

2)   Methods for assembling/joining (core and face sheet) components to create panels and blisters

3)   Integration of the blister with the bilge keel consistent with ship yard practices

4)   Methods for welding and inspecting full scale panels which are also applicable to second iteration 1/5th scale panels

The team has investigated fabrication methodologies for the three core topologies down selected from 1/12 th scale panel testing at NSWC, Carderock and the various simulation studies at Indian Head and ATR. Fabrication considerations include sub-component fabrication of various topologies including joining and inspection, and assembling them into a full scale blister. Attachment of the blister to the ship hull without effecting the ship's hydrodynamic performance was also considered in this effort. The team has identified a conceptual approach to the full scale fabrication of blister components (tiles), the assemble of these (tile) components into a full panels and the shipyard installation of these panels to create a blister on a ship. The team has sought to identify the critical issues that require further development thereby reducing the likelihood of surprises late in the program.

Blister Assembly Concept

Blister Layout

Sub-panel

All dimensions in feet

Tile

Tile to Sub-panel to Panel Configuration
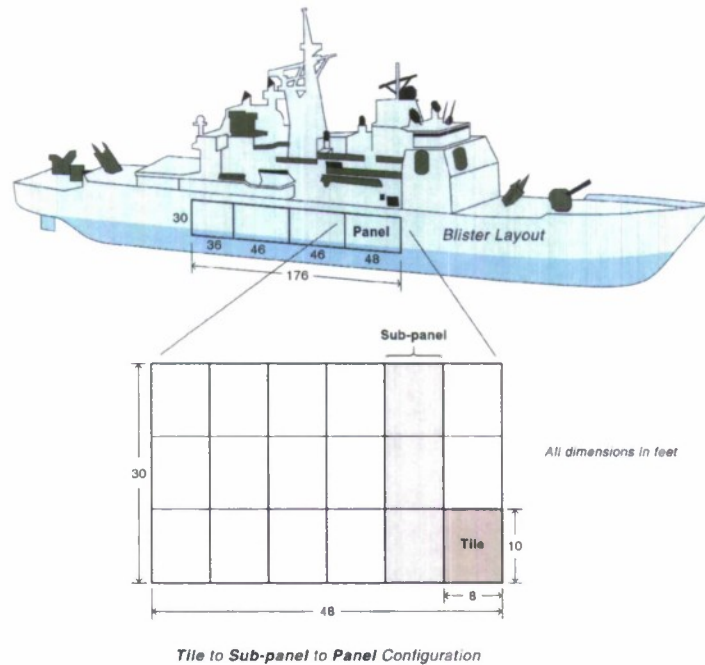
A typical preassembled blister panel will be nominally 30 feet high and a maximum length of 48 feet. The length will be shorter at other bulkhead locations and possibly limited to nominally 24 feet to facilitate fabrication and provide additional weld locations to the hull. The general approach for full scale fabrication involves fabrication of flat or curved tiles (10'x8'x2') outside the shipyard. Theses tiles are then assembled into sub-panels either at the shipyard or at an off-site vendor. The sub-panels are then attached to the ship hull. The shipyard has the lifting and sub-panel positioning and welding capabilities for this.

The blisters are intended to cover bulkhead stations 5-9 of a DDG class vessel. Panels are intended to be attached at each bulkhead location station. This results in 4 panels each about 48' wide (but note that the individual bulkhead separations vary from 36' -48') welded to the ship at the bulkheads.

Blister panel assembly concept
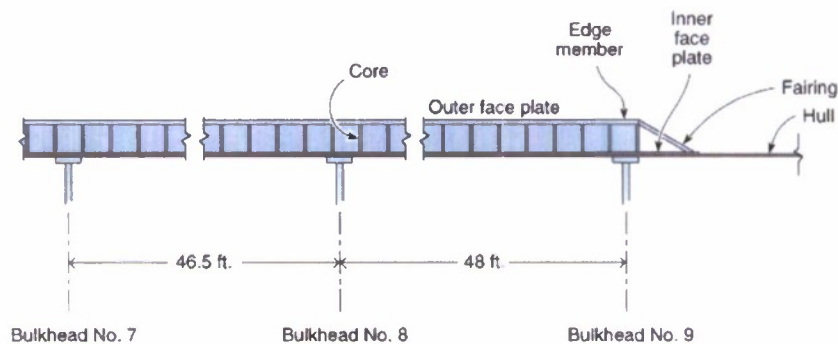
The blister panel consists of:

- The outer face plate,
- core,
- inner face plate,
- edge member, and
- the structural fairing.

The structural fairing will be joined to the top and bottom edge member by continuous longitudinal welds after the panels have been welded to the DH36/HY80 (upper longitudinal welds are to HY80 and have a pre-heat requirement) hull plate at the bulkhead and designated vertical frame locations.

Design guidelines

• Baseline design characteristics
- Core height = 24 inches
- Outer face thickness = .625 AL6XN
- Inner face thickness = .375 AL6XN
- Nominal hull thickness = .375" to 1"
-Core density = 0.04 to 0.05

• Sandwich panels preassembled into watertight sections (approx. 40' x 30') that are welded to ship hull at bulkheads and/or frame stations

• Structural fairing and edge member welded around entire perimeter designed to transfer sandwich panel membrane loads into hull (remove 'via welding')

A notional blister design has been proposed. It has been used as the baseline for an assessment of manufacturing approaches.

Shear and bending load analysis

Frame Stations

Ship Shear and Moment

Attachment of Blister to Hull

Moment

Shear

Max Ship Shear = 1339 Long Tons (Station 7)

Hull

Core

Weld

30'

Max Blister Shear = 490,000 Lbs/Side
Weld Shear Stress ~ 8000 psi
Blister Bending Stress ~ 12000 psi
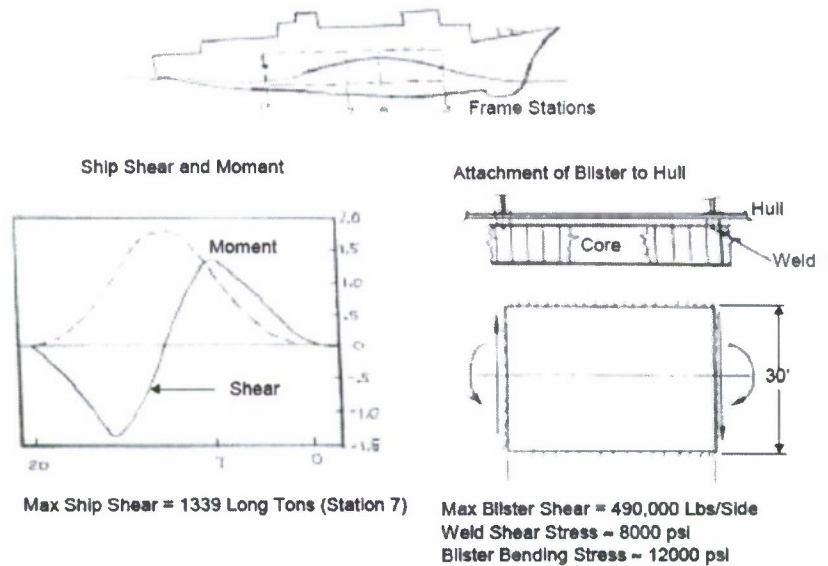
A preliminary analysis was made of the shear and bending loads on the ship hull and blister during ship hogging and sagging . Bending and shear loads during ship sagging were found to be less severe than hogging. Estimated bending stress and shear stress in the welds are well within acceptable limits. Maximum deflection of the blister between bulkheads 5 and 9 was estimated to be about one inch. Hence it was concluded that the blister will conform to ship bending and deflection during ship motion.

Sandwich core concepts

1: Square Honeycomb
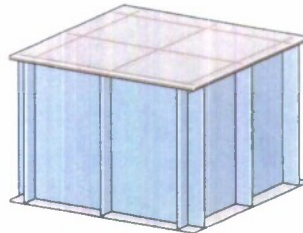
2 X - Truss
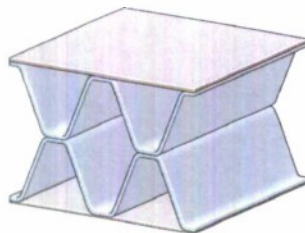
3 Pyramidal (3-layers)
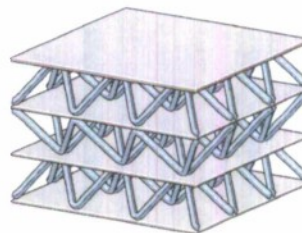
The 1/12 scale program identified three candidate core topologies and a preferred core thickness (2') for DDG protection. The three core topologies selected for 1/5 scale evaluation are shown above. The optimum relative densities have been identified by DYSMAS analysis (shown later). The tiger team has identified viable full scale fabrication approaches for the three topologies.

The fabrication process involves manufacture of the core tiles, their attachment to face sheets followed by sub-panel and blister assembly. 100% nondestructive evaluation of the node integrity is recommended during core tile fabrication. An acceptance criterion for the nodes needs to be identified by the SSM team, and the efficacy of node repair processes needs to be assessed.

Core Tile Fabrication

- Plate metal forming
- Precision cutting
- Core Assembly
- Joining/Welding

Each core topology has a different manufacturing path.

•X-core topology uses plate forming

•Square honeycomb requires precision cutting

•Pyramidal core requires bar forming or precision cutting depending on the fabrication method chosen

All core topologies require precision joining/welding of the nodal area. This requires precision indexing and joint fitting with weld (node inspection) conducted periodically during the fabrication sequence.

Various welding methods were considered: Gas Tungsten Arc Welding (GTAW) with a Pool Enhancing Compound (PEC), Micro Plasma Welding and Laser Welding. Each core has a different optimal welding approach.

Square honeycomb core plate metal assembly

Interlocking assembly of 24" wide, 0.375" thick AL6XN slotted plates, with the slots spaced at 18.75" to give a core relative density of 4%.

0.375"

Core density, $\rho = 2t / l$ (4%)

t

24"

l = 18.75"
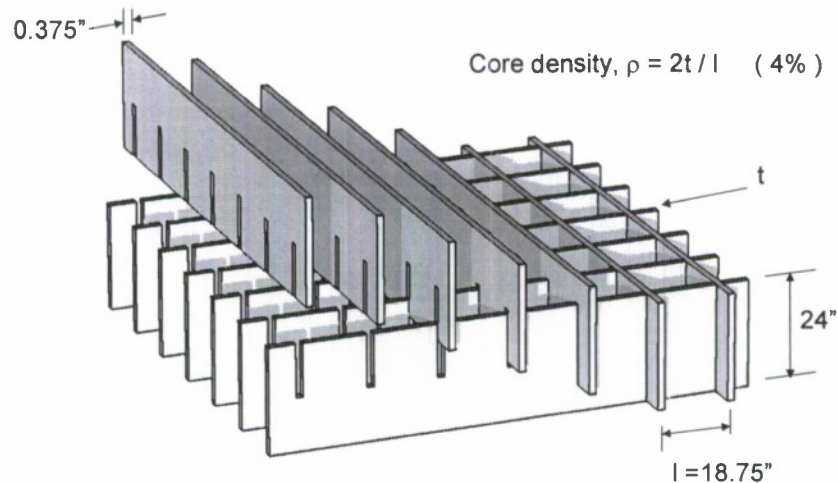
The slots in the plate strips can be by machining (milling), laser or abrasive water jet cutting. Design core relative density is 4%. Plates are assembled as shown and then welded by gas tungsten arc welding (the 18.75" box spacing is sufficient for weld head access). 100% weld inspection is recommended at this stage. The methods of weld inspection are discussed later. Fixturing to eliminate distortion and ensure tile fit is required. No stress relief heat treatment is believed (at this stage) to be necessary.

Note: No weld tabs are envisioned for face sheet- core attachment in the full scale system.

9

Plate bending for making individual 'hat' shaped unit cell for X-truss core

Press brake punch

Die
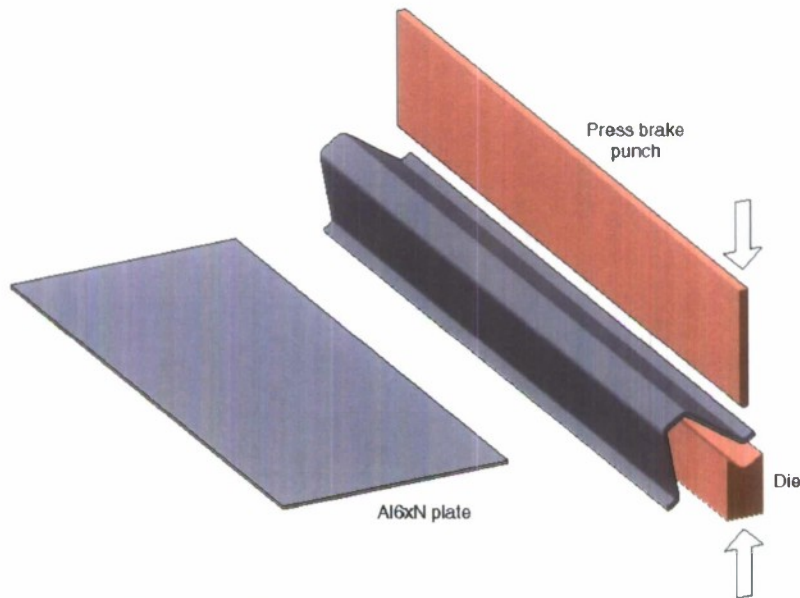
Al6xN plate

A 5% core density has been identified as optimal. This translates into a 3/8" thick Al6XN plate. The AL6XN plate can be shaped into individual corrugations using a press brake equipped with a tool that makes each bend sequentially. A faster but as yet untested approach would seek to fabricate each corrugation in a single step (a total of four bends) using a tool designed as indicated above. This approach would involve plate stretching and a high load capacity press.

Tolerances are a significant issue. Plate spring back can vary from plate to plate and even place to place within a plate. This results in changes to the angles of the corrugations and therefore variances in the depth of the corrugations. Subsequent joining operations must be able to fill the node gaps with no loss of node strength or durability.

Weld 'hat' shaped unit cells to form X-truss core

Bend radius R

60°

AI6xN plate unit cell

Add and weld unit cells to form X-truss core

Core density ~ 5%

$t = 0.375"$

$l_1 = 2.62"$

$l_2 = 18.72"$

$R/t = 50/r - 1$

Where, r is the % reduction in area in tension
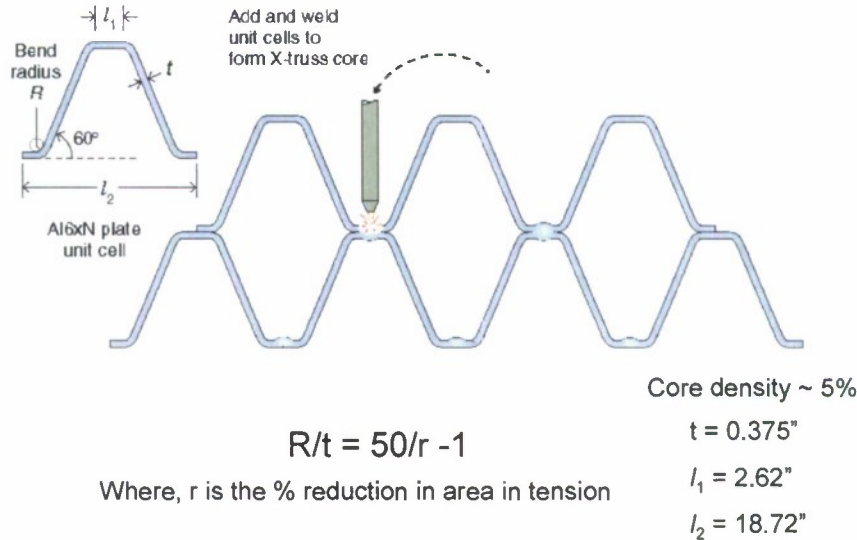
The fastest, least distorting approach for joining appears to be laser welding. These crack free bend features are established by the minimum bend radius of the plate material. The reduction in area of a tensile test coupon of AL6XN (r) is about 25%. Therefore, for AL6XN, R/t ~ 1. The proposed baseline approach also results in a significant crevice that may be susceptible to corrosion. Multiple welds that cover the nodal contact width (2.62") may be a solution. Further work is needed by the SSM team to address this issue.

Two competing approaches for pyramidal core fabrication

Step 1: Bend square or round bar into serpentine shape
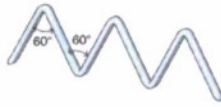
Step 2: Tilt strips and bring together bend points to form nodes

Step 3: Weld nodes
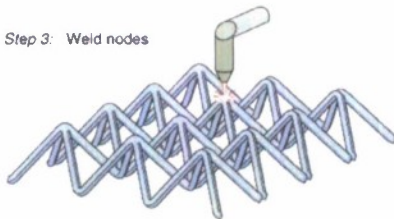
Step 1: Pattern cut strips
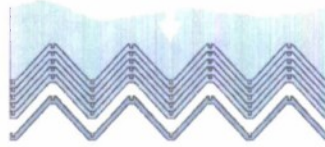
Step 2: Assemble slotted strips
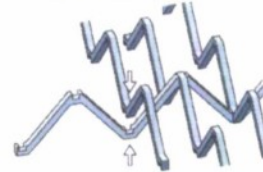
Step 3: Weld nodes
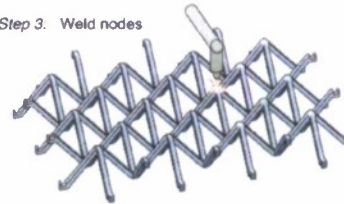
The optimal density for these cores is 5%. This translates into a truss member that is 5/8" thick. The node-to-node spacing is ~11". Two concepts have been identified (but not verified) for the manufacturing of pyramidal cores at the full scale level. Approach 1(bending of bar stock) appears the least expensive and has unresolved spring back issues affecting node gap tolerances. The precision cutting approach (from plate) will not suffer from this problem and the components can be more easily assembled into the pyramidal structure. Weld tooling might also be simpler. The preferred welding approach appears to be laser welding (with a filler metal). This results in a weld that is about the same dimensions as the node. The bending route will have minimum bend radius issues but these may be more easily resolved because the weld covers most of the node area. The machining route does not suffer from this issue. Further developmental efforts for to identify the best route for manufacture of full scale pyramidal cores are required.

Full-scale core fabrication issues

» PROS

- Square Honeycomb core
  - Better material utilization
  - Low manufacturing cost
  - Curvature friendly

- X-core
  - Best material utilization
  - Good weld access
  - Simple for flat panels

- Pyramidal core
  - Best curvature friendly
  - Acceptable material utilization

» CONS

- Square Honeycomb core
  - Precision cutting requirement for conformal fit to curved surface

- X-core
  - Large crevices at joints potential sites for corrosion

- Pyramidal core
  - Difficult to join individual nodes at the seams

From a strictly manufacturing perspective each of the three cores has pros and cons. All the problems can be overcome and we conclude that all concepts are manufacturable at the full scale. Technical cost modeling has not been attempted to determine if there will be significant cost differences.

Ship scale integration

Two approaches

1. Sandwich tiles ⟶ Assemble panels ⟶ Attach Panels to hull to form blister

2. Dry side face attachment ⟶ Core build-up ⟶ Wet side face sheet attachment

	PROS	CONS
Approach 1:	•Minimum Shipyard Fabrication •Use of Best Welding Practice for sandwich tiles •Assembly of sub-panels and panels done on the floor using shipyard welding practice	None
Approach 2:	Shipyard will have to develop In house manufacturing technology	•Additional shipyard capital investment •Deviate from current shipyard production

Conclusion: Choose Approach 1

Two approaches were considered for blister construction and ship attachment. The first approach looks at off-site fabrication of tiles and sub-panels in a controlled environment, and then integration of the sub-panels into panels to make up the blister at the shipyard, using available shipyard fabrication methodologies. The second approach requires the shipyard to perform the complete fabrication of all components of the blister and assemble the blister on to the hull, based on commercially available plate material sizes. In this second approach, the core build-up and face sheet attachments are more challenging than the first since all component attachments will need to be done on a vertical (or near vertical) plane in a dry dock. In approach 1, the precision welding of the core and the attachments can be performed by the vendor independent of the shipyard facility and delivered to shipyard for final blister assembly to the hull. Precision welding of the face sheet and core in the 2nd approach is more challenging as it would be very time consuming, costly, and difficult to control or compensate for weld distortion.

14

Panel Fabrication
(From Tiles to Panels)

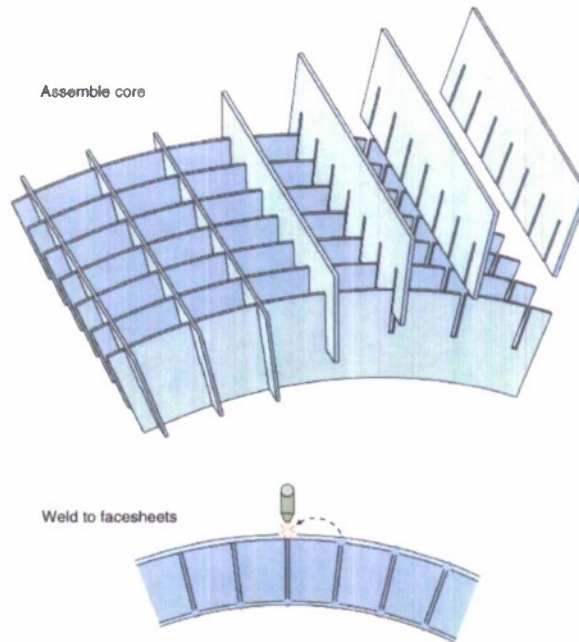**Panel Fabrication: square honeycomb**
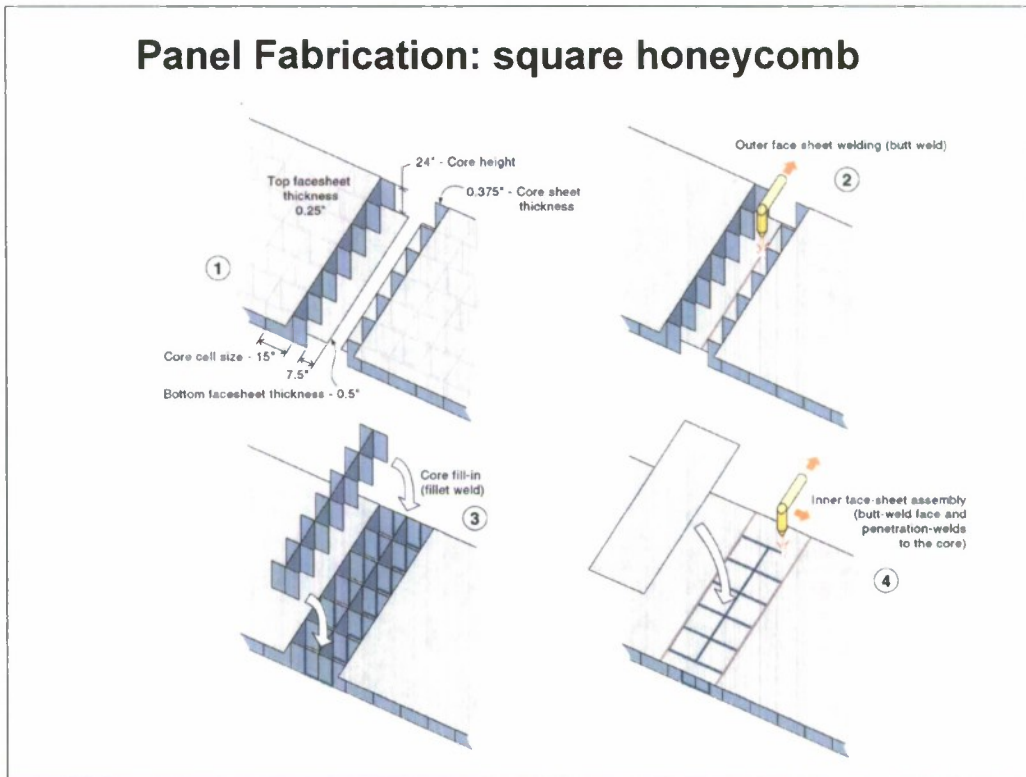
The tiles will be assembled into sub-panels using a seaming technique that allows wet side face sheets to be welded by conventional welding techniques such as plasma or GTAW. The center core fill-in section is welded to the tiles on either side and the dry side face sheet is welded to the core using the same welding method employed for joining the wet side face sheets. The issues that require special attention are blind welds on the dry side face sheet attachment to the core. This can be solved by key hole welding of the core fill-in section to the face sheet. **The amount of weldment needed still needs to be determined.**

Panel Fabrication: X-truss
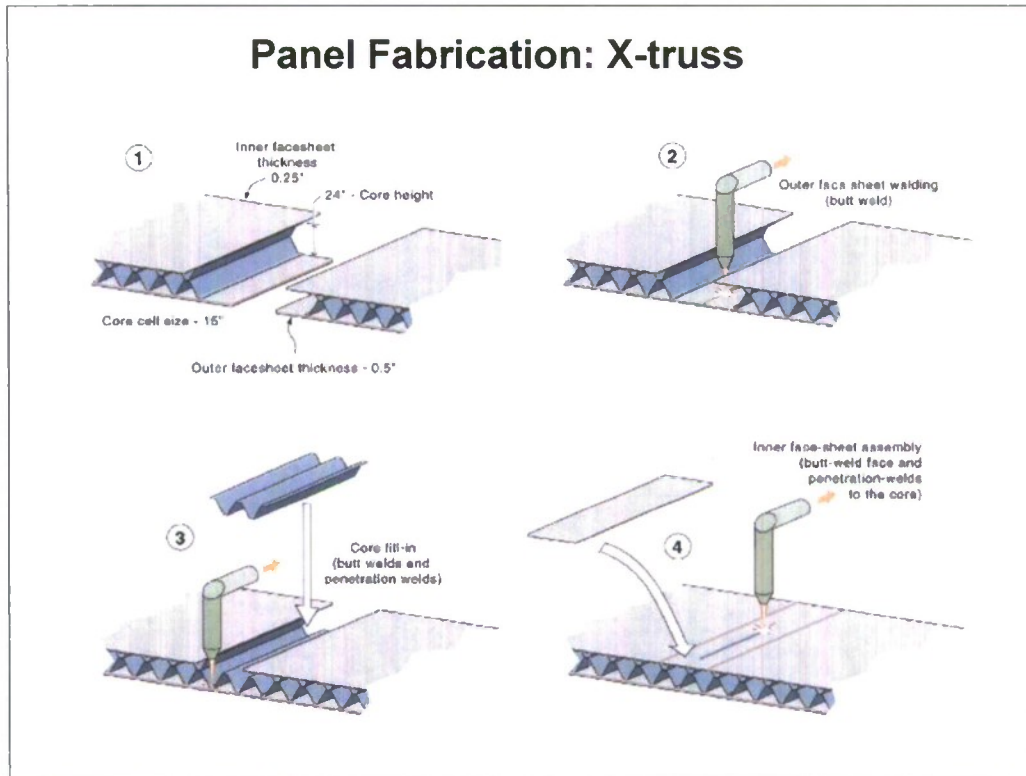
The tiles will be assembled into sub-panels using a seaming technique that allows wet side face sheets to be welded by conventional welding techniques such as plasma or GTAW. The center core fill-in section is welded to the tiles on either side and the dry side face sheet is welded to the core using the same welding method employed for joining the wet side face sheets. Note the butt welds are onside full penetration welds on both wet and dry side. The issues that require special attention are blind welds on the dry side face sheet attachment to the core. This can be solved by key hole welding of the core fill-in section to the face sheet.

Panel Fabrication: pyramidal core
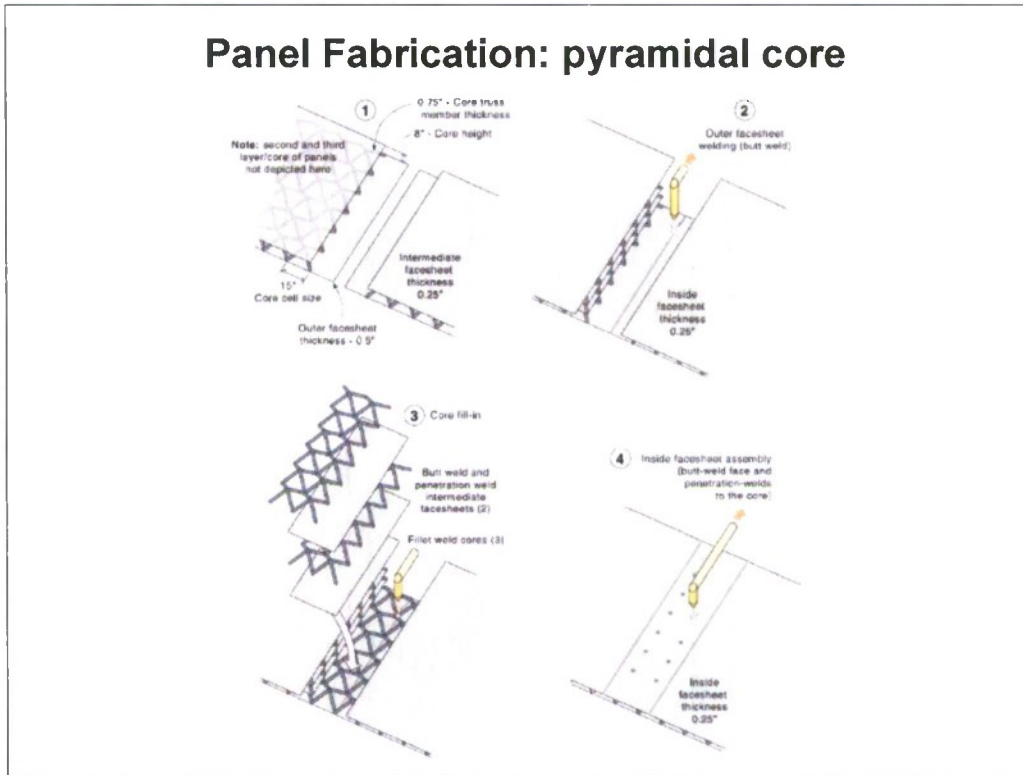
The fabrication methods for seaming the tiles are similar to the other two cores with some exceptions. The edges of the seaming core segments will not be joined. **Joining the dry side face sheets to the core nodes require blind welds at the nodal points and require careful location alignment through the face plate – an area that requires further development, especially for panels curved in two directions. We note that thermal wave or ultrasonic imaging (or visual imaging/indexing prior to face sheet installation) may provide solutions.**

Curved square honeycomb tile fabrication

Assemble core

Weld to facesheets

Curved square honeycomb core is more complicated to fabricate. The face sheets are prefabricated to accommodate the curvature of the core. The weld methods are similar to the ones describe for the flat honeycomb core. Communicating the curvature between the ship yard and the vendor could be an issue.

Curved X-truss tile fabrication

Assemble and weld core elements
(onto inner, dry facesheet)
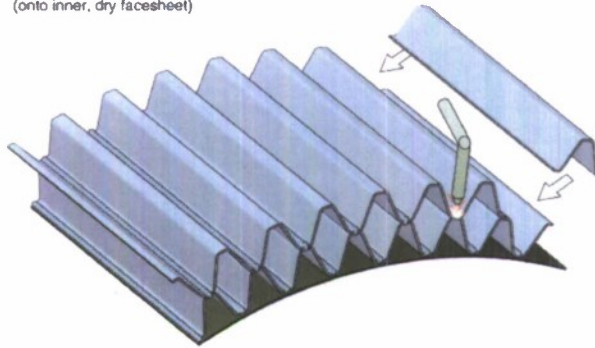
Weld outer (wet) facesheet
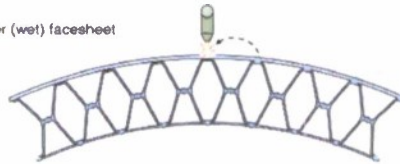
Must compensate for 2 different circumferences. This leads to Unit cell spacing with 2 different periodicities (the spacing on the wet side is larger than that on the dry side).

Curved pyramidal core tile fabrication

Step 1: Pattern cut curved slotted strips
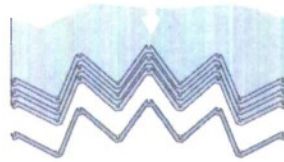
Step 2: Pattern cut straight slotted strips

Step 3: Assemble core
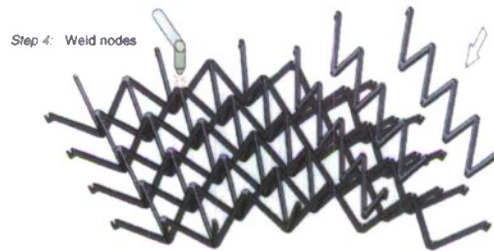
Step 4: Weld nodes

Step 5: Weld facesheets
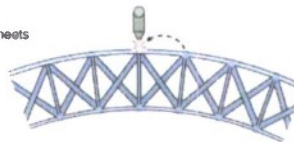
Alignment of the nodes, close tolerance requirement of the fit between the face sheets and the core are required. The fabrication methods are similar to ones used for flat tile fabrication.

Blister Assembly
(Panels to Blisters)

Panel attachment approaches

Two concepts

> Rail Attachment 1. Attachment to rails at transverse stiffeners
>
> Hull Attachment 2. Direct attachment to DH-36 hull

	PROS	CONS
Rail Approach 1:	•Rails provide flexibility to remove and attach blisters •Provides Manufacturing flexibility •Accommodates 'hungry horse' effect of the hull	•Need polymer filler to fill the gap between blister and hull to avoid slap •Added weight, process and cost
Hull Approach 2:	No parasitic rail weight	•Manufacturing difficult •Extremely time consuming and expensive

Conclusion: Choose Approach 1

Approach 1 allows bulk of the tile fabrication off site with easy access to the weldments. The sub-panels can be attached to the rails in place.

Approach 2 require full construction of all the blister components on site on the hull by progressive build up of each layer. The blister dry side contour has to closely match with the hull. Difficult to inspect the joints between the hull and the blister. Therefore approach 1 is more practical. Approach 2 is extremely difficult. It would involve paint removal for the entire area underneath the panels, which could only happen in a dry-dock facility for retro-fit of a DDG. Each weld would have to be inspected and repainted. It is much more expensive to fabricate something out on the shipways than in a controlled environment.

Rail placement detail
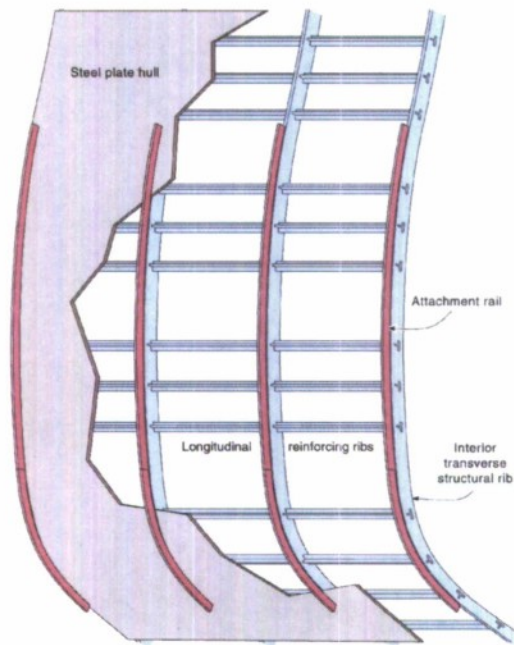
The rail materials has to be selected based on dissimilar metal joint strength.
The weld methods will use shipyard joining methods: i.e. GTAW, GMAW

Square Honeycomb, Sub-Panel to Sub-Panel Assembly – Rail Hull Attachment
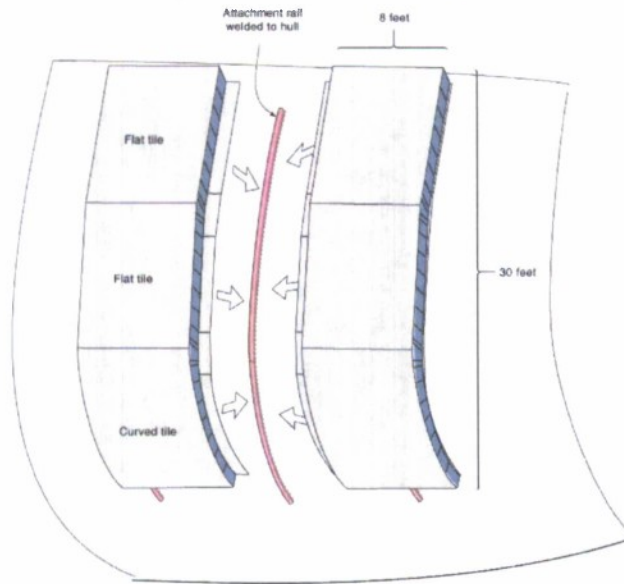
- Attachment rail shall be welded to hull at transverse stiffener location.

- Inner face sheet of sub-panels will be welded to attachment rail.

The attachment of sub-panels to the rails employ shipyard friendly fabrication practices. The joining methodology used herein is similar to the ones employed in joining tiles to assemble sub-panels. The dry side face sheet is attached to the rails on either side of the rail.

Square Honeycomb, Core Fill-in

Core filler added and welded
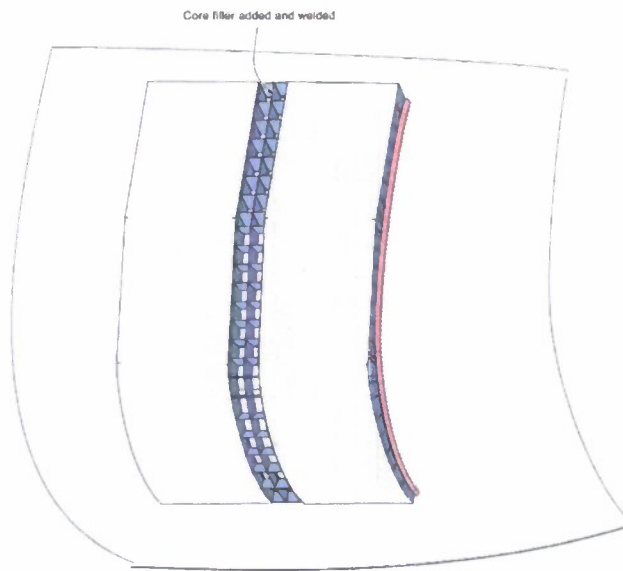
Full seam welds to achieve continuity of core.

The core segment is then attached to the dry side face sheet followed by attaching the edge members to the tiles.

Square Honeycomb, Wet Face Sheet Seam
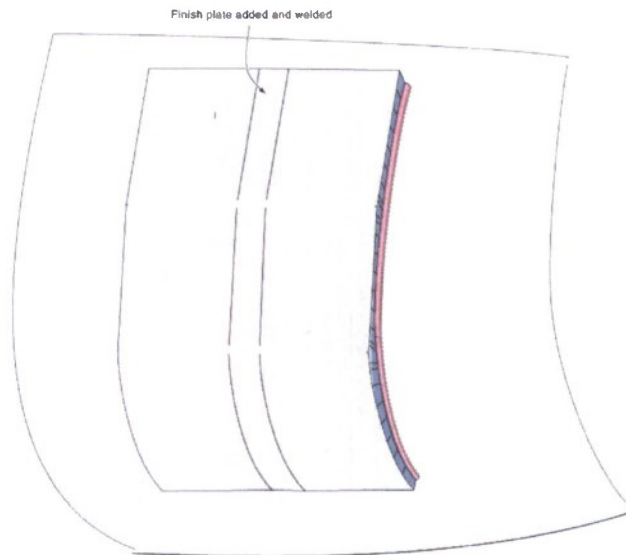
Finish plate added and welded

Full Seam welds to join face sheets with plug welds to core, as required.

Weld the wet side face plate seam to the core and the adjoining face sheets to close sub-panel to sub-panel joint. The adjoining face sheets are welded continuously while the core to face sheet interface is blind stitch welded. Thus a water tight seal will be established.

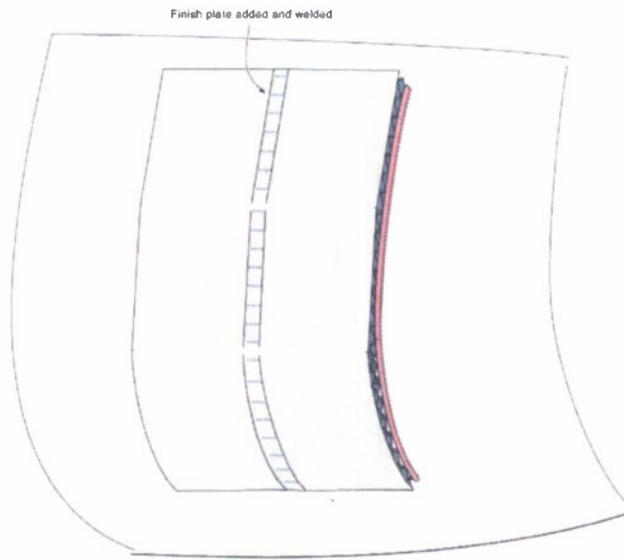**Issues:**

•Blind weld required

•Distortion should be minimized

X-Truss, Sub-Panel to Hull Attachment
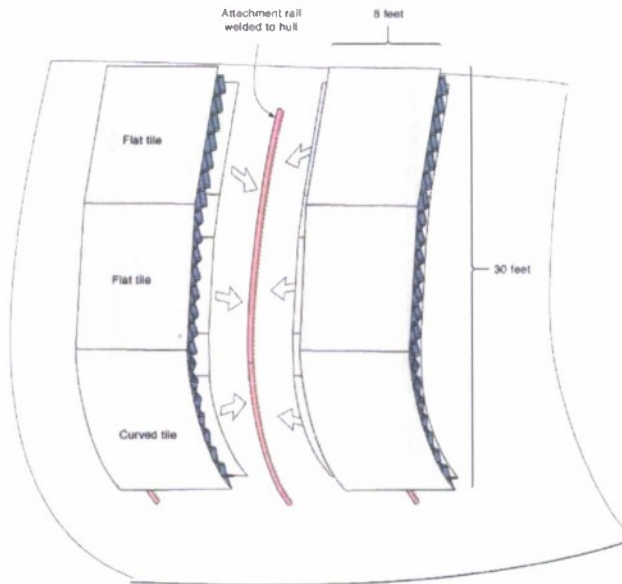
- Attachment rail shall be welded to hull at transverse stiffener location.

- Inner face sheet of sub-panels will be welded to attachment rail.

Same approach as honeycomb core. The attachment of sub-panels to the rails employ shipyard friendly fabrication practices. The joining methodology used herein is similar to the ones employed in joining tiles to assemble sub-panels. The dry side face sheet is attached to the rails on either side of the rail.

28

X-Truss Core Fill-In

Core filler added and welded
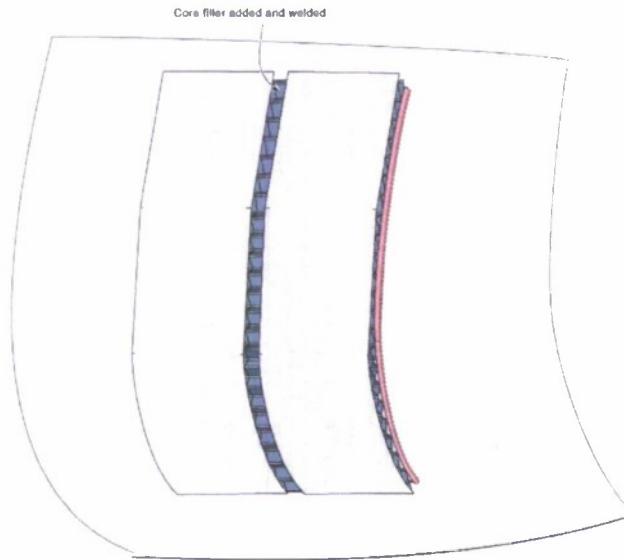
- Full seam welds to achieve continuity of core.

- Two core welding stages will be necessary. Through-penetration or plug welds will be used to join core to inner face sheet and core to core.

Same practice used as honeycomb core. The core segment is then attached to the dry side face sheet followed by attaching the edge members to the tiles.

X-Truss, Face Sheet Seam

Finish plate added and welded

Full Seam welds to join face sheets with plug welds to core, as required.

Weld the wet side face plate seam to the core and the adjoining face sheets to close sub-panel to sub-panel joint. The adjoining face sheets are welded continuously while the core to face sheet interface is blind stitch welded. Thus a water tight seal will be established.

Issues:

•**Blind weld required**

•**Distortion should be minimized**

Pyramidal core, Sub-Panel to Sub-Panel Assembly with Hull Attachment
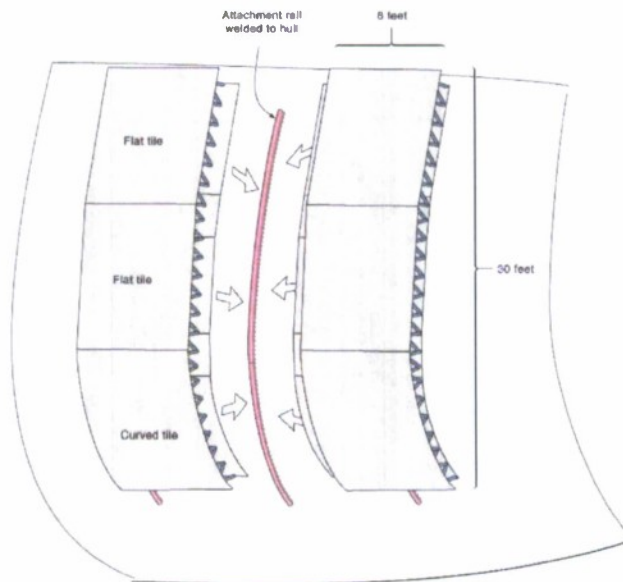
- Attachment rail shall be welded to hull at transverse stiffener location.

- Inner face sheet of sub-panels will be welded to attachment rail.

Same as other two cores. The attachment of sub-panels to the rails employ shipyard friendly fabrication practices. The joining methodology used herein is similar to the ones employed in joining tiles to assemble sub-panels. The dry side face sheet is attached to the rails on either side of the rail.

Pyramidal Core Fill-In

Core filler added and welded
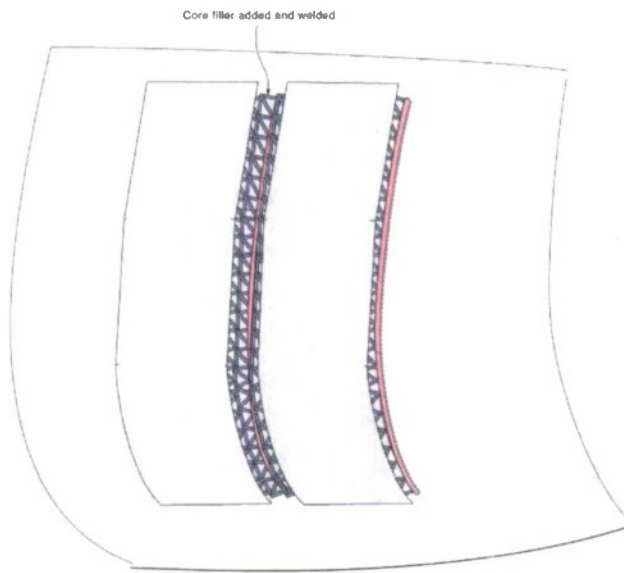
- Full core construction to achieve continuity of core.
- Multiple core welding stages will be necessary. Through-penetration or plug welds will be used to join core to inner face sheet and core to core.

Same as other two cores. The core segment is then attached to the dry side face sheet followed by attaching the edge members to the tiles.

# Pyramidal Core, Face Sheet Seam

Finish plate added and welded
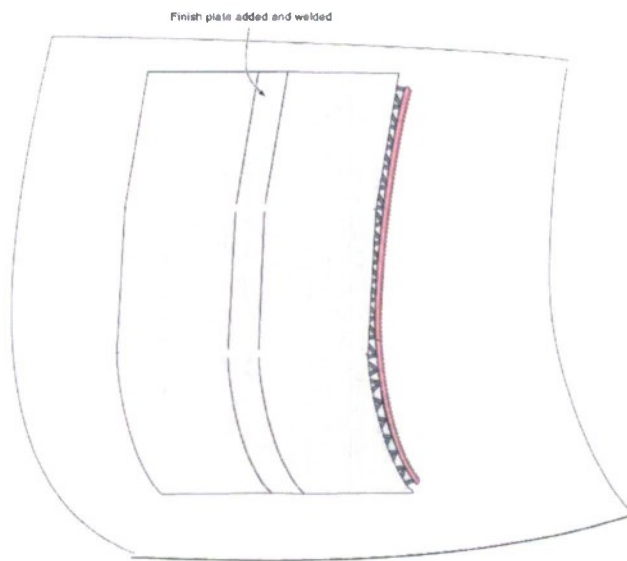
Full Seam welds to join face sheets with plug welds to core, as required.

Same as other cores. Weld the wet side face plate seam to the core and the adjoining face sheets to close sub-panel to sub-panel joint. The adjoining face sheets are welded continuously while the core to face sheet interface is blind stitch welded. Thus a water tight seal will be established.
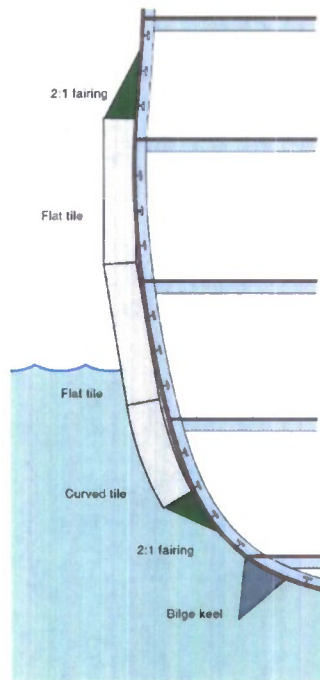
Issues:

•**Blind weld required**

•**Distortion should be minimized**

Two tile vs. Three tile option
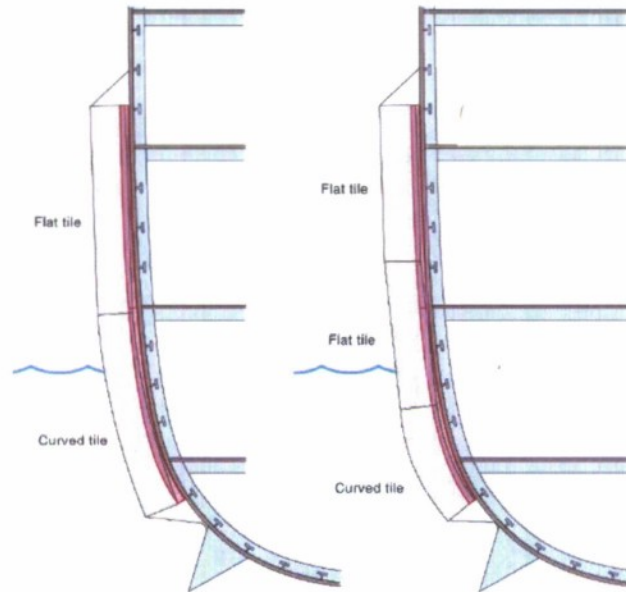
Two blister profiles are considered: In one case one flat section of 15 feet matched with a curved section 0f 15 feet with total vertical surface length of 30 feet. In the second case two 10 feet sections attached one 10 feet curved section giving essentially 30 feet . The waterline is assumed to be in the curved section in the first case while waterline is assumed in the flat section in the second scenario. A longitudinal weld joint will be made at a level coincident with a hull longitudinal stiffener. In both cases it is assumed that the waterline will be substantially away from the weld line. The first case calls for more curved panel surface on the blister in addition to calling for 8 foot by 15 foot tile. No decision was taken.
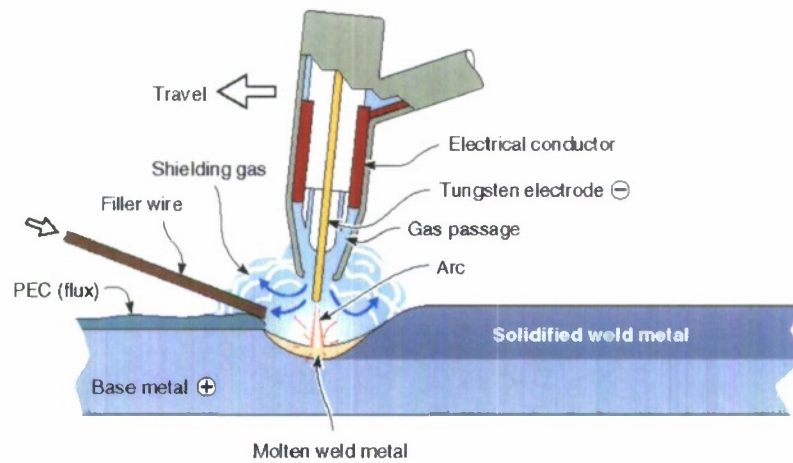
# Bilge Keel integration - Ship Roll Behavior

NSWC-CD Assessment :

•Rob Michelson has completed the evaluation and provided a report to Ed Johnson

•No issues were identified to the hydrodynamics of the ship resulting from this proposed blister attachment to the hull

•The base of the faring is to be attached to the hull above the Bilge Keel with one depth spacing

GTAW- PEC process

Travel

Shielding gas

Filler wire

PEC (flux)

Base metal ⊕

Electrical conductor

Tungsten electrode ⊖

Gas passage

Arc

Solidified weld metal

Molten weld metal

The Gas Tungsten Arc Welding process with penetration enhancing compound (GTAW-PEC) is

being considered for X-truss core tile manufacture.

Transferred Arc Plasma process
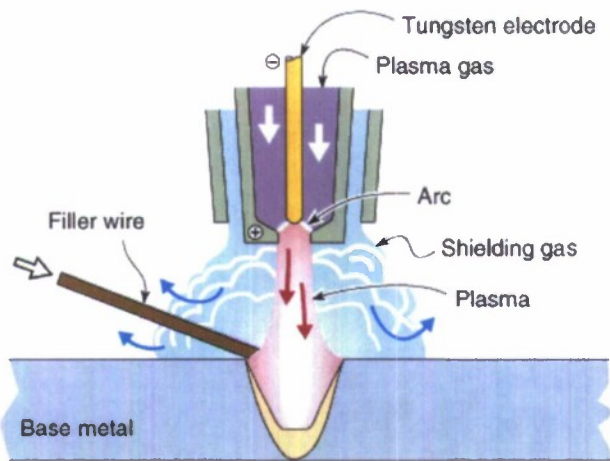
This transferred arc plasma process is being considered for X-core and Square honeycomb tile manufacture.

Welding methods for tiles

- Gas Tungsten Arc Welding(GTAW)- with Penetration Enhancing Compound (PEC):
  - GTAW most widely used methods
  - PEC's are commercially available
  - Precision can be achieved with articulated robotic systems and multi axis gantry layout
- Plasma Welding
  - Limited to <0.5" thick plates
  - Can be used effectively for core fabrication
- Laser Welding
  - Ideal for intense precision welding needs
  - Lower power consumption and high speeds are advantageous for cellular material panel manufacturing
  - Current technologies with fiber are very efficient
  - heat source providing least distortion
- Friction Stir Welding (FSW)
  - Solid state process with least heat input to work piece and hence the least distortion
  - Not readily adoptable of complicated weld geometries
  - High load bearing requirement prevent use on unsupportable joint welding

Cellular panels require multiple weld practices during the fabrication of the blister. Only GMAW, Pulsed Spray Transfer (GMAW-P), Flux Core Arc Welding (FCAW), Shielded Metal Arc Welding (SMAW), are current shipyard weld practices. These practices can be used to join sub-panels to form the blister. The shipyards make limited use of mechanized robots which are needed for tile manufacture. The welding techniques considered above are primarily for the manufacturing of tiles.

The GTAW-PEC process is being considered for the X-core, the PLASMA process for the X-Core and Square Honeycomb cores and the Laser Welding for the Pyramidal and Square Honeycomb cores. The Friction Stir Welding (FSW) process is being considered since it is a solid state process that requires the least heat input. Among the processes considered, GTAW gives the widest fusion zone while Laser Welding gives the narrowest fusion zone. The FSW process has no fusion zone.

The proposed approach is two investigate all four approaches for tile fabrication (outside the shipyard) and down select the best approaches. **The process conditions, geometry and joint fit requirements, the ability to minimize distortion, precision and quality of the welds, tooling requirements and the reproducibility are some of the parameters that require optimization. This is a key aspect of the ongoing program.**

Welding inspection methods

- Surface/and near sub-surface inspection techniques:
  - Eddy Current
  - Ultrasonic
  - Dye-penetrant
  - Thermography
- Inner layer inspection
  - Further investigations are required: eg. Ultrasound, x-ray tomography, infrared technologies (NSWC/CD will assist)

Require further investigation of adaptability of commercially available NDE systems to core topologies, accessibility to inner nodes in the panel, scale issues, and safety issues.

Evaluation could include round robin testing of full scale articles to compare methods and procedures and to lead to development of an optimized inspection scheme.

Weld repair methods also need further investigation.

Other Remaining issues

• (1) The addition of armor for ballistic protection has not been included. Based on preliminary results of ballistics tests, armor may not be needed for the X-truss and pyramidal panels but may be needed for honeycomb.

• (3) There is concern that a gap between the inner face plate and the hull will have to be designed into the attachment scheme to compensate for the hungry horse effect and distortion of the lower curved section during welding. Preliminary thinking is that a spacer plate be welded to the hull at the blister attachment joints. The face plates of the blister will then be welded to the spacer plates. The gap would then be filled with material; possibly a polymer. Selection of a filler material needs to be made based on ability to dampen hull vibrations, reduce noise, and mitigate shock pressure.

(2). The selection of a two-tile versus three-tile sub-panel assembly needs to be resolved based on the preference to minimize joints below the water line.

40
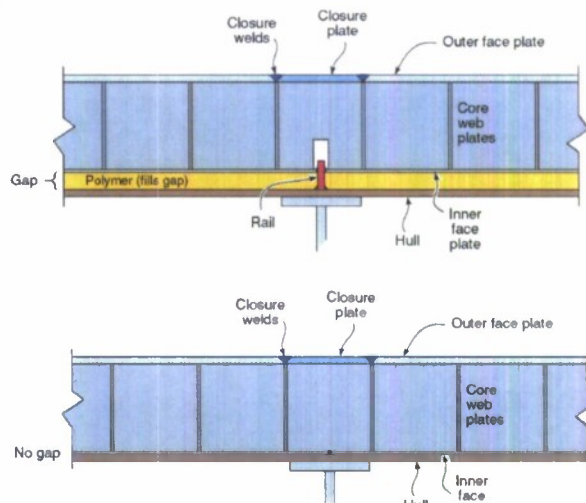
Final Report on

CONSTITUTIVE LAWS FOR METALLIC SANDWICH PANELS

A.G. Evans, R.M. McMeeking and F.W. Zok
Materials Department, University of California, Santa Barbara, CA 93106-5050

EXECUTIVE SUMMARY

A continuum constitutive law applicable to truss and prismatic cores has been implemented and assessed. The law is based on Hill's yield criterion for orthotropic materials, modified to account for the effects of mean stress and the associated compressibility upon plastic straining. Parameters characterizing initial yield are obtained from both approximate stress analyses and finite element calculations of unit cells. Finite element calculations have also been used to calibrate the hardening. Once calibrated, the law was used to simulate the bending response of various sandwich panels under either simply-supported or clamped end conditions. An assessment of the law has been made through comparisons with corresponding finite element calculations in which the core and face elements are fully meshed. Additional assessments have been made through experimental measurements on a family of sandwich panels fabricated from a ductile stainless steel. Comparisons have been made on the basis of the global load-displacement response as well as the distribution of shear strain within the core. Issues associated with end-effects, boundary conditions and deformation localization are addressed. Overall, the comparisons reveal that the proposed constitutive law is capable of predicting most of the pertinent features of honeycomb sandwich panels with high fidelity. Specifically, the onset of yield, the hardening rate, the peak loads, and the deformations within the core are adequately predicted. The largest apparent discrepancy pertains to the prediction of the onset of strain localization, especially when failure is core-dominated. When compared with both experiments and fully-meshed FE calculations, the continuum model overestimates the critical displacement. This discrepancy is largely attributable to the isotropic nature of the hardening law. That is, because strain hardening of the core is assumed to occur uniformly (without change in shape of the yield surface), some modes of deformation localization may be artificially delayed. This is the case, for example, when the law is calibrated by the shear stress-strain curve and localization occurs by core crushing at one of the loading points. This shortcoming has been remedied by extending the constitutive law to account for non-uniform hardening. The nature of this law and its implementation for dynamic loadings are described.

A dynamic version of the constitutive law has been proposed. It is calibrated by using dynamic unit cell simulations. The input embodies the material strain rate sensitivity as well as the inertial effect associated with buckling suppression. A 3-segment fit to the stress strain response reflecting these factors is used. Preliminary comparisons with dynamic experimental measurements have been performed involving impact by a metal foam projectile onto a square honeycomb panel at high impulse at strain rates of order 1,000/s. The calibration and validation of this approach will continue.

1. INTRODUCTION

The objective of the present study is to implement and assess a continuum constitutive law for prismatic cores for use in simulating the mechanical response of sandwich panels. To assess the adequacy of the constitutive law for panels subject to bending, an integrated measurement and analysis protocol is adopted, using designs that fail by plasticity mechanisms.

The report is laid out in the following manner:

(i)   An orthotropic constitutive law applicable to square honeycomb cores is presented. In this implementation, hardening is assumed to occur isotropically, with no change in the shape of the yield surface. The law is calibrated through a combination of approximate analytical results for initial yield and finite element calculations of elastic/plastic response.

(ii) Calculations are performed of the bending response of a variety of sandwich panels, using the calibrated constitutive law to describe core response. For comparison, finite element simulations are performed of the same structures, but with fully-meshed core members and faces. The objective is to ascertain deficiencies in the constitutive law as well as the sensitivity of the predicted structural response to the calibration procedure.

(iii) Additional validation is accomplished through a series of experiments designed to probe the fundamental core response in transverse shear, as well as the structural response of beams, subject to either simply-supported or clamped end conditions. For direct comparison with the measurements, the same tests are simulated by finite elements using the orthotropic constitutive law for the core response.

(iv) An extended version of the constitutive law, accounting for anisotropy of the hardening behavior, is described.

(v)   Select numerical simulations of the response of sandwich panels subject to high impulse loadings are presented.

2. CONSTITUTIVE LAW

2.1 General Framework

The constitutive law is based on Hill's yield criterion for orthotropic materials, characterized by an effective stress σ_e [Hill 1947]:

$$\sigma_e^2 = \{\sigma\}^T [P]\{\sigma\} \tag{1}$$

where

$$\{\sigma\}^T = \{\sigma_{11} \quad \sigma_{22} \quad \sigma_{33} \quad \sigma_{12} \quad \sigma_{23} \quad \sigma_{13}\} \tag{2}$$

$[P]$ is a symmetric 6 by 6 matrix that defines the anisotropy of yielding as well as its relative sensitivity to shear and pressure, and σ_{ij} are the stress components. The off-diagonal terms in $[P]$ in the 4th, 5th and 6th columns are zero. The yield criterion is

$$f = \sigma_e - \sigma_0 = 0 \tag{3}$$

where σ_0 is the uniaxial yield strength. In the current implementation, the hardening rule assumes that the yield surface does not change in shape upon exceeding the yield stress. A generalization that accounts for anisotropic hardening is described in Section 5.

The plastic strain rate must be normal to the yield function so that

$$\{\dot{\varepsilon}^p\} = \frac{\Lambda}{\sigma_e} [P]\{\sigma\} \tag{4}$$

where, in terms of the plastic strain rate components,

$$\{\dot{\varepsilon}^p\}^T = \{\dot{\varepsilon}_{11}^p \quad \dot{\varepsilon}_{22}^p \quad \dot{\varepsilon}_{33}^p \quad 2\dot{\varepsilon}_{12}^p \quad 2\dot{\varepsilon}_{23}^p \quad 2\dot{\varepsilon}_{13}^p\} \tag{5}$$

The plastic multiplier, Λ, is given by

$$\Lambda = \frac{1}{h\sigma_e} \{\sigma\}^T [P]\{\dot{\sigma}\} \tag{6}$$

with the hardening rate, h, defined to be

$$h = \frac{d\sigma_o}{d\bar{\varepsilon}^p} \tag{7}$$

and the effective plastic strain rate, $\dot{\bar{\varepsilon}}^p$, given by

$$\left(\dot{\bar{\varepsilon}}^p\right)^2 = \{\dot{\varepsilon}^p\}^T [P]^{-1} \{\dot{\varepsilon}^p\} \tag{8}$$

The preceding approach is limited to relative densities, $\bar{\rho}_c$, at which the core fails by plastic mechanisms (yielding and plastic buckling); it is not be applicable when the core members fail by elastic buckling. Core densities for subsequent calculations and experiments are selected to lie in the former domain.

2.2   Calibration of a General Orthotropic Core

In principle, the nine independent coefficients in the matrix [P] can be determined by either numerical simulation or experiment, or both. A complete characterization would require the following tests: core crushing with the faceplates attached, three uniaxial stress tests carried out with the faceplates detached and three simple shear tests. For cases in which the core is subjected to bending and tensile loads in one plane, only three such tests are needed. The ones that can be implemented and interpreted most readily are: transverse compression, σ_{33}, transverse shear, σ_{13}, and in-plane tension, σ_{11}. In either case, the pertinent coefficients can be obtained from an approximate stress analysis of a unit cell, subject to the appropriate boundary conditions. These results can then be assessed through select finite element analyses (FEA) of representative unit cells. FEA is also the preferred method for determining the plastic response subsequent to yielding. However, only one such stress/strain curve can be used to calibrate the constitutive law, since the implicit assumption is that the hardening (as well as softening and densification) are the same for all modes.

When the calibration is performed by a *transverse shear* test in the x_1 direction (x_3 being through thickness direction), the effective stress is

$$\sigma_e = \sqrt{P_{66}}\,|\sigma_{13}| \tag{9}$$

and the effective plastic strain is

$$\bar{\varepsilon}^P = \frac{2|\varepsilon_{13}^P|}{\sqrt{P_{66}}} \tag{10}$$

Since the matrix $[P]$ contains one disposable parameter that serves as a datum, the component P_{66} can be equated to unity and the other components calculated relative to that datum. With this choice, the stress-strain curve relating σ_{13} to $2\varepsilon_{13}^P$ provides the effective stress/plastic strain curve and its slope is the hardening modulus h. Other components of $[P]$ can be characterized by use of compression tests in the transverse and in-plane directions and through additional shear stress-strain responses. During the transverse crushing test, the strain response is nearly uniaxial because of the constraint of the face sheets. Without significant loss of accuracy, the plastic strain is assumed to be uniaxial, so that ε_{33}^P is the only non-zero strain. Setting $\varepsilon_{11}^P = \varepsilon_{22}^P = 0$ in Eqn. 4 yields two relationships between the components of the matrix $[P]$:

$$P_{11}\sigma_{11}^c + P_{12}\sigma_{22}^c + P_{13}\sigma_{33}^c = 0 \tag{11}$$

$$P_{12}\sigma_{11}^c + P_{22}\sigma_{22}^c + P_{23}\sigma_{33}^c = 0 \tag{12}$$

where σ_{ij}^c are the stress components at yield during crushing. Combination of Eqns. 13 and 14 with Eqn. 4 and recognition that all shear stresses are zero, provides the effective stress as

$$\sigma_e^2 = \left(P_{13}\sigma_{11}^c + P_{23}\sigma_{22}^c + P_{33}\sigma_{33}^c\right)\sigma_{33}^c \tag{13}$$

However, since the effective stress equals the magnitude of the transverse shear stress at yield, Eqn. 13 leads to

$$P_{13}\sigma_{11}^c + P_{23}\sigma_{22}^c + P_{33}\sigma_{33}^c = \frac{\left(\sigma_{13}^s\right)^2}{\sigma_{33}^c} \tag{14}$$

where σ_{13}^s is the stress at yield for simple shear in the transverse direction as noted above. A further five equations are obtained from the yield conditions for uniaxial stressing and simple shear. These provide

$$P_{11} = \left(\frac{\sigma_{33}^c}{\sigma_{11}^u}\right)^2 \qquad P_{22} = \left(\frac{\sigma_{33}^c}{\sigma_{22}^u}\right)^2 \qquad P_{33} = \left(\frac{\sigma_{33}^c}{\sigma_{33}^u}\right)^2$$

$$P_{44} = \left(\frac{\sigma_{33}^c}{\sigma_{12}^s}\right)^2 \qquad P_{55} = \left(\frac{\sigma_{33}^c}{\sigma_{23}^s}\right)^2 \tag{15}$$

where σ_{ij}^u is the stress at yield for uniaxial loading and σ_{ij}^s is the stress at yield for the relevant mode of simple shear. Eqns. 11, 12, 14 and 15 along with $P_{66} = 1$ therefore provide the 9 conditions for evaluating the non-zero elements of $[P]$.

Alternatively, when *transverse compression*, σ_{33}, is used for calibration, this stress-strain curve represents the relationship between the effective stress and the effective plastic strain, and its slope is the hardening modulus, h. Eqns. 13, 14, 15 and 17 are still operational but now the effective stress in Eqn. 13 is equal to σ_{33}^c and Eqn. 16 is replaced by

$$P_{13}\sigma_{11}^c + P_{23}\sigma_{22}^c + P_{33}\sigma_{33}^c = \sigma_{33}^c \tag{16}$$

Additionally, the condition for P_{66} becomes

$$P_{66} = \left(\frac{\sigma_{33}^c}{\sigma_{13}^s}\right)^2 \tag{17}$$

Thus Eqns. 11, 12, 15, 16 and 17 become the 9 conditions for evaluating the components of $[P]$. Finally, since

$$\dot{\bar{\varepsilon}}^p = \frac{\{\sigma\}^T \{\dot{\varepsilon}^p\}}{\sigma_e} \tag{18}$$

the crush test with the faceplates attached establishes the effective plastic strain as

$$\bar{\varepsilon}^p = \left| \varepsilon_{33}^{pc} \right| \tag{19}$$

where ε_{33}^{pc} is the axial plastic strain. Therefore, the stress-strain curve provides the relationship between σ_o and $\bar{\varepsilon}^p$ and its slope is h, as noted above. Without much loss of accuracy, the distinction between the plastic and total strains can be neglected in the calibration.

A simpler version of this law has been derived and used under the assumption that the plastic Poisson ratio subject to crushing is zero [Xue and Hutchinson, 2004]. This version is expected to be adequate for some core topologies and, under such circumstances, enjoys the advantage of computational simplicity. For present purposes, this simplification is not made and the full characterization is used.

2.3   Initial Yield of Square Honeycomb Core

Approximate stress analyses have been performed of the honeycomb core to ascertain the coefficients that characterize initial yield, under loadings of transverse compression, σ_{33}, in-plane shear, σ_{13}, and in-plane tension, σ_{11}. Analytic formulae are as follows.

In transverse compression, when unconstrained by the faces, the core yields at a normalized stress:

$$\frac{\sigma_{33}^u}{\sigma_y \bar{\rho}_c} = -1 \tag{20}$$

where σ_Y is the yield strength of the host material. When the faces are attached, such that lateral expansion is prohibited, the associated constraint increases the magnitude of the yield stress so that:

$$\frac{\sigma_{33}^c}{\sigma_y \bar{\rho}_c} = -\frac{2}{\sqrt{3}} \left[1 + \frac{(\sqrt{3}-1)\bar{\rho}_c}{8} \right] \tag{21}$$

and simultaneously the transverse stresses are

$$\frac{\sigma_{11}^c}{\sigma_y \bar{\rho}_c} = \frac{\sigma_{22}^c}{\sigma_y \bar{\rho}_c} = -\frac{1}{2\sqrt{3}}\left(1 + \frac{\bar{\rho}_c}{4}\right) \tag{22}$$

Subject to in-plane tension, unconstrained by the faces, yielding occurs at stress:

$$\frac{\sigma_{11}^u}{\sigma_y \bar{\rho}_c} = \frac{\sigma_{22}^u}{\sigma_y \bar{\rho}_c} = \frac{1}{\sqrt{3}}\left(1 + \frac{\bar{\rho}_c}{4}\right) \tag{23}$$

The shear response is characterized by the stress:

$$\frac{\sigma_{13}^s}{\sigma_y \bar{\rho}_c} = \frac{\sigma_{23}^s}{\sigma_y \bar{\rho}_c} = \frac{1}{2\sqrt{3}}\left[1 + \frac{(1+\sqrt{3}\xi)\bar{\rho}_c}{4}\right] \tag{24}$$

where ξ is the cell length to thickness ratio (L_c/H_c).

The components of $[P]$ can then be determined directly from Eqns. 20–24. To second order in the core density, the results are:

$$P_{11} = P_{22} = 4\left[1 - \frac{(3-\sqrt{3})\bar{\rho}_c}{4}\right] \tag{25a}$$

$$P_{12} = -\frac{4}{3}\left[1 - \frac{(7\sqrt{3}-5)\bar{\rho}_c}{4}\right] \tag{25b}$$

$$P_{13} = P_{23} = -\frac{2}{3}\left[1 + \frac{(9\sqrt{3}-11)\bar{\rho}_c}{8}\right] \tag{25c}$$

$$P_{33} = \frac{4}{3}\left[1 + \frac{(\sqrt{3}-1)\bar{\rho}_c}{4}\right] \tag{25d}$$

$$P_{44} = \frac{256}{3\bar{\rho}_c^2}\left[1 - \frac{(9-\sqrt{3})\bar{\rho}_c}{4}\right] \tag{25e}$$

$$P_{55} = P_{66} = 16\left[1 - \frac{(3-\sqrt{3}+2\sqrt{3}\xi)\bar{\rho}_c}{4}\right] \tag{25f}$$

These are the components of $[P]$ to be used when the effective stress-strain curve is calibrated to transverse crushing. As noted above, the components of $[P]$ for use when the effective stress-strain curve is calibrated to a shear test are obtained by dividing all of the preceding results by P_{66} given in Eqn. 25f.

The elastic properties of the core have been obtained by a combination of analytical estimates and finite element simulations. The results, in non-dimensional form, are:

$E_1/E = E_2/E = \overline{\rho}_c/2$, $E_3/E = \overline{\rho}_c$, $G_{13}/G = G_{23}/G = \overline{\rho}_c/2$, $G_{12}/G = 0.005\overline{\rho}_c$, $\nu_{13}=\nu_{23}=0.3$ and $\nu_{12}=0.01$,

where G is the shear modulus of the material $(G = E/(1+2\nu))$.

2.4 FEA of Square Honeycomb Core

To both assess the preceding analytical results for initial yield and ascertain the subsequent plastic response, finite element simulations have been performed of two representative honeycomb unit cells. In both, the normalized cell length is $L_c/H_c = 1$ (H_c being core thickness). Two wall thicknesses are considered, $t_c/H_c = 0.020$ and 0.051, with corresponding core relative densities of 4% and 10%, respectively. The finite element code ABAQUS is used to conduct the calculations. The elastic/plastic response of the host material is taken to be that of annealed 304 stainless steel, as shown in Figure 3. The loadings include transverse compression, transverse shear and in-plane tension. An eigen-value analysis is used to establish the buckling modes and to select the initial imperfections for both compression and shear loadings.

For compression, the boundary conditions are selected to give either uniaxial stressing (relevant to compression when the face sheets are absent) or uniaxial straining (to simulate the constraints when face sheets are attached). Evidently, the two boundary conditions lead to almost identical plastic responses for both core densities (Figure 4(a)). Additionally, although the normalized initial yield stress is insensitive to core density, the flow response at large plastic strains varies considerably. For instance, for low densities ($\overline{\rho}_c \leq 4\%$), core buckling occurs essentially at the yield point. This is followed by slight softening and then attainment of a saturation flow stress, typically $\sigma_{33}^c/\sigma_y\overline{\rho}_c \approx \sigma_{33}^u/\sigma_y\overline{\rho}_c \approx 0.7$. At higher densities, buckling occurs following a finite (but small) amount of plastic straining. With the associated work hardening, the buckling stress reaches $\sigma_{33}^c/\sigma_y\overline{\rho}_c \approx \sigma_{33}^u/\sigma_y\overline{\rho}_c \approx 1.4$ for a core density of 10%. Following

slight softening, the flow response again exhibits hardening: a consequence of the mutual constraints of the two sets of web members during plastic buckling.

The simulated in-plane tensile response exhibits a similarly weak sensitivity to the boundary conditions (Figure 4(b)). That is, uniaxial stressing and uniaxial straining yield essentially the same responses for both 4% and 10% relative densities. In this case, the response is one of monotonically increasing flow stress, essentially mimicking that of the base material itself (Figure 3). Furthermore, the effects of core density are small (provided the flow stress is normalized accordingly). The transverse shear response exhibits some sensitivity to core density (Figure 4(c)), intermediate to those of transverse compression and in-plane tension.

The hardening responses in the three preceding loading modes are compared on Figure 5. For this assessment, the flow stresses are normalized by the respective initial yield strengths. In this form, the in-plane tensile hardening rate is the greatest and that of transverse compression is the lowest. One of the consequences of the differing hardening rates is that, for subsequent calibration of the constitutive law, some judgment must be exercised in the selection of the calibrating curve, dictate by the dominant core failure mode. For instance, for bending-dominated loadings, core failure is expected to occur through core shearing; hence, the transverse shear response is the preferred choice for calibration. Additionally, since the transverse shear curve lies between the ones for compression and tension, this response has the advantage of better representing the average panel response for all modes, relative to that of the other loading modes. Indeed, most of the subsequent calculations are based on this calibration procedure. Select comparisons are made for the case where the calibration is performed using the compressive response, in order to gain insight into the sensitivity of the predicted response to the calibration procedure. Since the hardening rate is assumed to be the same in all modes, the latter calibration is expected to lead to the most conservative estimates of flow strength.

Table I presents comparisons of the predicted initial yield strengths, both from the approximate analytical solutions and the FE simulations. Acceptable agreement is obtained for both core relative densities, testament to the accuracy of the analytical solutions for initial yield.

3.   COMPARISONS WITH DISCRETE SIMULATIONS

An assessment of the constitutive law has been made through comparisons of two sets of FE simulations of sandwich panels: one based on a continuum representation of the core (using

the preceding constitutive law) and the other based on fully discretized core and face members. In all cases, the core dimensions are $L_c/H_c = 1$ and $t_c/H_c = 0.020$, with a resulting core relative density of 4%. The face sheet thicknesses were varied in order to probe failure modes: both of the core and of the faces. Details of the design procedure are outlined in the Appendix, with the key results summarized on Table II and Figure 6. In the latter, the coordinates are the face thickness, t_f, and the ratio of bending moment to shear force, $\ell = M/V$. Based on this map, five configurations have been designed, denoted I to V. The pertinent design parameters and predicted load capacities are listed in Table II. Two are expected to have initial non-linearity controlled by core shearing (II and IV), one by face yielding (V), and two by simultaneous core shearing and face yielding (I and III). Loads are applied in three point bending, with the ends being either simply supported (III, IV and V) or fully clamped (I and II). The meshes used to conduct discrete calculations are exemplified on Figure 7. Imperfections based on the eigen-value analysis are introduced into each core member with amplitude, $\xi = 0.01$. (Previous assessments have indicated that the results are not sensitive to the imperfection amplitude, *provided that an imperfection exists* [Wadley *et al.* 2003].The operating premise is that if the constitutive law is capable of predicting the behavior for these five cases, it should be adequate for most reasonable bending scenarios.

The load/deflection curves for the simply supported beams are summarized on Figures 8 and 9 and representative strain and displacement distributions shown in Figures 10 and 11. Both the discrete and the continuum model results exhibit: (i) a linear elastic domain, with essentially the same stiffness and initial yield strength being obtained from the two models (within about 10%); (ii) a strain-hardening plastic domain, and (iii) a strain-softening domain following the attainment of a load maximum. The loads at the onset of yield are in good agreement with the analytic estimates (Table III). For Case V (Figure 8(c) and 9(b)), the first non-linearity occurs as a consequence of face yielding, in accordance with the prediction on Figure 6. Core yielding follows at larger displacements, at about twice that of the elastic limit. For case IV, yielding occurs first within the core along the mid-plane (again consistent with Figure 6). The plasticity spreads and fully encompasses the core shortly thereafter (Figure 9(a)). Face yielding occurs at yet higher displacements (about 3 times the elastic limit). Although both the discrete and the continuum models predict a load maximum followed by a softening regime, the details of the deformation patterns in the localized region differ. Notably, in the discrete model, the peak is

associated with core buckling, followed by plastic buckling of the compressive face sheet (Figure 11(a)). The ensuing softening of the core is manifested in a rapid reduction in the global load-displacement response. In contrast, the continuum model predicts more gradual softening and more uniformly distributed strains in the core beneath the loading point. This discrepancy is attributable to the manner in which the constitutive law has been calibrated. That is, when the transverse shear curve is used for calibration, the hardening rate under transverse compression is overestimated (Figure 5). If, instead, the law is calibrated with the transverse compression curve, core crushing is predicted almost immediately after yield, followed by an extended plateau in which the stress remains essentially constant (Figure 8(a)). This results in an overly conservative estimate of the hardening rate in the initial plastic domain. Consequently, the shear curve is preferred for such calibration, despite the discrepancies that arise in the post-localization domain.

A further assessment is made through comparisons of the strain distributions within the core prior to the load maximum. One such comparison (case IV, at displacement $\delta/S=0.06$) is shown in Figure 10. Both models predict a broad zone between supports in which the core shear strain is relatively uniform, at about 14–18% (shaded regions in Figure 10), as well as steep strain gradients near the supports. Naturally, some of the details of the strain distribution in the real structures are absent in the continuum model prediction because of the tacit homogenization of the core structure. For instance, the strain gradients near the transverse core members (evident in the discrete model) are absent in the continuum model.

For the two clamped beam configurations, the loads for initial yield from the two models are consistent with one another (Figure 12 and Table III) and are essentially the same as those for the corresponding simply-supported cases (cases III and IV). Moreover, in the plastic domain, the continuum model predictions are in excellent agreement with the discrete model, provided that the shear curve is used for calibration. But significant differences arise between the two categories of end condition. Notably, for the clamped beams, membrane stresses develop when the displacements exceed a significant fraction of the panel thickness. These stresses have two consequences. First, they offset the compression in the face sheets, thereby preventing face buckling and the associated load maximum. Secondly, they elevate the hardening rate, relative to that of the simply-supported case. The resulting loads increase monotonically with displacement.

4. EXPERIMENTS

4.1 Materials and Test Procedures

As a further assessment of the constitutive law, comparisons have been made with a series of simply-supported and clamped bend tests, on honeycomb core panels with the designs summarized in Table II. The panels were fabricated using 304 stainless steel for both the core and the face sheets. To produce the core, an array of steel slotted strips was assembled in a wine-box configuration (Figure 1(a)). The core members were then simultaneously brazed to both each other and the face sheets. This was accomplished by placing at the intersection points small amounts of the braze material: a mixture of Nicrobraz Cement 520 and Nicrobraz 31 braze powder, both supplied by Wal Colmonoy (Madison Heights, MI). The assembly of core members and face sheets was then heated in a vacuum furnace for 2 hours at 1075°C. To enable gripping in the clamped bending experiments (described below), 6 mm thick steel plates were brazed onto the ends of some panels. During subsequent testing, these plates were keyed into a slot in the test fixture, to prevent lateral face displacement by pullout. Additionally, to maximize clamping pressure, the cells between the clamps were filled with an epoxy, typically over a distance of about 50 mm at each end. During testing, low magnification photographs were taken at periodic intervals. The resulting images were used subsequently to determine the core shear strains, through the rotation of the transverse core members relative to the faces.

For measurement of core properties, lap shear specimens were fabricated and tested. These had thick (12.7 mm) plates attached to the cores, to ensure adequate core constraint during testing. The specimens were loaded in uniaxial compression. To minimize the normal through-thickness stress, the specimen aspect ratio (length/thickness) was selected to be about 20, in accordance with ASTM Test Standard C273. This yields an inclination angle of only about 3°.

4.2 Core Properties

A representative stress-strain curve from the shear test and the test specimen are shown in Figures 13 and 14. Also shown are the predicted curves from the fully meshed FE calculations (Figure 15) using two sets of boundary conditions. In both, all displacements on $x_3=0$ are held at zero, the shear displacements u_1 of all elements on $x_3=H_c$ are fixed, and the average transverse surface tractions T_3 acting on the surfaces $x_3=0$ and $x_3=H_c$ are zero (see Figure 15 for coordinate system). The two boundary conditions differ in the treatment of the core members along

$x_1 = \pm L_c/2$. In one case, periodic boundary conditions are used in order to simulate an infinite array of cells. In another limit, wherein only one cell is present, the elements along $x_1 = \pm L_c/2$ are assumed to be traction-free. The resulting pair of results are expected to bound the behaviors of test specimens with a finite number of cells: the periodic boundary condition being more representative of specimens with many cells ($>>10$) and the traction-free condition being preferable when the number of cells is small. In all cases (simulations and experiment), the curves exhibit monotonic hardening, even upon plastic buckling of the longitudinal core members. Such buckling is evident both in the tested specimens (Figure 14) as well as in the simulations (Figure 15). Moreover, the two boundary conditions yield results that do indeed bound the experimental results. Here, the periodic condition yields results that are in closer agreement with the measurements, consistent with the large number of cells along the specimen length (about 12). The slight discrepancy (about 8%) can be ascribed to an end-effect. The effect is manifested macroscopically in differences in deformation patterns in the transverse members near the ends relative to those near the center (see insets of Figure 14(c)). The correlations between the measurements and the predictions provide validation of the accuracy of the shear simulations, which are used subsequently in calibrating the core constitutive law.

4.3   Simply-Supported Bending

The bend test results are plotted on Figure 16 and compared with the predictions of the FE simulations that employ the continuum core constitutive law. For moderate displacement levels ($\delta/S < 0.05$), the two agree reasonably well (within about 10%). Nevertheless, for cases III and IV, the model predictions underestimate the flow response in this domain. The direction and magnitude of this discrepancy is in accord with that obtained upon comparison of the continuum and discrete models (Figures 8(b) and (c)). For case V, the agreement in this domain is excellent: also in accord with the correlations illustrated on Figure 8(c). The main discrepancy here is in the predicted displacement at the load maximum and the subsequent hardening rate. Specifically, the peak is reached at lower displacements in the experiments when failure is core-dominated, as it is in cases III and IV. But, interestingly, the peak loads are predicted accurately for the three cases. The pertinent results are summarized in Tables III and IV.

Effects of the failure mechanism on the deformation pattern are demonstrated in the two sets of images of the test specimens in Figure 17. When dominated by core failure (case IV), the

core experiences large plastic shear strains. One consequence is plastic buckling of the longitudinal members, essentially identical to that observed in the shear tests (both experimental and simulated). Alternatively, when dominated by face yielding (case V), failure occurs through the formation of a plastic hinge at the center loading point. This is accompanied by stretching/contraction of the faces and local compressive crushing of the core; elsewhere, the core experiences minimal plastic deformation. These features are in broad agreement with the predictions of the design map in Figure 6 and the FE results in Figure 9.

Additional assessment of the model predictions is made through comparison of the core shear strains (Figure 18). For case IV, at displacement $\delta/S=0.06$, the measured values are in good agreement with the simulations along the entire beam length (within the precision of the measurements). For larger displacements, beyond the experimental peak load ($\delta/S=0.10$), the correlation is acceptable over most of the beam length. At the center loading point, however, the measured strains exceed the predicted values, by about 50%. This discrepancy is attributable to the onset of strain localization in the experiments: a phenomenon that is predicted to occur at a somewhat higher displacement ($\delta/S=0.17$) in the continuum model predictions. It demonstrates a deficiency in the model in locations that experience complex loading paths.

4.4   Clamped Bending

Results of the mechanical measurements and some pertinent observations of the clamped bend tests are summarized in Figures 19 and 20. The load-displacement curves exhibit many of the features identified in the preceding simulations: notably, a consistency in the loads at the onset of non-linearity and a high hardening rate in the stretching domain. Quantitatively, however, the simulated results consistently overestimate the measured loads, especially at large displacements. This discrepancy is attributable in part to differences in the boundary conditions. That is, in the experiments, the upper (tensile) face sheet exhibits finite (measurable) lateral displacements at the clamped ends: a consequence of face stretching and thinning and the ensuing loss of contact with the clamp surface. To establish a lower limit on the expected response, additional simulations were performed in which the bottom face sheet was rigidly fixed (Figure 19(b)) whereas the upper face sheet was free to displace without restraint. These conditions and the ones imposed experimentally are schematically illustrated in Figure 21. The two sets of load-displacement predictions bound the experimental results for both case I and case

II (Figure 19). The inference is that the true boundary conditions in the experiment lie between the two assumed (limiting) cases. As a further check on consistency, comparisons are made of the core rotations at the clamped boundaries. For instance, for Case I at δ/S =0.11, the rotations are 0° and 13° for the two sets of predictions (Figures 20(b) and (c)); by comparison, the measured value lies in between, at about 7° (Figure 20(a)).

A final assessment is made by comparing the core shear strains. One set of measurements and predictions are plotted on Figure 22 for Case I. The predictions for the fully clamped boundaries appear to correlate well with the experimental measurements. When the other boundary conditions are employed, the predicted strains are lower and differ noticeably from the measurements. These comparisons would imply that, among the two conditions, the fully clamped one is more representative of the experiments. The sensitivity of the global response and the shear strain distribution to intermediate levels of constraint has yet to be ascertained.

5.   SANDWICH PANELS UNDER BLAST LOADINGS

5.1   Dynamic Continuum Model of the Core

A continuum model has been developed that describes the dynamic elastic-plastic response of orthotropic sandwich core materials under multi-axial stressing. The model accounts for hardening or softening behavior that can differ for stressing in each of the six fundamental stressing histories in orthotropic axes. Mass is distributed uniformly throughout the thickness of the core such that overall inertial resistance is replicated. Material rate dependence is included as well as the effect of the strain-rate on strengthening by stabilizing against buckling.

The x_i axes are aligned with the orthotropic core axes. The overall stress, strain and plastic strain vectors are

$$\bar{\sigma} = (\sigma_1, \sigma_2, \sigma_3, \sigma_4, \sigma_5, \sigma_6) \equiv (\sigma_{11}, \sigma_{22}, \sigma_{33}, \sigma_{13}, \sigma_{23}, \sigma_{12})$$
$$\bar{\varepsilon} = (\varepsilon_1, \varepsilon_2, \varepsilon_3, \varepsilon_4, \varepsilon_5, \varepsilon_6) \equiv (\varepsilon_{11}, \varepsilon_{22}, \varepsilon_{33}, 2\varepsilon_{13}, 2\varepsilon_{23}, 2\varepsilon_{12}) \qquad (26)$$
$$\bar{\varepsilon}^P = (\varepsilon_1^P, \varepsilon_2^P, \varepsilon_3^P, \varepsilon_4^P, \varepsilon_5^P, \varepsilon_6^P,) \equiv (\varepsilon_{11}^P, \varepsilon_{22}^P, \varepsilon_{33}^P, 2\varepsilon_{13}^P, 2\varepsilon_{23}^P, 2\varepsilon_{12}^P)$$

Let the 6×6 symmetric matrices of overall elastic moduli and compliances representing the elastic response of the core in the unbuckled state be such that

$$\bar{\sigma} = \mathbf{L}\bar{\varepsilon}$$
$$\bar{\varepsilon} = \mathbf{M}\bar{\sigma} \qquad (27)$$

The basic inputs to the model are the six rate-dependent stress-strain curves that characterize the plastic response of the continuum core. Specifically, when σ_i is the only non-zero stress component, $\hat{\sigma}_i(\varepsilon_i^P, \dot{\varepsilon}_i^P)$ denotes the hardening (or softening) function specifying the dependence of σ_i on the associated plastic strain component, ε_i^P (when the plastic strain-rate, $\dot{\varepsilon}_i^P$, is positive and constant). Note that, by definition, the input functions, $\hat{\sigma}_i(\varepsilon_i^P, \dot{\varepsilon}_i^P)$, are positive. When compression is relevant in a particular application, as in the case of core crush, input data for compression can be substituted in place of tension data for any of the three uniaxial stress components.

Specific forms for the input functions $\hat{\sigma}_i(\varepsilon_i^P, \dot{\varepsilon}_i^P)$ are suggested for the square honeycomb core with emphasis on crushing, illustrating the process for all cores. The objective is to devise a simple description of each of the input functions that captures the most important features of the nonlinear behavior associated with plastic buckling, necking or even fracture. We illustrate how buckling can be modeled by choosing an input function $\hat{\sigma}_3$ which incorporates the strong rate dependence of the onset of plastic buckling. A form for $\hat{\sigma}_3$ with features similar to those in Fig. 23 is taken to be

$$
\hat{\sigma}_3 = \begin{cases}
k\overline{\sigma}_Y + E_t'\varepsilon_3^P & 0 \le \varepsilon_3^P \le \hat{\varepsilon}_3^P \\
\left(k\overline{\sigma}_Y + E_t'\hat{\varepsilon}_3^P\right) - 2E_t'\left(\varepsilon_3^P - \hat{\varepsilon}_3^P\right) & \hat{\varepsilon}_3^P < \varepsilon_3^P \le \left(0.25k\overline{\sigma}_Y / E_t' + 1.5\hat{\varepsilon}_3^P\right) \\
0.5k\overline{\sigma}_Y & \left(0.25k\overline{\sigma}_Y / E_t' + 1.5\hat{\varepsilon}_3^P\right) < \varepsilon_3^P \le 1 \\
0.5k\overline{\sigma}_Y + 2E_t'\left(\varepsilon_3^P - 1\right) & 1 < \varepsilon_3^P
\end{cases}
\tag{28}
$$

expressed in true stress and logarithmic strain. Here, the factor k incorporates the material strain rate dependence, $\overline{\sigma}_Y$ is the overall quasi-static yield stress defined as $\overline{\sigma}_Y = (2/\sqrt{3})\overline{\rho}_c\sigma_Y$, and the overall Young's modulus is $E' = (2/\sqrt{3})\overline{\rho}_c E$. The core response is elastic with $\sigma_3 = E'\varepsilon_3$ for $\varepsilon_3 \le k\overline{\sigma}_Y / E$, while $\varepsilon_3^P = \varepsilon_3 - \sigma_3/E'$ for $\varepsilon_3 \ge k\overline{\sigma}_Y / E$. The overall tangent modulus, E_t', is given in terms of the material tangent modulus in (3) by $E_t' = (2/\sqrt{3})\overline{\rho}_c EE_t/(E - E_t)$. The plastic strain parameter associated with the onset of buckling in the constitutive model is denoted by $\hat{\varepsilon}_3^P$; it is primarily a function of the strain rate $\dot{\varepsilon}_3^P$ but it also depends on the *material rate dependence and details of the core geometry*. It must be identified by calibration either with experimental data or with selected numerical simulations. The slope, $2E_t'$, governing softening

and compaction hardening in (28) was chosen after several trial and error iterations. An ellipsoidal yield surface is invoked that generalizes Hill's surface for orthotropic plastically incompressible materials. The ellipticity of the surface is allowed to change to account for differential hardening or softening. Associated plastic flow is also invoked such that plastic strain-rates are normal to the yield surface. Due to their open structure, many cores undergo relatively little transverse plastic strain when stressed uniaxially in any of the three directions of orthotropy. The plastic strain-rate ratios (analogous to Poisson ratios in the elastic range) are then well approximated as zero.

When the transverse plastic strains under uniaxial stressing parallel to the axes of orthotropy are zero, the ellipsoidal yield surface for orthotropic compressible materials can be written in the form

$$f \equiv \sigma_{eff} - \sigma_0 = 0 \tag{29}$$

where the effective stress σ_{eff} is defined by

$$
\begin{aligned}
\left(\frac{\sigma_{eff}}{\sigma_0}\right)^2 &= \left(\frac{\sigma_{11}}{\hat{\sigma}_{11}}\right)^2 + \left(\frac{\sigma_{22}}{\hat{\sigma}_{22}}\right)^2 + \left(\frac{\sigma_{33}}{\hat{\sigma}_{33}}\right)^2 + \left(\frac{\sigma_{12}}{\hat{\sigma}_{12}}\right)^2 + \left(\frac{\sigma_{13}}{\hat{\sigma}_{13}}\right)^2 + \left(\frac{\sigma_{23}}{\hat{\sigma}_{23}}\right)^2 \\
&= \sum_i \left(\frac{\sigma_i}{\hat{\sigma}_i}\right)^2
\end{aligned}
\tag{30}
$$

The stress quantity σ_0 is a *fixed* reference stress that can be chosen arbitrarily (e.g. $\sigma_0 = 1 MPa$); it is simply a scaling factor. Normality is assumed such that $\dot{\varepsilon}_i^P = \lambda \partial f / \partial \sigma_i$. The effective plastic strain rate, $\dot{\varepsilon}_{eff}^P$, defined such that the plastic work is given by $\sigma_{ij}\dot{\varepsilon}_{ij}^P = \sigma_{eff}\dot{\varepsilon}_{eff}^P$, turns out to be

$$\dot{\varepsilon}_{eff}^{P\,2} = \sum_i \left(\frac{\hat{\sigma}_i}{\sigma_0}\dot{\varepsilon}_i^P\right)^2 \tag{31}$$

The plastic strain-rate components are given by

$$\dot{\varepsilon}_i^P = \frac{\sigma_0^2 \sigma_i}{\sigma_{eff}\hat{\sigma}_i^2}\dot{\varepsilon}_{eff}^P \tag{32}$$

Two hardening laws for multi-axial stressing are proposed: *independent hardening* and *coupled hardening*. Both reproduce the six input stress-strain curves, $\hat{\sigma}_i(\varepsilon_i^P, \dot{\varepsilon}_i^P)$, precisely when σ_i acts singly such that $\dot{\varepsilon}_i^P$ is positive and constant.

5.2. Finite Element Simulation with the Continuum Model

Three-dimensional dynamic finite-element calculations have been used to simulate tests of 304 stainless steels honeycomb-core sandwich beams under shock loading imparted by Al-alloy foam projectiles (Fig. 24). The true stress/strain behavior is represented by the rate-dependent bilinear relation

$$\sigma = \begin{cases} E\varepsilon & \varepsilon \le \dfrac{k\sigma_Y}{E} \\ k\sigma_Y + E_t\left(\varepsilon - \dfrac{k\sigma_Y}{E}\right) & \varepsilon > \dfrac{k\sigma_Y}{E} \end{cases} \tag{33}$$

The following choice of material parameters were used: $E = 210GPa$, $\sigma_Y = 210MPa$, $E_t = 2.1GPa$, $\dot{\varepsilon}_0 = 4916s^{-1}$, $m = 0.154$, $\rho = 8000kg/m^3$, and Poisson's ratio $v = 0.3$.

The sandwich beam and projectile were both fully meshed using eight-node linear brick elements with reduced integration. The beams were rigidly clamped at both ends. The computations were conducted by imposing the initial velocity, v_0, uniformly on the projectile. By symmetry only a quarter of the system was modeled (Fig. 24b). The computations are carried out using ABAQUS Explicit.

Since the foam has minimal strain-rate dependence, a rate-independent constitutive law was adopted for the projectile. This constitutive law is capable of accurately modeling the dynamic response of the projectile under distributed pressure load. The six stress-strain curves calibrated by unit cell model calculations were used as the input data. Preliminary results are summarized on Figures 25-27, where they are compared with the corresponding experimental measurements and with results from fully-meshed discrete model calculations. The response most sensitive to the choice of the constitutive law is the core crushing strain. We note that this version of the constitutive law provides reasonable estimates, but nevertheless, underpredicts the crushing strain at the highest impulse. To address this discrepancy, this effort is continuing by examining such issues as mesh size dependence, strain rate sensitivity in shear and imperfections.

Appendix: Panel Design Procedures

The panel geometries selected for both the finite element simulations and the experiments were based on design and optimization procedures described elsewhere (Rathbun *et al.* 2004a). The procedures employ approximate analytical models that describe the conditions for both core and face failure by either plastic yielding or buckling. Practical considerations associated with the thicknesses of commercially available materials and the size limitations imposed by the furnace used for brazing were also taken into account. A synopsis of the procedures follows.

Basic Mechanics

Analyses were performed for sandwich panels subject to generalized bending, with maximum moment M and maximum transverse shear V (both per unit width). The pertinent non-dimensional load index for strength-based designs is V^2/EM [Ashby *et al.* 2000] where E is Young's modulus. The ratio of the maximum M and V defines a characteristic length scale, $\ell \equiv M/V$ [Wicks and Hutchinson 2001]. The non-dimensional weight index is $\Psi = W/\rho\ell$ [Ashby *et al.* 2000], where W is the structural weight per unit area and ρ the density of the solid material. Designs that minimize weight, Ψ, for specified load, V^2/EM, are found by establishing the load capacity for all possible failure modes, within the core as well as the faces, and then varying the dimensions to determine the lowest weight [Ashby *et al.* 2000, Wicks and Hutchinson 2001, Rathbun *et al.* 2004a]. These procedures also define the operative failure modes and their transitions.

The four possible failure modes for the square honeycomb core sandwich structure are face sheet yielding, face sheet buckling, core web yielding and core web buckling. The associated constraint functions in the optimization are [Rathbun *et al.* 2004a]:

Face yielding: $\dfrac{V^2}{EM}\dfrac{1}{\varepsilon_y}\dfrac{\ell^2}{t_f H_c} \leq 1$ (A1)

Face buckling: $\dfrac{V^2}{EM}\dfrac{\xi^2(1-v^2)}{3.3}\dfrac{H_c\ell^2}{t_f^3} \leq 1$ (A2)

Core yielding: $\dfrac{V^2}{EM}\dfrac{\sqrt{3}\xi}{\varepsilon_y}\dfrac{\ell}{t_c}\le 1$ (A3)

Core buckling: $\dfrac{V^2}{EM}\dfrac{12\xi^3(1-v^2)}{\pi^2(5.4+4\xi^2)}\dfrac{H_c^2\ell}{t_c^3}\le 1$ for $\xi\le 1$ (A4a)

$\dfrac{V^2}{EM}\dfrac{12\xi^3(1-v^2)}{\pi^2(5.4\xi^2+4)}\dfrac{H_c^2\ell}{t_c^3}\le 1$ for $\xi>1$ (A4b)

A failure mode is considered active when the associated constraint function reaches unity. From geometry, the areal density of the square honeycomb core sandwich panel is given by:

$$\Psi=\dfrac{W}{\rho\ell}=2\dfrac{t_f}{\ell}+\dfrac{2t_c}{L_c}\dfrac{H_c}{\ell}$$ (A5)

Design Map and Load Capacity

For the square honeycomb core panels considered in the current study, H_c, L_c, and t_c were held fixed (Table II), leaving t_f and ℓ as the only free variables. The domain boundaries, couched in terms of t_f and ℓ, were then determined by equating pairs of constraint functions. For example, the boundary between face buckling and core yielding was obtained by setting Eqns. A2 and A3 equal to one another, yielding:

$$\ell=\dfrac{3.3\sqrt{3}}{(1-v^2)\xi\varepsilon_y t_c H_c}t_f^3$$ (A6)

Analogously, the boundary between face yielding and face buckling is given by:

$$t_f=\left[\dfrac{(1-v^2)\varepsilon_y}{3.3}\right]^{1/2}\xi H_c$$ (A7)

and that for face yielding and core yielding is:

$$\ell=\dfrac{\sqrt{3}\xi H_c}{t_c}t_f$$ (A8)

These results are plotted on Figure 6. For the choices of H_c, L_c, and t_c used in the current study, the core yielding constraint function exceeds that of core buckling at all loads and hence the latter mechanism does not appear on the map.

The strength contours on Figure 6 were determined by setting the appropriate constraint function equal to unity and solving for the combinations of ℓ and t_f that yield prescribed values of V^2/EM. An analogous procedure was used to obtain the predicted yield loads of the specific honeycomb panels used here, as summarized in Table II.

Structural Efficiency

Structural efficiency, ϕ, is defined as the ratio of the load capacity of the sandwich panel (at initial yield) to that of a solid plate with the same areal density [Ashby 1992]. From elementary beam theory, the latter load is given by [Zok *et al.* 2003]:

$$\frac{V^2}{EM} = \frac{\Psi_s^2 \varepsilon_y}{6} \tag{A.8}$$

Similarly, the *maximum* structural efficiency, ϕ_m, is taken as that of the fully optimized sandwich panel, where the free geometric parameters are H_c, t_f, L_c, and t_c. Pertinent procedures and numerical results for the optimization are presented elsewhere [Rathbun *et al.* 2004a]. The resulting values of ϕ and ϕ_m are summarized in Table II.

References

Ashby, M.F., 1992, *Materials Selection in Mechanical Design* (Pergamon Press, Oxford), 132–151.

Ashby, M.F., Evans, A.G., Fleck, N.A., Gibson, L.J., Hutchinson, J.W., Wadley, H.N.G., 2000, *Metal foams: A design guide* (Butterworth Heinemann, Boston).

Deshpande, V.S., Fleck, N.A., Ashby, M.F., 2001, *Journal of the Mechanics and Physics of Solids*, **49**,1747-1769.

Hill, R., 1947, *Proceeding of the Royal Society*, **A193,** 281-297.

Qiu, X., Deshpande, V.S. and Fleck, N.A., 2003, *European Journal of Mechanics A – Solids*, **22** (6), 801-814.

Rathbun, H.J., Zok, F.W., Evans, A.G., 2004a, *International Journal of Solids and Structures*, submitted.

Rathbun, H.J., Radford, D.D., Xue, Z., Yang, J., Deshpande, V., Fleck, N.A., Hutchinson, J.W., Zok, F.W., Evans, A.G., 2004b, *International Journal of Solids and Structures*, submitted.

Wadley, H.N.G., Fleck, N.A. and Evans, A.G., 2003, *Composites Science and Technology*, **63** (16), 2331-2343.

Wicks, N., Hutchinson, J.W., 2001, *International Journal of Solids Structures*, **38**, 6165–5183.

Wicks, N. and Hutchinson, J.W., 2004, *Mechanics of Materials*, **36** (8), 739-751

Xue Z.Y., Hutchinson J.W., 2003, *International Journal of Mechanical Sciences*, **45** (4), 687-705.

Xue Z.Y., Hutchinson J.W., 2004, *Int. J. Numer. Meth. Engng*, in press.

Zok, F.W., Rathbun, H.J., Wei, Z. Evans, A.G., 2003, *International Journal of Solids Structures* **40**, 5707-5722.

Zok, F.W., Waltner, S.A., Wei, Z., Rathbun, H.J., McMeeking, R.M., Evans, A.G., 2004, *International Journal of Solids and Structures*, in press.

Table I   **Summary of Initial Yield Stresses of Honeycomb Cores**

		Finite Element Analysis		Analytical Predictions	
		$\bar{\rho}_c = 4\%$	$\bar{\rho}_c = 10\%$	$\bar{\rho}_c = 4\%$	$\bar{\rho}_c = 10\%$
Transverse Compression	$\dfrac{\sigma_{33}^{u}}{\bar{\rho}_c \sigma_y}$	-0.97	-1.02	-1.00	-1.00
	$\dfrac{\sigma_{33}^{c}}{\bar{\rho}_c \sigma_y}$	-0.98	-1.13	-1.16	-1.16
In-plane Tension	$\dfrac{\sigma_{11}^{u}}{\bar{\rho}_c \sigma_y}$	0.57	0.57	0.58	0.59
Transverse Shear	$\dfrac{\sigma_{13}^{s}}{\bar{\rho}_c \sigma_y}$	0.29	0.29	0.29	0.30

Table II. **Design Parameters for Sandwich Panels**

	I	II	III	IV	V
Face thickness, t_f (mm)	0.76	1.22	0.76	1.22	0.76
Core member thickness, t_c (mm)	0.25	0.25	0.25	0.25	0.25
Cell size, L_c (mm)	12.7	12.7	12.7	12.7	12.7
Core thickness, H_c (mm)	12.7	12.7	12.7	12.7	12.7
Loading span, S (mm)	254	254	127	127	184
End condition	Clamped	Clamped	Simple support	Simple support	Simple support
Load capacity at yield[1], $V^2/EM \times 10^6$	2.31	2.31	2.31	2.31	1.14
Structural efficiency[2], ϕ	13.5	6.4	13.5	6.4	14.0
Maximum structural efficiency[3], ϕ_m	13.9	9.6	13.9	9.6	20.2
Efficiency ratio, ϕ/ϕ_m	0.97	0.67	0.97	0.67	0.69

[1] Based on analytical model presented in Appendix.
[2] Defined as ratio of load capacity of sandwich panel to that of equivalent *solid* plate (Appendix).
[3] Structural efficiency of *optimized* panel of same weight (Appendix).

Table III   Initial Yield Loads of Honeycomb Core Panels

	Yield load[4]: $V^2/EM \times 10^6$				
	I	II	III	IV	V
Analytical model (Appendix)	2.31	2.31	2.31	2.31	1.14
Discrete FEA	2.27/2.43	2.29/2.50	2.26/2.43	2.30/2.53	1.34/1.51
Continuum FEA (shear input)	2.44/2.57	2.57/2.65	2.51/2.58	2.62/2.71	1.47/1.63
Experimental	1.6/2.4	2.0/2.6	2.1/2.5	2.1/2.7	1.2/1.5

---

[4] The two values correspond to load at onset of non-linearity and load at an offset displacement of $\delta/S=10^{-3}$.

Table IV   Load Capacities and Associated Displacements of Simply Supported Beams

	Load maximum: $V^2/EM \times 10^6$			Displacement at load maximum: δ/S		
	III	IV	V	III	IV	V
Discrete FEA	4.60	5.67	2.30	0.094	0.067	0.06
Continuum FEA (shear input)	4.34	5.86	2.34	0.090	0.174	0.052
Experimental	3.9	5.6	2.4	0.040	0.083	0.055

(a)

(b)
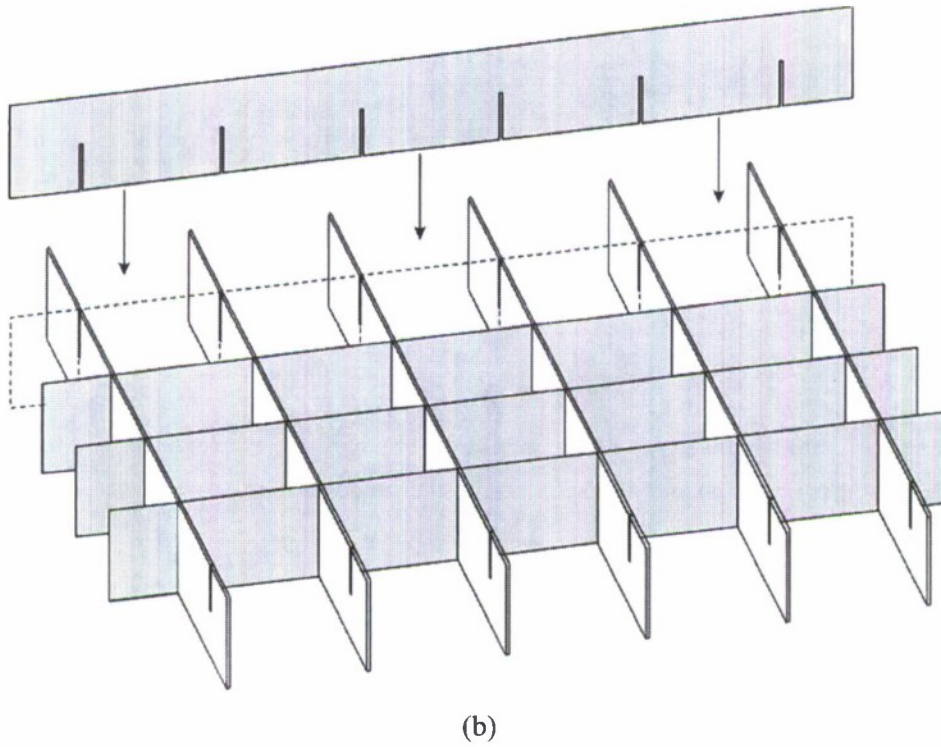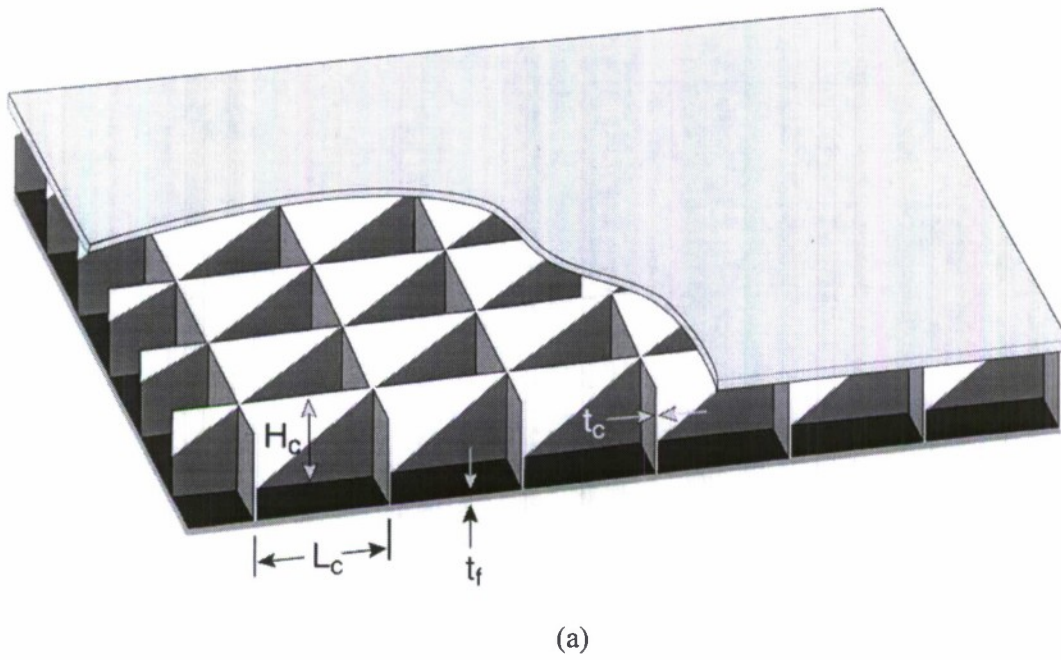
Figure 1. Schematics of (a) square honeycomb panel and (b) method of core assembly.
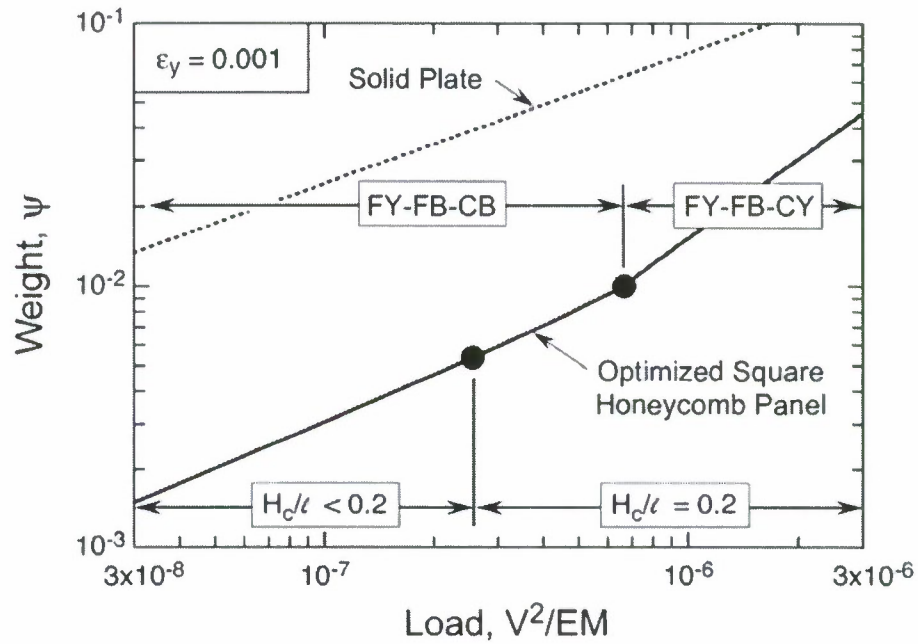
Figure 2. A synopsis of analytical results for minimum weight design of square honeycomb panels and associated transitions in design constraints.
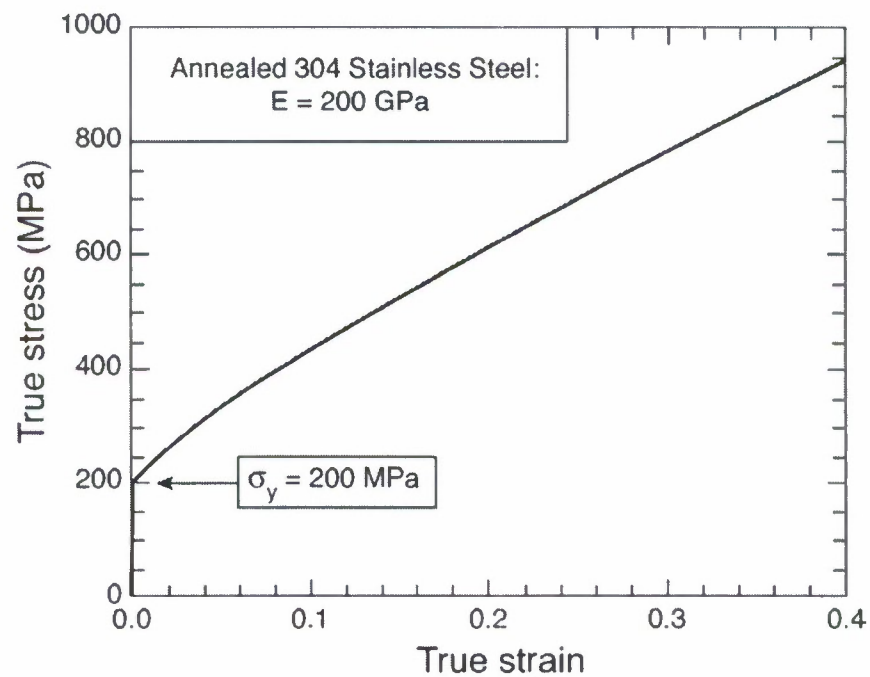
Figure 3   Stress-strain curve for annealed 304 stainless steel, measured in uniaxial tension.

(a) Transverse Compression

(b) In-plane tension
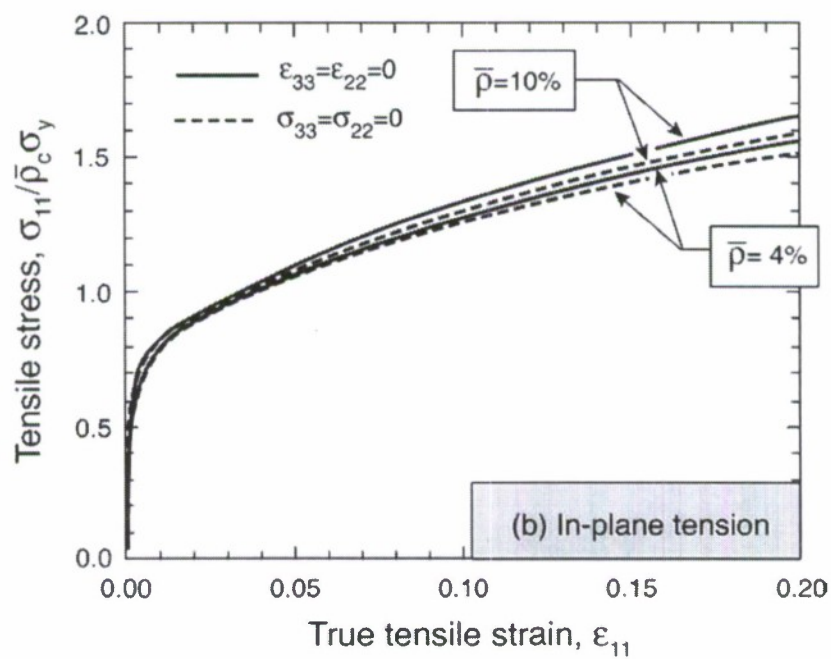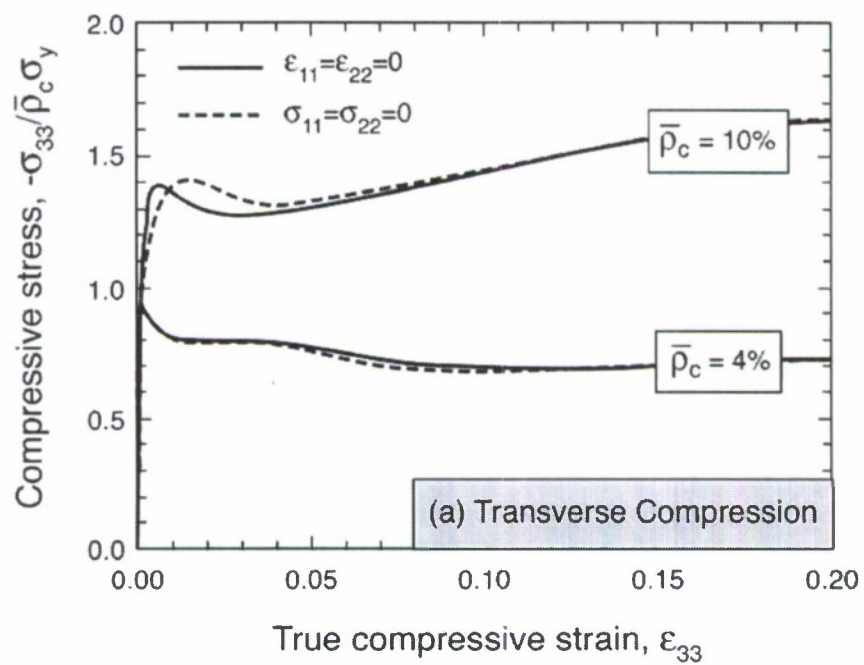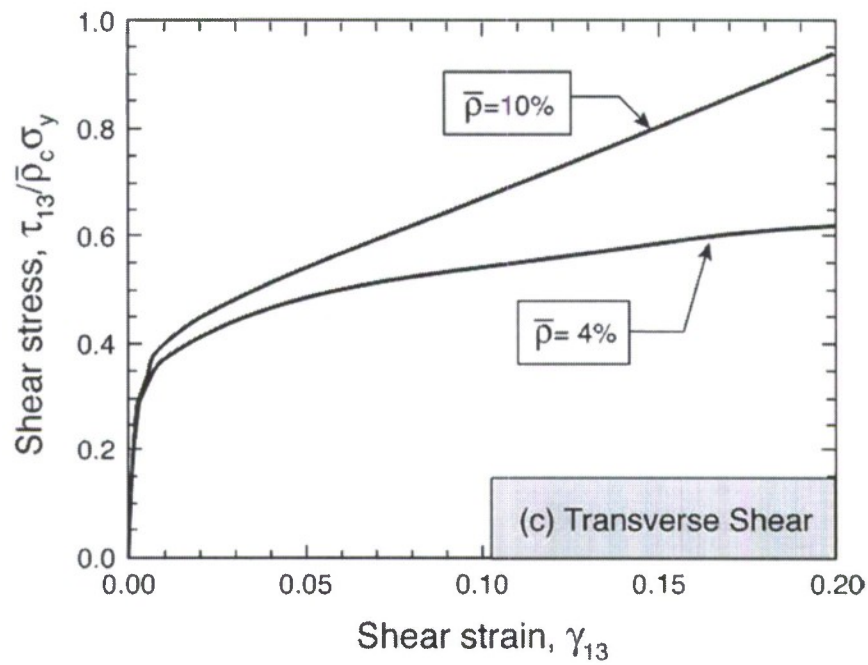
Figure 4

Figure 4   FE simulations of tress/strain curves for square honeycomb cores made from 304 stainless steel with either 4% or 10% relative density.
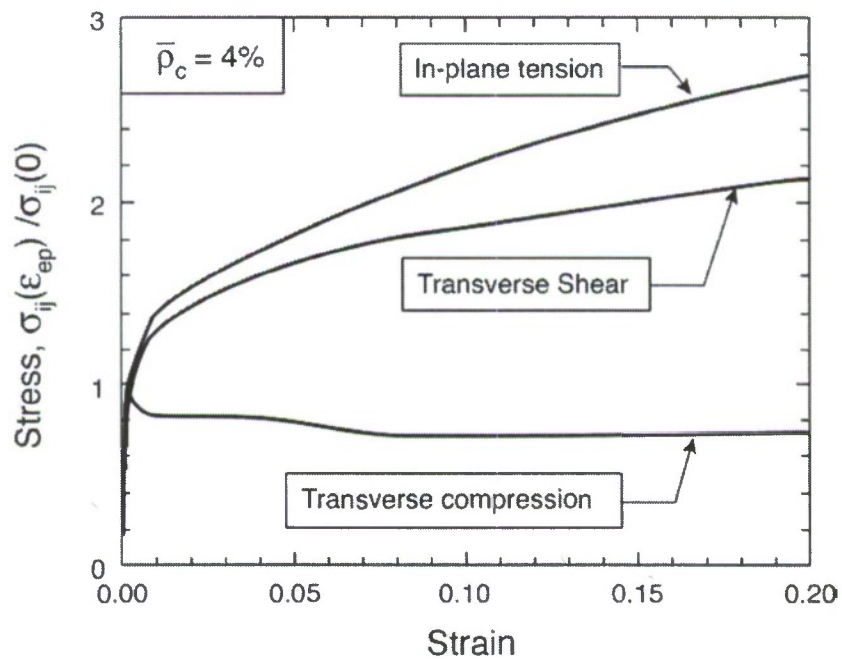
Figure 5   Hardening response of honeycomb cores, with stress normalized by respective yield strength.
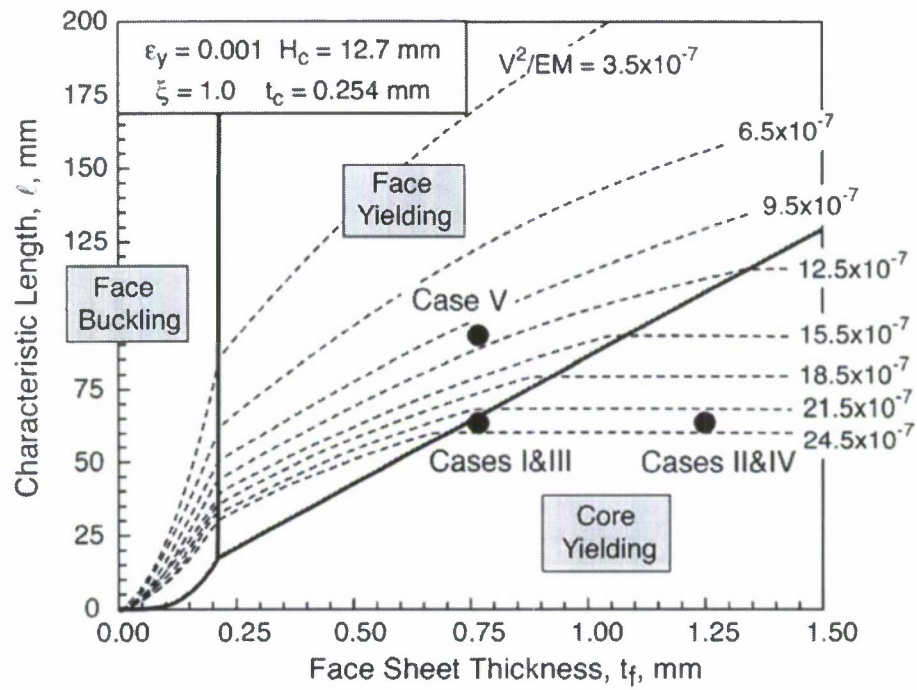
Figure 6   A design map used to select test configurations that probe the role of the core in the load capacity.

(a)   (b)
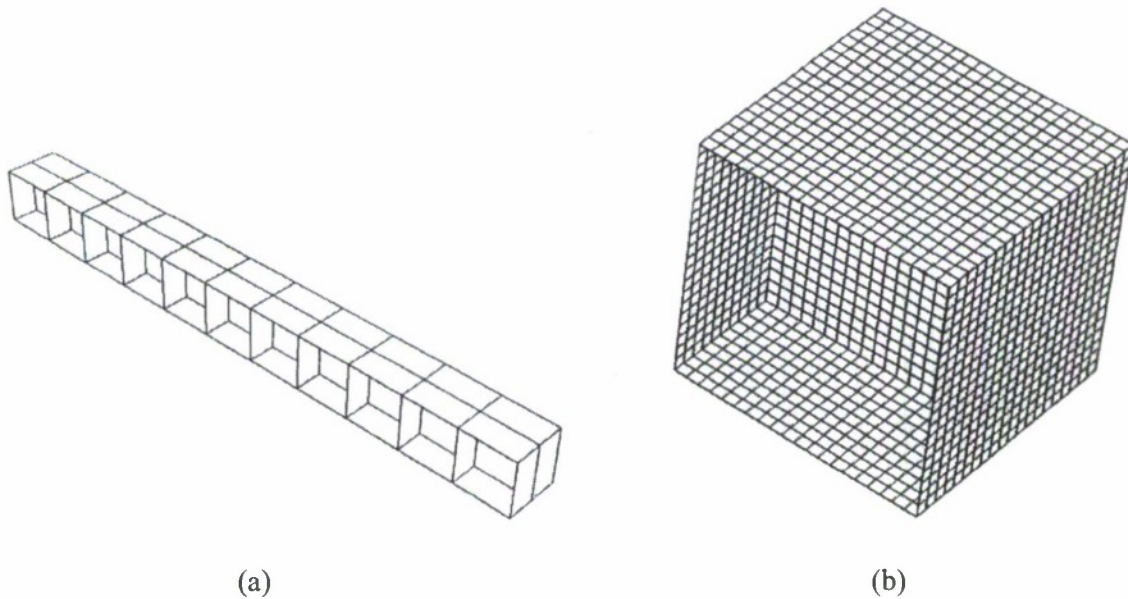
Figure 7   An example of the finite element mesh used for discrete analysis: (a) arrangement of core and face members, (b) detail of FE mesh within a single unit cell.
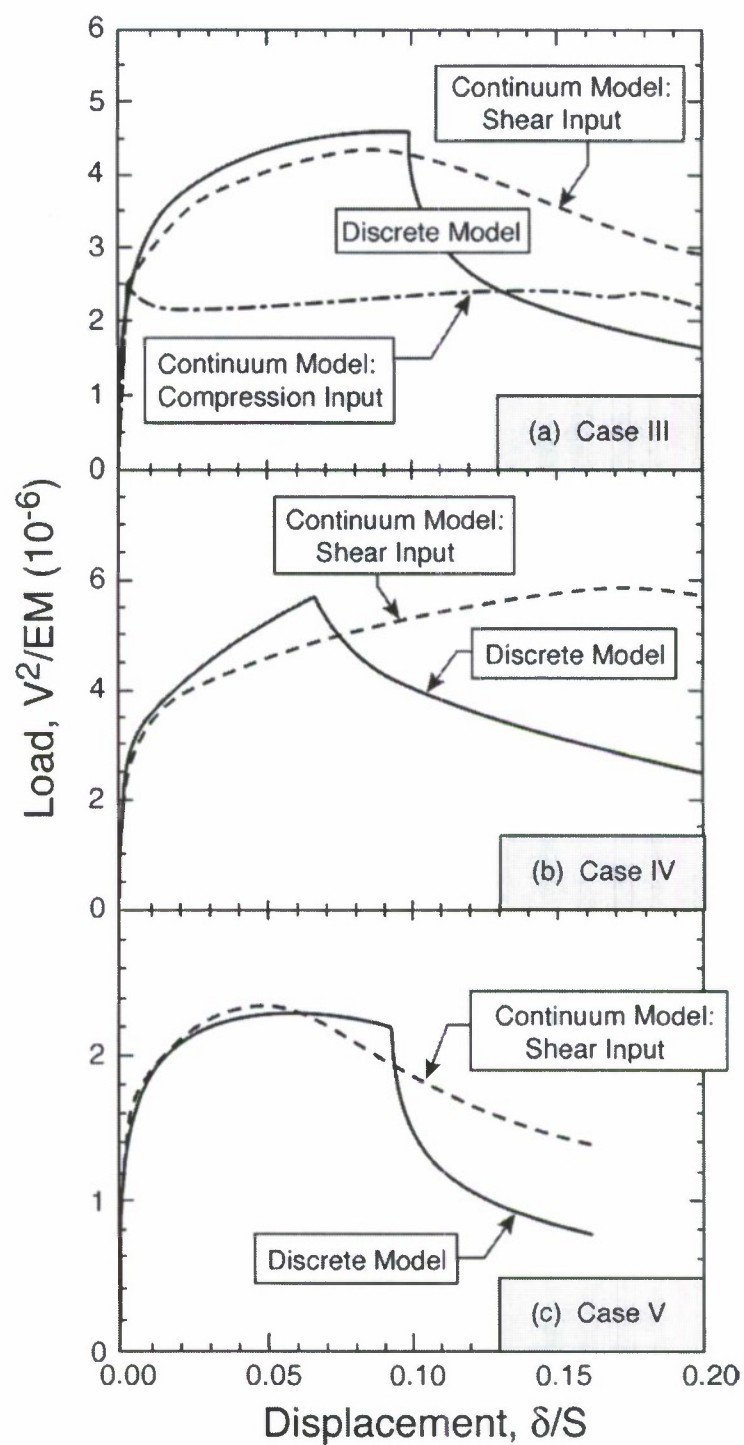
Figure 8   Comparison between discrete and continuum calculations for tests with simply
supported boundaries.
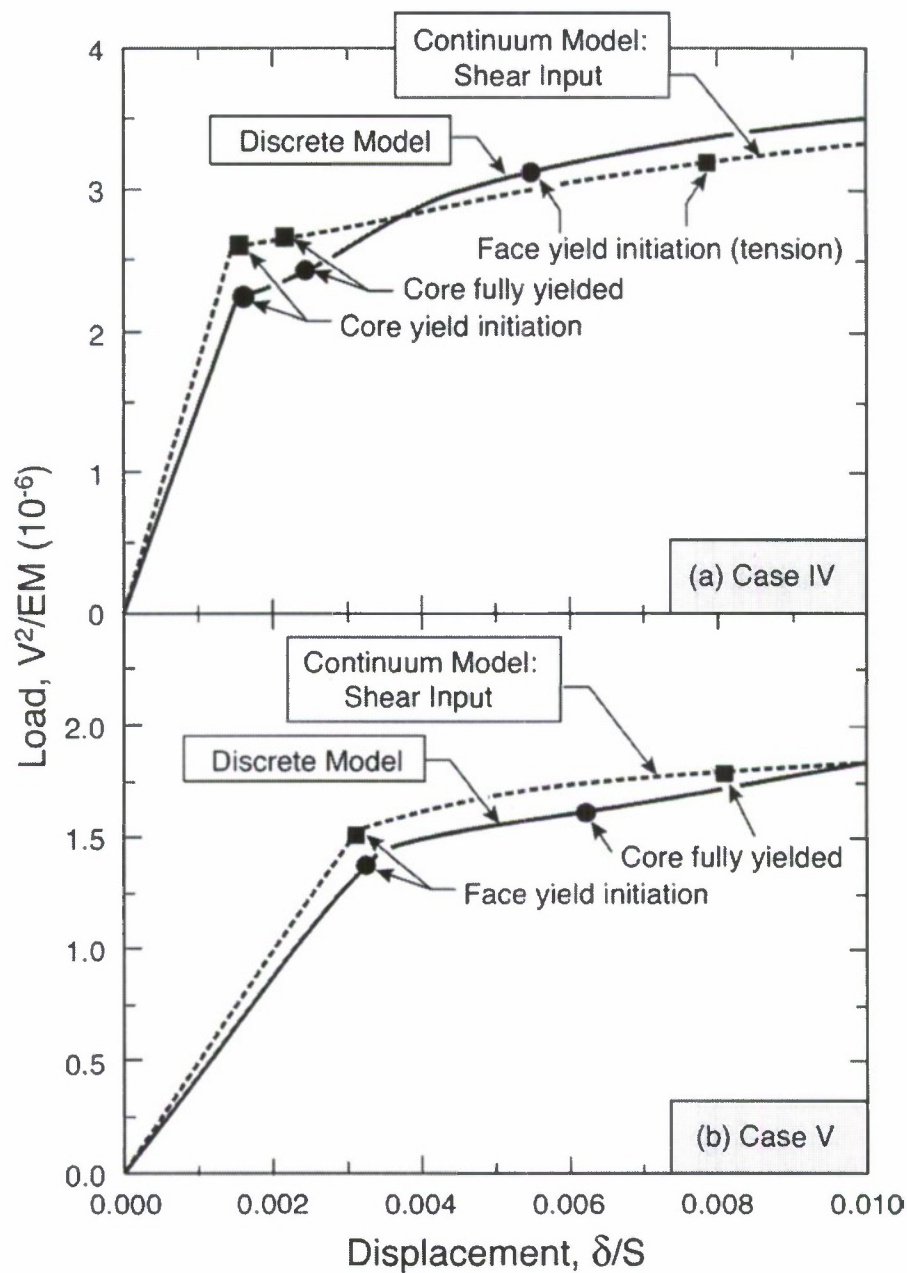
Figure 9   Small strain behavior of simply supported beams (from Figure 8), showing critical loads for core and face yielding.

Distribution of shear strain (%)
Case IV – δ/S=0.06

(a) Discrete Model
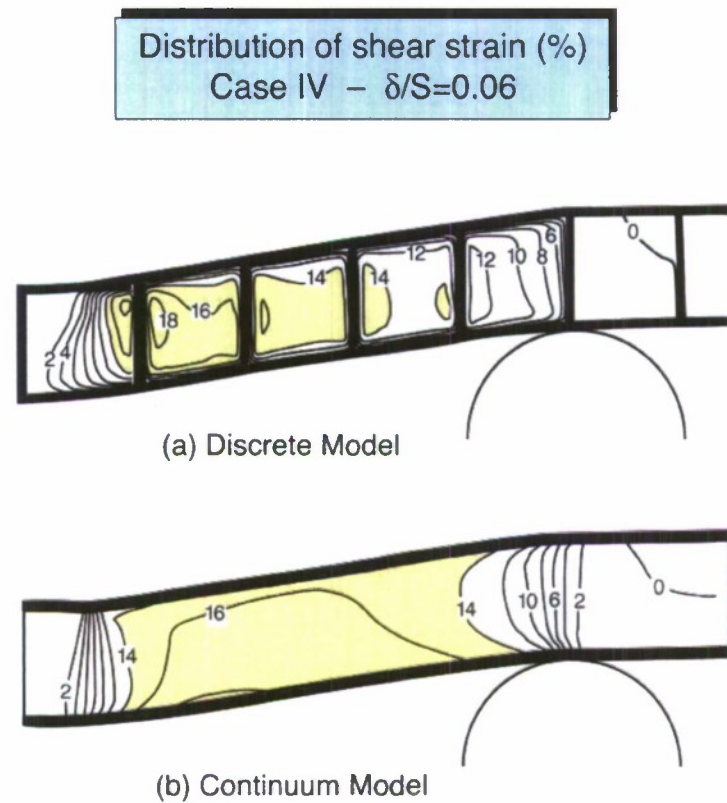
(b) Continuum Model

Figure 10   Comparison of predicted shear strain distributions within the core from both discrete and continuum models. Shading denotes regions of high strain: γ≥14%.

(a) Discrete Model   (b) Continuum Model
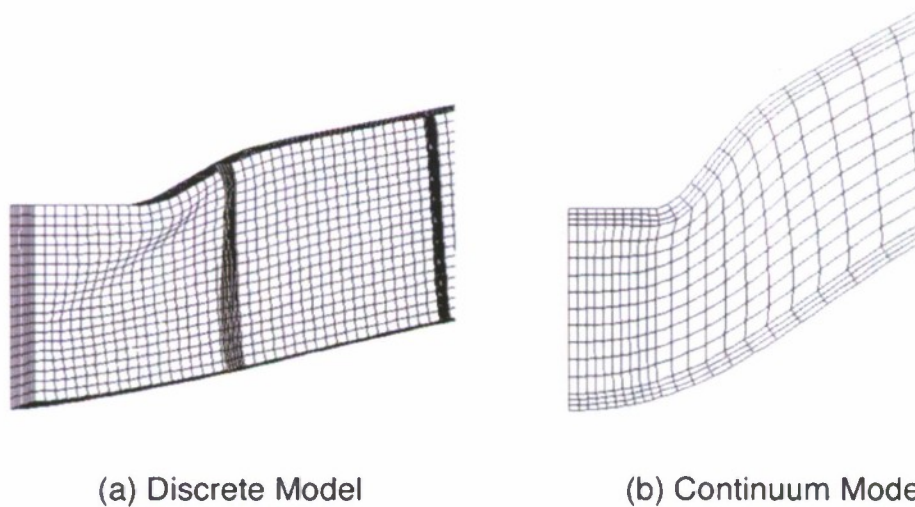
Figure 11   Deformation pattern within core in the region directly beneath the loading platten, shortly after attainment of the load maximum (case IV).
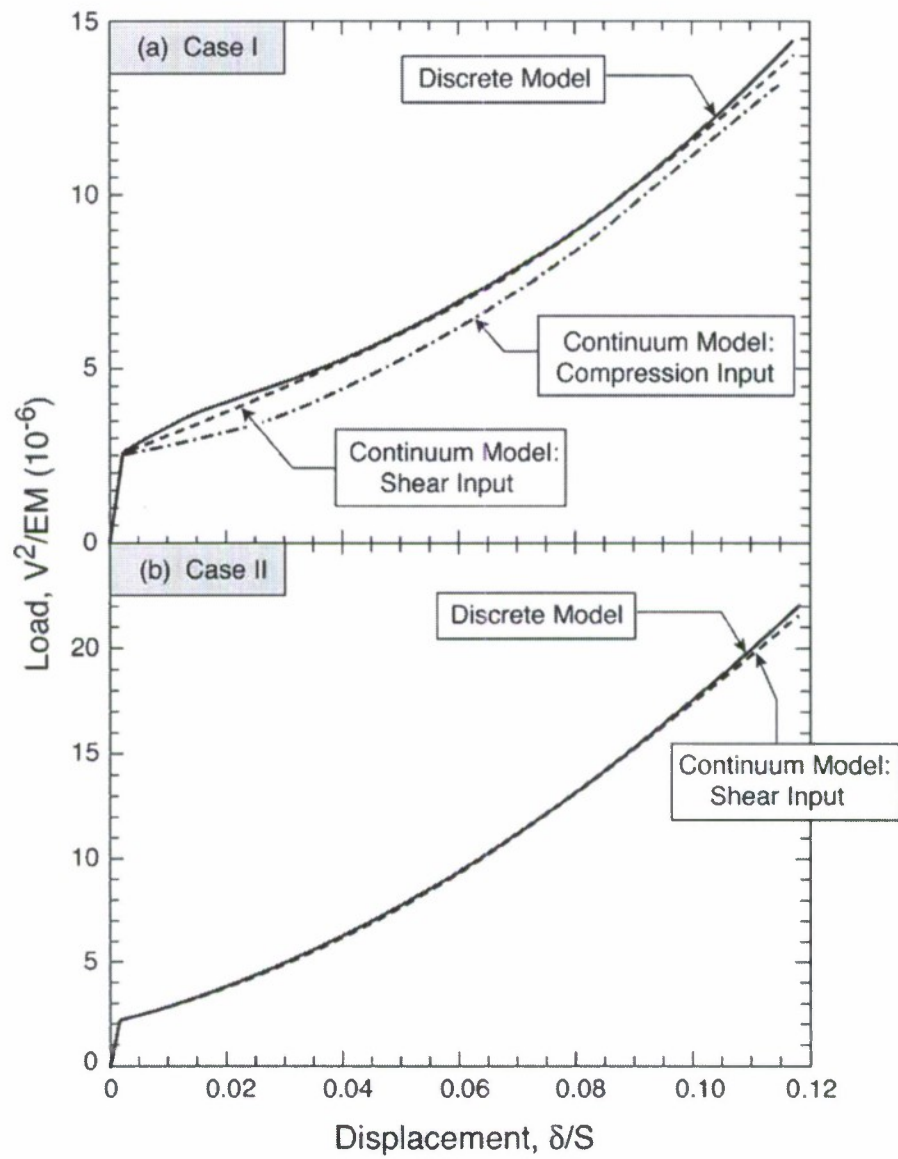
Figure 12 Comparison between discrete and continuum calculations for tests with clamped boundaries.
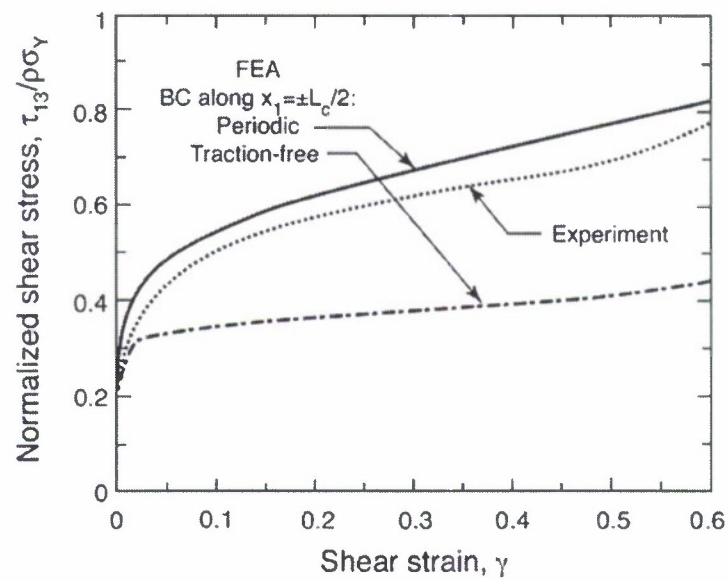
Figure 13   Comparisons of measured and predicted stress-strain curves in out-of-plane shear.
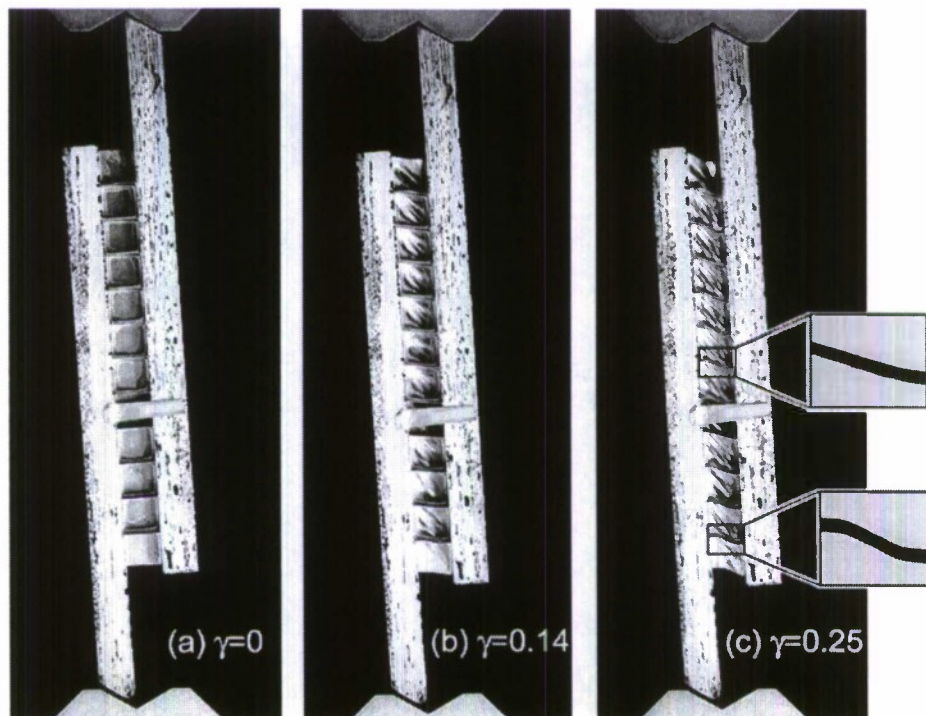
Figure 14   Sequence of photographs showing (a) shear test specimen (prior to loading) and (b, c) deformation and buckling of core members during plastic straining. Insets in (c) illustrate differences in deformation patterns of transverse core members near the edge and in the specimen center.
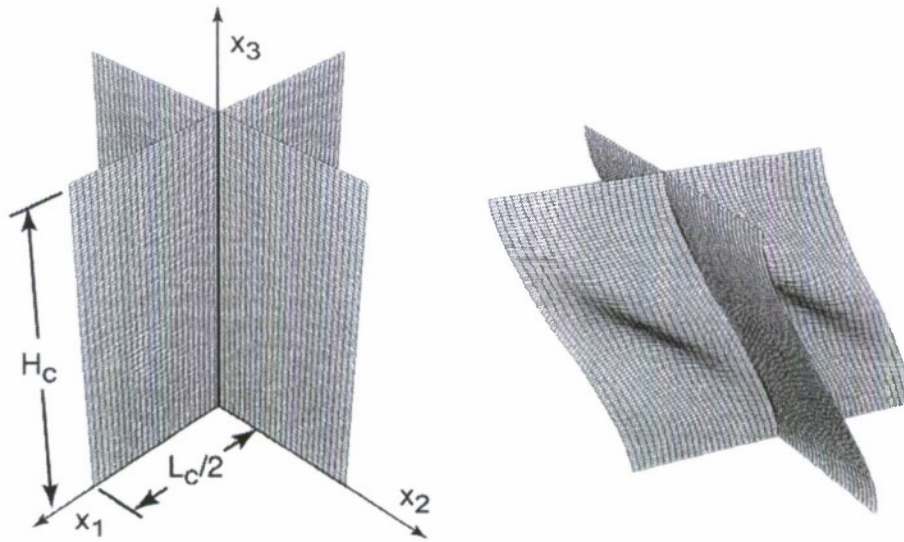
Figure 15   Finite element mesh of honeycomb core under shear loading.
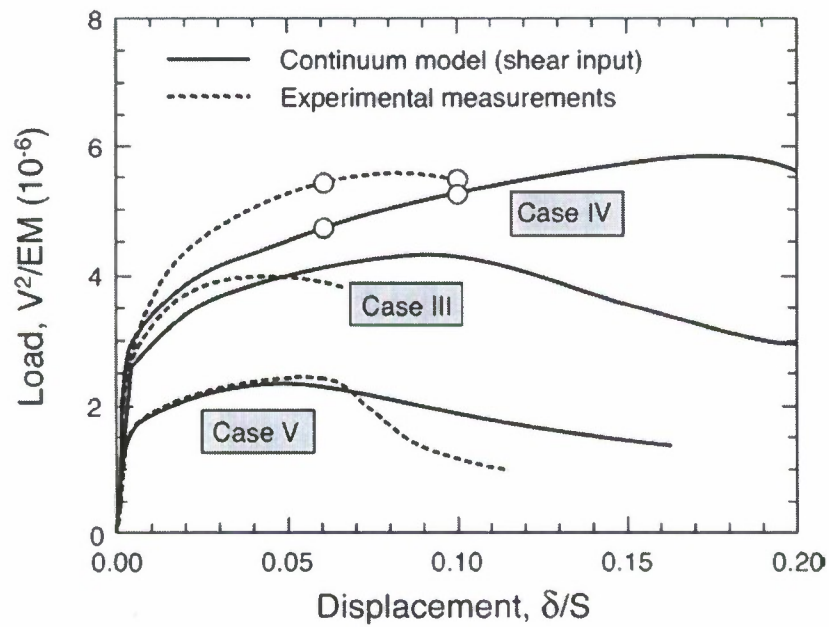
Figure 16   Comparisons of measured and simulated bending responses for simply supported end conditions. Open circles on curves for case IV correspond to points associated with Figures 17 and 18.
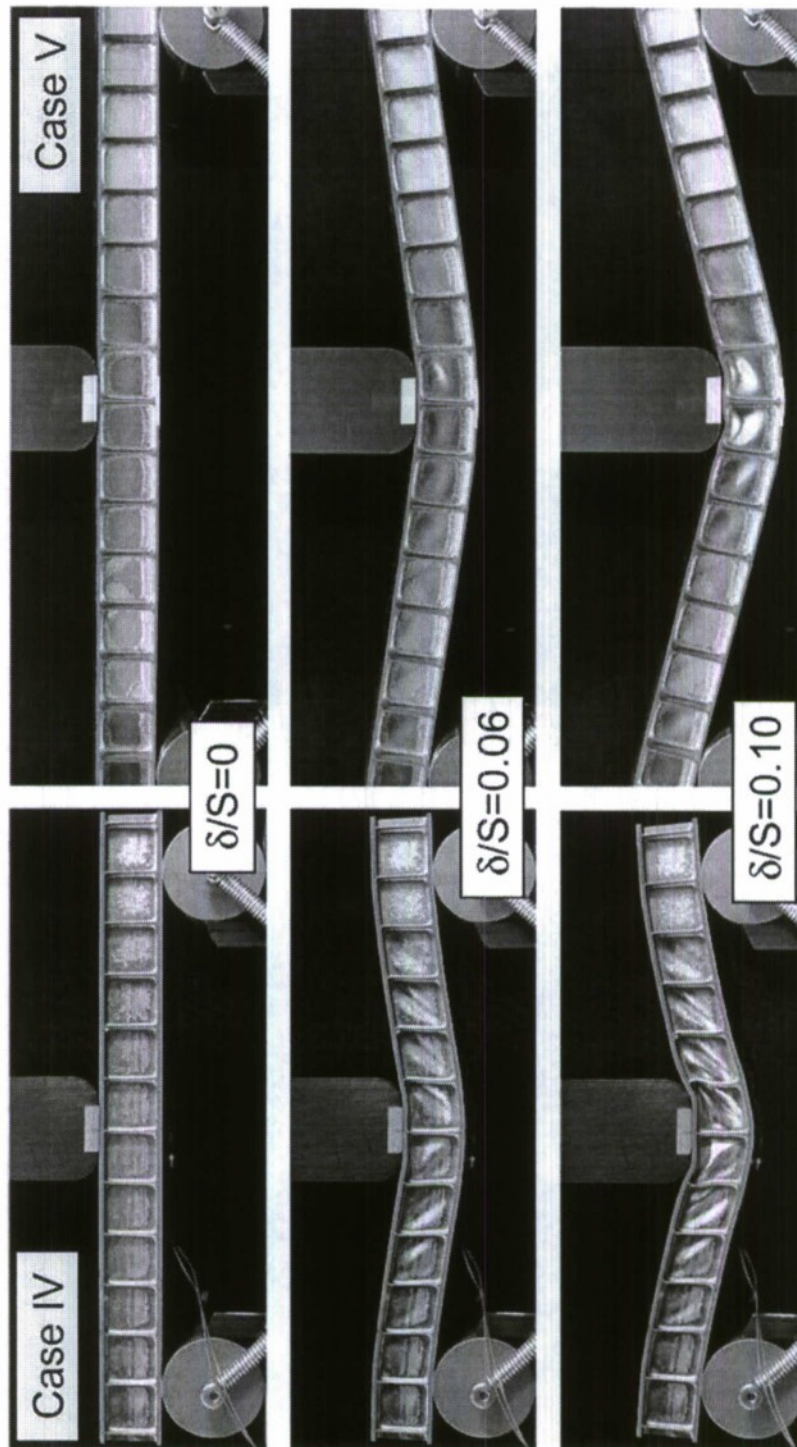
Figure 17   Beam deformation at increasing load-point displacement for cases IV and V.
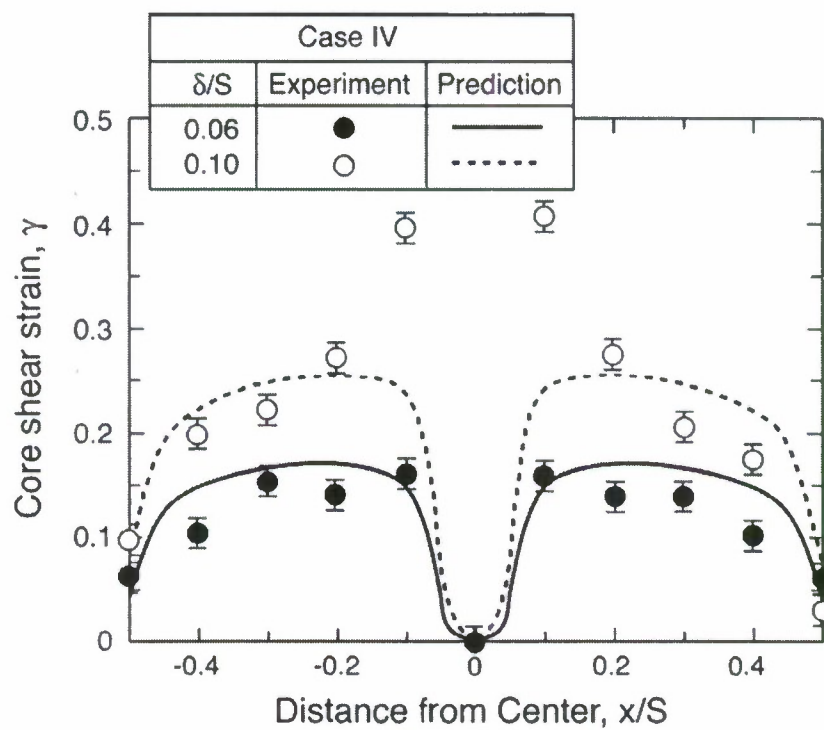
Figure 18   Distributions of core shear strain, both measured and predicted, for specimen designed to fail by core shear.
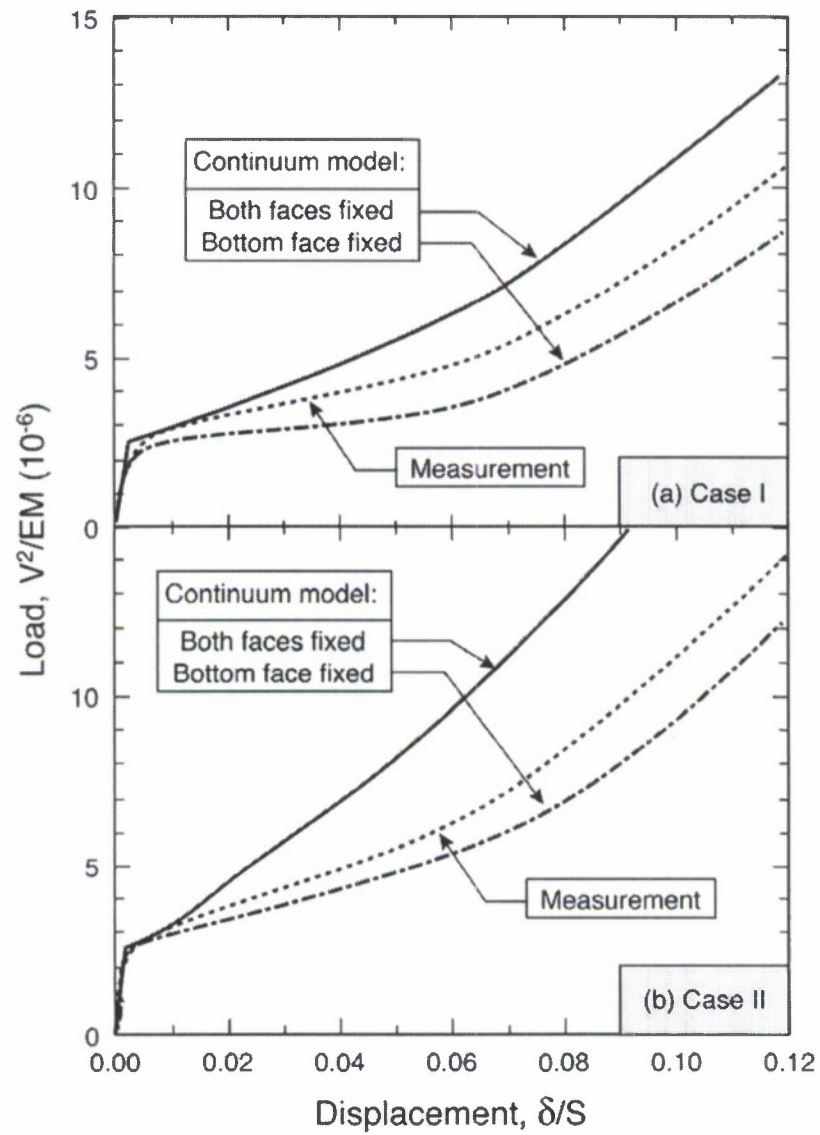
Figure 19   Measured and simulated bending responses for clamped end conditions.
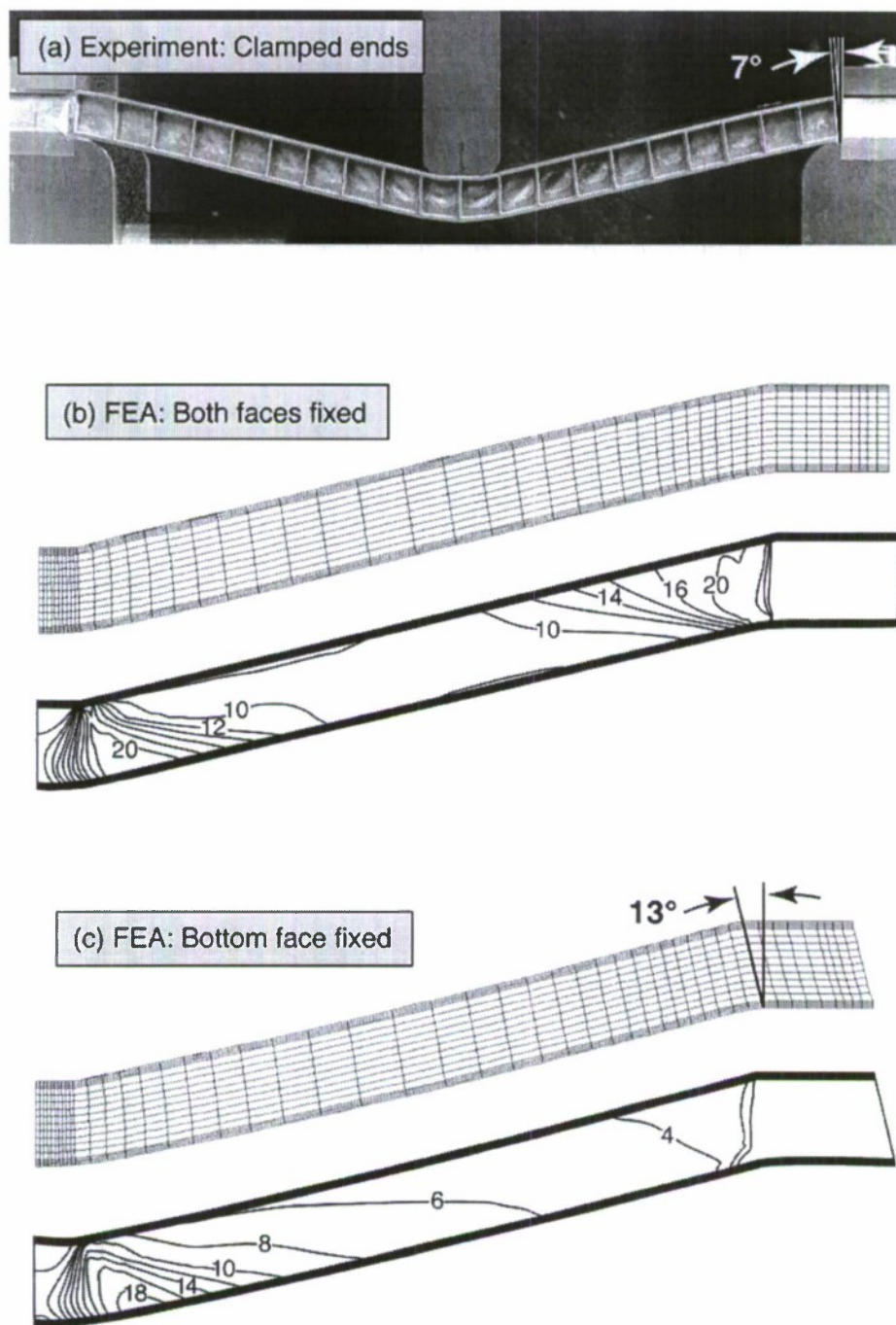
Figure 20   Comparisons of FEA and experimental observations on a clamped bending test. Note the differences in the degree of core rotation due to face stretching at the clamped boundaries: (a) 7° in the experiment, (b) 0° when both faces are fully clamped, and (c) 13° when only the bottom face is clamped. Contours in (b) and (c) are shear strains in %.
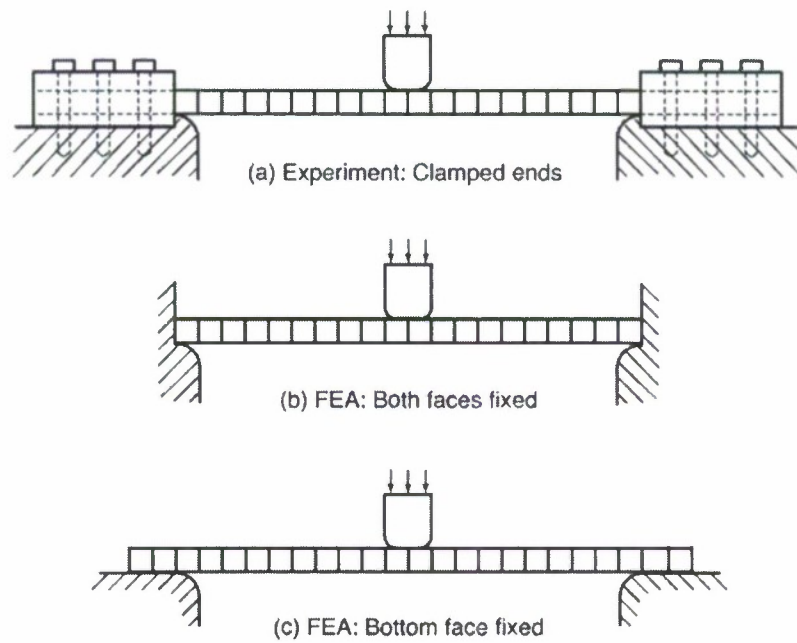
Figure 21   Schematic illustrations of the boundary conditions in both the experiments and the finite element calculations.
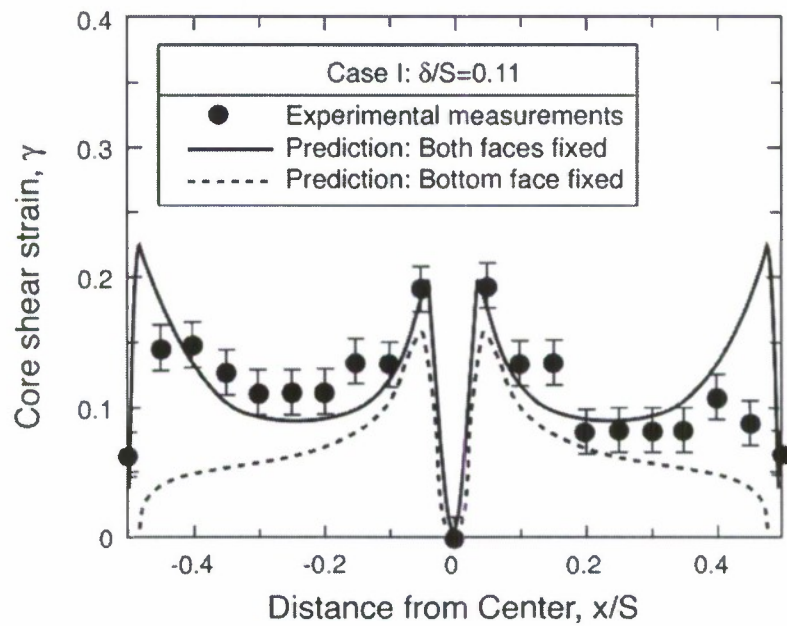
Figure 22   Distribution of core shear strain for clamped specimen.
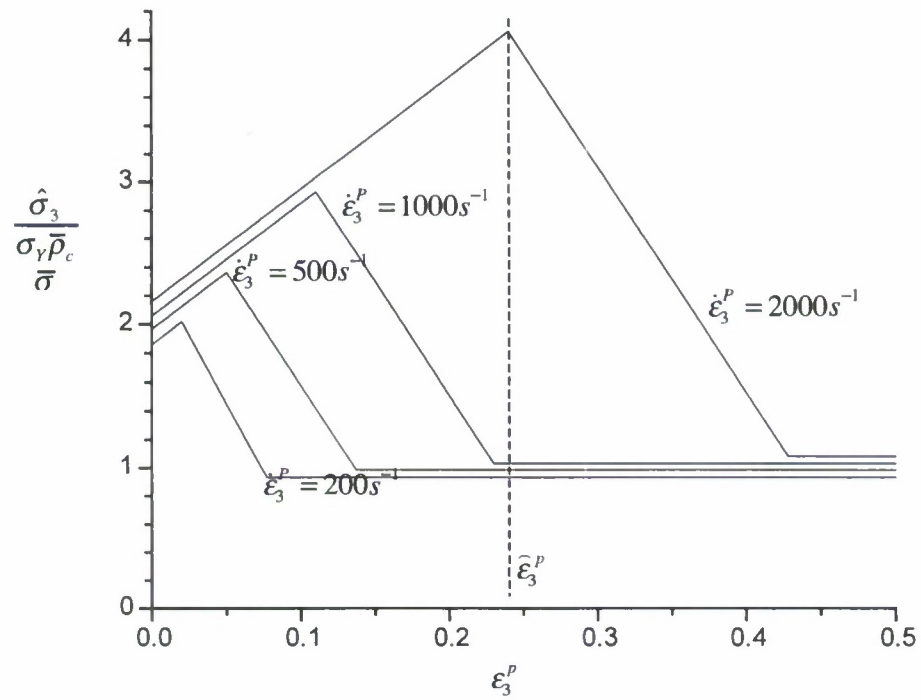
Figure 23   Form of the input function assumed for dynamic crushing of square honeycomb core.
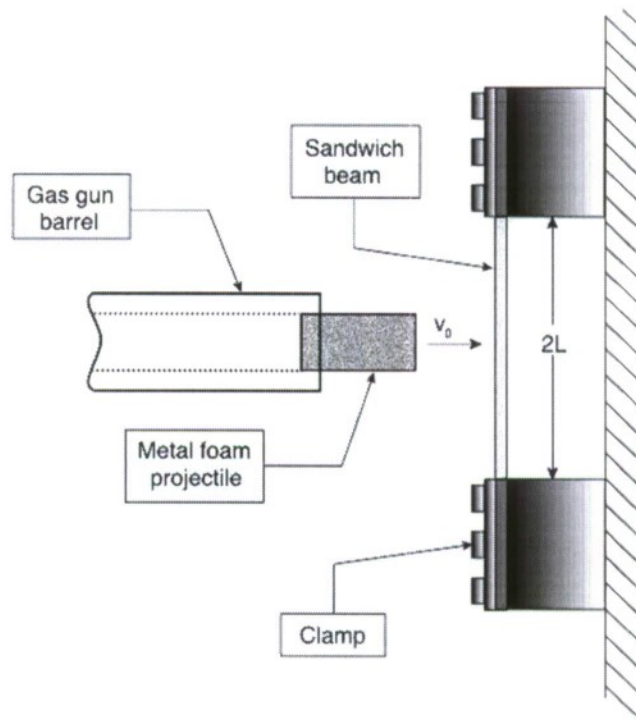
(a)
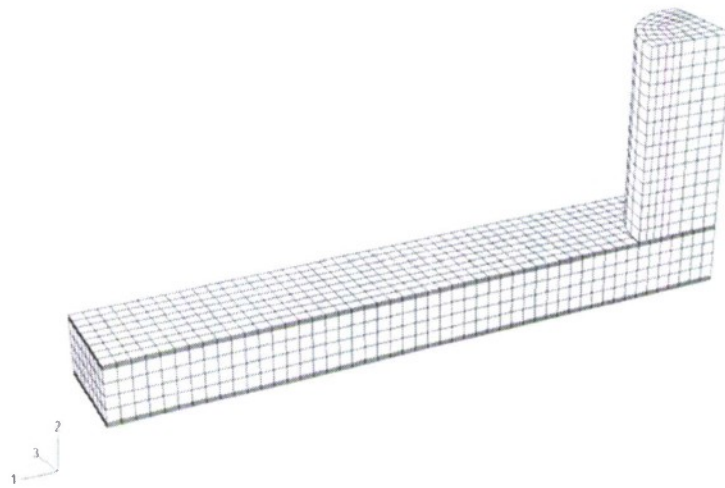
(b)

Figure 24 (a) A schematic showing the test used to impose an impulse representative of a blast.
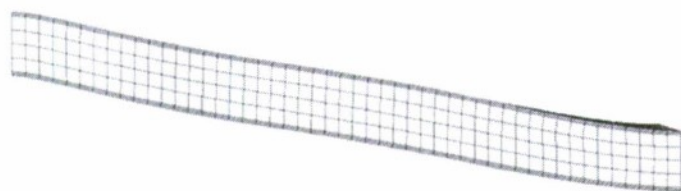(b) A typical finite element mesh for a quarter of the system.
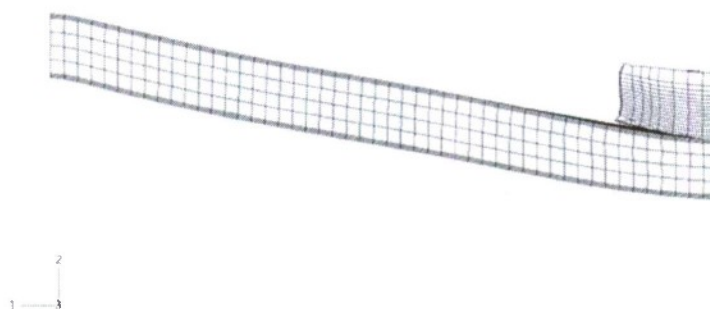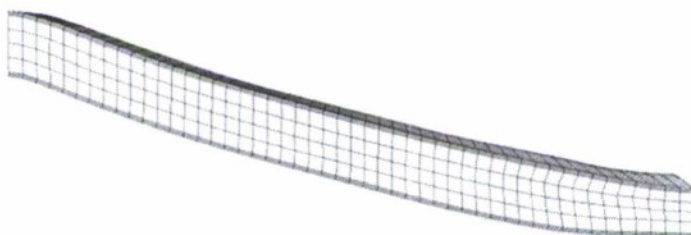
(a)
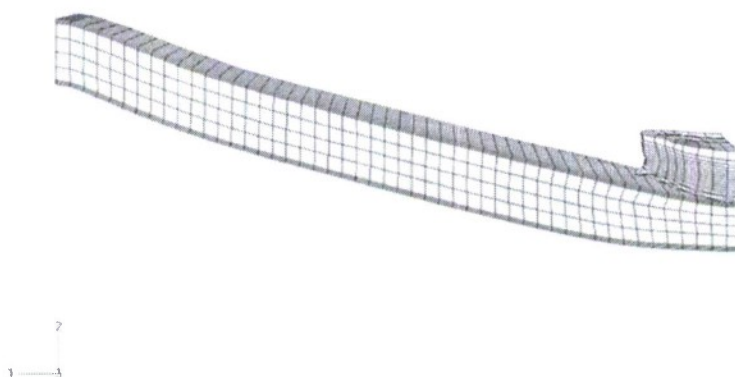
(b)

Figure 25.   Representative projectile and sandwich beams at the maximum deflection from the finite element simulation, at impulse levels: (a) 3.8 and (b) 4.6 kPa s
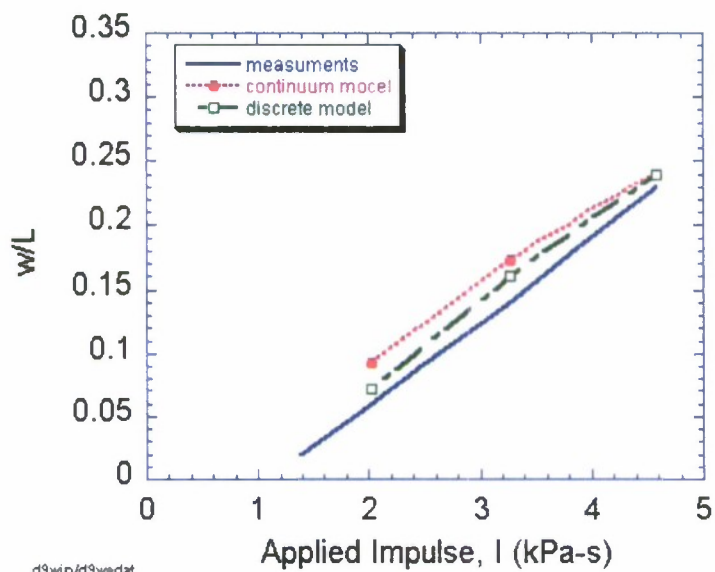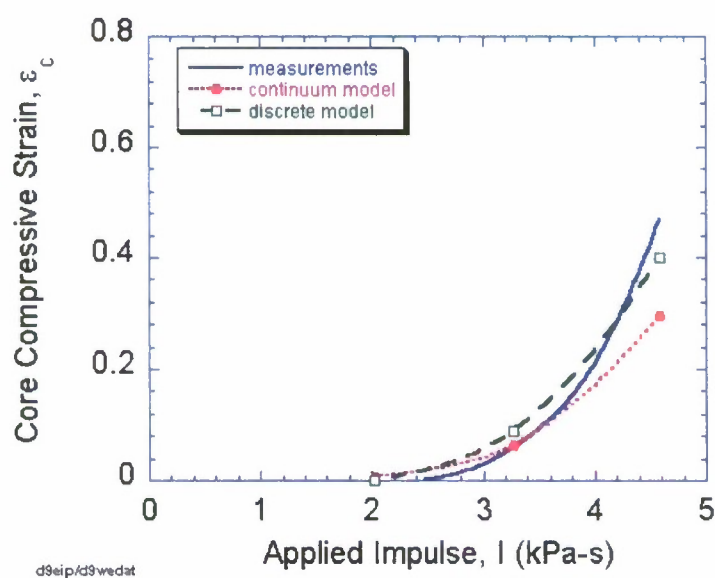
(a)

(b)

Figure 26   Representative sandwich beams following dynamic testing from the finite element simulation, at impulse levels: (a) 3.8 and (b) 4.6 kPa s

(a)

(b)

Figure 27 (a) Measurements and simulations of back face deflections as a function of applied impulse. (b) Core compressive strain in sandwich beams at impact site.